Dimerization and exotic criticality in spin-S chains

THÈSE N^{O} 7621 (2017)

PRÉSENTÉE LE 23 MARS 2017

À LA FACULTÉ DES SCIENCES DE BASE
CHAIRE DE THÉORIE DE LA MATIÈRE CONDENSÉE
PROGRAMME DOCTORAL EN PHYSIQUE

ÉCOLE POLYTECHNIQUE FÉDÉRALE DE LAUSANNE

POUR L'OBTENTION DU GRADE DE DOCTEUR ÈS SCIENCES

PAR

Natalia CHEPIGA

acceptée sur proposition du jury:

Prof. R. Houdré, président du jury
Prof. F. Mila, directeur de thèse
Prof. T. Giamarchi , rapporteur
Prof. U. Schollwöck , rapporteur
Prof. H. Rønnow, rapporteur

ÉCOLE POLYTECHNIQUE
FÉDÉRALE DE LAUSANNE

Suisse
2017

Some people believe that the teacher robs his students.
Others - that students rob the teacher.
I think that both are right and participation in this mutual robbery is amazing.
— L.D. Landau

To my teachers. . .

Acknowledgements

I would like to thank Prof. Frédéric Mila for his careful supervision, endless ideas and his sincere interest in my PhD and further career. He encourages a sense of exploration in his students, and I have benefited from frequent travels, learning about other people and countries from around the globe. I also appreciated the balance he has found between providing guidance and encouraging independence in his students, for example in choice of projects, courses, teaching etc.

I would also like to thank our collaborator Prof. Ian Affleck, whose contribution to our projects has brought them to a new level. His knowledge and ideas have inspired me and encouraged me to further develop numerics in order to confirm his analytical predictions.

I would like to thank all former and present members of our group who make these years unforgettable, inside and outside of the office: Frédéric Michaud for his patience and guidance of my master project; Jérôme Dufour for three weeks in Benasque and two days in Heathrow airport; Francisco and Sandrine Kim for lending their guitar; Andy Smerald, Carolin Boos, Miklos Lajko, Grégoire Vionnet, Pierre Nataf and Tommaso Coletta for scientific discussions, Friday ice-skating and table-tennis matches.

I would like to acknowledge two secretaries - Anna-Maria De Domenico and Tanya Castellino - who always assist and take care of all the paper-work regarding our travels, contracts, visas, apartments etc. That makes our life much easier, thank you!

Finally, I would like to thank my husband for his support and understanding and my mother who always believes in me and constantly reminds me that I am a woman, as well as a physicist.

Lausanne, 8 Mars 2017 Natalia Chepiga

Abstract

In this thesis we have studied the emergence of spontaneously dimerized phases in frustrated spin-S chains, with emphasis on the nature of the critical lines between the dimerized and non-dimerized phases. The main numerical method used in this thesis is the Density Matrix Renormalization Group (DMRG). The DMRG algorithm is a relatively old and well established method for the investigation of the ground-state. In this thesis, we show how to use this algorithm to calculate the excitation spectra of one-dimensional critical systems, known in the context of conformal field theory as conformal towers of states. We have demonstrated that the method works very well for two simple minimal models (the transverse-field Ising model and the three-state Potts model), and we have used it systematically to identify the universality classes and the underlying conformal field theories of various one-dimensional spin systems. It has been known for a long time that the transition to a spontaneously dimerized phase in a spin-1 chain can be either continuous, in the Wess-Zumino-Witten (WZW) $\mathrm{SU}(2)_2$ universality class, or first order. By combining a careful numerical investigation with a conformal field theory analysis, we were able to detect in a frustrated spin-1 chain with competing next-nearest-neighbor and three-site interactions the presence of yet another type of continuous phase transition that belongs to the Ising universality class. In contrast to the WZW $\mathrm{SU}(2)_2$ critical line, at which the singlet-triplet gap closes, the Ising transition occurs entirely in the singlet sector, while the singlet-triplet gap remains open. The use of the standard DMRG approach, along the lines mentioned above, has allowed us to provide explicit numerical evidence for the presence of a conformal tower of singlets inside the spin gap. Moreover, according to field theory, a WZW $\mathrm{SU}(2)_k$ critical line can turn into a first order transition due to the presence of a marginal operator in the WZW $\mathrm{SU}(2)_k$ model. A careful investigation of the conformal towers along the critical lines has allowed us to find the precise location of this point in both $S = 1$ and $S = 3/2$ chains. We have also shown that the nature of the continuous dimerization transitions is related to the topological properties of the corresponding phases, and that the phase diagrams of various frustrated spin chains can be effectively extracted by looking at the local topological order parameter - the degeneracy of the lowest state in the entanglement spectrum. When coupled with the conformal field theory of open systems, DMRG appears to be an extremely powerful tool to characterize not only the phase diagram and the ground-state correlations of quantum one-dimensional systems, but also the excitation spectrum and the conformal structure along critical lines.

Key words: One-dimensional quantum magnetism, frustrated spin chains, three-site interac-

tion, spontaneous dimerization, quantum phase transition, critical lines, universality class, Conformal Field Theory, conformal towers of states, excitation spectrum, Density Matrix Renormalization Group, Matrix Product State, Wess-Zumino-Whitten transition, Ising transition, Kosterlitz-Thouless transition

Résumé

L'objectif principal de cette thèse consiste à étudier l'émergence de phases spontanément dimérisées dans les chaînes de spin-S frustrées, avec une attention particulière sur la nature des lignes critiques entre les phases dimérisées et non-dimérisées. La méthode numérique principalement employée est la méthode du groupe de renormalisation de la matrice densité (DMRG), une méthode bien établie et efficace pour étudier l'état fondamental. Nous expliquons dans cette thèse comment utiliser cet algorithme pour calculer les spectres d'excitation des systèmes critiques unidimensionnels connus sous le nom de tours conformes d'états dans le contexte de la théorie conforme des champs.

Tout d'abord, nous avons démontré que la méthode fonctionne parfaitement sur deux modèles minimaux simples, à savoir le modèle d'Ising et le modèle de Potts à trois états en champ-transverse. Ensuite, nous l'avons utilisée de manière systématique pour identifier les classes d'universalité et les théories conformes des champs sous-jacentes dans différents systèmes de spin. Il est admis depuis longtemps que la transition vers la phase spontanément dimérisée dans une chaîne de spin-1 est continue dans la classe d'universalité de Wess-Zumino-Witten (WZW) $\mathrm{SU}(2)_2$, ou du premier ordre dans le cas contraire. En combinant une étude numérique minutieuse avec une analyse de la théorie conforme des champs, nous avons pu détecter la présence d'un nouveau type de transition de phase qui appartient à la classe d'universalité d'Ising dans la chaîne de spin-1 frustrée avec des interactions entre second voisins qui sont en concurrence avec des interactions à trois sites. Contrairement à la ligne critique de WZW $\mathrm{SU}(2)_2$ où le gap singulet-triplet se ferme, la transition d'Ising se manifeste entièrement dans le secteur singulet et le gap reste ouvert. L'utilisation du DMRG standard nous a permis de démontrer explicitement la présence d'une tour conforme d'états singulets dans le gap de spin. En outre, la ligne critique de WZW $\mathrm{SU}(2)_k$ peut devenir une transition du premier ordre selon la théorie des champs, à cause de la présence d'un opérateur marginal dans le modèle de WZW $\mathrm{SU}(2)_k$. Une analyse approfondie des tours conformes d'états le long des lignes critiques nous a permis de trouver l'emplacement précis de ce point dans les chaînes de spin $S = 1$ et $S = 3/2$. Nous avons également démontré que la nature des transitions de dimérisation continues est liée aux propriétés topologiques des phases correspondantes, et que les diagrammes de phase des chaînes de spin frustrées peuvent être déduits du paramètre d'ordre topologique local — la dégénérescence de l'état le plus bas dans le spectre d'intrication.

Lorsque le DMRG est utilisé en parallèle avec la théorie conforme des champs des systèmes ouverts, il constitue un outil puissant pour caractériser non seulement le diagramme de phase et les corrélations de l'état fondamental des systèmes quantiques unidimensionnels, mais

également le spectre d'excitation et la structure conforme le long des lignes critiques.

Mots clefs : Magnétisme quantique unidimensionnel, chaînes de spins frustrés, interactions à trois sites, dimérization spontanée, transition de phase quantique, lignes critiques, classe d'universalité, théorie conforme des champs, tours d'états conformes, spectre d'excitation, méthode du groupe de renormalisation de la matrice densité, état de produits matriciels, transition de Wess-Zumino-Witten, transition d'Ising, transition de Kosterlitz-Thouless

Contents

List of Figures

List of Tables

1 Introduction

The quantum many-body problem is one of the most prominent and at the same time most challenging fields of modern condensed matter physics. The low-dimensional strongly correlated systems such as one- and two-dimensional frustrated magnets, ultra-cold atomic gases, high-temperature superconductors and many others are of particular interests. Various novel quantum phenomena emerge in low-dimensional strongly correlated systems, such as, topologically protected phases, quantum spin liquids, and quantum criticality, to name just a few. The theoretical understanding of such quantum systems is based on simplified models that reflects the essential physical properties of real systems. For example, the Hubbard model and the t-J model are used to describe high-temperature superconductors, the ultra-cold atoms trapped in optical lattices are studied with the Bose-Hubbard model, and the Heisenberg model and its extensions deal with quantum magnets. In spite of the apparent 'simplicity' of these models, they can be solved exactly (analytically) only in a few very special cases.

A large portion of the field of strongly interacting systems is devoted to quantum magnets. If a single local condition imposed by the Hamiltonian of the model is unable to lead to a simple pattern for an extended system, the model is said to be frustrated. As an example, let us consider the classical nearest-neighbor Heisenberg model, defined by the Hamiltonian

$$H_{\text{class}} = \sum_{\langle ij \rangle} J_{ij} \mathbf{S}_i \cdot \mathbf{S}_j, \tag{1.1}$$

where the sum runs over nearest neighbors i and j, $\mathbf{S}_i$ are classical three-dimensional vectors that describe spin at the site i, and $J_{ij} > 0$ is an set of antiferromagnetic coupling constants. The local rule that minimizes the energy of this Hamiltonian imposes that every pair of neighboring spins are antiparallel to each other. This constraint can be easily satisfied on a square lattice, and more generally on a bipartite lattice, and leads to a global pattern of antiparallel spins known as the Néel state. On the other hand, this local rule cannot be satisfied on all bonds of a triangular lattice even for nearest-neighbor coupling and leads to geometrical frustration.

The phases with long range order usually can be described by classical approaches, e.g. mean

field, and quantum fluctuations provide minor corrections to the classical wave-function.This in not true however for one-dimensional frustrated magnets, which can exhibit only short-range order with exponentially decaying correlations, or quasi-long-range order with correlations decaying algebraically. The latter is associated with critical regimes. Quantum effects are then essential in one-dimensional systems and lead to various novel phases and exotic criticalities.

The simplest one-dimensional quantum spin model is given by the transverse field Ising Hamiltonian:

$$H_{\text{Ising}} = J\sum_i S_i^x S_{i+1}^x + hS_i^z, \tag{1.2}$$

where S_i^x and S_i^z are the projection of spin-1/2 operators $\mathbf{S}_i$ on two orthogonal axes. The first term corresponds to the classical Ising model. The second term corresponds to the transverse magnetic field and leads to a quantum critical point at $h = \pm J/2$. The system with periodic or open and free boundary conditions is exactly solvable by methods of statistical physics, and by mapping the Hamiltonian to a quadratic form of Fermi operators using Jordan-Wigner transformation[68, 80]. Moreover the critical transverse field Ising model is an example of a minimal model exactly solvable by a conformal field theory.

The simplest isotropic spin model is given by the quantum version of the Heisenberg Hamiltonian:

$$H_{\text{Heis}} = J\sum_i \mathbf{S}_i \cdot \mathbf{S}_{i+1}. \tag{1.3}$$

The exact solution of this model for one-dimensional systems was obtained by the celebrated Bethe ansatz in 1931 [13]. More that fifty years later, in 1983, Haldane predicted a finite gap for Heisenberg chains with integer spins, in contrast to critical chains for half-integer spins. Nevertheless, non-critical chains with integer spins can be driven into a critical regime by adding a frustration. One of the text-book examples is the spin-1 chain with bilinear-biquadratic nearest-neighbors interactions, defined by the Hamiltonian:

$$H_{J_1-J_b} = J_1\sum_i \mathbf{S}_i \cdot \mathbf{S}_{i+1} + J_b\sum_i (\mathbf{S}_i \cdot \mathbf{S}_{i+1})^2 \tag{1.4}$$

Positive biquadratic interactions J_b leads to an extended critical quadrupolar trimerized phase for $J_b \geq J_1$[34], while negative biquadratic coupling leads to a spontaneously dimerized phase for $J_b < -J_1$. Numerical investigation of the bilinear-biquadratic chain have shown that the transition occurs directly from the dimerized to the ferromagnetic state [63], although according to the field theory some intermediate gapped spin-nematic phase appears between the two phases[27]. The system at the quantum critical point $J_b = -J_1$ turns out to be exactly solvable by the Bethe ansatz[9, 96]. According to conformal field theory, this critical point belongs the Wess-Zumino-Witten $SU(2)_2$ universality class [1, 5, 6].

Experimental realizations of quasi-one-dimensional quantum magnets are mostly based on first-row transition-metal ions. Compounds based on Cu^{2+}, V^{4+} and Co^{2+} realize spin-1/2 systems, compounds with Ni^{2+} and V^{3+} ions realize spin-1 chains, V^{2+} and Cr^{3+} ions correspond to spin-3/2, Fe^{2+} realize spin-2 and Ir-based compounds can realize spin-5/2.

A quantum spin-1/2 chain was first investigated experimentally in $CuCl_2{\cdot}2NC_5H_5$ in 1974[30, 44]. The spin-1/2 antiferromagnetic Heisenberg chain has also been realized for instance in $KCuF_3$ and Sr_2CuO_3. In fact, the SrCuO family of materials realizes a large variety of one dimensional spin chains with competing interactions as well as spin ladders with different numbers of legs.

In spin-1 chains, Haldane gap has been observed for the first time in the Ni-based compound $Ni(C_2H_8N_2)_2NO_2ClO_4$ (NENP) [86, 85, 83]. Other experimental realizations of quasi-one-dimensional spin-1 antiferromagnets that realizes Haldane gap include $Ni(C_5H_{14}N_2)_2N_3(PF_6)$ (NDMAP) [49, 51, 22], $Ni(C_5H_{14}N_2)_2N_3(ClO_4)$ (NDMAZ) [50], $AgVP_2S_6$ [73, 8, 97, 98], $PbNi_2V_2O_8$ [100, 107], $SrNi_2V_2O_8$ [107, 11, 79] and Y_2BaNiO_5 [105, 28] to mention just a few.

Explicitly dimerized phases of spin-1 chains have been realized experimentally in the Ni-based compound $Ni(C_9D_{24}N_4)(NO_2)ClO_4$ (abbreviated as NTENP) [74, 106, 84], that exhibits field-induced Ising quantum critical point [42]. The dimerized phase in alternating spin-3/2 chain has been observed only recently in $Cr_2(BP_3O_{12})$[52] and $YCrGeO_5$ and $SmCrGeO_5$[43]. In the two latter compounds, the authors provide evidence of a finite singlet-triplet gap and suggest that the ground state is in the fully dimerized phase. So far, there is no known example of spontaneous dimerization in spin-S chains with $S > 1/2$.

One-dimensional quantum magnetism deals with numerous effective models, and a large variety of methods have been developed to treat them: *i)* exact solutions including Bethe ansatz and mapping onto free fermions via Jordan-Wigner transformation; *ii)* quantum field theory methods, including conformal field theory and bosonization; *iii)* classical mean-field solutions and quantum perturbations around it; *iv)* and finally a large varieties of numerical methods, among which exact diagonalization, Quantum Monte Carlo, and the Density Matrix Renormalization Group.

The Density Matrix Renormalization Group algorithm, invented by S.R.White in 1992 [103, 90], has established itself over the past twenty-five years as the most versalite and powerful numerical tool for one-dimensional strongly correlated systems. Its reformulation in terms of local tensors[90, 78] leads to a new class of numerical algorithms for one- and two-dimensional strongly correlated systems named Tensor Networks.

Frustrated spin-1/2 chains have attracted a lot of attention in the past decades. However much less is known about frustrated chains with $S > 1/2$. Spin-S chains with competing nearest- and next-nearest interactions have been studied numerically in Ref.[56, 57, 88], where authors suggested the presence of a first order phase transition for integer spins, and of a continuous Kosterlitz-Thouless transition between critical and dimerized phases for half-integer spins.

However, to quote the authors, the nature of the phase transition has been obtained with 'highly indirect evidence only'.

Recently, it has been shown that a three-site interaction $J_3\,[(\mathbf{S}_{i-1}\cdot\mathbf{S}_i)(\mathbf{S}_i\cdot\mathbf{S}_{i+1})+\text{H.c.}]$ that reduces to the next-nearest neighbor interaction for spin-1/2 is also able to induce a spontaneous dimerization in spin-S chains for arbitrary S, and that, at least up to $S=2$, the transition is in the $\text{SU}(2)_{2S}$ WZW universality class[71, 70]. The study of the model with nearest-neighbor and three-site interactions has been restricted to positive values of both coupling constants, while the full phase diagram of this model remains unexplored.

Three-site interaction appears in the next-to-leading order expansion of the two-band Hubbard model, together with next-nearest-neighbor and biquadratic terms. Therefore it is important to consider also a combination of these terms. The first step in this direction has been in Ref.[81], in which the competition between next-nearest-neighbor and biquadratic interactions has been studied.

The general goal of this thesis is to study this family of one-dimensional models with $S>1/2$, revisiting on the way the conclusions of Ref.[81], and to determine as accurately as possible the phase diagram of these models and the nature of the critical lines that separates different phases, with emphasis on spontaneously dimerized phase and exotic critical lines. The present work is mostly based on numerical results obtained with Density Matrix Renormalization Group algorithm.

The rest of the thesis is organized as follows: We start with a brief review of the Density Matrix Renormalization Group and variational Matrix Product State algorithms. Chapter 2 discusses an extension of the standard approaches that enables one to calculate the excitation spectrum of critical systems at very low computational cost. In Chapter 3 we used this method to extract the conformal towers in two minimal models - the transverse field Ising model and the three-state Potts model - and verify the boundary conformal field theory predictions for these models made by Cardy [20, 21]. The next Chapter 4 is dedicated to a spin-1 chain with nearest-neighbor, next-nearest-neighbor and an additional three-site interactions. The latter induces a spontaneous dimerization and leads to an exotic quantum phase transition. Using extensive numerical simulations and a conformal field theory analysis, we show that the transition to the spontaneously dimerized phase can be of three types: continuous in the Wess-Zumino-Witten $\text{SU}(2)_{k=2}$ universality class, continuous in the Ising universality class, or first order. In Chapter 5, we revisit the phase diagram of the spin-1 chain with nearest-neighbor, next-nearest neighbor and biquadratic interactions, previously studied in the Ref.[81], and we show that that the two models have essentially the same phase diagram. Therefore the properties we have obtained for the critical lines appears to be generic for spin-1 chains. Chapters 4 and 5 rely to a large extend on Refs.[24, 25, 23]. Chapter 6 generalizes the results of Chapter 4 to the spin-3/2 chain with next-nearest neighbor and three-site interaction with a number of new features related to the half-integer nature of the spin. The Heisenberg model with three-site interactions including positive coupling constants for both terms is discussed

in Chapter 7. Finally, in Chapter 8, we review and summarize the main results of this PhD.

2 Density Matrix Renormalization Group algorithm

The modern quantum many-body physics to a large extend relies on the numerical simulations. Among different algorithms, the Density Martix Renormalization Group (DMRG)[103, 90] has established itself as the most powerful tool for strongly correlated one-dimensional systems. The DMRG has been developed as an algorithm for the ground state search for one-dimensional systems. The reformulation of the algorithm in terms of local tensors - Matrix Product States (MPS) [78, 91] - not only has lead to the simplification of the traditional method, but has also boosted the generalization of the DMRG to higher dimensions, now known as Tensor Network algorithms.

In the present chapter we will briefly describe the variational MPS algorithm, that is to a large extend equivalent to the traditional DMRG. Some technical details on the implemented algorithm such as the number of kept states, the Matrix Product Operator tensors, convergence etc. will be mentioned. We will set up and test an efficient extension of the standard variational MPS (DMRG) that allows one to extract about 20 lowest states in the excitation spectra of critical systems. Although the proposed method is not generic and cannot in principle provide reliable results for systems far from criticality, it still produce reliable excitation energies for systems with localized impurities and low-lying edge states.

2.1 Variational Matrix Product States

2.1.1 MPS representation

The Hilbert space of the total system grows exponentially fast with the number of sites d^N, where d is the size of the local Hilbert space. The limitation on the memory restricts the maximal number of sites for which the quantum state can be written explicitly to $N \approx 20$. The key point of the MPS representation is to overcome this restriction and to write the state as a product of local tensors. This can be done since any quantum states of a bipartite system can be effectively represented in a compact basis constructed with the Schmidt decomposition. It relies on a tool known from linear algebra as Singular Values Decomposition (SVD). For any

rectangular matrix M of dimension $m \times n$ there exists a decomposition

$$M = USV^\dagger, \tag{2.1}$$

where

- U is of dimension $m \times \min(m,n)$ and is left-normalized, i.e. $U^\dagger U = I$. If $m \leq n$, U is unitary and also $UU^\dagger = I$
- V is of dimension $n \times \min(m,n)$ and is right-normalized, i.e. $VV^\dagger = I$. If $m \geq n$, V is unitary and also $V^\dagger V = I$
- S is a diagonal matrix of dimension $\min(m,n) \times \min(m,n)$ with non-negative entries. The Schmidt rank s of matrix M is given by the number of non-zero singular values $S_{ii} > 0$.

Figure 2.1 shows step-by-step how a generic state of N particles with s_i local degrees of freedom can be decomposed into N three-dimensional tensors (the tensors on the first and the last sites are considered as three-dimensional with one bond dimension equal to one). First, the many-particle state that has the dimension of the total Hilbert space of the system 2^N is reshaped into a rectangular matrix. The matrix is SVD decomposed into $USV^\dagger$. The left-normalized matrix U is treated as a local tensor A for the first site, while $SV^\dagger$ is reshaped into another rectangular matrix. Repeating these steps one can construct a local left-normalized tensors for every sites. The obtained MPS representation is then called left-normalized. Equivalently, one can start from the right edge and treat $V^\dagger$ as a local right-normalized tensor B, then the MPS representation is called right normalized.

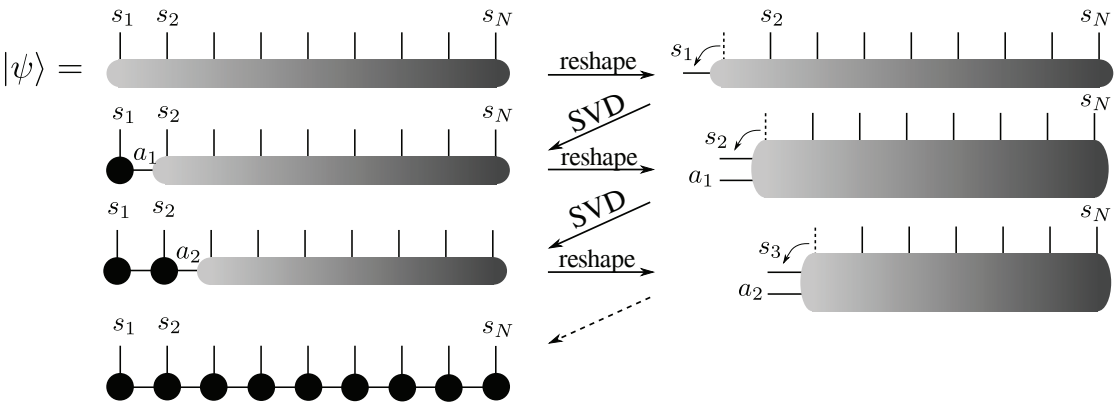

Figure 2.1 – Decomposition of a generic quantum state into MPS form via reshaping and singular value decomposition.

In practice the most convenient representation is a mixed one with all left-normalized tensors on the left and the right-normalized tensors on the right side of the chain. The Mixed-state representation is sketched in Figure2.2(a). The contraction of the left-normalized tensors with

their conjugate over left and physical bonds is equal to the identity matrix (Figure2.2(b)). The same is true for the right normalized tensors contracted though their right and physical bonds (Figure 2.2(c)).

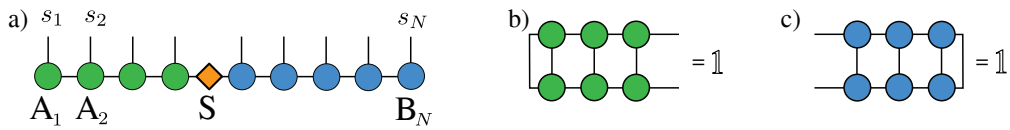

Figure 2.2 – Different types of MPS normalization: (a) state in mixed representation. Identity matrix matrix as a result of contraction for (a) left- and (b) right-normalized tensors

The bond dimension $a_i = \min(d^i, d^{N-i})$ grows exponentially with distance to the edges $\min(i, N-i)$, therefore the performed decomposition itself does not reduce the required amount of memory. However, for strongly correlated systems, the Schmidt values $S_{i,i}$ decay fast with i. Therefore the exact decomposition of the matrix in Eq.2.1 could be replaced by an approximate one:

$$M_{k,l} \approx \sum_{i=1}^{D} U_{k,i} S_{i,i} V^{\dagger}_{i,l}, \tag{2.2}$$

with summation index i running over just a few of the largest Schmidt values $D < \min(m, n)$. With this approximation, the bond dimension a_i of the MPS representation is given by $a_i = \min(d^i, d^{N-i}, D)$. In practical applications, the number of kept Schmidt values is between a few hundreds and a few thousands, which is much smaller than the size of the total Hilbert space.

2.1.2 Matrix Product Operator

The exponential growth of the Hilbert space implies also the exponential growth of the operators, such as Hamiltonian. Therefore, the Hamiltonian should also be reformulated in terms of local tensors - Matrix Product Operators (MPO). MPO is a tensor of rank four with two legs and two auxiliary legs. The physical legs are contracted to the MPS, while auxiliary legs connect the MPOs on different sites. Let us consider the Heisenberg model with only nearest-neighbor interaction J_i and external magnetic field h_i. The Hamiltonian of this model is:

$$H = \sum_{i=1}^{N-1} J_i \left(S_i^+ S_{i+1}^- + S_i^- S_{i+1}^+ + S_i^z S_{i+1}^z \right) + \sum_{i=1}^{N} h_i S_i^z, \tag{2.3}$$

where $S_i^{\pm} = (S_i^x \pm i S_i^y)/\sqrt{2}$ are rescaled raising and lowering spin operators at site i. In order to construct MPO at site i, it is useful to rewrite the Hamiltonian explicitly as a tensor product of $d \times d$ identity matrix I and spin S operators and to look explicitly at the operator that appears at site i (the middle column of the Table 2.1).

From Table 2.1 it is easy to deduce that there are only five different states for the spins $1 \ldots i-1$,

index	$1...i-1$	i	$i+1...N$	index
5	$I...I$	$h_i S_i^z$	$I...I$	1
2	$I...I J_{i-1} S_{i-1}^+$	S_i^-	$I...I$	1
3	$I...I J_{i-1} S_{i-1}^-$	S_i^+	$I...I$	1
4	$I...I J_{i-1} S_{i-1}^z$	S_i^z	$I...I$	1
5	$I...I$	$J_i S_i^+$	$S_{i+1}^- I...I$	2
5	$I...I$	$J_i S_i^-$	$S_{i+1}^+ I...I$	3
5	$I...I$	$J_i S_i^z$	$S_{i+1}^z I...I$	4
1	$I...I$ full $I...I$	I	$I...I$	1
5	$I...I$	I	$I...I$ full $I...I$	5

Table 2.1 – Hamiltonian of Eq.2.3 represented as a tensor product operator with operators on sites $1...i-1$, operator on site i and operators on site $i+1...N$. The second and third columns contain five different states each. These states form a basis for the local MPO. The basis states are labeled by their indices as they appear in the MPO of Eq.2.4

which form a basis of the first index of the MPO. The basis set of the second index also contains five vectors and is given by the states for sites $i+1...N$. The dimension of two physical bonds are hidden in the operators I and S, that are $d \times d$ square matrices. Thus the size of the obtained MPO is $d \times d \times 5 \times 5$. The local tensor is given by:

$$H_i = \begin{pmatrix} I & & & & \\ S_i^- & & & & \\ S_i^+ & & & & \\ S_i^z & & & & \\ h_i S_i^z & J_i S_i^+ & J_i S_i^- & J_i S_i^z & I \end{pmatrix}, \tag{2.4}$$

where blank spaces correspond to zeros entries. The square matrix of Eq.2.4 is in fact a four-dimensional tensor. This representation of the MPO is correct for $1 \leq i \leq N-1$. The MPO on the first site is given by the last row and the MPO on the last site is given by the first column of the MPO of Eq.2.4.

Let us now construct the MPO representation of the $J_1 - J_2 - J_3$ Hamiltonian given by:

$$H = \sum_i (J_1 \mathbf{S}_i \cdot \mathbf{S}_{i+1} + J_2 \mathbf{S}_{i-1} \cdot \mathbf{S}_{i+1}) + \sum_i J_3 \left[(\mathbf{S}_{i-1} \cdot \mathbf{S}_i)(\mathbf{S}_i \cdot \mathbf{S}_{i+1}) + \mathrm{H.}c. \right] \tag{2.5}$$

A significant role in the successful convergence is played by an efficient representation of the Hamiltonian in terms of MPO. As it will become clear later, the complexity of the algorithm is proportional to the auxiliary bond dimension. The straightforward MPO representation of the $J_1 - J_2 - J_3$ model has a bond dimension $d = 17$ ($3+3$ for J_1 and J_2 terms, 9 for J_3 interaction, 1 for unity matrix and 1 for full term). Using the spin commutation relations this number can be reduced to $d = 14$. Below we show slightly different approach that allows to reduce the bond dimension to $d = 8$.

The efficient MPO representation naturally appears when the J_3-term is rewritten in terms of quadrupolar operators:

$$\sum_i J_3 \left[(\mathbf{S}_{i-1}\cdot\mathbf{S}_i)(\mathbf{S}_i\cdot\mathbf{S}_{i+1}) + \mathrm{H.}c.\right] = \sum_i \sum_{\alpha,\beta=x,y,z} J_3 S^{\alpha}_{i-1} Q^{\alpha\beta}_i S^{\beta}_{i+1}, \tag{2.6}$$

where $Q^{\alpha\beta}_i = S^{\alpha}_i S^{\beta}_i + S^{\beta}_i S^{\alpha}_i$. Generally speaking Q is not a traceless tensor, and therefore it is not a quadrupolar operator, but let us keep the Q-notation for simplicity. Combining the new expression for the J_3 term with the J_2 term, one obtains the Hamiltonian in the following form:

$$H = \sum_i J_1 \mathbf{S}_i\cdot\mathbf{S}_{i+1} + \sum_i \sum_{\alpha,\beta=x,y,z} S^{\alpha}_{i-1}\left(J_2\delta^{\alpha\beta} + J_3 Q^{\alpha\beta}_i\right) S^{\beta}_{i+1} \tag{2.7}$$

The term inside the brackets can be written in matrix form as:

$$\begin{pmatrix} J_2 I + J_3 Q^{xx} & J_3 Q^{xy} & J_3 Q^{xz} \\ J_3 Q^{xy} & J_2 I + J_3 Q^{yy} & J_3 Q^{yz} \\ J_3 Q^{xz} & J_3 Q^{yz} & J_2 I + J_3 Q^{zz} \end{pmatrix}, \tag{2.8}$$

In terms of rescaled lowering and raising operators $S^{\pm}_i$ a complete MPO tensor reads:

$$H_i = \begin{pmatrix} I & & & & & & & \\ S^-_i & & & & & & & \\ S^+_i & & & & & & & \\ S^z_i & & & & & & & \\ & J_2 I + J_3 Q^{+-} & J_3 Q^{--} & J_3 Q^{-z} & & & & \\ & J_3 Q^{++} & J_2 I + J_3 Q^{+-} & J_3 Q^{+z} & & & & \\ & J_3 Q^{+z} & J_3 Q^{-z} & J_2 I + J_3 Q^{zz} & & & & \\ h S^z_i & J_1 S^+_i & J_1 S^-_i & J_1 S^z_i & S^+_i & S^-_i & S^z_i & I \end{pmatrix}, \tag{2.9}$$

where blank spaces correspond to zero entries. The MPO Hamiltonians for the first and the last sites are given by the last row and the first column of tensor (2.9) respectively.

2.1.3 Ground state search

The search for the ground state consists in finding an MPS representation of the state $|\psi\rangle$ that minimizes the energy:

$$E = \frac{\langle\psi|H|\psi\rangle}{\langle\psi|\psi\rangle} \tag{2.10}$$

The algorithm operates iteratively, namely while all but two tensors are kept constant, a selected couple of tensors are updated by solving the corresponding eigenvalue problem.

The code consists of four parts:

1. Infinite-size DMRG (sketched in Fig.2.3): We start with some initial guess for the tensors at the first and last sites. Without loss of generality one can fix these tensors to be identity matrices. We contract the guess tensors over physical indices with an MPO in order to obtain left and right 'environments' L_1 and R_N (see Fig.2.4 for a pictorial representation of the environments). The effective Hamiltonian for four sites is then obtained by contracting these environments with MPOs on sites 2 and $N-1$ over their auxiliary bonds. The ground-state obtained from diagonalization of the effective Hamiltonian is then decomposed by SVD into left-normalized tensor A_2 and right-normalized tensor B_{N-1}. These tensors together with the corresponding MPO are contracted with previously obtained environments in order to get L_2 and R_{N-1}. These new environments contracted with the pair of MPOs on sites 3 and $N-2$ give an effective Hamiltonian for 6 spins. Then, its ground state is decomposed into tensors A_3 and B_{N-2}. By repeating these steps, the system size grows by two until the tensor network reaches the required length N. For an odd total number of spins N, the same procedure is performed until the system reaches a size of $N-1$, in this case only one tensor is multiplied to the environment. Assuming without loss of generality that the left environment was updated and therefore contains an effective basis for $(N-1)/2$ spins, one can reuse the right environment for $(N-3)/2$ spins and insert the local Hamiltonian for two additional spins in order to reach a system size with N odd.

In this part of the code, we usually keep 44 singular values, however, close to the critical lines, this number is increased to 66 or 88. These values (that seem strange at a first glance) have been chosen in such a way, that after increase by 50% during each of the two half-sweeps in the warm-up, the resulting number of states are 100, 150 and 200 respectively. Although the infinite-size DMRG can be used independently in order to get some observables in the thermodynamic limit, here we use infinite-size DMRG only to create a good starting point for the following finite-size routines. At each iteration environment tensors L_n and R_n are stored on a hard disk and will be reused during the following finite-size sweeps. The tensors A, S and B are also stored and will be reused while creating an initial guess for the iterative eigensolver (here Lanczos).

2. The warm-up function consists of an incomplete finite-size sweep. Iterating from the middle of the chain to its right end we calculate site-by-site local tensors A_n and corresponding left

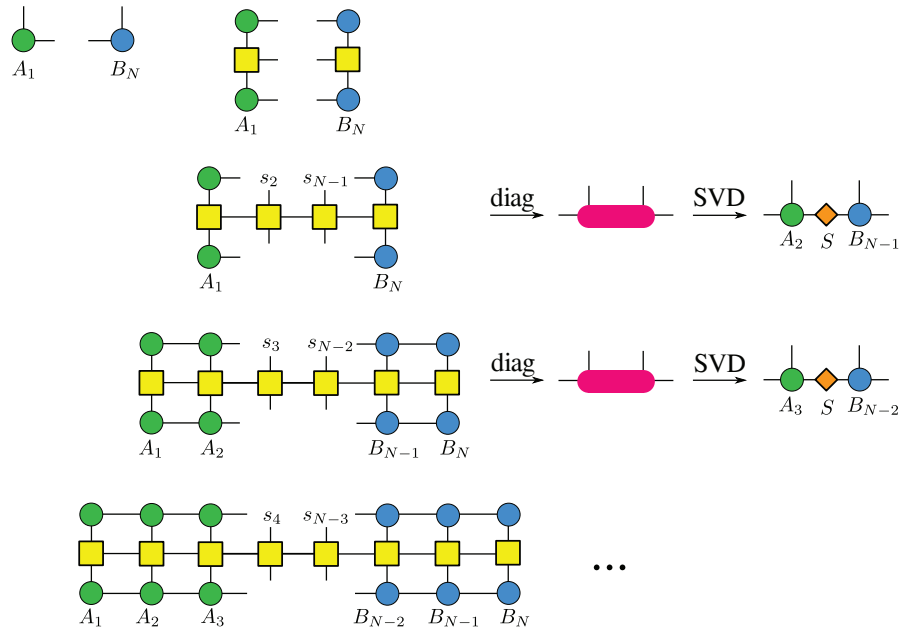

Figure 2.3 – Sketches of the few steps in infinite-size DMRG. Green and blue circles are left and right normalized MPS, yellow boxes are on-site MPOs, magenta boxes are a ground states of effective Hamiltonians, orange diamonds are diagonal matrices with Schmidt singular values. The system size grows from 2 to the required length N by inserting two-site MPO and diagonalizing an effective Hamiltonian at each iteration

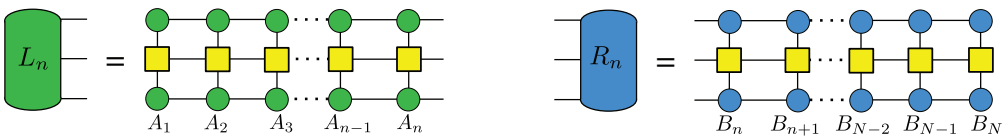

Figure 2.4 – Graphical representation of left and right environments

environments L_n. Sweeping back from the right end to the left, we update the tensors B_n and right environments R_n. We increase the maximal number of states while sweeping from left to right and from right to left by a factor 1.508. Thus in the end of the warm-up the number of kept states is 100 (or 150 and 200 for 66 and 88 states in infinite-size DMRG). A few steps of finite-size DMRG are sketched on Fig.2.5

3. The 'main body' of the algorithm consists in sweeping from left to right and back locally updating the tensors. We usually perform 6-7 sweeps for open boundary conditions and up to 16 sweeps for periodic chains. We keep up to 700 singular values for $N < 200$ and up to 900 states for larger systems. We implemented two-site DMRG, which turns out to be significantly more stable and to converge faster, despite the obvious growth of complexity by a factor $(2S+1)^2 = 9$. Roughly speaking, the number of kept states 700 and 900 for two-site DMRG is equivalent to 1210 and 1560 for the one-site routine, although there is no simple one-to-one correspondence.

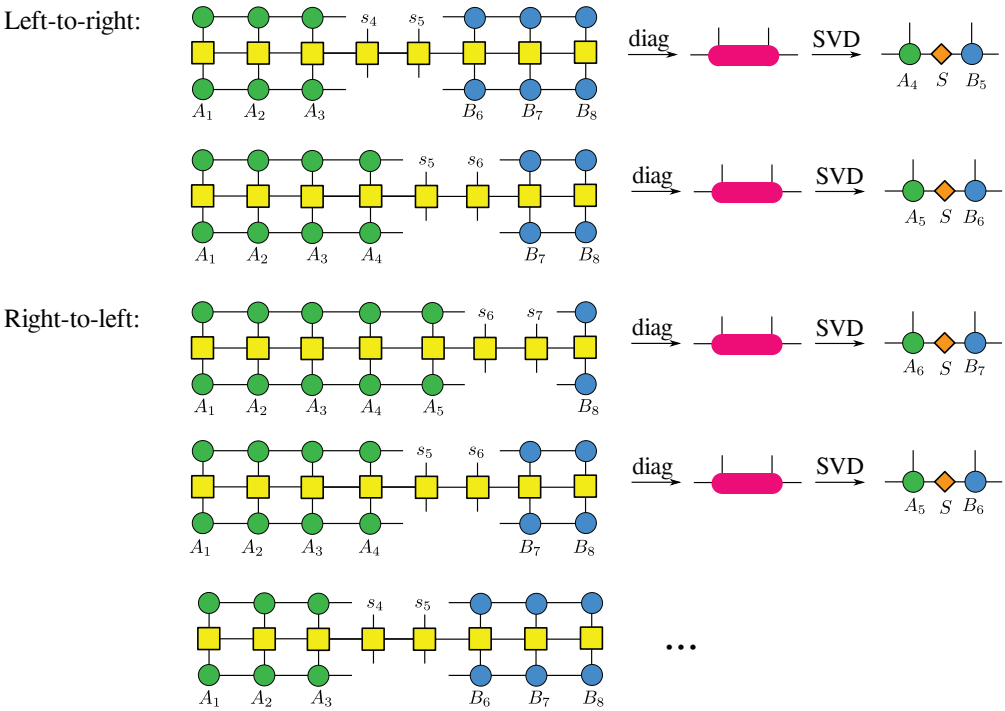

Figure 2.5 – Sketches of a few steps in finite-size DMRG, starting from the warm-up. At each iteration the ground-state of the effective Hamiltonian is decomposed via SVD into left- and right-normalized tensors A_i and B_{i+1}. The A tensors are contracted with the left environment, while sweeping from left to right and B tensors are contracted with the right environment while sweeping back.

4. During the 'final sweep' we do not increase the number of states anymore, but at each iteration we measure the set of local observables such as on-site magnetization, nearest-neighbor spin-spin correlations and entanglement entropy. The left and right normalized tensors and vectors of the Schmidt decomposition are stored and used later in order to calculate the observables which involve more than two spins (energy in the middle of the chain, long-range correlations, structure factor, etc.) or to extract the entanglement spectrum.

The total Hilbert space contains d^N basis vectors. In exact diagonalization one exploits on-site representation: to each of d states on a single site one assign a local label, e.g. spin projection S^z, colors etc. Then the basis of the total Hilbert space of N particles is formed by all possible combinations of N on-site labels. In this basis the Hamiltonian can be written exactly as $d^N \times d^N$ matrix. By truncating the bond dimension in SVD, we reduce the number of basis vectors. The use of the basis formed by on-site states is no longer optimal, instead, linear combinations of the basis vectors should be used. The constructed tensors A and B perform a basis rotation in such a way that the new basis becomes the best set of basis vectors for the selected state - the ground state. Thus, the effective Hamiltonian shown in Fig.2.3 and Fig.2.5 can be understood as a full Hamiltonian of size $d^N \times d^N$ written in a rotated and truncated basis of size $(Dd)^2$ (see Fig.2.6).

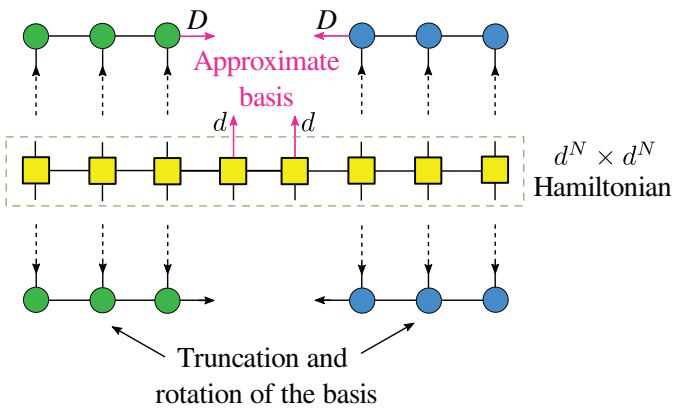

Figure 2.6 – The row of on-site MPO (yellow boxed) contracted through the auxiliary bonds is a $d^N \times d^N$ matrix of the **total** Hamiltonian. A collection of A_n and B_n tensors approximates the basis via rotation and truncation. The approximate basis contains $(dD)^2 \ll d^{2N}$ vectors.

2.2 Excitation spectrum with MPS

The DMRG algorithm has first been developed as a method for the ground-state search. When the knowledge of excited states or excitation spectrum is necessary, the implementation becomes rather advanced. Several approaches were developed on the basis of standard DMRG algorithm:

1. If some symmetry can be imposed on the wave-function and the excited state of interest is the lowest-energy state of some symmetry sector, the search for the excited state is then simply a ground-state search within the corresponding symmetry sector. In particular, this approach allows rather straightforward calculation of singlet-triplet gap, by accessing the lowest energy states in the sectors of total magnetization $S^z_{\text{tot}} = 0$ and $S^z_{\text{tot}} = 1$. In the following chapters we use both codes with and without the implementation of the conserved total magnetization. The latter is used for Ising and three-states Potts model, the former for all remaining models discussed below.

If the Hamiltonian does not preserve any discrete symmetry or if the excitation occurs in the symmetry sector of the ground state or other excitations with lower energies, the algorithm has to be modified significantly:

2. In conventional DMRG, the density matrix is constructed not only from basis vectors of the ground state, but also from basis vectors of low-lying excitations. This approach can also be applied in variational MPS. Then, the tensors A_n and B_n have to encode a mixed state. All excited states are then calculated together with the ground-state, but the price to pay is the fast increase of the bond dimension D with the required number of eigenstates.

3. The MPS representation allows significant improvement: After the construction of the ground-state, one can search for an eigenstate that is orthogonal to the ground state and has the smallest energy. For higher excitations, the state is orthogonalized to all previously

constructed eigenvectors of the Hamiltonian. Although this method is systematic and rather controlled, the algorithm has to be re-run for each eigenstate. Moreover, the states should be well converged, otherwise the error will accumulate in the following runs.

Here we propose to use a simpler method - to target excitation energies by calculating several eigenvalues of the effective Hamiltonian, written in the effective basis constructed for the ground state only. Of course, in general case this method gives only a poor estimate for the excitation spectrum - the basis chosen for ground-state is not the best set of vectors to calculate the excited states. However, in some particular cases the proposed method reveals itself as the most efficient way of calculating the excitation spectrum. Below we consider three situations, where the excitation energies can be obtained rather accurately from the Hamiltonian written in the ground-state basis: *i)* localized excitations; *ii)* in-gap states in open chain; *iii)* critical systems. The latter is perhaps the most important in view of its possible application for the identification of the underlying conformal field theory of critical systems.

2.2.1 Local excitations and impurities

Let us first discuss localized excitations by considering the Heisenberg Hamiltonian with alternating coupling constants on spin-1/2 chain:

$$H = J_1 \mathbf{S}_1 \cdot \mathbf{S}_2 + J_{\text{even}} \sum_{i=1}^{N/2-1} \mathbf{S}_{2i} \cdot \mathbf{S}_{2i+1} + J_{\text{odd}} \sum_{i=2}^{N/2-1} \mathbf{S}_{2i-1} \cdot \mathbf{S}_{2i} + J_{N-1} \mathbf{S}_{N-1} \cdot \mathbf{S}_N \tag{2.11}$$

where $J_{\text{odd}} = 1$ and $J_{\text{even}} = 0.1$. Local bond impurities are imposed at the edges by changing the coupling constants J_1 and J_N on the first and last bonds. In the absence of impurities ($J_1 = J_N = J_{\text{odd}}$) the ground state of of the Hamiltonian (2.11) corresponds approximately to spin-1/2 singlets located on every strong (odd) bond. The system has a finite gap to the first triplet excitation. By changing locally the coupling of a particular odd bond one can manipulate the energy needed to excite the selected bond to a triplet state. We introduce two different edge impurities by reducing the coupling of the first and the last bonds to $J_1 = 0.3$ and $J_{N-1} = 0.8$.

We calculate the ground-state energy and the energy of the few lowest excitations in the symmetry sectors with total magnetization $S^z_{tot} = 0$ and 1 in an open chain with $N = 28$ sites. Figure (2.7a) shows the energies obtained at each iteration in variational MPS by targeting several eigenvalues of the effective Hamiltonian. As expected, the ground state is a singlet with an energy about $E_0 \approx -9.838$. Singlets appear only in the $S^z_{tot} = 0$ sector (blue lines). The value of the energy of the first excited state in this sector depends on the position at which the effective Hamiltonian is diagonalized. Thus, when the diagonalization is performed close to the left edge J_1, the energy of the first excited state obtained around the left edge is about $E_1 \approx -9.539$. By contrast, when the diagonalization is performed around the right edge J_{N-1}, the excited state has higher energy $E_2 \approx -9.042$. The excitation energies obtained numerically

$E_1 - E_0 \approx 0.299$ and $E_2 - E_0 \approx 0.796$ agree with the rough expectations $\Delta_1 = J_1$ and $\Delta_N = J_N$ for the singlet-triplet excitations in case of decoupled dimers. Thus our interpretation of these two excitation levels is correct. The DMRG data agree within 10^{-8} with exact diagonalization results (see Fig.2.7(d)). The energies E_1 and E_2 therefore corresponds to the first and second excited states of the complete chain. The energies of the higher excited states in the $S^z_{tot} = 0$ symmetry sector have local minima close to the middle of the chain and takes value around $E_{3,4} \approx -8.9$. We increase the number of kept states linearly over the first five sweeps and perform three more sweeps with $D^{\max}$. The results for different number of states are provided in Figure (2.7b). Interestingly, in most cases except the two last sweeps with $D^{\max} = 1000$, there are small intervals where the first excited state in the $S^z_{tot} = 0$ sector converges to the bulk excitation $E_3 > E_1, E_2$ while changing between E_1 and E_2. This happens when the number of kept basis vectors for the left and right environment tensors are not sufficiently large to see the edge excitation within each tensor. On the other hand, the environment tensors converges well to the ground state and the bulk excitation is seen properly. This is what we expect also for much larger systems - the localized edge excitations can be seen only in the vicinity of the corresponding edges. Numerically we will see it later in the context of spin-1 $J_2 - J_3$ model.

In the sector $S^z_{tot} = 1$ (red lines), the state with the lowest energy is the one with the triplet on the first bond. The first excited state in this sector corresponds to a triplet on the last bond. The number of kept states is not sufficient to see this excitation far away from the right edge and it appears only when the effective Hamiltonian is diagonalized at the right half of the chain. On the other hand, the number of states has to decrease close to the edge by MPS construction and therefore the left environment block is written in the basis vectors that has the largest weight in the ground state and poorly describe the excited state that belongs to different symmetry sectors. In the present case, that would corresponds to the basis vectors that describes the triplet state in the left environment better than a singlet one. This leads to the double-through structure of the first excitation energy. The first excited state in the sector $S^z_{tot} = 1$ calculated close to the right edge does not converge to the energy E_2 that corresponds to the singlet on the left and triplet on the right bond, however it converges to the state that corresponds to the simultaneous excitations of the first and last bonds to the triplet states with energy about $E \approx -8.743$. Since dimers are not completely decoupled but connected with $J_{\text{even}} = 0.1$, the two triplet bonds at the edges coupled together and form a triplet (two excitations also form a singlet state, which however is not seen in $S^z_{\text{tot}} = 0$ sector and a quintuplet, which is probably missed due to small size of the Hilbert space at the edges).

From Fig.2.7(c) and (d) we can deduce that eigenvalues of the effective Hamiltonian written in the basis of the ground state are correct for the local excitations, while for the bulk excitation the discrepancy with the exact results is significant (of the order of 10^{-3}). It is not surprising, since for the localized excitations most of the system is in the same state as in the ground-state. In other words, the triplet excitation localized at the right edges implies that the left environment tensor is essentially the same (exactly the same for completely localized excitations) as that of the ground-state. Moreover, by tracing the excitation energy as a function of iterations (or equivalently as a function of position index of the currently optimized tensors), one can

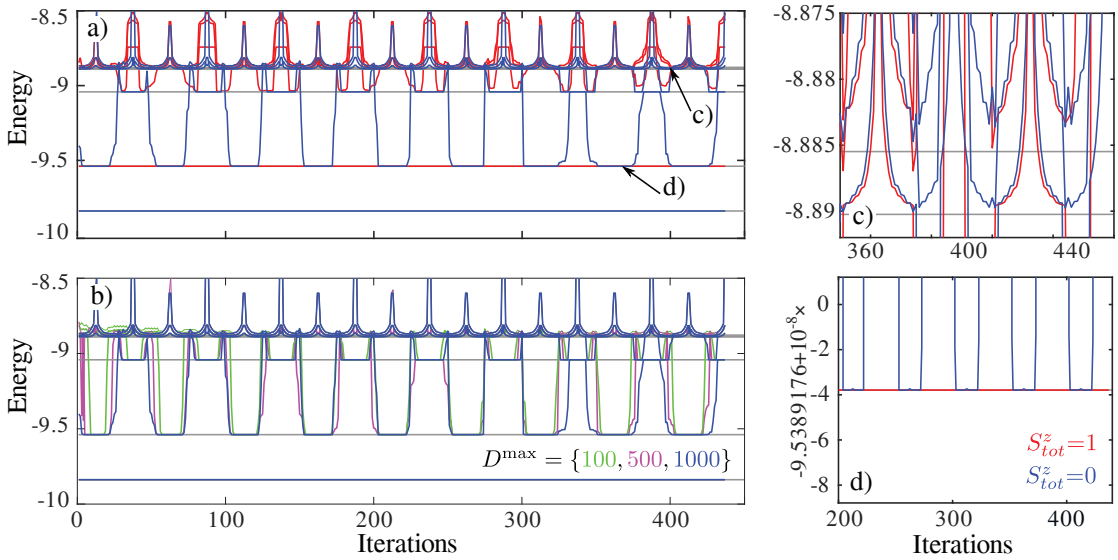

Figure 2.7 – Local excitation energy in alternating Heisenberg chain with bond impurities. (a) Energy as a function of iteration for the alternating Heisenberg chain with $J_{\text{odd}} = 1$ and $J_{\text{even}} = 0.1$ and weak first $J_1 = 0.3$ and last $J_N = 0.8$ bonds for $N = 28$. Results obtained with exact diagonalization are shown with gray lines for reference. The lowest states and several excited states in the $S^z_{tot} = 0$ (blue) and $S^z_{tot} = 1$ (red) sectors of total magnetization. The number of states increases during warm-up and first five up to $D^{\max} = 1000$ and kept constant over the last three sweeps. b) Ground state and several excited states in the sector $S^z_{tot} = 0$ for different number of kept states $D^{\max} = 100$ (green), 500 (magenta) and 1000 (blue) with the same growing procedure as in (a). (c) and (d) enlarged parts of plot (a) around bulk and edge excitation levels. In (d) the gray line for the exact diagonalization results is completely hidden behind the red line

distinguish the excitation energies of different impurities. Thus the proposed approach is an efficient alternative to the existing methods for excited states calculation in the context of localized excitations or local impurities.

2.2.2 Detection of low-lying in-gap states

Many topologically non-trivial phases could be characterized by the edge states that appear in open systems inside the phase and disappear at the phase boundary. However, exponentially small gap to the low-lying in-gap states make their detection challenging. The method of targeting several eigenvalues of the effective Hamiltonian written in the ground-state basis turns out to be useful in the detection of edge states and allows one to extract the excitation energy with sufficiently high precision.

As a toy model we consider the spin-1 Heisenberg chain. The model has a singlet ground state and a finite bulk gap[41]. The topologically non-trivial nature of the Haldane phase implies the existence of edge states[54, 40] with a gap vanishing exponentially fast with the system size.

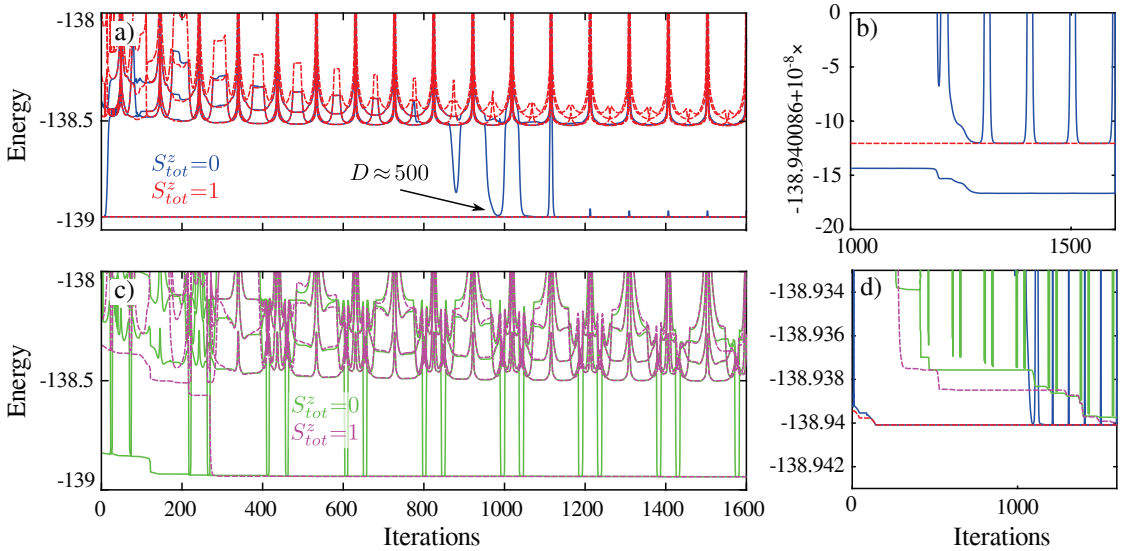

Figure 2.8 – (a) Ground-state and excitation energies calculated in the sectors of $S^z_{tot} = 0$ (blue) and $S^z_{tot} = 1$ (red) in open Haldane chain with $N = 100$ sites. (b) An enlarged part of (a) around the ground-state energy. (c) Ground-state and excitation energies sectors of $S^z_{tot} = 0$ (green) and $S^z_{tot} = 1$ (magenta) in periodic Haldane chain with $N = 100$ sites and one broken bond between 25th and 26th sites. (d) enlarged part of (a) and (c) around the ground state energy.

Since for an even number of sites, the ground-state of the model is a singlet and the low-lying in-gap state is a triplet (known as Kennedy triplet [54]), the obtained value of the energy for the excited state in the sector of zero total magnetization $S^z_{\text{tot}} = 0$ is compared to a checked with a reliable result for ground state in the sector $S^z_{\text{tot}} = 1$.

Fig.2.8(a) and (b) shows our DMRG results for energies for an open Haldane chain with $N = 100$ spins. As one can notice the Kennedy triplet starts to appear only when the number of kept states exceed 500 in two-site DMRG. Of course, this number would increase for larger systems and in the case of more complicated Hamiltonians.

In contrast to the case of localized excitations, here the best estimate of energy appears in the middle of the chain, therefore by looking only at the excitation energy as a function of iterations it is impossible to conclude whether it corresponds to edge or very low bulk excitations. In principle, to answer this question one has to access the excited state explicitly and to compute observables, however this would require to re-run the algorithm. Below we will show how this information can be obtained at very low computational cost.

By looking at Fig.2.8(b), one can see that far enough from the edges, where the Hilbert space is too small, the energy of the in-gap excitation is essentially flat - we employ this as an indicator of the convergence.

Of course, the real worth of this method shows up when the fist excited states cannot be calculated simply as a lowest state in different symmetry sector. For instance in the Haldane

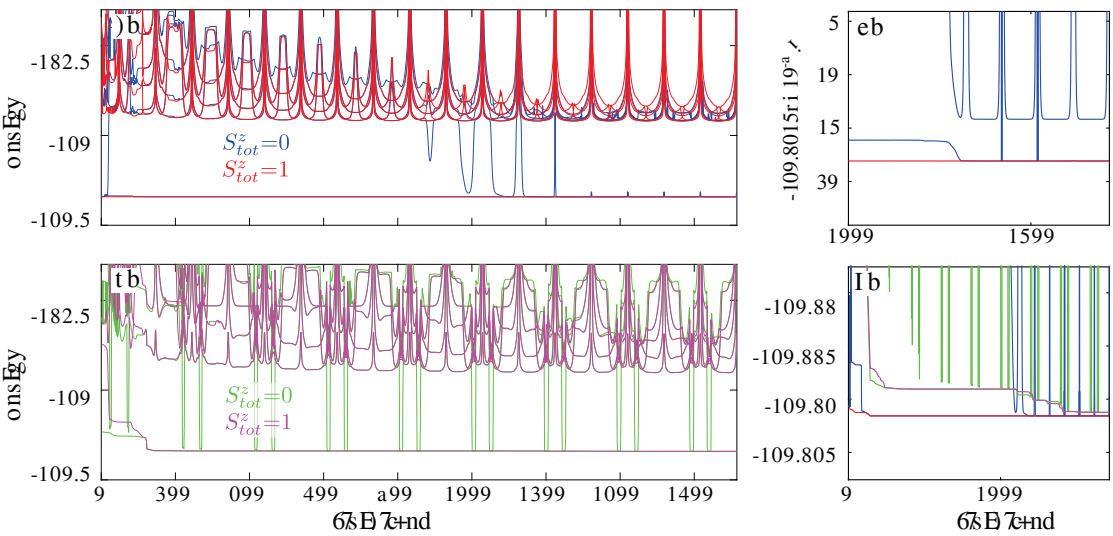

Figure 2.9 – Same as Fig.2.8 for $N = 101$ with the triplet ground state the singlet in-gap state.

chain with an odd number of sites, where the ground state is a triplet and the low-lying edge excitation belongs to the singlet symmetry sector and is thus seen as the second lowest state in the sector of $S^z_{tot} = 0$. The example for $N = 101$ is shown in Fig.2.9.

In many practical applications it is important to figure out whether the edge states are present or not, without knowing explicitly the excitation energy of low-lying in-gap states. It could be achieved at very small computational cost by representing an open system as a closed chain with one broken bond. Here we break a bond between 25th and 26th sites, that is sufficiently far from the edges, where the Hilbert space is too small, and from the middle of the chain. The singlet-triplet edge excitation are then seen as local excitation of the bond $(25, 26)$. This local excitation can be captured immediately with the effective Hamiltonian, even if the bond dimension is small $D < 50$. As expected, the convergence of the periodic DMRG is slower than the open one within the same scheme of the increase of the bond dimension (Fig.2.8(d)).

To summarize, the detection of the edge states by targeting several eigenstates of the effective Hamiltonian provides rather accurate results, although it requires sufficiently large bond dimension D. In contrast, treating an open chain as a periodic one with one broken bond allows to detect the edge states at very low computational cost, although the estimate of the energy is rather crude.

2.2.3 Critical systems

Perhaps the most important application of the described method is the calculation of the excitation spectra of critical systems. According to conformal field theory, the excitation spectrum calculated at the critical line forms a so-called conformal tower that reveals the universality class of the transition and of the underlying critical theory. Traditionally, the

universality class of the transition is extracted by computing the central charge and the critical exponents of some observables (on-site magnetisation, spin-spin correlations etc.). The latter is extremely sensitive to the logarithmic corrections of the theory (if any). In principle, the excitation spectrum contains more information on the underlying critical theory and can be used as a complement to the central charge. In cases, where the latter cannot be extracted or provide inconclusive results (e.g. due to strong finite-size effects), the conformal tower becomes the method of choice.

The main difficulty to obtain the excitation spectra with DMRG is its large computational cost. In order to identify the critical theory one has to compute energies for sufficiently large numbers of excited states (at least 4-5 states). Therefore, whether one uses traditional DMRG with mixed-state density matrix or re-orthogonalization scheme in MPS, the computational cost is enormous. In the following, we show that by targeting many eigenvalues of the effective Hamiltonian written in the ground-state basis, the construction of conformal towers becomes a relatively easy problem.

As a toy model let us consider the Ising model in transverse field:

$$H = -J \sum_i S_i^x S_{i+1}^x + h S_i^z, \tag{2.12}$$

where $S_i^{x,z}$ are spin-1/2 operators at site i. The system is critical at $h = J/2$. The underlying conformal field theory will be discussed in details in the next chapter. Three low-lying levels of the Ising conformal tower were obtained within each symmetry sector by Evenbly and Vidal [31] with scale-invariant MERA - another type of tensor network algorithm.

In Fig.2.10 we show the convergence of the 30 low-energy states computed by targeting many states of the effective Hamiltonian in DMRG calculation of the ground-state. One can immediately notice that the structure of the excitation energies typical of the conformal tower is well preserved. A fast increase of the energy occurs close to the chain boundary and comes from the fact that the Hilbert space is too small at the edges by MPS construction. The flattening of the energies in the middle of the chain signals the convergence.

On a finite chain with open boundary conditions the Hamiltonian (2.12) can be rewritten as a quadratic form of Fermi operators using Jordan-Wigner transformation. Following Ref.[68, 80] the eigenvalue problem on the Hilbert space of size 2^N can be reduced to a problem of the diagonalization of an $N \times N$ matrix, which can be solved exactly on sufficiently large clusters. The full spectrum can then be deduced from linear combinations of the obtained eigenvalues. The obtained spectrum is taken as a reference while comparing with the DMRG results (grey lines in Fig.2.10 and Fig.2.11).

As shown in Fig.2.11, the described method provides an energy spectrum that is in perfect agreement with the exact data, when the system is critical. By contrast, in gapped systems

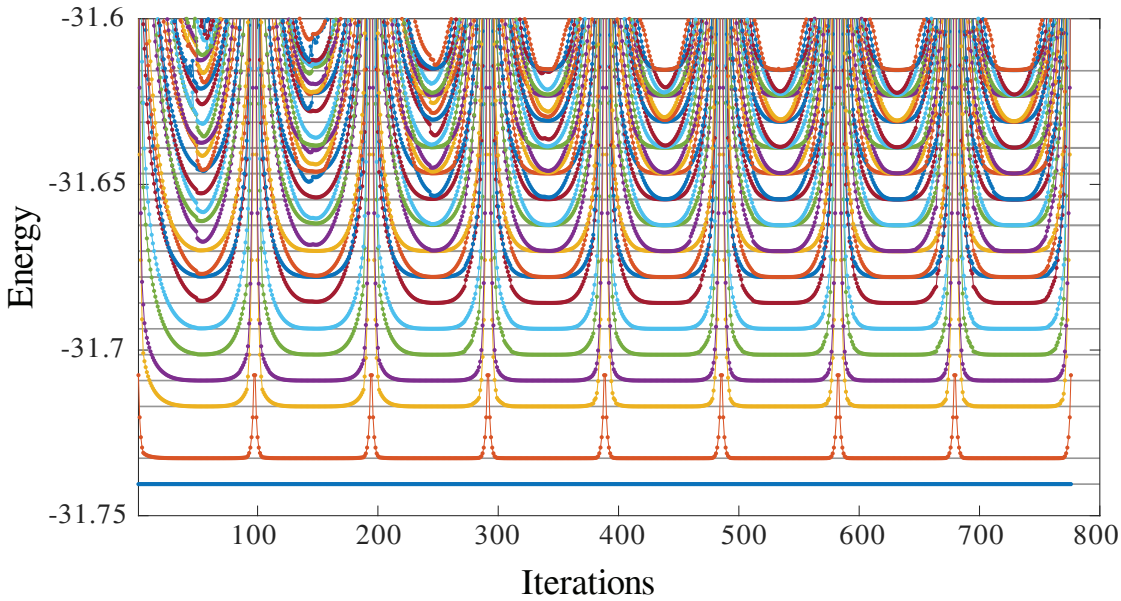

Figure 2.10 – Energy of the 30 low-energy states in the critical Ising model in a transverse field with $N = 100$ sites as a function of iterations. The flattening of the energies in the middle of the chain signals the convergence. A periodic increase of the energy occurs close to the chain boundary and is the result of the reduced Hilbert by MPS construction. Exact results are provided for reference and shown with grey lines. The plot starts with the first full sweep, the result from infinite-size DMRG and warm-up are not shown.

the agreement is rather poor and moreover some states are missed. In the gapped phases, low-lying states can be significantly different from each other and can even belong to different symmetry (here parity) sectors, requiring essentially different sets of basis vectors. By contrast, at the critical point, the excitation spectrum is obtained by applying some descendant operators on primary fields. Therefore it is natural that the basis obtained from the ground state describes the excited states also with high accuracy.

This hypothesis agrees with the observation made by Läuchli in Ref.[62], where conformal towers for different critical models were extracted via entanglement entropy. Both cases show that the ground-state contains not only the central charge or critical exponents, but essentially all the information about the critical theory.

The described method can be applied to more complicated systems in order to extract the excitation spectrum. Let us consider a spin-1 chain with next-nearest neighbor coupling and three-site interaction given by the Hamiltonian:

$$H = J_2 \sum_i \mathbf{S}_i \cdot \mathbf{S}_{i+2} + J_3 \sum_i (\mathbf{S}_{i-1} \cdot \mathbf{S}_i)(\mathbf{S}_i \cdot \mathbf{S}_{i+1}) + \text{H.c.}, \tag{2.13}$$

with $J_2, J_3 > 0$. The motivation to study this model and its properties will be discussed in

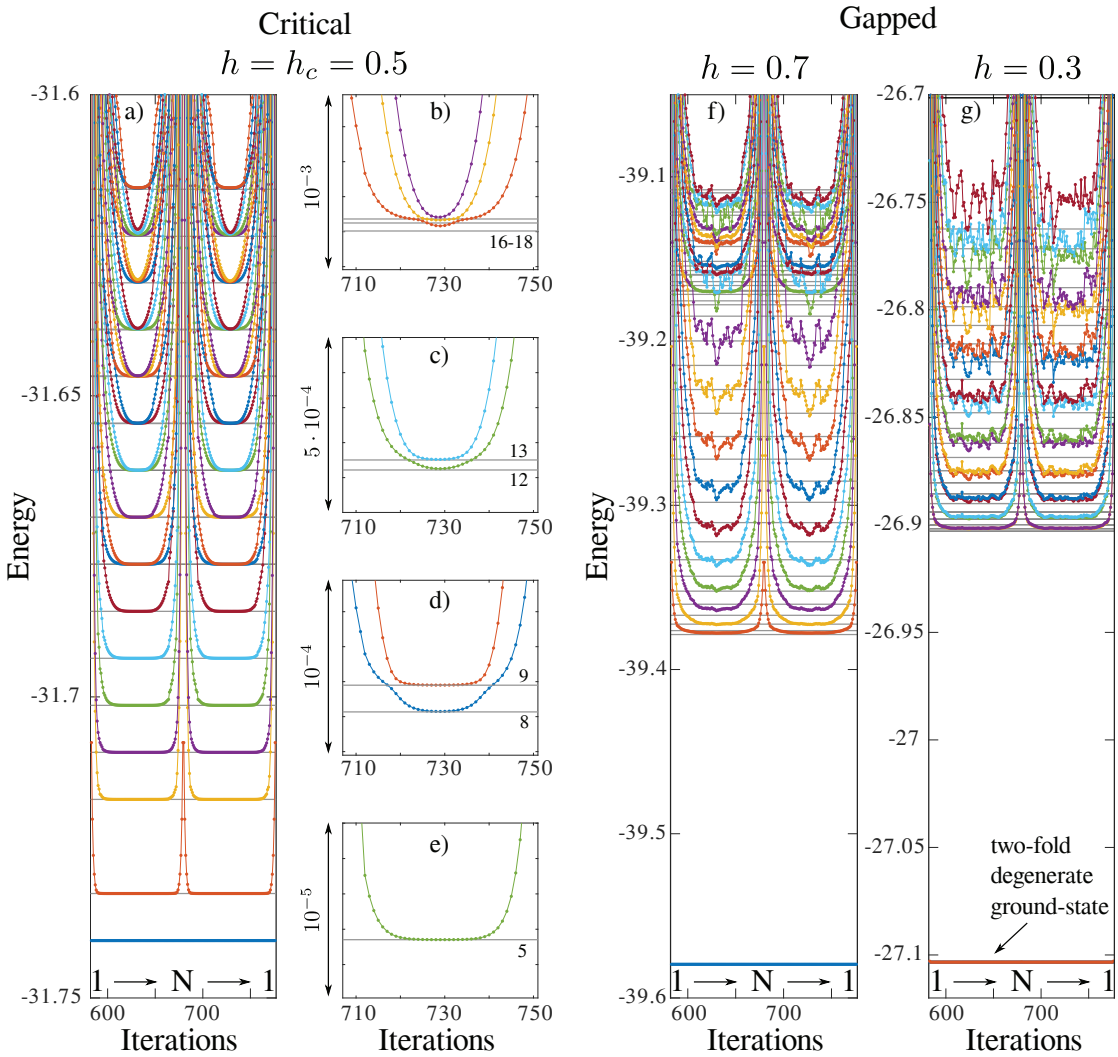

Figure 2.11 – Excitation energies obtained with one DMRG sweep in the critical (a)-(e) and gapped (f),(g) transverse field Ising model for an open chain with $N = 100$ sites. Exact results are provided for reference and shown with grey lines. (a) DMRG results agree with exact energies. (b)-(e) Enlarged parts of (a) around different excitation levels. The ordinal number of states are indicated in each plot, 1 corresponds to the ground-state. The number at the left side of plots (b)-(e) indicates a window around the selected energy level. (f) and (g) Far from criticality DMRG results poorly agree with the exact ones, some states are missed, and strong oscillations appear.

Chapter 4. Antiferromagnetic next-nearest neighbor coupling favors two Haldane chains on next-nearest neighbor bonds, while a strong J_3 term leads to a dimerized phase. The transition between these two phases occurs at $J_3/J_2 = 0.352$. In the absence of the J_3 term, each Haldane chain has free edge spins. When the two chains are coupled together by the J_3 interaction pairs of spins at each boundary couple to each other and form singlets, and the entire system does not have edge states anymore. On the other hand, each of the two boundary singlets can be

excited to the triplet state with relatively small excitation energies. These triplet excitations are localized at the edges and should be distinguished from the bulk excitation while constructing the conformal tower.

In Fig.2.12(a), DMRG results for the energies of a few low-lying states of the $J_2 - J_3$ model in an open chain are shown as a function of iterations for one selected sweep. We show results in the sector of zero total magnetization $S^z_{\text{tot}} = 0$ for $N = 300$ sites, for which the energy of the edge excitations is approximately equal to the bulk gap. By looking at the energy as a function of iterations along one sweep, edge and bulk excitations can be distinguished by the position of their local minima.

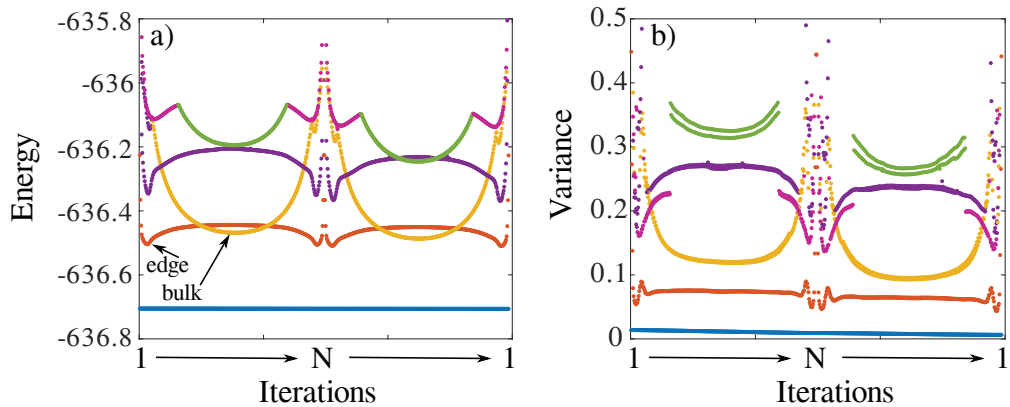

Figure 2.12 – DMRG result for the calculation of the excitation spectra in $J_2 - J_3$ open chain with $N = 300$ sites. a) Energy of the ground-state (blue), two-fold degenerate localized edge excitations (red,violet, magenta) and bulk excitations (yellow, green) as a function of iterations. Edge excitations can be distinguished from bulk ones by the position of the local minima. b) Variance $\langle\psi|H^2|\psi\rangle - (\langle\psi|H|\psi\rangle)^2$ as a function of iteration. The minimum of the energy occurs at the same position (iteration) as the minimum in the variance. Therefore the energy extracted at the local minima provides the best estimate of the energy of some eigenstates of the Hamiltonian.

The energy of the localized edge excitations is the smallest close to the edges and increases in the middle of the chain, where the ground-state basis does not describe the edge excitations properly (red, violet, magenta). The minima that appear at both edges mean that each level is two-fold degenerate - excitations can be localized on left or right edges. The lowest edge excitations (red) correspond to a singlet-triplet excitations of the bond at one of the edges. This was checked by computing two low-energy states in the sector of $S^z_{\text{tot}} = 1$. The nature of the other edge excitations (violet, magenta) is not clear and would requires further investigation. Presumably, they are triplet and quintuplet excitations of triangles close to the edges, obtained by breaking one Haldane bond. Bulk excitations have minima of the energy in the middle of the chain (yellow and green dots in Fig.2.12(a)). In cases where bulk and edge excitation energies are approximately equal several line crossing occur during the sweep.

In order to check that the local minima indeed correspond to the best estimate of the excita-

tion energies, we computed the variance $\langle\psi|H^2|\psi\rangle - (\langle\psi|H|\psi\rangle)^2$, as shown in Fig.2.12,(b). It vanishes when states obtained with DMRG are close to the true eigenstates of the Hamiltonian. The variance of the bulk excitations (yellow and green) indeed has a minimum in the middle of the chain. The large value of the variance (0.1 and 0.25) indicates that in the selected sweep the convergence has not been reached yet. Although it is not clear why the variance of the lowest edge excitations oscillates close to the edges (red), its minimum occurs at the same position as the local minimum in energy.

2.3 Convergence

In the last section of this chapter we will address rather technical questions on the algorithm convergence. The latter depends on many different factors: how far the system is from the critical line, the size of a chain, boundary conditions (open or periodic, free or fixed), the type of effective Hamiltonian (one-site, two-site etc.), the growing scheme for the bond dimension and many others. In the following we will shortly discuss how the convergence can be checked and controlled, and how results can be extracted even if the convergence cannot be reached.

The first example of convergence was already shown for the critical Ising model in Fig.2.10. We have noticed that the convergence of the excitation energies obtained by targeting many eigenvalues of the effective Hamiltonian depends not only on the number of kept states D, but is also extremely sensitive to the number of Lanczos iterations. In Fig.2.13 we show the convergence of the energy spectra in critical Ising chain, when the number of Lanczos iterations is restricted to 200.

There are several ways to control the convergence: Traditional DMRG exploits the so-called truncation error or discarded weight, defined as the sum of the discarded singular values. The discarded weight is zero by construction in one-site DMRG, while one can access it in two- or more-site DMRG. The convergence of the ground state is achieved when the energy of the ground state does not change anymore with the sweeps and with the increase of the number of states D. We use the latter when compute the ground-state only as a good indicator of convergence, however there is a risk that the energy will be stuck at a local minimum and converges to some excited state instead of the ground-state. The same could happen when the convergence is checked by the variance, that signals convergence to an eigenstate, but not necessary to the ground state. The only way to check this (although it does not provide any guarantee) is to increase the number of kept states in different ways.

One can start with different numbers of states in infinite-size DMRG and let the bond dimension grow linearly or as a geometric series (or in a more complicated way). In most of the cases we use a linear increase of the bond dimension at each half-sweep. Then one can check the convergence with both the number of performed sweeps and the number of kept states. Close to the critical point DMRG converges very slowly and a large number of states has to be kept in order to get reliable results. Therefore for critical systems, it is reasonable to increase the bond dimension very fast during the first few sweeps (lets us say till $D \approx 800$) and continue

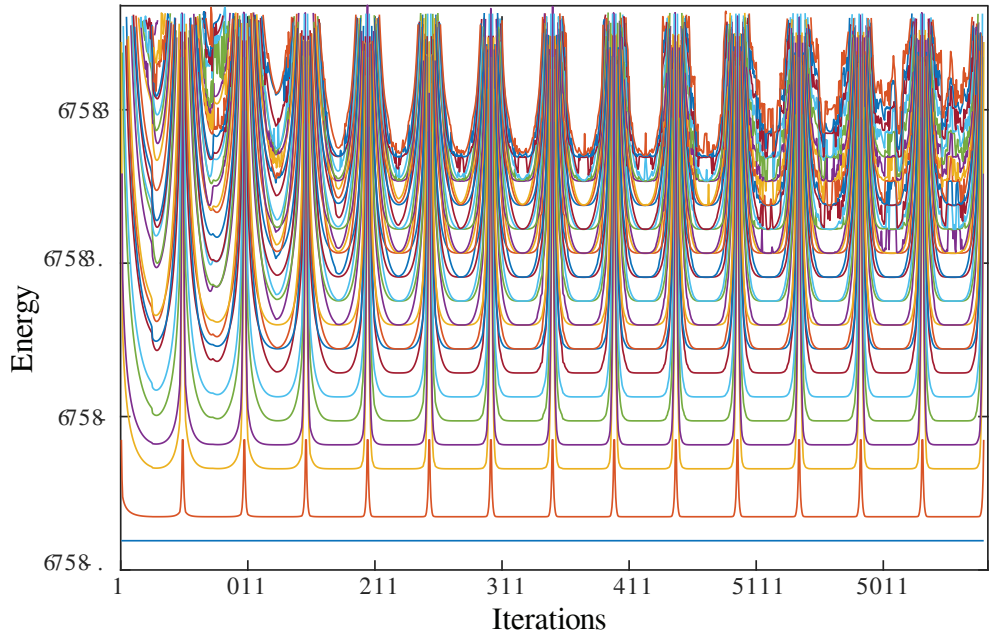

Figure 2.13 – Same as Fig.2.10 obtained with at most 200 Lanczos iterations. When the number of Lanczos iterations is sufficiently large the noise in higher excited states is suppressed as shown in Fig.2.10 obtained with at most 500 Lanczos iterations

sweeping through the tensor network with large number of kept states. In order to avoid convergence to a wrong eigenstate, one has to shake the system either by a slow increase of the bond dimension (say 20-50 states during one sweep) or by shaking the wave-function with decreasing and increasing the number of states until the convergence is reached (e.g. decrease by 20-30 while sweeping left-to-right and increase by 50-80 while sweeping back). One can try different approaches to see whether all of them converge to the same state.

In Fig. 2.14(a), we have plotted the ground-state energy of periodic chains for spin-1 $J_1 - J_2 - J_3$ model at Ising critical line (see Chapter 4) as a function of the inverse number of sweeps. Note that we plot measurements after each passage through the system, whereas a sweep corresponds to going back and forth. So the variable sweep takes half-integer as well as integer values. The almost flat part of the curves for large number of sweeps indicates that convergence was reached. For each curve, we have used the slope of the last few points to extrapolate the results for infinite number of sweeps. We do up to 16 sweeps and keep up to 900 states. In the first 6-7 sweeps the number of kept states increases from 100 to approximately 90% of the maximal value, and we reaches the maximim while by increasing and decreasing number of states.

The lack of convergence can also be a problem for higher excited states even with open boundary conditions as shown in Fig.2.14 (b) and (c). As pointed out in the previous section, the convergence of the excited state is reached if the energy as a function of iterations becomes flat in the middle of the chain. In some complicated cases such as $J_1 - J_2$ models with either

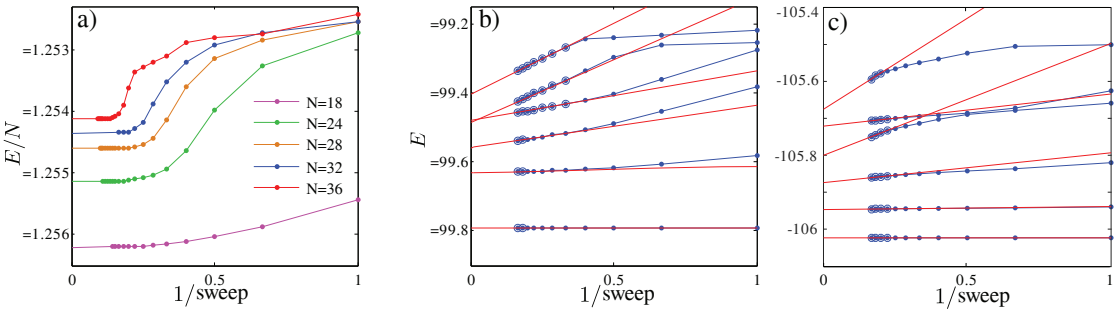

Figure 2.14 – Extrapolation of the DMRG results towards infinite number of sweeps. (a) Ground state energies for periodic chains with different numbers of sites. The continuation of the line is a fit linear in 1/sweep of the last few points. (b) and (c) Ground-state energy and energy of the lowest excited states as a function of the inverse number of DMRG sweeps (equivalently inverse number of states) for $J_1 - J_2 - J_3$ model in open chain with $N = 80$ (b) and 85 (c) sites. Dots are DMRG results while red lines are linear fits of the last few points for each curve marked with large circles.

three-body interactions (J_3) or biquadratic coupling (J_b) a large number of states should be kept. This leads to a very slow convergence starting from rather small systems. Fig. 2.14(b) provides the convergence for several energy levels as a function of the inverse number of sweeps. Although convergence is reached only for the ground-state and the lowest excited state, one can estimate energies of few more levels by extrapolating the last few points of each curve to infinite number of sweeps (here we use linear fit in $1/sweep$). We do 7-9 sweeps and the number of kept states increase linearly from 100 to 900. Therefore finite-size scaling of the energy with the number of sweeps is equivalent to scaling with number of kept states.

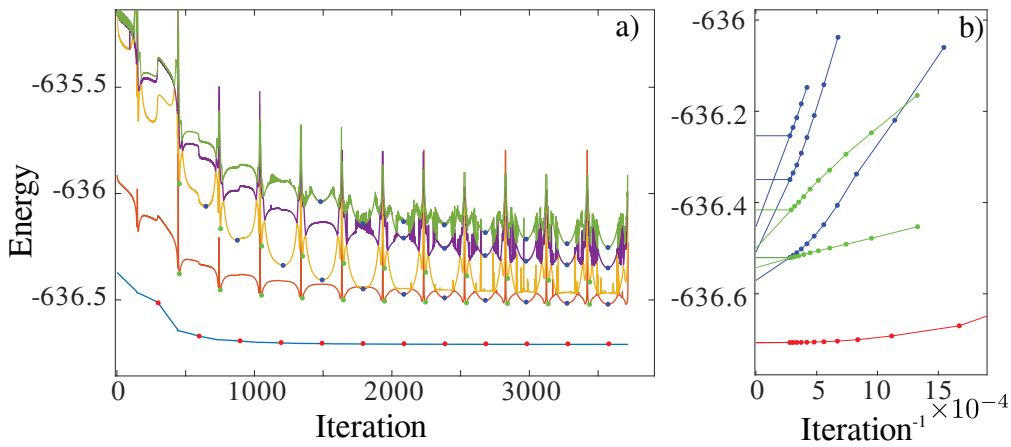

Figure 2.15 – a) Energy of the ground state and of the first four low-lying excited states as a function of iterations. The ground-state energy, bulk and edge excitation are marked with red, blue and green dots respectively. b) Energy scaling with the number of iterations. The values of the energies are taken at the points marked on the left panel. The lower bound estimates are linear fits of the last two available points. The upper bound is the value of the last available point

The convergence is even more complicated in the case of the $J_2 - J_3$ model for which, as briefly discussed above, low-lying localized edge excitations appears below slowly convergent bulk excitations. An example of convergence for $N = 300$ sites and the extrapolation of the energies with the number of sweeps is provided in Fig.2.15. As before we increase the number of states linearly so the extrapolation with the number of sweeps in Fig.2.15(b) is equivalent to the extrapolation with the number of states. In the provided example, the convergence has not been reached for the excited states, therefore we estimate the errorbar with linear fits of the last two available points as a lower bound and the the values of the last available points as an upper bound. Later we shall see that despite the poor convergence, the underlying critical theory still can be extracted from these results.

2.4 Summary

In this section we have discussed the implementation details of the DMRG algorithm that has been used to obtain most of the numerical results presented in the following chapters. In particular, we have provided an efficient representation of the Hamiltonian in terms of on-site matrix product operators for the $J_1 - J_2 - J_3$ model. A new method of extracting the excited states from a single-run DMRG has been described. The key point is to follow the excitation spectrum during the sweeps, this enables to distinguish bulk and edge excitations and check the convergence of the excitation energies. Although the established method is not universal, it can be applied to many relevant problems such as the excitation energies of the localized impurities, the detection of the low-lying in-gap states, and the excitation spectra of critical systems. Finally, the convergence of the results has been discussed and some examples for the extrapolation of non-convergent results have been provided.

3 Minimal models

This chapter is dedicated to the numerical investigation of particularly simple critical points in one-dimensional quantum systems described by minimal models of conformal field theory (CFT). We start with a brief review of general properties of the minimal models following Ref.[35]. According to boundary CFT, one can switch between primary fields or combinations of several primary fields by changing the boundary conditions in the Hamiltonian. Therefore, a particular advantage of the minimal models is that they are described by a finite number of primary fields. The excitation spectrum of these systems is then given by a conformal tower built from each primary field. Thus, by playing with boundary conditions, one can in principle observe all possible conformal towers that appear in the minimal model. The boundary CFT for the transverse field Ising and three-state Potts models were worked out by Cardy in Ref.[21]. The excitation spectra for open chains reveal the formation of conformal towers under different boundary conditions: free, fixed or mixed. The goal of this chapter is twofold: first, to confirm the predictions of boundary CFT for two selected models - the transverse field Ising model and the three-state Potts model; second, to test the numerical approach for the calculation of the excitation spectrum proposed in the previous chapter.

3.1 Introduction

The model is called minimal if the corresponding CFT contains a finite number of local fields with well-defined scaling behavior. The minimal models can be labeled by two positive integers (p, p') that reflect the periodicity properties of the conformal dimension

$$h_{r,s} = h_{r+p',s+p}. \tag{3.1}$$

The central charge of the critical theory can be expressed in terms of these integers as [35]:

$$c = 1 - 6\frac{(p-p')^2}{pp'} \tag{3.2}$$

For minimal models the conformal dimension h is given by Kac formula[53, 35]:

$$h_{r,s} = \frac{(pr - p's)^2 - (p - p')^2}{4pp'}, \tag{3.3}$$

where the pair of integers (r, s) label the various conformal dimensions and range in the intervals $1 \leq r \leq p' - 1$ and $1 \leq s \leq p - 1$. The conformal dimension obeys the following symmetry property (see Eq.A.1 for derivation):

$$h_{p'-r,p-s} = h_{r,s} \tag{3.4}$$

A minimal model is unitary if and only if $|p' - p| = 1$ [37, 35]. In this case, the minimal conformal dimension is $h_{1,1} = 0$ and it corresponds to the primary conformal field identity $\phi_{(1,1)} = I$. Without loss of generality we assume $p > p'$, then for unitary minimal models the central charge of Eq.3.2 can be rewritten as

$$c = 1 - \frac{6}{p(p-1)}. \tag{3.5}$$

The first non-trivial ($c > 0$) unitary model is labeled by $(4, 3)$ and corresponds to the critical Ising model in a transverse field[10, 35]. The following pairs $(5, 4)$ and $(6, 5)$ label the tri-critical Ising model [36, 35] and the three-state Potts model [29, 99, 35] respectively. The first and the last cases will be investigated numerically in the following sections.

One of the fundamental characteristic of a conformal field theory is a central charge, as first realized in Ref.[10]. In practice, the universality class of a critical theory is usually determined by extracting the central charge from numerical data. Although it is not always feasible to deduce the critical theory from the central charge in a unique way, the number of candidates for possible CFTs is reduced to just a few. The selection among them often can be based on simple physical intuition. In addition, the critical exponents can be extracted from the scaling of some physical operators (on-site magnetization, correlations etc.). Moreover, in case of conformally invariant boundary conditions the excitation spectrum forms so-called conformal tower. Various boundary conditions correspond to primary fields with different conformal dimensions that result in various conformal towers or their superposition. In cases, where there is no physical intuition on the type of the critical theory, or when the numerical computation of the central charge is complicated (see the following chapters for examples) the study of the excitation spectra provides a systematic and complete way to extract the parameters of the underlying critical theory.

In the minimal model labeled by (p, p'), the irreducible character is given by

$$\chi_{(r,s)}(q) = K_{r,s}^{(p,p')}(q) - K_{r,-s}^{(p,p')}(q), \tag{3.6}$$

where

$$K_{r,s}^{(p,p')}(q) = \frac{q^{-1/24}}{\varphi(q)} \sum_{n\in\mathbb{Z}} q^{(2pp'n+pr-p's)^2/4pp'}, \tag{3.7}$$

and $\varphi(q)$ is the Euler function:

$$\frac{1}{\varphi(q)} = \prod_{n=1}^{\infty} \frac{1}{1-q^n} \tag{3.8}$$

The structure of the excitation spectra for a particular CFT can be deduced from the small-q expansion of the characters in Eq.3.6.

3.2 Ising model in a transverse field

The simplest one-dimensional model that exhibits a quantum phase transition is the Ising model in a transverse field. It is given by the following Hamiltonian:

$$H_{\text{Ising}} = J\sum_i S_i^x S_{i+1}^x + hS_i^z, \tag{3.9}$$

where positive (respectively negative) coupling constant J corresponds to antiferomagnetic (respectively ferromagnetic) Ising models. In both cases, a quantum phase transition occurs at the critical values of the magnetic fields $h = \pm J/2$.

As pointed out in the introduction, the critical Ising model is described in CFT by the minimal model with $(p, p') = (4, 3)$[10, 35]. According to Eq.3.5, the central charge of the critical theory is $c = 1/2$. The theory has three operators: identity I with conformal dimension $h_{1,1}$, spin operator σ with $h_{1,2} = 1/16$ and energy density ϵ with conformal dimension $h_{2,1} = 1/2$ (see table 3.1).

	$s=1$	$s=2$	$s=3$
$r=1$	$h_{1,1}=0$	$h_{1,2}=1/16$	$h_{1,3}=h_{2,1}$
$r=2$	$h_{2,1}=1/2$	$h_{2,2}=h_{1,2}$	$h_{2,3}=h_{1,1}$

Table 3.1 – Conformal dimension $h_{r,s}$ of the field $\phi_{(r,s)}$ in the Ising critical theory. The repeating dimensions due to the symmetry properties of Eq.3.4 are shown in gray

The finite size spectrum of the Ising model with different types of boundary conditions in open chain were all worked out by Cardy[21]. For open and free boundary condition the excitation spectrum is the superposition of I and ϵ conformal towers. The two towers are separated when the edge spins are fixed. For $\uparrow,\uparrow$ boundary conditions only the conformal tower I occurs and for $\uparrow,\downarrow$ boundary conditions, only ϵ occurs. The conformal tower σ is induced by mixed boundary conditions, when the spin at one edge is fixed to either $\uparrow$ or $\downarrow$ while the spin at the

other edge remains free.

The characters of these conformal towers, that determine the multiplicities of the excited states, were first calculated in Ref.[87]. In Appendix A we repeat the calculations of characters using the definition of Eq.3.6 and keeping up to eight orders in q. The obtained expansions are listed below:

Identity conformal tower:

$$\chi_I = q^{-1/48}\left(1+q^2+q^3+2q^4+2q^5+3q^6+3q^7+5q^8\right) \tag{3.10}$$

ϵ conformal tower:

$$\chi_\epsilon = q^{1/2-1/48}\left(1+q+q^2+q^3+2q^4+2q^5+3q^6+4q^7+5q^8\right) \tag{3.11}$$

σ conformal tower:

$$\chi_\sigma = q^{1/16-1/48}\left(1+q+q^2+2q^3+2q^4+3q^5+4q^6+5q^7+6q^8\right) \tag{3.12}$$

The terms inside the brackets gives the structure and the multiplicities of the excitation spectrum. More precisely, a term mq^n corresponds to the n's energy level with multiplicity m. The ground state corresponds to $n=0$, therefore the scaling of the ground-state is given by the prefactor equal to $q^{h_{r,s}-c/24}$:

$$E = \varepsilon_0 N + \varepsilon_1 + \frac{\pi v}{N}\left[-\frac{1}{48}+x\right] \tag{3.13}$$

where ε_0 and ε_1 are non-universal constants and x is the corresponding conformal dimension: $x = h_I = 0$ for the identity, $x = h_\epsilon = 1/2$ for ϵ and $x = h_\sigma = 1/16$ for σ conformal towers. When the excitation spectrum is given by the superposition of several conformal towers, the corresponding characters are added and therefore x equal to the smallest conformal dimension of these towers. Thus, for free boundary condition, since $h_I < h_\epsilon$ the ground-state belongs to the I conformal tower and scales according to Eq.3.13 with $x=0$.

We have computed the excitation spectrum of the critical Ising model in open chains under different boundary conditions by targeting many eigenvalues of the effective Hamiltonian in the DMRG (the method was described in details in the section 2.2).

The DMRG results on the scaling of finite-size spectra are shown in Fig.3.1. Figures 3.1(a),(b),(c) and (d) show the scaling of the ground-state energy for different boundary conditions. Non-universal terms ε_0, ε_1 and the velocity v are treated as fitting parameters. Numerically obtained values of the velocities $v_{\text{free}} = 0.491$, $v_{\uparrow\uparrow} = v_{\uparrow\downarrow} = 0.509$ coincides within 2% with the value $v_{Ising} = 1/2$.

Figures 3.1(e),(f),(g) and (h) show levels of conformal towers obtained numerically as $n =$

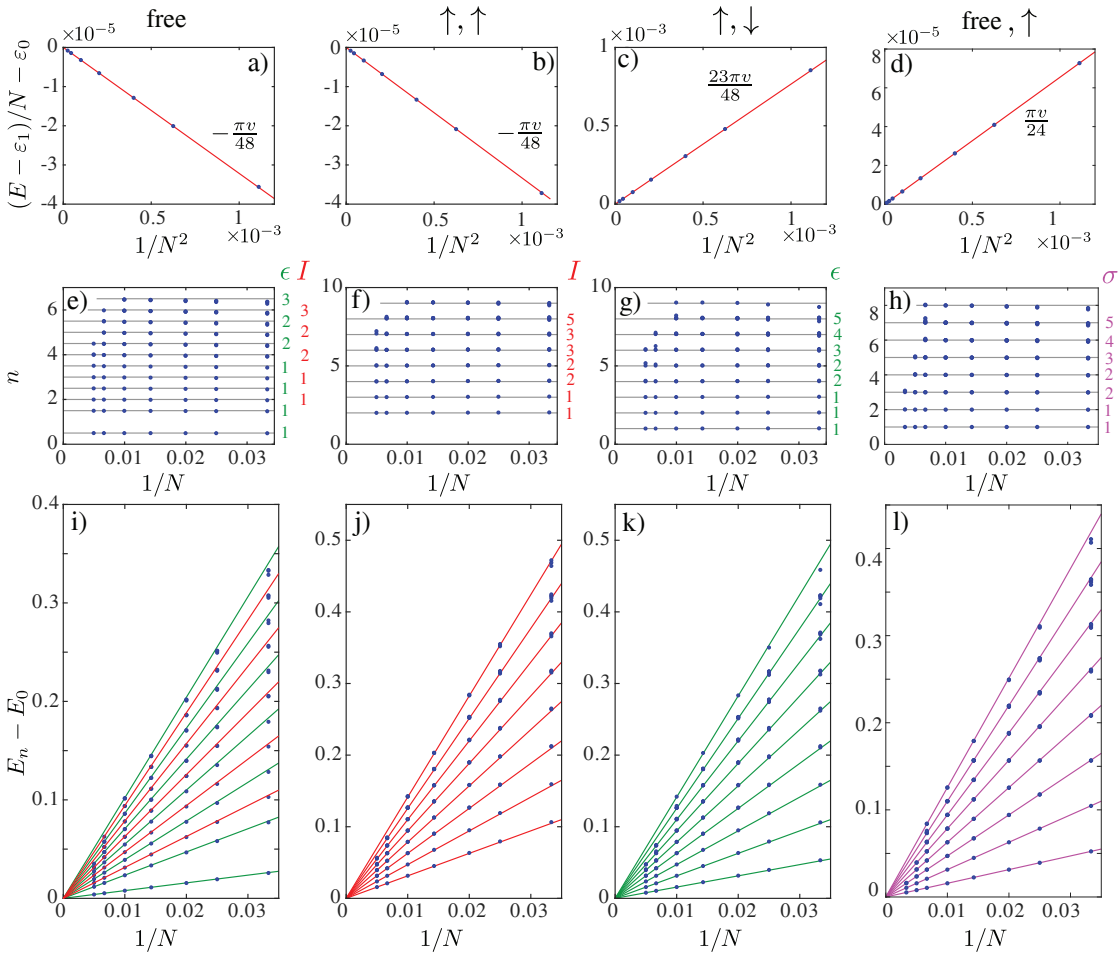

Figure 3.1 – Finite-size scaling of the energies of the critical Ising model in open chains with different boundary conditions: (a),(e),(i) - free at both edges; (b),(f),(j) - fixed with both edge spins pointing up; (c),(g),(k) - fixed with one edge spin pointing up and other pointing down; (d),(h),(l) - fixed at one edge and free at second one. (a),(b),(c) and (d) finite-size scaling of the ground-state energy after removing ground-state energy in the thermodynamic limit ε_0 and boundary terms ε_1. (e), (f), (g) and (h) conformal towers of the excitation spectra. Blue dots are the DMRG data for $n = (E_n - E_0)/(\pi v N)$ with $v = v_{Ising} = 1/2$. The CFT predictions are shown with gray lines for reference. The multiplicities of the levels are indicated on the right of each tower. (i), (j), (k) and (l) Finite-size scaling of the excitation energies. Blue dots are DMRG data, red, green and magenta lines are conformal towers for identity I, energy ϵ and spin σ fields.

$(E_n - E_0)/(\pi v_{Ising} N)$. The DMRG results (dots) are in good agreement with CFT predictions (gray lines). Note that due to the absence of logarithmic corrections in the Ising model, the structure of the conformal tower is independent of the system size and can be observed starting from very small system sizes ($N \approx 30 - 40$). The multiplicities of each level observed numerically are shown on the right of the Figures 3.1(e),(f),(g) and (h) and coincide with the expansion of the characters of Eq.3.10, Eq.3.11 and Eq.3.12.

The finite-size scaling of the gap is shown in Figures 3.1(i),(j),(k) and (l). They contain essentially the same amount of information as the three figures above. The DMRG results for up to 20 states are marked with blue dots, red, green and magenta lines show the CFT prediction for the scaling of I and ϵ and σ conformal towers respectively. The consistence can be checked by extracting the velocities from the finite-size scaling of the ground-state and every excited state. The obtained velocities are listed in the table A.1 and agree within 2% with $v_{Ising} = 1/2$.

Previously, the conformal towers of the critical Ising modelhave been computed numerically by Evenbly and Vidal[31] using scale-invariant MERA, where three lowest levels were computed for each tower. The conformal towers with twelve levels has been obtained from entanglement spectrum in chains with open free and periodic boundary conditions by Läuchli [62].

3.3 Three-state Potts model

The next minimal model that we probe numerically is the three-state Potts model, which is an extension of the transverse field Ising model to a system with a local Hilbert of dimension $d = 3$. For convenience, we label single-particle states by A, B and C. The model is defined by the Hamiltonian:

$$H_{\text{Potts}} = -J \sum_{i=1}^{N-1} \sum_{\mu=1}^{3} P_i^{\mu} P_{i+1}^{\mu} - h \sum_{i=1}^{N} P_i, \tag{3.14}$$

where $P_i^{\mu} = |\mu\rangle_{ii}\langle\mu| - 1/3$ projects spin at site i along the μ direction and $P_i = |\lambda_0\rangle_{ii}\langle\lambda_0| - 1/q$ aligns spins along the direction $|\lambda_0\rangle_i = \sum_{\mu} |\mu\rangle \sqrt{q}$. The first term in the Hamiltonian plays the role of the ferromagnetic interaction, while the second one is a generalized transverse field.

In the context of CFT the model is labeled by $(p, p') = (6, 5)$[29, 99, 35] for which Eq.3.2 gives the central charge $c = 4/5$. The corresponding minimal model has ten different fields, with the conformal dimensions listed in the Table 3.2.

	$s=1$	$s=2$	$s=3$	$s=4$	$s=5$
$r=1$	$h_{1,1}=0$	$h_{1,2}=1/8$	$h_{1,3}=2/3$	$h_{1,4}=h_{4,2}$	$h_{1,5}=h_{4,1}$
$r=2$	$h_{2,1}=2/5$	$h_{2,2}=1/40$	$h_{2,3}=1/15$	$h_{2,4}=h_{3,2}$	$h_{2,5}=h_{3,1}$
$r=3$	$h_{3,1}=7/5$	$h_{3,2}=21/40$	$h_{3,3}=h_{2,3}$	$h_{3,4}=h_{2,2}$	$h_{3,5}=h_{2,1}$
$r=4$	$h_{4,1}=3$	$h_{4,2}=13/8$	$h_{4,3}=h_{1,3}$	$h_{4,4}=h_{1,2}$	$h_{4,5}=h_{1,1}$

Table 3.2 – Conformal dimension $h_{r,s}$ of the field $\phi_{(r,s)}$ in the critical three-state Potts model. The repeating dimensions due to symmetry properties of Eq.3.4 are shown in gray

The small-q expansion of the characters for these ten fields is provided in the Appendix A. Six of them appear in the description of the operators I of zero dimension, σ of dimension 1/15, ϵ

of dimension 2/5, and ψ of dimension 2/3. The corresponding characters are:

$$\chi_I = \chi_{1,1} + \chi_{4,1} \qquad \chi_\epsilon = \chi_{2,1} + \chi_{3,1} \qquad \chi_\sigma = \chi_{\sigma^\dagger} = \chi_{2,3} \qquad \chi_\psi = \chi_{\psi^\dagger} = \chi_{1,3} \tag{3.15}$$

The small-q expansion of these characters gives:

$$\chi_I = q^{-1/30}\left(1 + q^2 + 2q^3 + 3q^4 + 4q^5 + 7q^6\right) \tag{3.16}$$
$$\chi_\epsilon = q^{-1/30+2/5}\left(1 + 2q + 2q^2 + 4q^3 + 5q^4 + 8q^5 + 11q^6\right) \tag{3.17}$$
$$\chi_\sigma = q^{-1/30+1/15}\left(1 + q + 2q^2 + 3q^3 + 5q^4 + 7q^5 + 10q^6\right) \tag{3.18}$$
$$\chi_\psi = q^{-1/30+2/3}\left(1 + q + 2q^2 + 2q^3 + 4q^4 + 5q^5 + 8q^6\right) \tag{3.19}$$

The appearance of different conformal towers under various applied boundary conditions was studied by Cardy[21]. In an open chain with free boundary conditions at both ends, the excitation spectrum corresponds to the superposition of three conformal towers $\chi_I \oplus 2 \times \chi_\psi$. Strictly speaking, the conformal tower in this case is given by $\chi_I \oplus \chi_\psi \oplus \chi_{\psi^\dagger}$. However, the characters of the field ψ and its conjugate are equal $\chi_{\psi^\dagger} = \chi_\psi$. The three towers split according to $\chi_I \oplus 2 \times \chi_\psi$ under fixed boundary conditions. If only the local state A is allowed at both edges, then the boundary condition is of the type A-A and the excitation spectrum is given by the identity conformal tower I. When the allowed state is different at the edges, the boundary conditions are then A-B and A-C, and in both cases the excitation spectrum is given by the conformal tower of ψ. Numerically, the conformal towers for free, and periodic boundary conditions were obtained previously from entanglement spectra by Läuchli [62].

The finite-size scaling of the ground-state is given by:

$$E = \epsilon_0 N + \epsilon_1 + \frac{\pi v}{N}\left[-\frac{1}{30} + x\right], \tag{3.20}$$

where ε_0 and ε_1 are non-universal constants. In the case of free and A-A boundary conditions, the ground state belongs to the conformal tower I with conformal dimension $x = h_I = 0$, while the spectrum of A-B (and A-C) boundary condition belongs completely to the ψ conformal tower with conformal dimension $x = h_\psi = 2/3$. DMRG results on the ground-state scaling are summarized in Fig.3.2(a), (b) and (c). ε_0 and ε_1 together with the velocity v are treated as fitting parameters. The obtained values of the velocities are $v_{\text{free}} = 0.827$, $v_{\text{A-A}} = 0.857$ and $v_{\text{A-B}} = 0.862$.

Figures Fig.3.2(d),(e) and (f) show levels of conformal towers obtained numerically as $n = (E_n - E_0)/(\pi v_{A-A} N)$. The DMRG results (dots) are in good agreement with CFT predictions (gray lines). Note that the structure of the conformal towers does not depend on the system size and the excitation spectra do not reveal finite-size corrections. The multiplicities of each

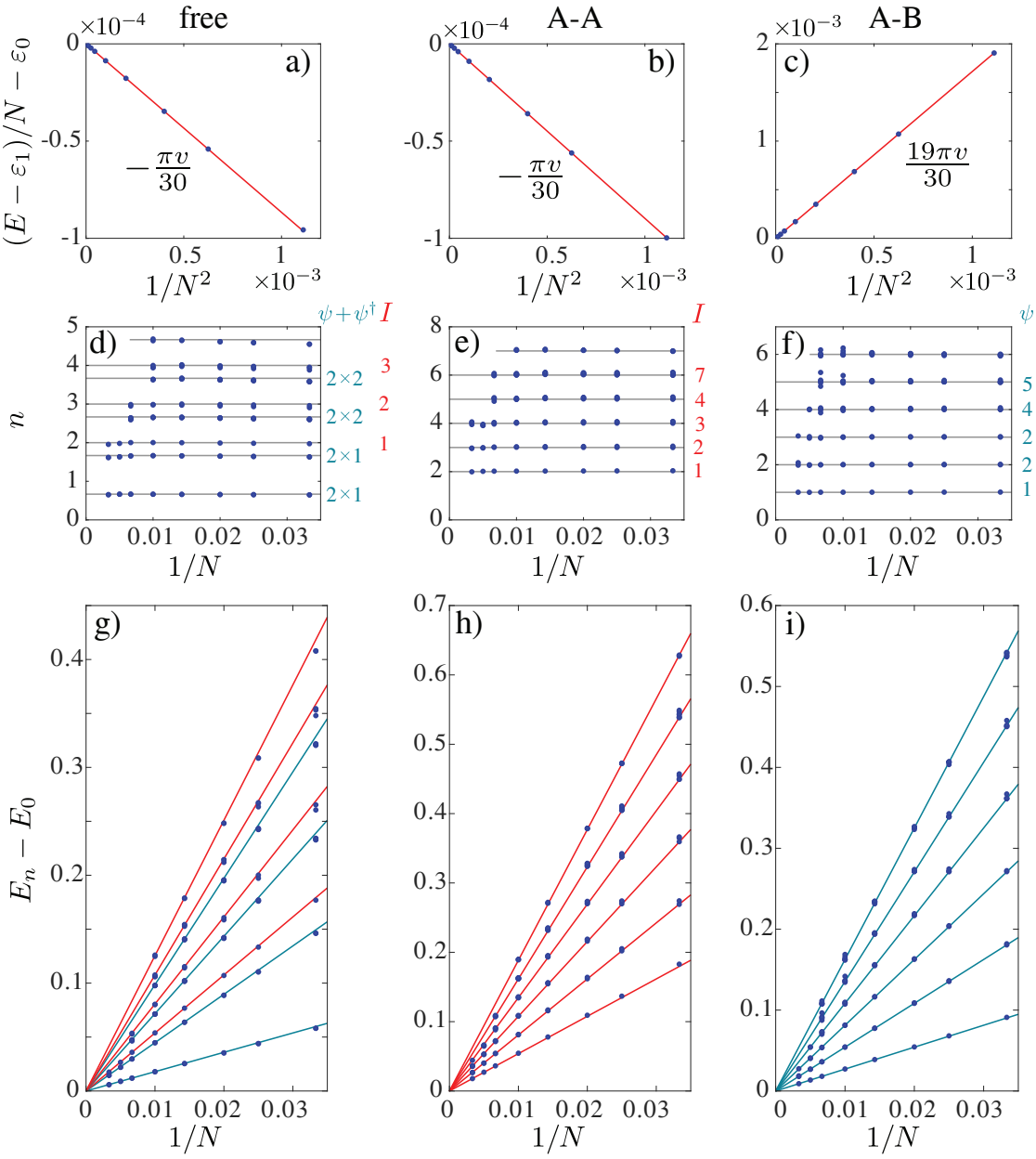

Figure 3.2 – Finite-size scaling of the energies of the critical three-state Potts model in open chains with different boundary conditions: (a),(d),(g) - free, (b),(e),(h) - fixed with the same state at both edges, (c),(f),(i) - fixed with different states on the left and right edges. (a),(b),(c) finite-size scaling of the ground-state energy after removing ground-state energy in the thermodynamic limit ε_0 and boundary terms ε_1. (d), (e), (f) conformal towers of the excitation spectra. Blue dots are the DMRG data for $n = (E_n - E_0)/(\pi v N)$ with $v = v_{\text{A-A}} = 0.857$. The CFT predictions are shown with gray lines for reference. The multiplicities of the levels are indicated on the right of each tower. (g), (h), (i) Finite-size scaling of the excitation energies. Blue dots are DMRG data, red and blue lines are conformal towers for I and ψ fields respectively

level observed numerically are shown on the right of the Figures 3.1(d),(e) and (f) and coincide with the expansion of the characters of Eq.3.16, 3.17, 3.18 and 3.19.

The finite-size scaling of the excitation energies for different boundary conditions are provided in Fig. 3.2(g),(h) and (i). The DMRG results for up to 20 states are marked with blue dots, red and blue lines show the CFT prediction for the scaling of I and ψ conformal towers respectively. The consistence can be checked by extracting the velocities from the finite-size scaling of the ground-state and every excited state. The obtained velocities are listed in Table A.2.

In agreement with Cardy's prediction [21], the conformal towers of ϵ and σ appear under partially fixed boundary conditions, when two states are allowed at the edges, while the third one is suppressed. When the same pair of states are allowed at both edges, the boundary conditions are of type AB-AB and the energy spectrum is described by the superposition of two conformal towers $I \oplus \epsilon$ (see Fig.3.3(d) and (g)). The ground state scales according to Eq.3.20 with $x = h_I = 0$ as shown in Fig.3.3(a). When different pairs of states are allowed at two edges of a chain, the boundary is of type AB-AC and the energy spectrum is a superposition of $\sigma \oplus \psi$ conformal towers (see Fig.3.3(e) and (h)). The ground-state scales according to Eq.3.20 with $x = \min(h_\sigma, h_\psi) = h_\sigma = 1/15$ as shown in Fig.3.3(b).

Surprisingly, the excitation levels that belong to σ or ϵ towers exhibit strong finite-size effects, while towers I and ψ remain unaffected. Most clearly it can be observed in Fig.3.3(g) and (h). The discrepancy between the numerical data and CFT predictions for σ and ϵ towers is significant only for small systems $N < 100$ and suppressed while approaching thermodynamic limit, for which CFT predictions apply.

The velocity extracted from the ground-state scaling AB-AB boundary condition $v_{AB,AB} = 0.857$ is in good agreement with previous results. By contrast, in the case of AB-AC boundary conditions the ground state scaling gives the velocity $v_{AB-AC} = 1.05$, that is more that 20% off the velocities obtained with other boundary conditions. Perhaps this discrepancy is due to the observed finite-size effect, since the ground-state belongs to the σ conformal tower. The velocities extracted from the finite-size scaling of the excitation energies are summarized in Table A.3.

When the applied boundary condition fixes one edge and partially fixes the second one, the energy spectrum is described by only one tower. If the allowed states at the two edges are different (A-BC boundary), the whole spectrum belongs to the ϵ conformal tower, otherwise the excitation spectrum is described by σ conformal tower (A-AB boundary). The ground state scales according to 3.20 with $x = h_\epsilon = 2/5$ (Fig.3.4(b)) and $x = h_\sigma = 1/15$ (Fig.3.4(a)). As in the case of partially fixed boundary conditions (AB-AB and AB-AC), strong finite-size effects appear in both σ and ϵ conformal towers (Fig.3.4(g) and (h)).

In order to see the towers for the remaining four primary fields, namely for $\phi_{(1,2)}$, $\phi_{(2,2)}$, $\phi_{(3,2)}$ and $\phi_{(4,2)}$, the boundary conditions should be fixed or partially fixed only at one edge while at the second edge the spin remains free [21]. The superposition of the towers with conformal

dimensions $h_{2,2} = 1/40$ and $h_{3,2} = 21/40$ appear under AB-free boundary condition. The other two towers with $h_{1,2} = 1/8$ and $h_{4,2} = 13/8$ are superposed under A-free boundary conditions.

In the case of AB-free boundary conditions the ground state scales according to Eq. 3.20 with $x = h_{2,2} = 1/40$, that corresponds to a very small numerical prefactor for the universal term $-\pi v/120N$ (Fig.3.3 (c)). Numerically, the calculated conformal towers $\chi_{2,2}$ and $\chi_{3,2}$ are shown in Fig.3.3 (f) and (i). Significant finite-size effects appear in both towers.

If the spin is fixed only at one edge (A-free boundary condition) $x = h_{1,2} = 1/8$ in the ground-state scaling of Eq.3.20 (Fig.3.4 (c)). The calculated conformal towers match the theoretical by predicted $\chi_{1,2}$ and $\chi_{4,2}$. Note that the finite-size discrepancy does not appear in these two towers and the structure of the energy spectrum is clear starting from small systems (Fig.3.4 (f) and (i)).

The velocities extracted from the finite-size scaling of the ground-state and excitation energies are listed in the Table A.2 for A-free and in Table A.3 for AB-free boundary conditions.

3.4 Summary

In the present chapter we have provide a solid numerical confirmation for the predictions of boundary conformal field theory for the critical Ising and three-state Potts models. An extensive DMRG calculation has allowed us to reproduce the excitation energies for up to 20 low-energy states. The obtained numerical results suggest strong finite-size effects in the scaling of the ground-state and excitation energies for the conformal towers ϵ, σ, $\chi_{2,2}$ and $\chi_{3,2}$. By contrast, other conformal towers of the Potts model do not exhibit deviation from the linear scaling for small sizes.

The study of minimal models has allowed us to set up and test an extension of the DMRG algorithm that gives access to many energy levels within a single run and at low computational cost. Thus, the method described in the previous chapter indeed provides accurate results for the excitation spectrum of finite-size systems and allows one to extract the underlying critical theory. Moreover, by changing boundary conditions one changes primary fields and therefore the structure of the excitation spectrum. Thus, the excitation spectrum obtained for different boundary conditions can in principle identify the underlying critical theory in a complete and unique way. As we will show in the next chapters, this method turns out to be a powerful tool in the identification of the universality class of critical lines even in more complicated models including the $J_1 - J_2 - J_3$ and the $J_1 - J_2 - J_b$ models.

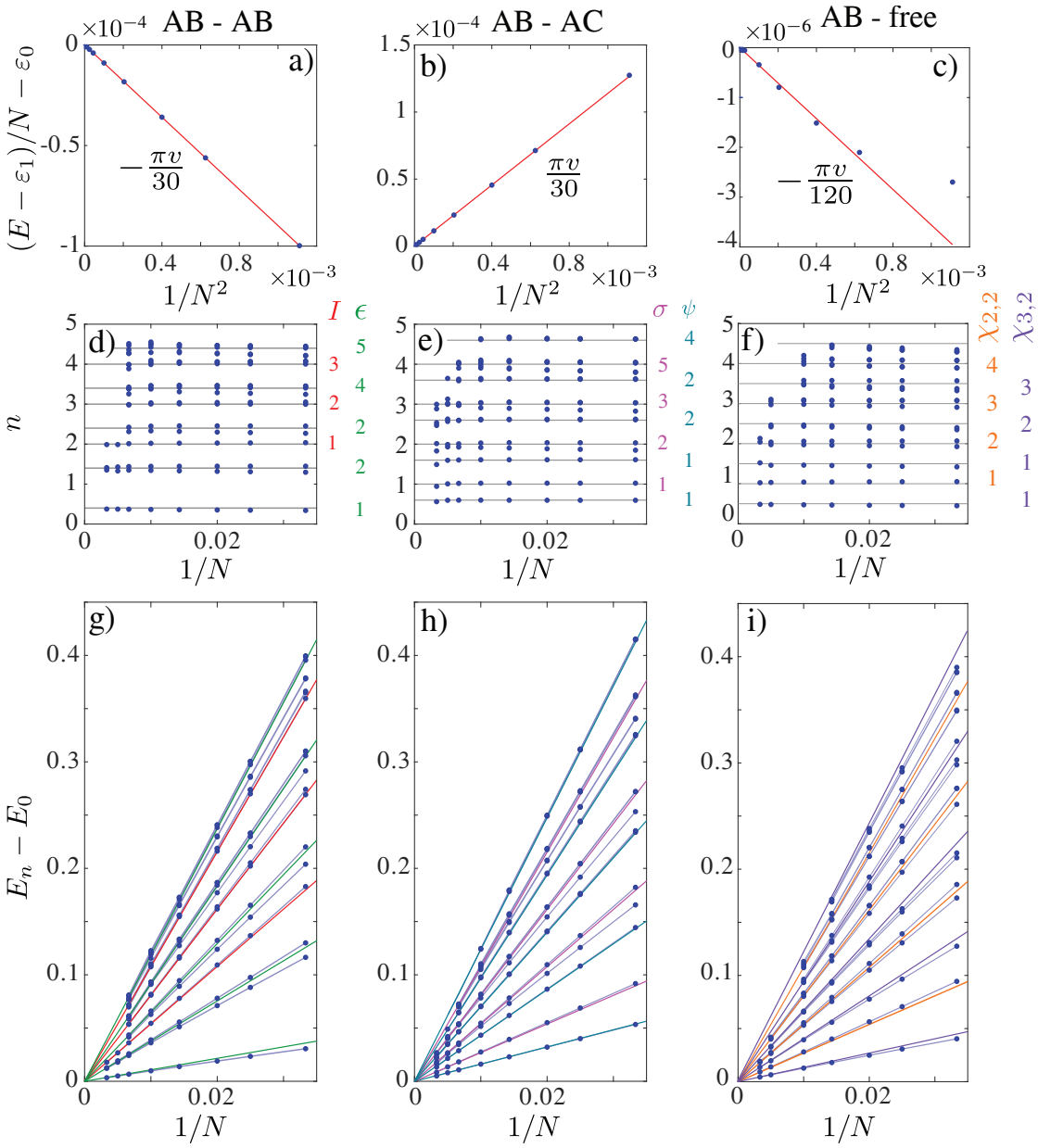

Figure 3.3 – Finite-size scaling of the energies of the critical three-state Potts model in open chains with partially fixed boundary conditions: (a),(d),(g) - only two states are allowed at the edges and excluded state is the same for left and right edge; (b),(e),(h) - only two states are allowed at the edges and excluded state is different for left and right edge; (c),(f),(i) - only two states are allowed at one edge while second edge remains free. (a), (b) and (c) finite-size scaling of the universal term in the ground-state energy. (d), (e) and (f) conformal towers of the excitation spectra. Blue dots are the DMRG data for $n = (E_n - E_0)/(\pi v N)$ with $v = v_{A-A} = 0.857$. The CFT predictions are shown with gray lines for reference. The multiplicities of the levels are indicated on the right of each tower. (g), (h) and (i) Finite-size scaling of the excitation energies. Blue dots are DMRG data, lines of different colors correspond to different conformal towers

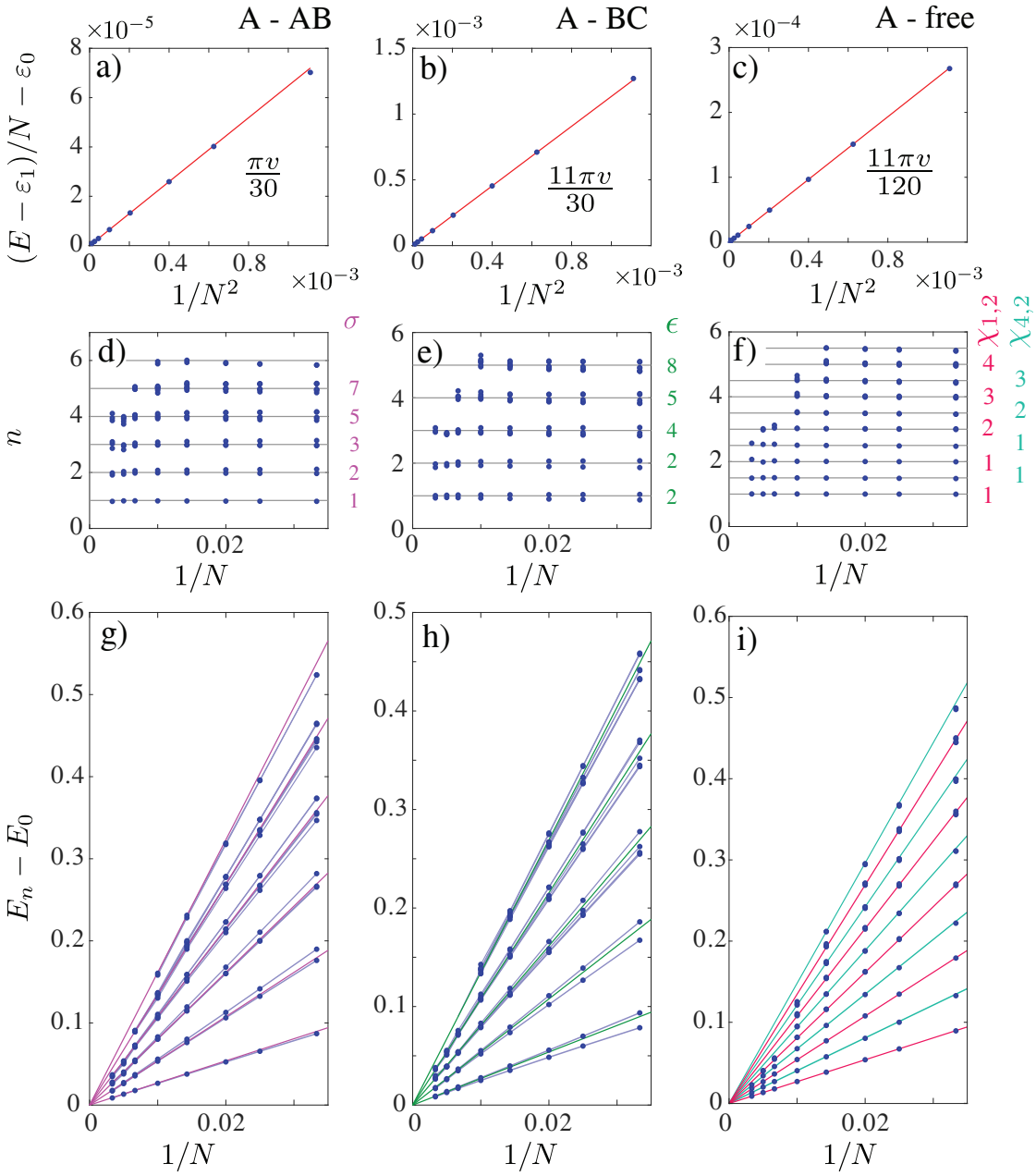

Figure 3.4 – Finite-size scaling of the energies of the critical three-state Potts model in open chains with mixed boundary conditions: (a),(d),(g) - only two states are allowed at one edge and only one of these two is allowed at the second edge; (b),(e),(h) - only two states are allowed at one edge and only one different from these two is allowed at the second edge; (c),(f),(i) - only one state is allowed at one edge while second edge remains free. (a), (b) and (c) finite-size scaling of the universal term in the ground-state energy. (d), (e) and (f) conformal towers of the excitation spectra. Blue dots are the DMRG data for $n = (E_n - E_0)/(\pi v N)$ with $v = v_{A-A} = 0.857$. The CFT predictions are shown with gray lines for reference. The multiplicities of the levels are indicated on the right of each tower. (g), (h) and (i) Finite-size scaling of the excitation energies. Blue dots are DMRG data, lines of different colors correspond to different conformal towers

4 The spin-1 chain with next-nearest-neighbor and three-site interactions

4.1 Introduction

The simplest isotropic model of a spin chain includes only nearest-neighbor interaction and is described by the Heisenberg Hamiltonian:

$$H_{\text{Heis}} = J \sum_i \mathbf{S}_i \cdot \mathbf{S}_{i+1}. \tag{4.1}$$

Heisenberg spin chains have been studied intensively over the years. The celebrated Bethe ansatz published in 1931 [13] provides an exact solution of this model. Adding frustration through competing interactions leads to a variety of new phases and quantum phase transitions. The most famous example is probably the $J_1 - J_2$ spin-1/2 chain:

$$H_{J_1-J_2} = J_1 \sum_i \mathbf{S}_i \cdot \mathbf{S}_{i+1} + J_2 \sum_i \mathbf{S}_{i-1} \cdot \mathbf{S}_{i+1}, \tag{4.2}$$

for which the ground-state is exactly dimerized when $J_2/J_1 = 1/2$ [69]. This point belongs to an extended spontaneously dimerized and gapped phase that appears when the ratio of the next-nearest neighbor interaction to the nearest-neighbor one exceeds $J_2/J_1 = 0.2411$ [77].

In 1983 Haldane predicted a finite gap for Heisenberg chains with integer spins, in contrast to critical chains for half-integer spins. An important milestone in the confirmation of Haldane's prediction was the construction of an exact ground state at the Affleck-Kennedy-Lieb-Tasaki (AKLT) point $J_b/J_1 = 1/3$ [7] of the bilinear-biquadratic spin-1 chain:

$$H_{J_1-J_b} = J_1 \sum_i \mathbf{S}_i \cdot \mathbf{S}_{i+1} + J_b \sum_i (\mathbf{S}_i \cdot \mathbf{S}_{i+1})^2 \tag{4.3}$$

At the AKLT point, the Hamiltonian $H_{J_1-J_b}$ is a parent Hamiltonian for the so-called valence-bond-solid (VBS) ground state. The VBS state is the unique state with a single valence bond connecting each nearest-neighbor pair of spins. As shown in Fig.4.1, the spin-1 at each site can be represented graphically as a pair of spin-1/2 dots, each of which is connected by a

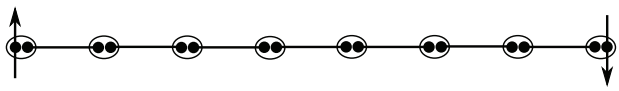

Figure 4.1 – Graphical representation of the VBS state on spin-1 chain. Spin-1 at each site (oval) is represented by a pair of dots (spins-1/2). Each dot is connected to one of its nearest neighbor by a line (valence bond singlet). In open chain, one dot at each edge remains unconnected and leads to spin-1/2 edge states

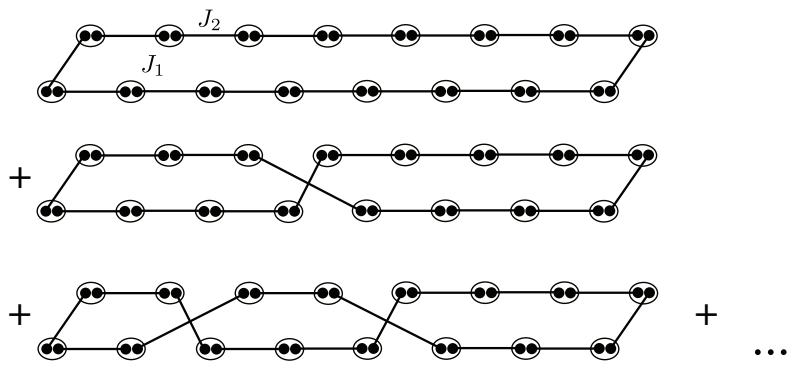

Figure 4.2 – Graphical representation of intertwined NNN-Haldane chains. $J_1 - J_2$ chain is presented as a zig-zag ladder with J_1 rungs and J_2 legs. In the following, only the top sketch will be used to label NNN-Haldane phase

valence bond line to one of its neighbors.

The VBS state is used to describe an extended Haldane phase that is usually associated with the spin-1 Heisenberg Hamiltonian and is robust under small perturbations of the Hamiltonian. The Haldane phase is topologically non trivial, and the ground state has a hidden order characterized by a non-local string order parameter. For open boundary conditions, a spin-1/2 at each edge remains unpaired that gives rise to edge states. The excitation energy of the low-lying in-gap state (so-called Kennedy triplet [54, 40]) vanishes exponentially fast with the system size. More recently, it was shown that the Haldane phase is characterized by the double degeneracy of the entanglement spectrum [82]. This degeneracy is protected by the same set of symmetries that protect the stability of the Haldane phase. If the Hamiltonian is deformed while preserving these symmetries, the degeneracy can be lifted only by crossing a phase boundary.

In the spin-1 chain, by contrast to the spin-1/2 chain, the next-nearest neighbor interaction J_2 does not lead to dimerization, but induces a first-order phase transition into a phase that consists of intertwined next nearest-neighbor (NNN) Haldane chains [56, 58] sketched in Fig.4.2.

The spin-1 $J_1 - J_2$ model, given by Hamiltonian (4.2), has been studied using a variational ansatz and DMRG. The authors have shown that the Haldane phase is stable until $J_2 = 0.7444(6)$, where a phase transition to the NNN-Haldane phase takes place. According to

DMRG calculations, the spin gap remains open. The finite jump in the string order parameter suggests that the phase transition is first order, although no discontinuity could be identified in the first derivative of the energy at the transition. Disorder and Lifshitz points (i.e. points, where the correlation function in real space becomes incommensurate with a wave-vector $q \neq 0, \pi/2, \pi$, or where the structure factor has two peaks at $q \neq 0, \pi/2, \pi$, respectively) were identified at $\alpha_d = 0.284(1)$ and $\alpha_L = 0.3725(25)$.

Spontaneous dimerization has long been known to be induced in spin-1 chains by a negative biquadratic interaction J_b exactly opposite to the bilinear one: $J_b/J_1 = -1$. The critical point is integrable with Bethe ansatz [9, 96], and it is in the $SU(2)_2$ Wess-Zumino-Witten (WZW) universality class [1, 5, 6] .

The combined effect of J_2 and J_b for the spin-1 chain has recently been investigated by Pixley et al [81], who came to the conclusion that the phase diagram only consists of the phases previously identified in the models with only one of these frustrating interactions (J_2 or J_b): the Haldane phase, a spontaneously dimerized phase, and the NNN-Haldane phase. They also carefully investigated the short-range correlations, which become incommensurate through Lifshitz and disorder transition line. The dimerization transition was argued to be either in the $SU(2)_{k=2}$ WZW universality class, or to be first order. The nature of the critical lines will be re-investigated in the next chapter.

Together with next-nearest-neighbor and biquadratic interactions, a three-site interaction $J_3\,[(\mathbf{S}_{i-1}\cdot\mathbf{S}_i)(\mathbf{S}_i\cdot\mathbf{S}_{i+1}) + \text{H.c.}]$ appears in the next-to-leading order in the strong-coupling expansion of the two-band Hubbard model. It has been shown that a three-site interaction of this form, that reduces to the next-nearest neighbor interaction for spin-1/2, is also able to induce a spontaneous dimerization in spin-S chains for arbitrary S. Michaud et al. [71, 70] have shown that there is an exactly dimerized point for all spin-S chains for the $J_1 - J_3$ model at $J_3/J_1 = 1/(4S(S+1)-2)$. For spin-1/2, this model reduces to the $J_1 - J_2$ model with $J_2 = J_3/2$, and this exactly dimerized state can be seen as the generalization of the Majumdar-Ghosh point of the spin-1/2 $J_1 - J_2$ chain. For $S = 1$ there is a transition at $J_3 \simeq 0.111$ [71] to a spontaneously dimerized phase. This transition is continuous and belongs to the $SU(2)_{k=2}$ WZW universality class [6].

In this chapter we will focus on $J_1 - J_2 - J_3$ model that combines nearest-neighbor, next-nearest neighbor and three-site interactions:

$$H_{J_1-J_2-J_3} = J_1 \sum_i \mathbf{S}_i \cdot \mathbf{S}_{i+1} + J_2 \sum_i \mathbf{S}_{i-1} \cdot \mathbf{S}_{i+1} + J_3 \sum_i [(\mathbf{S}_{i-1} \cdot \mathbf{S}_i)(\mathbf{S}_i \cdot \mathbf{S}_{i+1}) + \text{H.}c.]\,, \tag{4.4}$$

We set $J_1 = 1$ throughout this chapter and concentrate on the case of $J_2, J_3 \geq 0$. The main results for $J_1 - J_2$ and $J_1 - J_3$ are summarized in phase diagram 4.3.

Further investigations have shown that the result of Michaud et al. [71] can be extended to the case where a next-nearest neighbor exchange interaction J_2 is included [102]. Indeed,

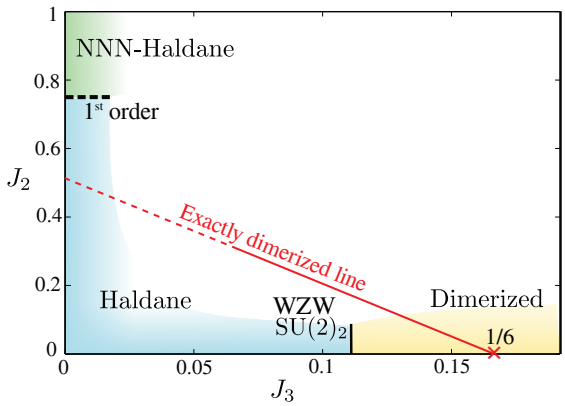

Figure 4.3 – Summary on the results from previous study on $J_1 - J_2$ and $J_1 - J_3$ models. The exactly dimerized state is an eigenstate along the red line, but it is a ground-state only for small values of J_2 (schematically shown as solid line)

provided that

$$\frac{J_3}{J_1 - 2J_2} = \frac{1}{4S(S+1) - 2}. \tag{4.5}$$

the two fully dimerized states are eigenstates along a line in the $J_2 - J_3$ parameter space, and they are ground states if J_2 is not too large. Now, for $J_3 = 0$ and $S = 1$, it has already been shown by Roth and Schollwöck that the ground state is not dimerized for $J_2 = 1/2$, but that it lies in the Haldane phase [56, 57]. This suggests that, for spin 1, the transition between the dimerized phase and the Haldane phase, which is continuous for $J_2 = 0$, has to become first order somewhere on the line $J_2 + 3J_3 = 1/2$.

4.2 Main results

Let us first summarize the main results obtained numerically with DMRG simulations and exact diagonalizations (ED). The phase diagram as a function of J_2 and J_3 couplings consists of three phases, each of which may be schematically illustrated by a diagram with lines indicating valence bond singlets formed between various sites, (see Fig. 4.4): a Haldane phase with one valence bond per J_1 bond, a next-nearest neighbor (NNN)-Haldane phase with one valence-bond per J_2 bond, and a dimerized phase with two valence-bonds on every other J_1 bond.

The transition between the Haldane and the NNN Haldane phase is always first order (the energy per site has a kink), in agreement with previous results for $J_3 = 0$ [56]. It is topological: the two phases cannot be distinguished by any local order parameter, but the Haldane phase is topological (supports gapless edge states and non-zero string-order parameter), while the NNN-Haldane is not (see Fig. 4.1 and Fig. 4.2).

For small J_2, the transition between the Haldane and dimerized phases is in the $SU(2)_2$ WZW

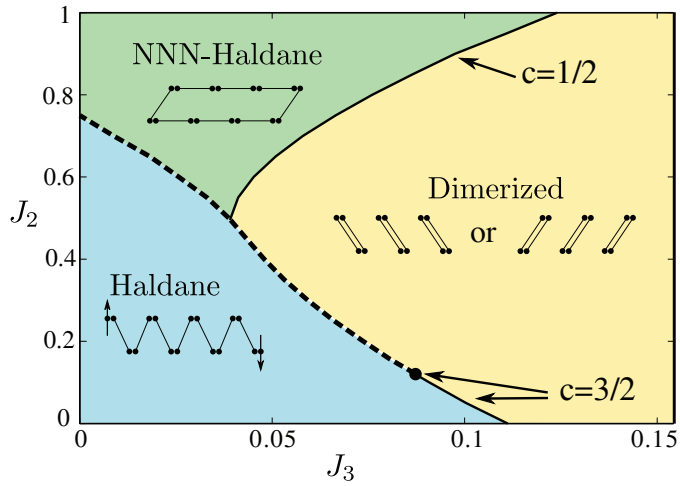

Figure 4.4 – Phase diagram of the spin-1 chain with next-nearest neighbor coupling J_2 and 3-site interaction J_3. The transition from the dimerized phase to the Haldane phase is continuous along the solid line, with central charge $c = 3/2$, and first order along the dashed line. The transition from the NNN-Haldane to the dimerized is a continuous transition in the Ising universality class with central charge $c = 1/2$. The transition between the Haldane phase and the NNN-Haldane phase is always first order.

universality class with central charge $c = 3/2$ from $J_2 = 0, J_3 \simeq 0.111$ [71] up to and including at a critical end point beyond which the transition becomes first order. This first-order line connects smoothly, at an unusual triple point, with the first-order transition between the Haldane and NNN-Haldane phases.

Finally, the transition between the NNN Haldane and dimerized phases is in the Ising universality class. As it will be shown later, singlet excitations become critical while the magnetic excitations remain gapped at the transition.

In addition to these phases, which can be distinguished by their topological properties or by the development of long-range dimerization, we have also identified regions of the phase diagrams characterized by various types of short-range order. The lack of long-range order to distinguish these regions prevents them from being true phases in the thermodynamic sense. However, they play an important role in understanding the evolution of correlations in the phase diagram, and we will nevertheless refer to them as phases.

The correlation function $C(x) = \langle \mathbf{S}(0) \cdot \mathbf{S}(x) \rangle$ can be well accounted for throughout by the product of the two-dimensional Ornstein-Zernicke (OZ) form:

$$C_{OZ}(x) \propto \cos(q \cdot x) \frac{e^{-x/\xi}}{\sqrt{x}}, \tag{4.6}$$

with, in some cases, a prefactor $1 + \delta(-1)^x$, leading to the dimerized Ornstein-Zernicke (DOZ)

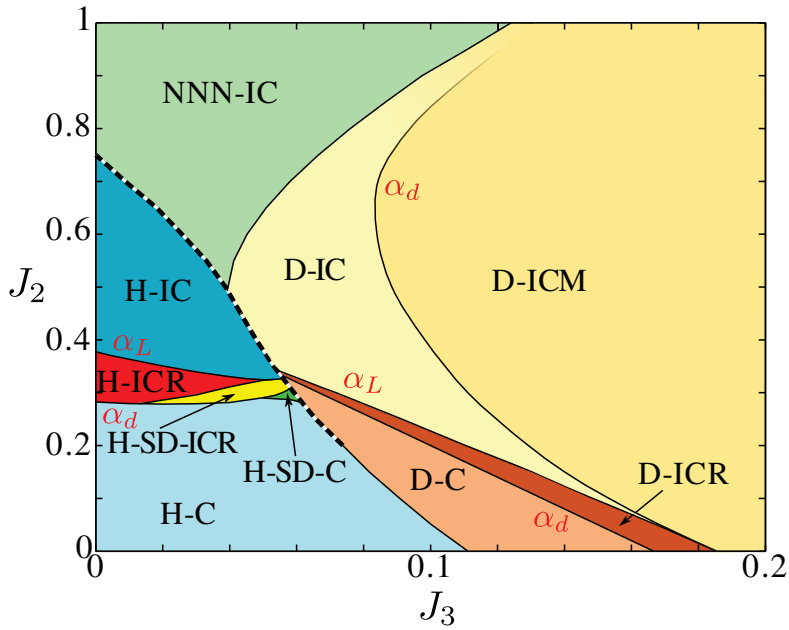

Figure 4.5 – Phase diagram based on the type of short-range order realized in the phases of Fig.4.4. The notations for the different phases are described in the text. Note that the disorder line α_d is distinct from the Lifshitz line α_L in both Haldane and dimerized phases. The line where the fully dimerized state is an exact ground state coincides with the disorder line α_d in the dimerized phase.

form:

$$C_{\mathrm{DOZ}} \propto (1+\delta(-1)^x) C_{OZ}(x), \tag{4.7}$$

The wave number q, the correlation length ξ, and the dimerization parameter δ are fitting parameters that depend on the couplings J_2 and J_3. Note that the same form applies to the dimerized and non-dimerized phases, except, of course, a line of continuous WZW $\mathrm{SU}(2)_2$ phase transition, at which the spin-spin correlation decays algebraically $C(x) \propto (-1)^x/|x|^{3/4}$ up to logarithmic corrections. The dimerized phase is characterized by the development of long-range correlations of the two-spin operator $\mathbf{S}_i \cdot \mathbf{S}_{i+1}$.

The structure factor is defined by the Fourier transform of real space correlations $\langle \mathbf{S}_i \cdot \mathbf{S}_j \rangle$:

$$SF(q) = \frac{1}{N} \sum_{i,j} e^{iq(i-j)} \langle 0|\mathbf{S}_i \cdot \mathbf{S}_j|0\rangle \tag{4.8}$$

Various short-range commensurate and incommensurate phases are shown in Fig.4.5. Below we provide a short description of each phase. The detailed discussion of the form of the correlations that led to the identification of short-range order can be found in Section 4.8.

Haldane Phase

- **H-C:** Short-range antiferromagnetic order with commensurate real-space correlation function. $C(x)$ is well described by the OZ form with $q = \pi$ and no dimerization ($\delta = 0$). The structure factor $SF(q)$ has a single peak at $q = \pi$.
- **H-SD-C:** Short-range dimer phase with commensurate real-space correlations ($q = \pi$). $C(x)$ is well described by the dimerized OZ form with $q = \pi$ and $\delta > 0$. $SF(q)$ has a single peak at $q = \pi$.
- **H-SD-ICR:** Short-range dimer phase with incommensurate real-space correlations, characterized by $q > \pi$ and $\delta > 0$ in Eq.4.7. $SF(q)$ has a single peak at $q = \pi$.
- **H-ICR:** Short-range antiferromagnetic order with incommensurate real-space correlations. $C(x)$ is well described by the OZ form with $q \neq \pi$ and no dimerization ($\delta = 0$). $SF(q)$ has a single peak at $q = \pi$.
- **H-IC:** Short-range antiferromagnetic order with incommensurate correlations in both real and momentum spaces. $C(x)$ is well described by the OZ form with $q > \pi$ and no dimerization ($\delta = 0$), but $SF(q)$ has two symmetric peaks at $q \neq \pi$.

Dimerized phase

- **D-C:** The spin correlations are commensurate in both, real and momentum space. $C(x)$ is well described by the dimerized DOZ form with $q = \pi$ and $\delta > 0$. $SF(q)$ has a single peak at $q = \pi$.
- **D-ICR:** Real-space correlations are incommensurate, and $C(x)$ is well fitted by the DOZ form with $\delta > 0$ and $q > \pi$. $SF(q)$ still has a single peak at $q = \pi$.
- **D-IC:** The spin correlations are incommensurate in both real and momentum space, $C(x)$ is well fitted by the DOZ form with $\delta > 0$ and $q > \pi$, but $SF(q)$ has two symmetric peaks at $q \neq \pi$.
- **D-ICM:** The spin correlations are incommensurate in momentum space, $SF(q)$ has two symmetric peaks at $q \neq \pi, \pi/2$. Real space correlations are commensurate with $q = \pi/2$.

NNN-Haldane phase

- **NNN-IC:** The spin-spin correlations are incommensurate in both, real and momentum space. $C(x)$ is reasonably well fitted by the OZ form with $q > \pi$ and no dimerization ($\delta = 0$). $SF(q)$ has two symmetric peaks at $q \neq \pi$.

4.3 Phase diagram

In the following section, we will explain how the phase boundaries in Fig.4.4 were obtained by looking at different quantities: dimerization, ground-state energy, entanglement spectra and

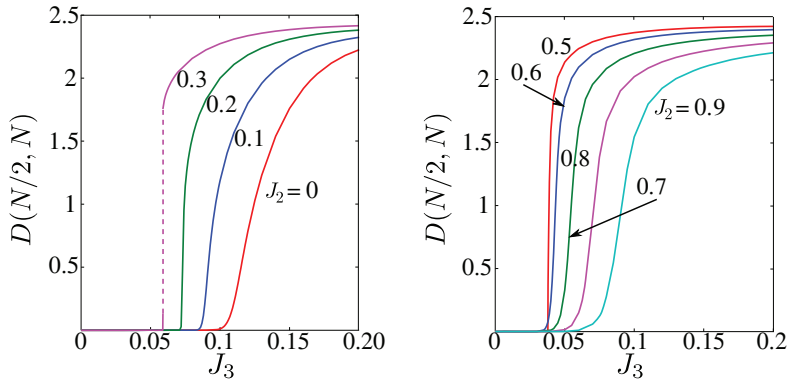

Figure 4.6 – Finite-size ($N = 150$) dimerization $D(N/2,N)$ as a function of J_3 for $0 \le J_2 \le 0.3$ (left panel) and $0.5 \le J_2 \le 0.9$ (right panel). The dashed line indicates a first order phase transition.

Berry phase. Phase boundaries obtained with all these methods will be compared at the end of the section.

4.3.1 Dimerization

The natural order parameter to identify the dimerized phase is the dimerization parameter defined by

$$D(j,N) = |\langle \mathbf{S}_j \cdot \mathbf{S}_{j+1} - \mathbf{S}_j \cdot \mathbf{S}_{j-1} \rangle|, \tag{4.9}$$

where j is a position index and N is the total number of sites. The best estimate for the thermodynamic limit can be obtained from open finite-size chains when $j = N/2$ for which edge effects are the smallest. Fig. 4.6 shows numerical results for the dimerization of a chain with $N = 150$ sites as a function of J_3 obtained by DMRG.

In moderately large systems ($N > 120$) and close to the first order phase transition the variational MPS algorithm suffers from a kind of hysteresis: the algorithm converges to the first excited state instead of the ground state. This results in an unphysical jump in the total energy curve (see Fig.4.7) and in an abrupt change of dimerization before the actual phase transition. These results were discarded when discussing the nature of the phase transition, and Fig.4.6 presents only dimerization curves for which the finite-size energy is continuous.

In order to determine the boundary of the dimerized phase in the thermodynamic limit we have performed a finite-size extrapolation of the dimerization parameter $D(N/2,N)$ for chains with $N = 30$, 60, 90, 120 and 150 sites. A chain is in the dimerized phase if the dimerization stays finite for $N \to \infty$, which we associate with a convex curve in a log – log plot. By contrast, a concave scaling curve leads to a vanishing dimerization in the thermodynamic limit and therefore means that the system is in the Haldane or NNN-Haldane phase. The phase transition then corresponds to a straight line in the scaling. Some examples of finite-size scaling

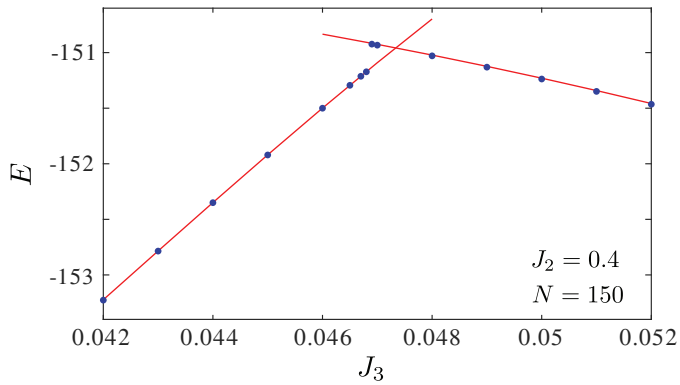

Figure 4.7 – Total energy of a chain with $N = 150$ sites as a function of J_3 coupling for fixed value of $J_2 = 0.4$. In the vicinity of critical line algorithm converges to the excited (dimerized) state, that results in a finite jump in the total energy. The position of the true transition in finite-size chain corresponds to the crossing point of the energy levels

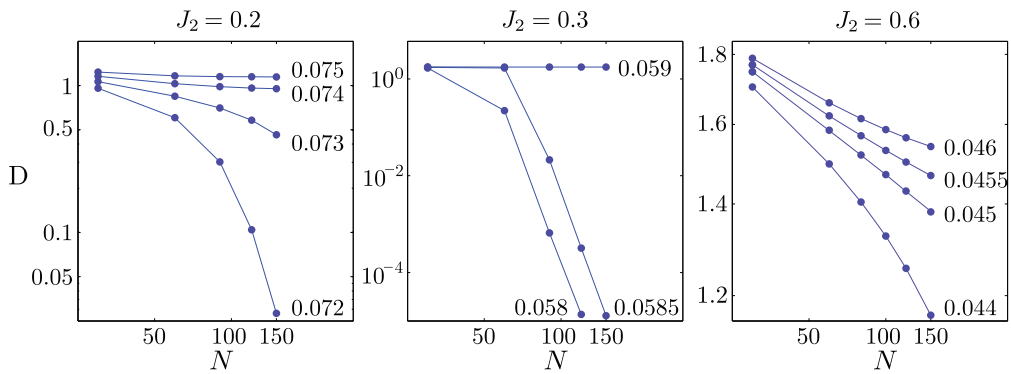

Figure 4.8 – Finite-size scaling of the dimerization parameter for $J_2 = 0.2$, 0.3 and 0.6. The value of J_3 is attached to each curve. The phase transition is continuous at $J_2 = 0.2$ and 0.6. The abrupt change of scaling at $J_2 = 0.3$ indicates a first order phase transition.

are shown in Fig. 4.8. A smooth change of the scaling curvature implies that the dimerization curve is continuous in the thermodynamic limit Fig.4.8 (a) and (c), while a first order phase transition with a finite jump in the dimerization curve leads to an abrupt change from concave to convex scaling at the critical point Fig.4.8 (b).

The investigation of dimerization has led to a precise determination of the transition line, and of the nature of the phase transition (continuous or first order) except in the vicinity of the end point of the continuous transition between the Haldane phase and the dimerized phase, where first order phase transition is seen as continuous on finite-size systems (see section 4.6).

4.3.2 Ground-state energy

In view of the hysteretic behavior of the system, and to complete the phase diagram in regions where the ground-state energy appears to be discontinuous, we have carefully investigated the

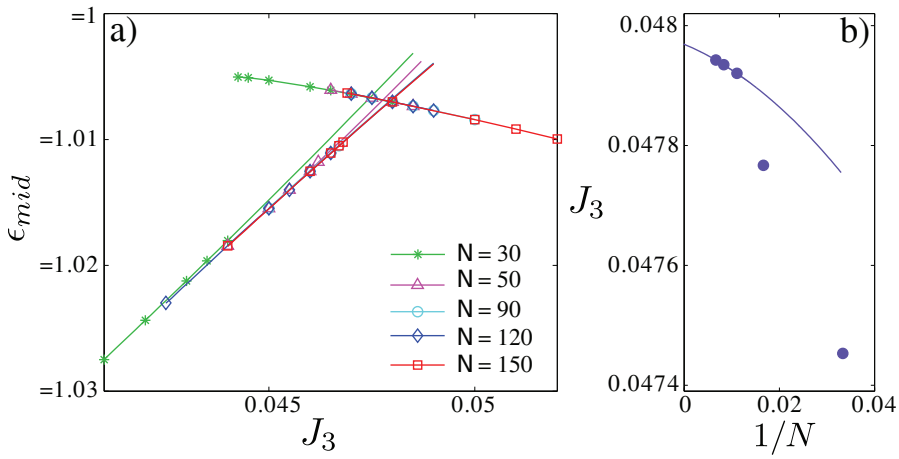

Figure 4.9 – (a) Energy of the central bonds for $J_2 = 0.4$ as a function of J_3 for finite-size chains with $N = 30, 60, 90, 120$ and 150 sites. Solid lines are polynomial fits. The kink was created by letting the two fits cross. (b) Position of the kink in ϵ_{mid} as a function of size. The fitting curve is a quadratic function in $1/N$.

behavior of the energy in the vicinity of the transition lines. An estimate of the ground-state energy in the thermodynamic limit is provided by the value of the energy of the central bonds:

$$\epsilon_{mid} = \epsilon_1 + \epsilon_2 + \epsilon_3, \tag{4.10}$$

where

$$\epsilon_1 = \frac{J_1}{2}\langle \mathbf{S}_{i-1}\cdot\mathbf{S}_i + \mathbf{S}_i\cdot\mathbf{S}_{i+1}\rangle,$$

$$\epsilon_2 = J_2\langle \mathbf{S}_{i-1}\cdot\mathbf{S}_{i+1}\rangle,$$

$$\epsilon_3 = J_3\langle(\mathbf{S}_{i-1}\cdot\mathbf{S}_i)(\mathbf{S}_i\cdot\mathbf{S}_{i+1}) + \mathrm{H.}c.\rangle,$$

and where $(i, i+1)$ is the central bond. The dependence on J_3 of ϵ_{mid} for chains with $N =$ 30, 60, 90, 120 and 150 sites for $J_2 = 0.4$ is presented in Fig. 4.9(a). The energy curves are discontinuous due to the edge effects and due to hysteresis of the variational MPS algorithm for $N = 120, 150$. In order to determine as precisely as possible the location of the first order phase transition in the thermodynamic limit, we have extrapolated the lines until they cross. Then, a finite-size scaling of the position of the kink is presented in Fig. 4.9(b).

For $0.25 \leq J_2 \leq 0.45$, the ground-state energy and the dimerization parameter lead to the same estimate for the location of the phase transition. For larger next-nearest-neighbor coupling, the kink disappears for small clusters but it is still present in large chains (see Fig. 4.10). The phase transition line continues towards small J_3 and end up at $J_3 = 0$ and $J_2 = 0.75$, close to the value 0.0744(4) obtained by Kolezhuk et al. [56, 57].

In order to confirm the location of the continuous phase transition deduced from the dimerization parameter, we have calculated the second derivative of ϵ_{mid} with respect to J_3. Examples for $N = 90$ and 150 are shown in Fig. 4.11. A kink in the energy implies a divergence of its

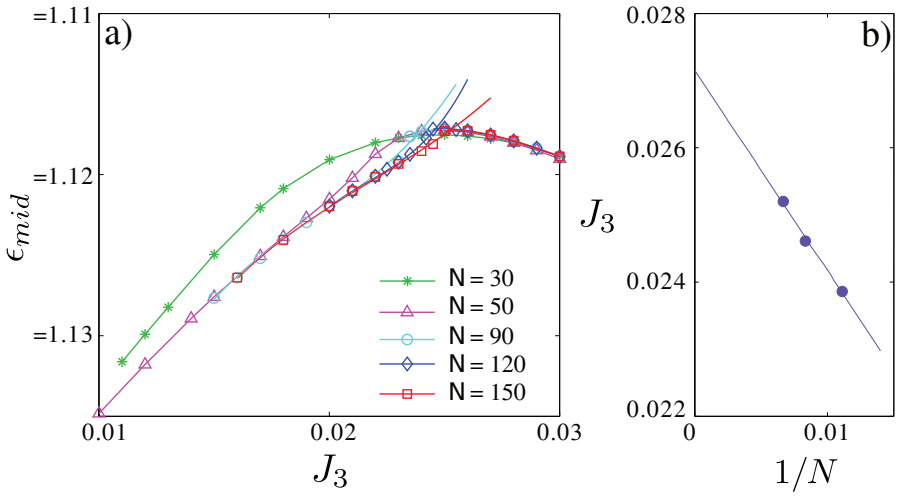

Figure 4.10 – Same as Fig. 4.9 for $J_2 = 0.6$

second derivative. Besides divergences, one can see the appearance of pronounced minima, which agree with the continuous finite-size phase transitions found with the dimerization parameter. For the first order transition between the Haldane phase and the NNN-Haldane phase, a kink is visible in the energy only for non-zero J_3. In order to extract the phase boundary at $J_3 = 0$, and although the phase transition is believed to be first order at this point, we have looked at the minimum of the second derivative of the energy. The finite-size effect slightly increase with increasing J_2. The positions of the minima are in good agreement with the phase boundaries found with the dimerization parameter for $J_2 \leq 0.2$ and $J_2 \geq 0.5$ (see scaling comparison on Fig. 4.20).

4.3.3 Entanglement spectrum

As mentioned in the introduction, the Haldane phase of the spin-1 chain is an example of a symmetry protected topological phase in one dimension [39]. It is distinct from the topologically trivial NNN-Haldane and dimerized phases, and it can be characterized by the finite value of the string order parameter, a criterion already used for the $J_1 - J_2$ model [56]. More recently, it has been proposed to characterize topological phases by their entanglement spectrum, obtained by dividing the system into two parts, tracing out one of them, and diagonalizing the reduced density matrix of the remaining part [67, 66, 55]. This creates artificial edges without breaking the inversion symmetry.

In the present case, a system with open ends may be partitioned across a certain bond and the wave function can then be Schmidt decomposed as:

$$|\Psi\rangle = \sum_{\alpha} \lambda_{\alpha} |L_{\alpha}\rangle |R_{\alpha}\rangle, \tag{4.11}$$

where $|L_{\alpha}\rangle$ and $|R_{\alpha}\rangle$ are orthonormal basis vectors of the left and right parts. In variational

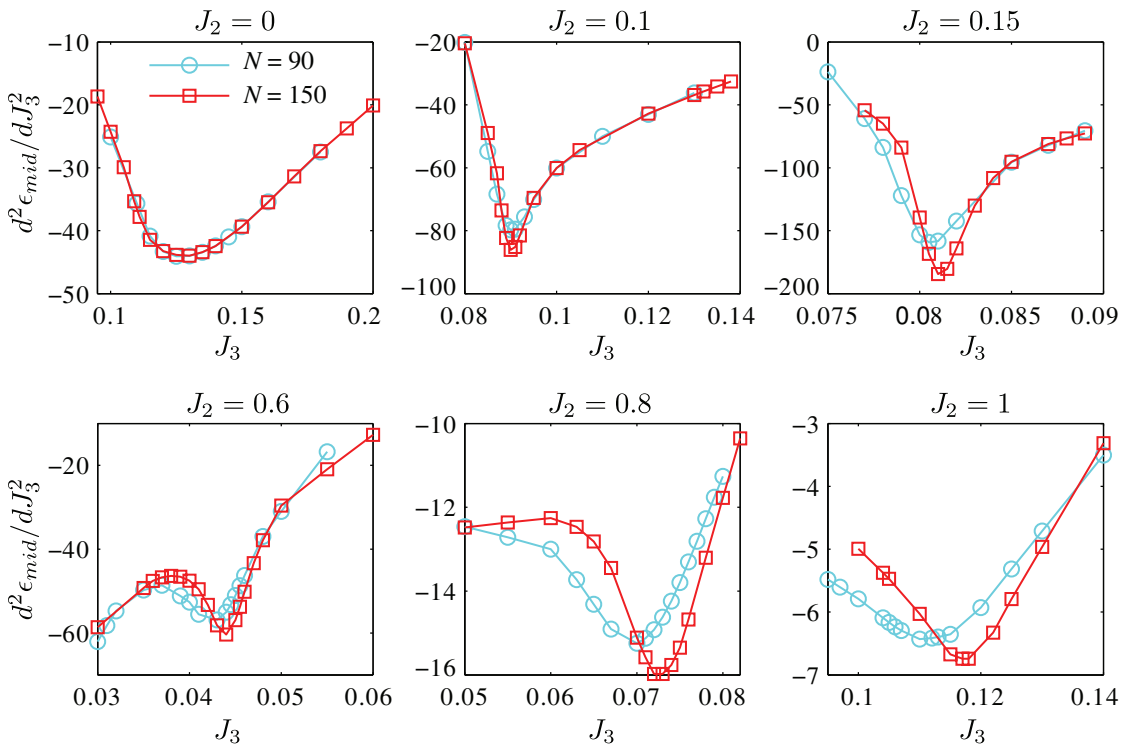

Figure 4.11 – Upper panels: second derivative of ϵ_{mid} with respect to J_3 for $N = 90, 150$ and $J_2 = 0, 0.1, 0.15$ across continuous phase transition between Haldane and dimerized phases. Lower panels: second derivative of ϵ_{mid} for $N = 90, 150$ and $J_2 = 0.6, 0.8, 1$ across the transition line between NNN-Haldane and dimerized phases

MPS, the Schmidt values λ_α are obtained naturally at each iteration. Now, the multiplicity of the Schmidt values is related to the number of edge states that appear due to partitioning: Any topologically non-trivial phase is characterized by at least two-fold degeneracy. Pollmann et al. [82] have shown that the Haldane phase of $S = 1$ chains is characterized by a twofold degeneracy of the entanglement spectrum.

An example of finite-size entanglement spectrum containing all three phases is shown in Fig. 4.12. Three VBS (valence bond solid) sketches are attached in order to show how edge states are formed in each phase. In complete agreement with previous works, the entanglement spectrum in the Haldane phase is twofold degenerate, the edge states being spins 1/2. By contrast, the entanglement spectrum is non-degenerate in the NNN-Haldane phase because there are no edge states. For the dimerized phase, it depends where the system is cut. For a system with open boundary conditions and an even number of sites, the ground state is non degenerate and consists of alternating strong and weak bonds. If the system is cut in the middle of a weak bond, no edge states appear, and the entanglement spectrum is non degenerate, and cannot distinguish the NNN-Haldane phase from dimerized one (see Fig.4.13). However, if the system is cut on a strong bond, i.e. on a bond which is essentially a singlet made of two spins 1, as done in Fig. 4.12, the entanglement spectrum is threefold degenerate

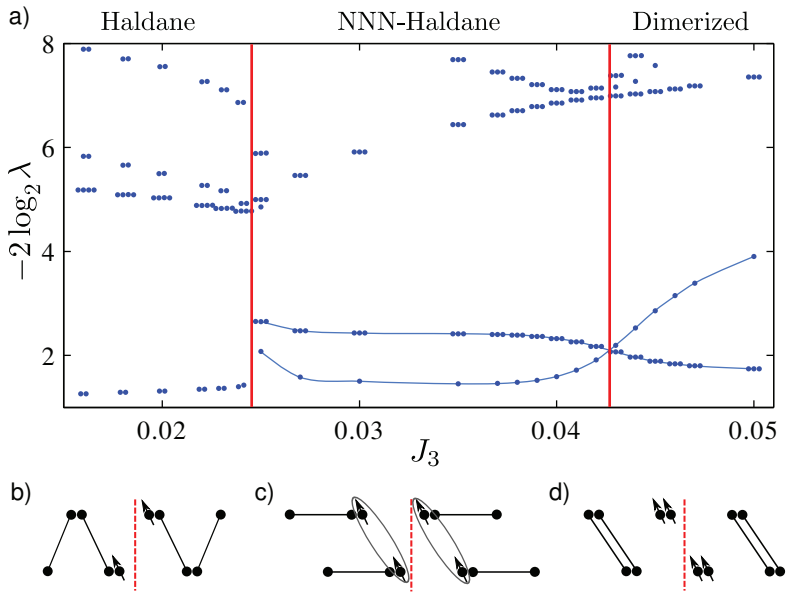

Figure 4.12 – (a) Entanglement spectrum for an open chain with $N = 150$ sites as a function of J_3 (only the lower part of the spectrum is shown). The dots show the multiplicity of the Schmidt values. The plot for $J_2 = 0.6$ is shown here as an example. Lower panels: VBS sketches of various boundaries created by the bipartition of the chain inside the (b) Haldane, (c) NNN-Haldane and (d) dimerized phases. (b) The black arrows at each edge stand for two free spins 1/2, which form a singlet, leading to a twofold degenerate entanglement spectrum. (c) The two spin-1/2 created at each edge couple with each other, which is represented as a gray ellipse. There are no edge states, and the entanglement spectrum is non-degenerate. (d) The edge spins are spins 1 and form a singlet, which leads to a three-fold degenerate entanglement spectrum.

because spin-1 edge states are created, and the NNN-Haldane phase can be distinguished from the dimerized phase.

In small systems an intermediate phase with a three fold degenerate entanglement spectrum and a low-lying non-degenerate level appears between the Haldane and NNN-Haldane phases (see Fig.4.14). This phase disappears for larger system sizes and is thus a finite-size effect.

The resulting phase diagram is shown in Fig. 4.15. It is consistent with other approaches, but finite-size effects are strong, especially for the transition between the NNN-Haldane phase and the dimerized phase.

4.3.4 Berry Phase

Another powerful tool to characterize topologically non-trivial phases is the Berry phase [12]. It can be defined for any Hamiltonian $H(\phi)$ which depends periodically on a parameter ϕ. If $|GS(\phi)\rangle$ is a single-valued ground state of $H(\phi)$, the Berry connection is given by $A(\phi) =$

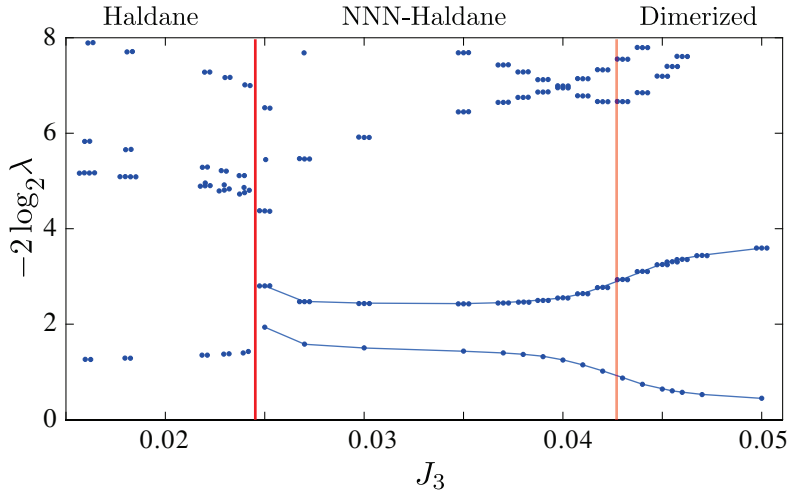

Figure 4.13 – Same as Fig.4.12(a) for cut across weak bond. The transition between NNN-Haldane and dimerized phase does not show up

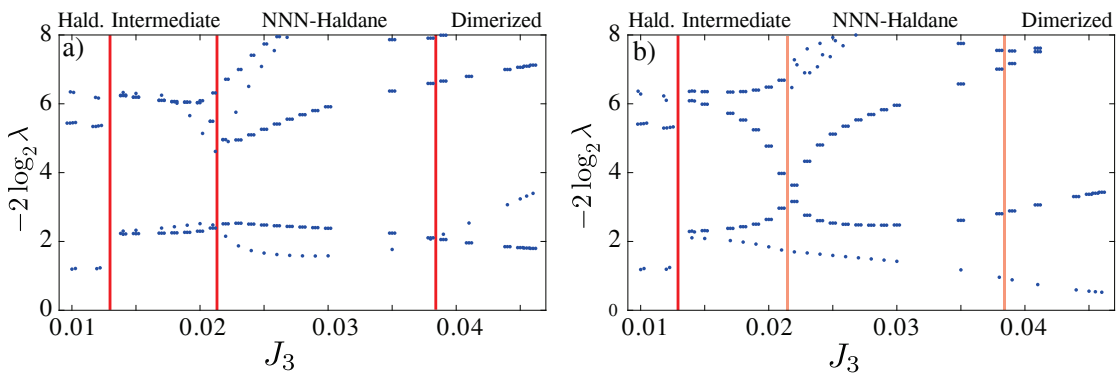

Figure 4.14 – Entanglement spectra as a function of J_3 coupling for $N = 60$ and $J_2 = 0.6$ for chain cut across (a) strong and (b) weak bonds. Intermediate phase with three-fold degenerate lowest level in entanglement spectrum appears between Haldane and NNN-Haldane phases

$\langle GS(\phi)|\partial_\phi|GS(\phi)\rangle$, and the Berry phase is the integration of the Berry connection over a loop:

$$i\gamma = \oint A(\phi)\,d\phi \tag{4.12}$$

It was proposed by Hatsugai et al. [48] to use the angle ϕ of the twist of the transverse component of the spin-spin interaction on a given bond (i, j)

$$S_i^+ S_j^- + S_i^- S_j^+ \to e^{i\phi} S_i^+ S_j^- + e^{-i\phi} S_i^- S_j^+ . \tag{4.13}$$

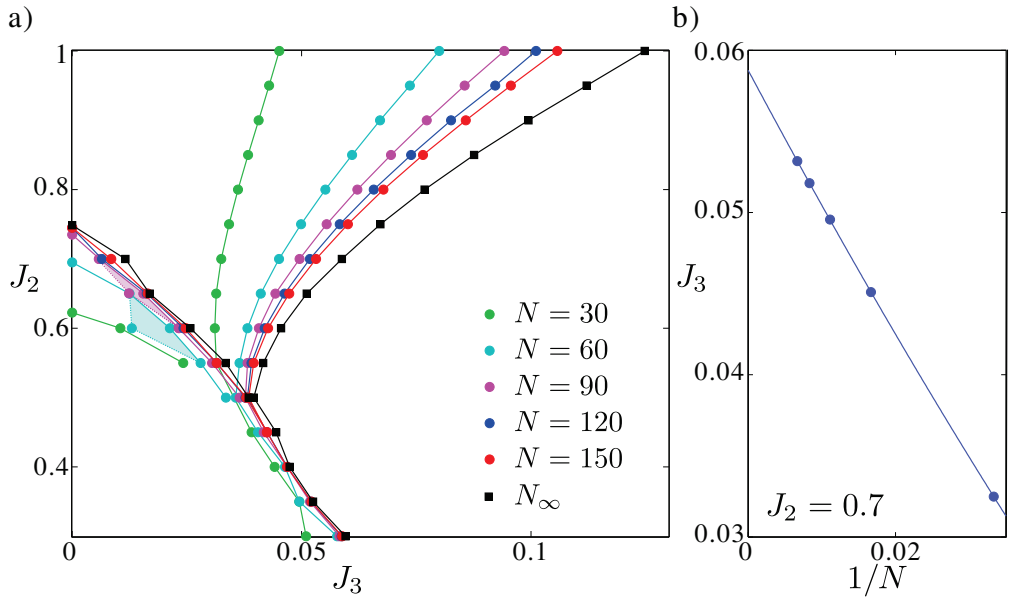

Figure 4.15 – (a) Phase boundaries deduced from the entanglement spectrum for chains with $N = 30$, 60, 90, 120, and 150 sites, and after finite-size scaling (N_∞). Shaded area: intermediate phase for $N = 60$ and 90. (b) Example of finite-size scaling for $J_2 = 0.7$ with a quadratic fit.

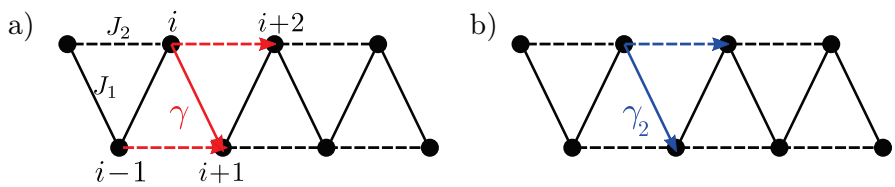

Figure 4.16 – a) Berry phase applied on three bonds to be consistent with anti-periodic boundary conditions for the transverse component of the spin-spin interaction at $\phi = \pi$. This Berry phase $\gamma = \pi$ in the Haldane phase and $\gamma = 0$ otherwise. b) Berry phase applied on two bonds to distinguish the dimerized phase ($\gamma_2 = 0$) from the Haldane and NNN-Haldane phases ($\gamma_2 = \pi$).

Then the number of valence bond singlets B_{ij} on the bond (i, j) is related to the Berry phase by:

$$\gamma = B_{ij} \cdot \pi, \qquad \mathrm{mod}(2\pi). \tag{4.14}$$

In other words, the Berry phase gives access to the parity of the number of valence bond singlets on a given bond.

Previous studies of the Berry phase in spin systems have demonstrated that topological phase transitions can be reliably captured when the applied twist at $\phi = \pi$ is equivalent to anti-periodic boundary conditions for the transverse component of the interaction. To fulfill this requirement, three bonds must be simultaneously twisted as shown in Fig. 4.16a. The twist applied on a bond $(i, i+1)$ implies that the transverse component of the interaction in the initial Hamiltonian is changed in all terms where the term $\mathbf{S}_i \cdot \mathbf{S}_{i+1}$ appears, i.e. both in the J_1

and J_3 terms. The twist of an $(i, i+2)$ bond changes only the J_2 term.

In the dimerized phase, there is no singlet on next-nearest neighbor bonds $(i-1, i+1)$ and $(i, i+2)$, while bonds $(i, i+1)$ have either zero or two singlets. So the Berry phase γ, which is defined only up to 2π, is equal to zero. In the NNN-Haldane phase, the bonds $(i-1, i+1)$ and $(i, i+2)$ contain one spin-1/2 singlet each and there is no singlet on the link $(i, i+1)$, so that $\gamma = 0$ as in the previous case. By contrast, the Berry phase is equal to π in the Haldane phase, in which there is one VBS singlet on the bond $(i, i+1)$ and no VBS singlet on the bonds $(i-1, i+1)$ and $(i, i+2)$.

We have calculated the Berry phase γ for chains with periodic boundary conditions using exact diagonalizations. According to a general result for planar contours [12], the Berry phase will be equal to 0 if the gap does not close inside the contour, and it will be equal to π if the gap closes at one point inside the contour. In the present model, one can detect the change of the γ berry phase by computing the gap at one particular point on the contour $\phi = \pi$. The computational cost are reduced drastically: for each value of J_3 instead of computing numerically the integral of Eq.4.12, one computes the two lowest energies at one point on the integration contour. Moreover, unlike the quantized berry phase, energies are continuous and smooth functions of J_3, therefore the transition could be extracted with higher precision. An example of level crossing is shown in Fig.4.17.

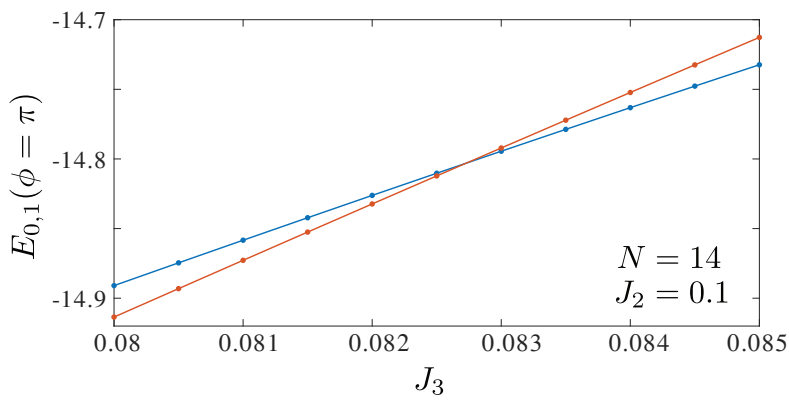

Figure 4.17 – Two lowest energies of the Hamiltonian with three bonds twisted as in Fig.4.16(a) according to Eq.4.13 with $\phi = \pi$. The level crossing corresponds to the change of the Berry phase.

The results for finite sizes are presented in Fig. 4.18a-c, and the finite-size scaling based on chains of length $N = 8, 10, 12, 14$ sites in the interval $0 \leq J_3 \leq 0.25$ is shown in Fig. 4.18d). The results from the finite-size extrapolation are also included in Fig. 4.18a). Systems close to the first order phase transition have strong finite-size effects, and no meaningful extrapolation could be performed with only four points. There is also a clear indication of an even-odd effect: the scaling for $N = 8, 12, ..., 4k$ is different from the one for $N = 10, 14, ..., 2(2k+1)$. For $J_2 \geq 0.3$, the results for $N = 12$ (the largest accessible chain with an even number of spin pairs) are taken as the Berry phase estimates of the phase boundary. Quite remarkably, the finite-size

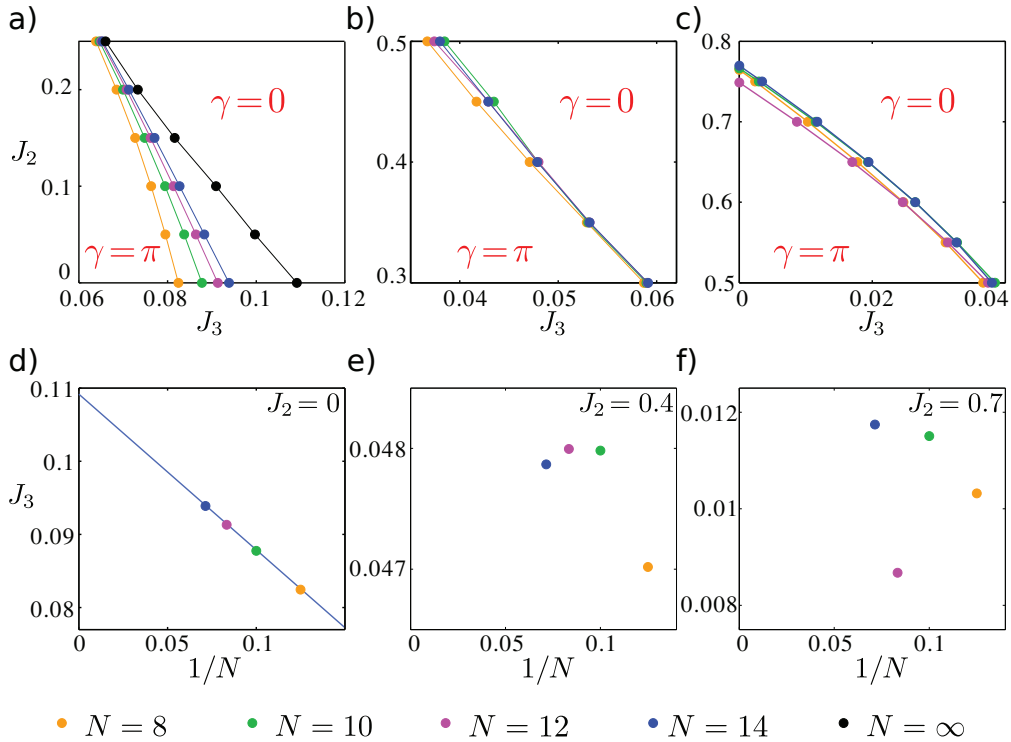

Figure 4.18 – Results of the Berry phase calculation in a periodic chain with $N = 8, 10, 12, 14$. Upper panels: Finite size phase transitions captured by the Berry phase for J_2 in the range a) $0 \leq J_2 \leq 0.25$, b) $0.3 \leq J_2 \leq 0.5$, and c) $0.5 \leq J_2 \leq 0.78$. The results of finite-size extrapolation are shown in a) as a black line. Lower panels: Size dependence of the boundaries deduced from Berry phase. d) Finite-size scaling for $J_2 = 0$ performed with a cubic fit in $1/N$. e) and f) Examples of strong finite-size effects that do not allow one to make a finite-size extrapolation.

results for such small chains are already very close to the phase boundaries obtained in the thermodynamic limit with other techniques (see Fig.4.20 and 4.21).

When the twist used to define the Berry phase does not correspond to anti-periodic boundary conditions at $\phi = \pi$, the Berry phase can still reflect some local properties of the system and capture phase transitions. To distinguish the dimerized phase from the NNN-Haldane phase, we propose to define the Berry phase by twisting two links as shown in Fig. 4.16b. Similarly to what was done for the three-bond Berry phase, we apply the twist on two bonds $(i, i+1)$ and $(i, i+2)$ simultaneously. In the Haldane phase there is only one VBS singlet on the bond $(i, i+1)$, in the NNN-Haldane phase one VBS singlet on the $(i, i+2)$ bond, and in both cases $\gamma_2 = \pi$. In the dimerized phase the bond $(i, i+1)$ contains either zero or two singlets while the $(i, i+2)$ bonds have no singlets, and the Berry phase $\gamma_2 = 0$. The finite-size results for $N = 12$ and $N = 14$ are shown in Fig. 4.19. Qualitatively, this Berry phase gives the same phase boundaries as the dimerization parameter, which is also shown as a reference line. There is a strong finite-size effect however, and the extrapolation to the thermodynamic limit requires bigger system sizes.

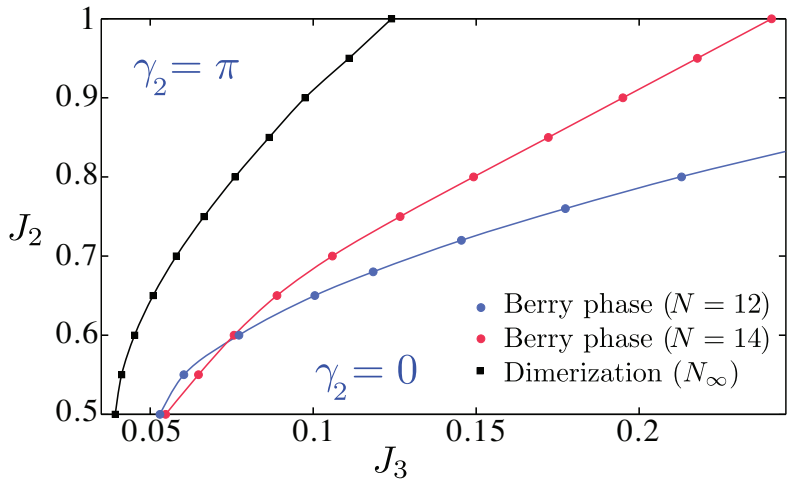

Figure 4.19 – Phase transition obtained by the γ_2 Berry phase for periodic chains with $N = 12$ (blue circles) and $N = 14$ (red circles) sites. The phase transition, obtained with finite-size scaling of the dimerization parameter (black squares) is shown as a reference.

4.3.5 Comparison

To show that all approaches presented above capture essentially the same phase diagram, we provide examples of comparative finite-size scaling (Fig. 4.20) and phase diagrams obtained with different criteria (Fig. 4.21).

We compare the phase boundaries deduced from the dimerization, energy, entanglement spectra and Berry phase (Fig. 4.21). For $J_2 = 0$ the second derivative in the energy gives a phase boundary different from the one obtained with the dimerization parameter. Except for this point, the two boundaries are in rather good agreement. They also agree with the 'entanglement boundary' between the NNN-Haldane phase and the dimerized phase. The first order phase transition from Haldane to the dimerized phase is well located by all methods. The most reliable phase boundary between Haldane and NNN-Haldane phases is obtained by the kink in the energy of the central bond. Since on the one hand, the kink in the ϵ_{mid} for large J_3 has vanishing finite-size effect (see Fig. 4.9b) and on the other hand the kink for small J_3 appears only in large systems, we determined the boundary of the phases with the energy of the central bonds of the largest cluster to which we have access $\epsilon_{mid}(N = 150)$. We cannot see a kink for $J_3 = 0$ and to locate the phase transition on the J_2 axis we have used the minimum in the second derivative of the energy with respect to J_2. The error in the 'entanglement boundary' is due to the abrupt change of the degeneracy from two in the Haldane phase to one in the NNN-Haldane or three in the dimerized. The finite-size results of the Berry phase for $N = 12$ agree with the 'energy boundary' except for $0.5 \leq J_2 \leq 0.6$. The finite-size extrapolation of the Berry phase is close to the 'dimerization boundary'.

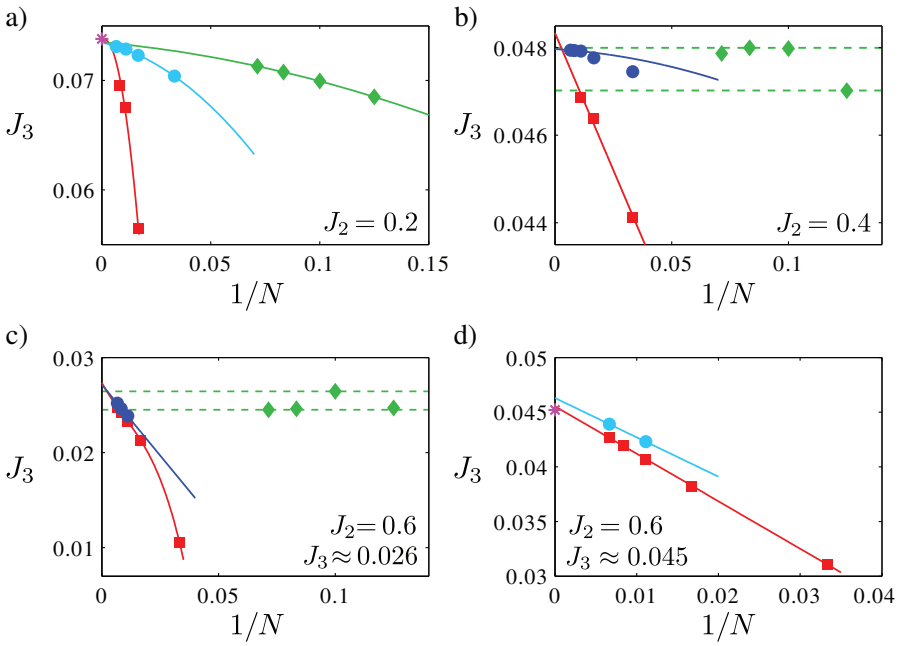

Figure 4.20 – Comparison of finite-size scaling for a) $J_2 = 0.2$, b) $J_2 = 0.4$, c) $J_2 = 0.6$ and $J_3 \simeq 0.026$, d) $J_2 = 0.6$ and $J_3 \simeq 0.045$. Finite-size results for: entanglement spectra (red squares), the Berry phase (green diamonds), kink in the energy of the central bond ϵ_{mid} (blue circles), minimum in the second derivative of ϵ_{mid} (cyan circles). Results from finite-size scaling of the dimerization parameter (magenta stars). All fitting curves are polynomial in $1/N$. Dashed green lines shows the interval between the smallest and the biggest values deduced from the Berry phase.

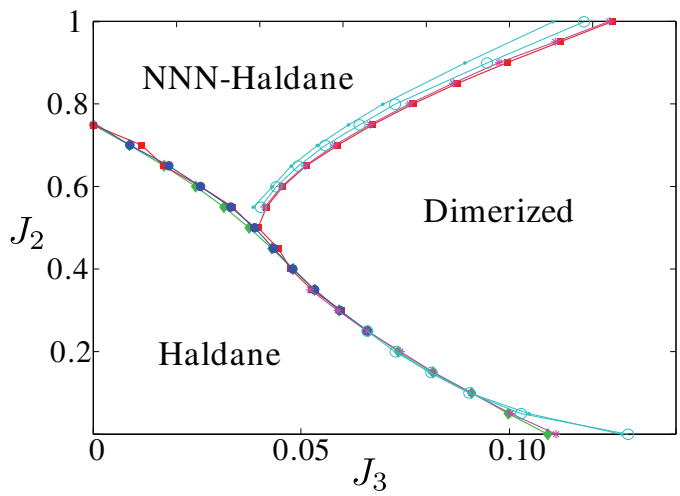

Figure 4.21 – Comparative phase diagram obtained by dimerization parameter (magenta stars), kink in the energy of the central bond ϵ_{mid} (blue circles), $\epsilon_{mid}(N = 150)$ and $\epsilon_{mid}(N = 90)$ (cyan open circles and dots), entanglement spectra (red squares), and Berry phase (green diamonds)

4.4 Field theory

The conformal field theory for the $J_1 - J_2 - J_3$ model has been developed in Ref.[24]. In this section we provide a brief review of the obtained critical theory, focusing on the most important aspects necessary for understanding the following numerical results.

Phase diagram 4.22 and the nature of the various transitions can be understood using conformal field theory (CFT) techniques. We begin near the $SU(2)_{k=2}$ critical point where the low energy degrees of freedom of the spin chain can be written:

$$\begin{aligned} \vec{S}_j &\approx [\vec{J}_R(j) + \vec{J}_L(j)] + C_1(-1)^j \mathrm{tr}[g(j)\vec{\sigma}] \\ \vec{S}_j \cdot \vec{S}_{j+1} &\approx C_2 T(j) + (-1)^j C_3 \mathrm{tr} g(j) \end{aligned} \tag{4.15}$$

where $g(x)$ is the $SU(2)$ Wess-Zumino-Witten field with $k = 2$, $\vec{J}_{R/L}$ are the right/left current operators, T is the energy density and the C_i are non-universal constants.

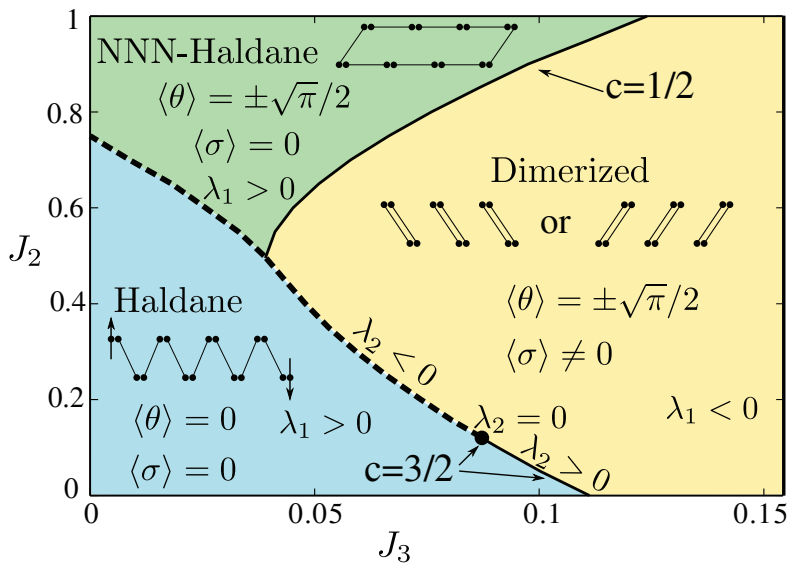

Figure 4.22 – Same as Fig.4.4 with indicated expectation values for Ising σ and boson θ operators

The Hamiltonian density is that of the $SU(2)_2$ WZW model with one relevant and one marginal perturbation allowed by symmetry:

$$\mathcal{H} = \mathcal{H}_{WZW} + \lambda_1(\mathrm{tr} g)^2 + \lambda_2 \vec{J}_R \cdot \vec{J}_L. \tag{4.16}$$

The relevant coupling constant, λ_1, controls the Haldane to dimerized transition. When $\lambda_1 < 0$, energy is minimized when $\langle \mathrm{tr} g \rangle$ is non-zero corresponding to dimerisation [6], as we see from Eq. (4.15). When $\lambda_1 > 0$ the energy is minimized when second term is suppressed $\langle \mathrm{tr} g \rangle = 0$ that correspond to a non-dimerized Haldane phase. The marginal coupling constant, λ_2,

normalizes to zero if it is initially negative. In this regime the Haldane to dimerized transition is second order, with the WZW model occurring along the critical line with logarithmic corrections to scaling behavior due to λ_2. These logarithmic corrections vanish at the end of the critical line where $\lambda_2 = 0$. When $\lambda_2 > 0$ we expect λ_1 to produce a first order transition. To understand the full phase diagram, it is very useful to use a conformal embedding (also called a coset construction), an exact representation of the $SU(2)_2$ WZW model as a direct product of a free boson and an Ising model. [32]

$$\begin{aligned}
\mathrm{tr}g &\propto i\sigma \sin\sqrt{\pi}\theta \\
\mathrm{tr}g\vec{\sigma} &\propto \sigma(i\sin\sqrt{\pi}\phi, i\cos\sqrt{\pi}\phi, \cos\sqrt{\pi}\theta) \\
(\mathrm{tr}g)^2 &\propto \epsilon - C_4\cos\sqrt{4\pi}\theta \\
\vec{J}_L\cdot\vec{J}_R &\propto \epsilon\cos\sqrt{4\pi}\theta + C_5\partial_x\phi_L\partial_x\phi_R.
\end{aligned} \tag{4.17}$$

with $C_4 > 0$. Here σ is the Ising order parameter of dimension $h_\sigma + \bar{h}_\sigma = 1/16 + 1/16 = 1/8$ and ϵ is the Ising energy density operator of dimension $h_\epsilon + \bar{h}_\epsilon = 1/2 + 1/2 = 1$. The value of the central charge is correctly reproduced: $c = 3/2 = 1 + 1/2$. The Ising model corresponds to the coset $SU(2)_2/U(1)$. To see how λ_1 induces the Haldane to dimerized transition, note that a positive λ_1 pins θ at 0 whereas a negative λ_1 pins it at $\pm\sqrt{\pi}/2$, leading to $\langle\sin\sqrt{\pi}\theta\rangle \neq 0$. Positive coefficient of ϵ corresponds to the disordered phase whereas a negative coefficient to the ordered phase with $\langle\sigma\rangle \neq 0$, thus we obtain $\langle\mathrm{tr}g\rangle \neq 0$ for $\lambda_1 < 0$. Note that in both phases $\langle\mathrm{tr}g\vec{\sigma}\rangle = 0$ as it should be since spin-rotation symmetry is unbroken. Remarkably, in this representation of the WZW model, a second order transition occurs simultaneously in Ising and boson sectors.

To see how λ_1 induces the Haldane to Dimerized transition, note that a positive λ_1 pins θ at 0 whereas a negative λ_1 pins it at $\pm\sqrt{\pi}/2$, leading to $\langle\sin\sqrt{\pi}\theta\rangle \neq 0$. Positive coefficient of ϵ corresponds to the disordered phase whereas a negative coefficient to the ordered phase with $\langle\sigma\rangle \neq 0$ thus we obtain $\langle\mathrm{tr}g\rangle \neq 0$ for $\lambda_1 < 0$. Remarkably, in this representation of the WZW model, a second order transition occurs simultaneously in Ising and boson sectors.

The first order transition for $\lambda_2 > 0$ can be understood intuitively in this representation. A large positive λ_2 favors states with $\langle\epsilon\rangle\langle\cos\sqrt{4\pi}\theta\rangle < 0$. There are then two degenerate gapped states with $\langle\epsilon\rangle < 0$ and θ pinned at 0 corresponding to the Haldane phase or $\langle\epsilon\rangle > 0$ and θ pinned at $\pm\sqrt{\pi}/2$ corresponding to the dimerised phase. Turning on λ_1 splits the degeneracy, leading to a first order transition.

So, far we have focused on the vicinity of the WZW critical point. Let us now consider what may happen as we move far from it along the first order transition line. It is now no longer permissible to only consider the couplings which are relevant at the critical point so the Ising and boson transitions could occur at different places in the phase diagram. For instance, a term that does not contains Ising field $\lambda_3\cos 3\sqrt{4\pi}\theta$ would favor either $\langle\theta\rangle = 0$ or $\langle\theta\rangle = \pm\sqrt{\pi}/2$ depending on its sign. If λ_3 changed sign along a line in the phase diagram the transition could

occur in the boson sector without occurring simultaneously in the Ising sector. This phase with $\langle\theta\rangle = \pm\sqrt{\pi}/2$, $\langle\sigma\rangle = 0$ corresponds to the NNN-Haldane phase. This can be seen from the presence of gapless S=1/2 edge excitations when $\langle\theta\rangle = 0$ but not when $\langle\theta\rangle = \pm\sqrt{\pi}/2$. These can be understood from the numerical observation that an open boundary condition promotes local dimerisation even in the Haldane phase, and hence $\langle \mathrm{tr} g(x)\rangle$ becomes non-zero near the boundary. Thus we might expect, from Eq. (4.17), that $\theta(x)$ takes the value $\pm\sqrt{\pi}/2$ at an open end. On the other hand, $\langle\theta(x)\rangle = 0$ far from the boundary in the Haldane phase. This rotation of $\theta(x)$ corresponds to an induced near an open boundary in the Haldane phase. On the other hand there is no induced magnetisation in the NNN-Haldane phase since $\langle\theta(x)\rangle = \pm\sqrt{\pi}/2$ in the bulk, so it does not rotate at the boundary. So this phase has no gapless edge modes but also has no dimerisation since $\langle\sigma\rangle = 0$. Thus, we may identify it with the NNN-Haldane phase.

The above argument also implies that a domain wall between Haldane and dimerized phases has a $\pm\sqrt{\pi}/2$ rotation of θ corresponding to an $S = 1/2$ excitation, whereas a domain wall between NNN-Haldane and dimerized phases has no rotation of θ and hence no spinful excitations. This prediction will be confirmed with numerical calculations in the section 4.7.

We note that θ and ϕ are not simply periodic bosons but rather (θ,σ) should be identified with $(\theta+\sqrt{\pi},-\sigma)$ and (ϕ,σ) should be identified with $(\phi+\sqrt{\pi},-\sigma)$. Therefore, for $\lambda_1 < 0$, there are only 2 inequivalent ground states, not 4, corresponding to the sign of $\langle\sigma\sin\sqrt{\pi}\theta\rangle$. In the Haldane phase where $\langle\sigma\rangle = 0$, there is only one ground states with θ pinned at 0 or $\sqrt{\pi}$ being equivalent. Likewise, in the NNN Haldane phase where $\langle\sigma\rangle = 0$, θ being pinned at $\pm\sqrt{\pi}/2$ are equivalent.

We now see that a third transition can also take place in which θ remains pinned at $\pm\sqrt{\pi}/2$ while the sign of the ϵ term in the Hamiltonian changes. This corresponds to an Ising transition from NNN-Haldane to dimerized phases. All spinful excitations must remain gapped at this transition since there is a gap in the boson sector at the transition. This follows since all excitations of non-zero S^z are in the boson sector. Due to the $SU(2)$ symmetry there can therefore be no multiplets of non-zero spin among the Ising excitations. Various universal predictions for the NNN-Haldane to dimerized transition follow from this derivation. Since $\beta = 1/8$ for the Ising model, the dimerisation order parameter should scale as

$$(J_3 - J_{3c})^{1/8} \tag{4.18}$$

As discussed above, an open boundary condition corresponds to a non-zero boundary magnetic field in the Ising model, leading to a dimerisation which decays away from the boundary on the critical line in the same way that the magnetisation in the critical Ising model with a boundary magnetic field decays, $\langle\sigma(x)\rangle \propto 1/x^{1/8}$. For a finite system with an even number of sites, N, this becomes

$$<\sigma(x)> \propto \frac{1}{[(N/\pi)\sin(\pi x/N)]^{1/8}} \tag{4.19}$$

On a finite chain, we define the local dimerization as $D(j,N) = |\langle \vec{S}_j \cdot \vec{S}_{j+1}\rangle - \langle \vec{S}_{j-1} \cdot \vec{S}_j\rangle|$. Identifying the local dimerization with σ, this leads to

$$D(j,N) \propto 1/[N \sin(\pi j/N)]^{1/8}, \tag{4.20}$$

and in particular to $D(N/2,N) \propto 1/N^{1/8}$. The central charge, $c = 1/2$ can be measured from the entanglement entropy or finite-size scaling of the ground-state energy. With an extensive DMRG calculations we investigate the nature of the different critical lines. We start our discussion with the most unexpected Ising transition.

4.5 Ising transition

4.5.1 Critical scaling of dimerization

We start the numerical investigation of the Ising transition by locating precisely the critical line in the $J_2 - J_3$ parameter space. We use the middle chain dimerization $D(N/2,N)$ as an order parameter to distinguish the dimerized phase from the non-dimerized NNN-Haldane phase. In finite-size chains dimerization changes very slowly with J_3 (see Fig.4.23(c)). Therefore one has to take large enough systems in order to distinguish scalings that correspond to dimerized and non-dimerized phases as can be seen from Fig.4.23(a). Here we take chains with up to $N = 800$ spins.

By perforforming finite-size extrapolation of the dimerization as shown in Fig.4.23(a) we determine the expectation values of the dimerization in the thermodynamic limit. According to field theory $\lim_{N\to\infty} D(N/2,N) \propto |J - J_c|^{\beta}$ with critical exponent $\beta = 1/8$ for the Ising model in a critical transverse field. The critical exponent extracted numerically from extrapolated values of the dimerization $\beta \approx 0.123$ is consistent with field theory predictions. The corresponding critical point is located around $J_3^c \approx 0.05814$.

As briefly discussed in Section 4.3.1, for any fixed value of J_2 , the critical value of J_3 can also be associated to a separatrix in the log-log plot of the finite-size scaling of the dimerization parameter $D(N/2,N)$, as shown in Fig.4.23(b). The slope of the separatrix corresponds to the scaling dimension $d \approx 0.129$ and it is in a good agreement with the Ising prediction 1/8 (see Eq.4.20).

Open boundaries favor dimerization. This can be seen in Fig.4.24 as a rapid increase of the dimerization parameter $D(j,N)$ around both edges. The dimerization along the chain scales according to Eq.4.20. The value of the scaling dimension $d \approx 0.128$ obtained from the numerical fit again agrees with Ising 1/8.

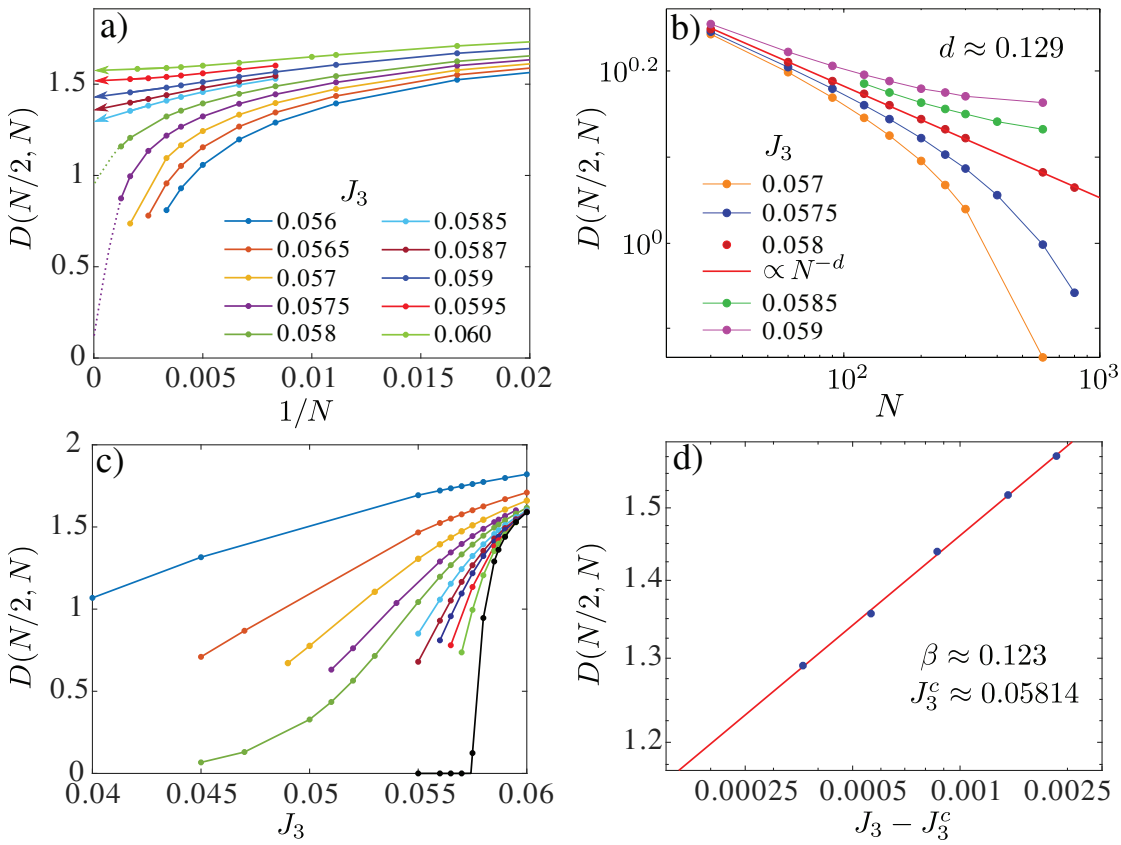

Figure 4.23 – Scaling of the middle-chain dimerization $J_2 = 0.7$ and different values of J_3. (a) Scaling of the dimerization $D(N/2,N)$ with $1/N$. $J_3 \geq 0.585$ belongs to the dimerized phase. The extrapolation is a linear fit of the last two points. Phase transition occur approximately around $J_3 = 0.58$. Quadratic fit for $J_3 = 0.058$ and $J_3 = 0.0575$ is not reliable and most likely overestimated the dimerization in the thermodynamic limit. (b) Log-log plot of the dimerization. The linear curve corresponds to the Ising critical point, and the slope to the critical exponent. This leads to $J_{3c} = 0.058$, and to a slope 0.129, in good agreement with the prediction 1/8 for Ising (see Eq.4.20). (c) Dimerization as a function of J_3 for different system sizes from $N = 30$ (dark cyan) till $N = 600$ (light green) and extrapolation to the thermodynamic limit as shown in (a). (d) Critical exponent β for the scaling away from critical line as $(J_3 - J_3^c)^\beta$. Computed critical exponent 0.123 is in the good agreement with Ising prediction 1/8

4.5.2 Finite-size scaling of the energy spectra

The underlying conformal field theory of a critical system can be extracted from its energy spectrum. The scaling of the ground-state and excitation energies with the system size for the critical transverse field Ising model has been discussed in Section 3.2. The finite-size spectrum of the Ising model does not exhibit logarithmic corrections, and it can be deduced from relatively small systems. CFT predicts that all excitation energies, for any conformally invariant boundary conditions, are of the form $(\pi v/N)x_n$ where v is the velocity and the dimensionless numbers x_n are universal scaling dimensions of operators [20]. Different

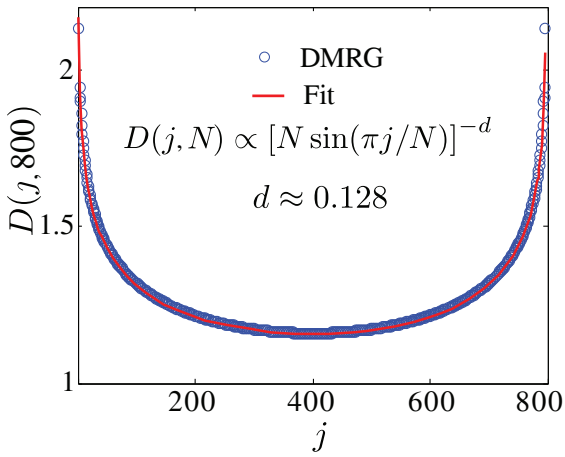

Figure 4.24 – Site dependence of $D(j,N)$ at the critical point fitted to $1/[N\sin(\pi j/N)]^d$. This determines an exponent $d = 0.128$, close to the Ising prediction1/8.

boundary conditions in the critical Ising model correspond to conformal towers of different primary fields with different conformal dimensions x_n. The correspondence between different boundary conditions in the critical Ising model and the corresponding Ising operators was worked out by Cardy [20, 21] and discussed at length in Section 3.2. Furthermore, the ground state energy contains a universal term $-\pi v c/(24N)$ for open boundary conditions (OBC) and $-\pi v c/(6N)$ for periodic boundary conditions (PBC) where c is the central charge.

We identify OBC with $\uparrow,\uparrow$ boundary conditions in the Ising model for N even and $\uparrow,\downarrow$ boundary conditions for N odd, where the arrows refer to the directions of the boundary magnetic fields. The identification of boundary conditions follows because OBC favor the same sign of the dimerisation at both ends of the system for N even but opposite signs for N odd. Similarly we identify PBC on the spin chain with PBC on the Ising model for N even but anti-periodic boundary conditions on the Ising model for N odd. We have calculated the ground state energies in all 4 cases and the lowest 4 excited state energies for OBC and both parities of N (see Fig. 4.25). Note that, in stark contrast to the singlet sector, the singlet-triplet gap in Fig. 4.25(c) and (d) goes to a non-zero value at $1/N \to 0$.

The data on singlet energies determines ten x_n parameters. The nine parameters extracted from OBC all agree to within 5% with the conformal field theory predictions for the Ising model (see Table I in 4.1).

The agreement is not as good for PBC because the sizes accessible to DMRG are much smaller. We plot the excited states energies in the upper panels of Fig. 4.25c and 4.25d. The expected conformal tower structure of excited states is clearly revealed.

Note that the extraction of the central charge from the entanglement entropy for PBC and OBC using the Calabrese-Cardy formula [17] is tricky because of the presence of strong oscillations, but the results are also consistent with $c = 1/2$.

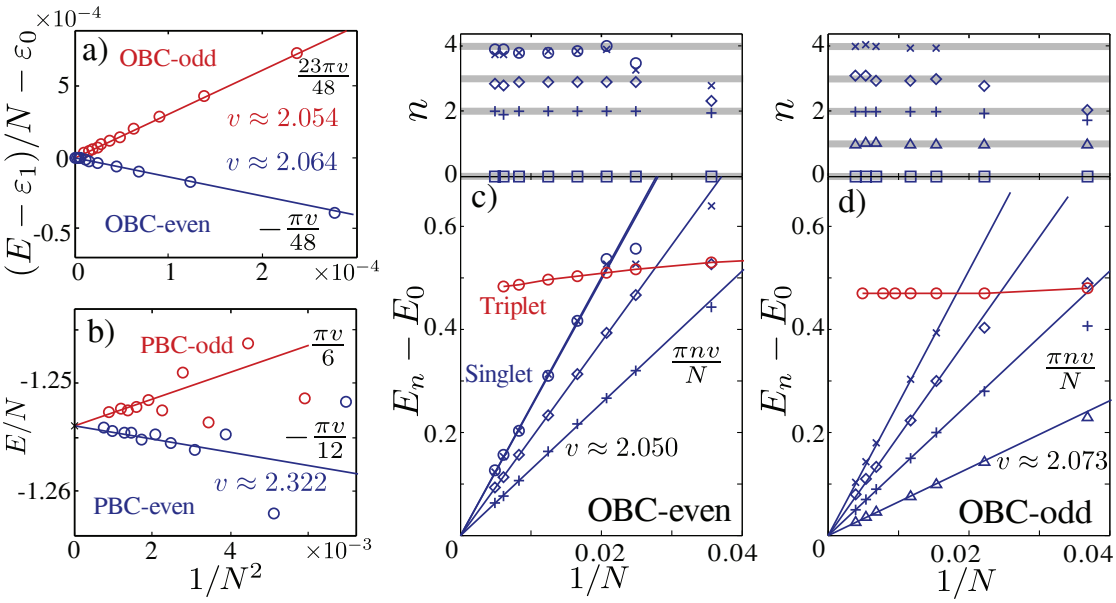

Figure 4.25 – Ground state and excitation energy at $J_2 = 0.7$ and $J_3 = 0.058$, on the Ising line. a) Linear scaling of the ground state energy per site in open chain with $1/N^2$ after subtracting ε_0 and ε_1 terms. b) Linear scaling of the ground state energy per site with $1/N^2$ for periodic chain. c) and d) Energy gaps in singlet and triplet sectors for OBC as a function of $1/N$ for even and odd number of sites. The slope of singlet gap gives values of the velocity. Inset: Conformal towers. Grey lines show Ising conformal towers I (N even) and ϵ (N odd); blue symbols are DMRG data.

4.5.3 Central charge from entanglement entropy at the Ising transition

For a periodic chain with N sites, the entanglement entropy of a subsystem of size n is defined by $S_N(n) = -\mathrm{Tr}\rho_n \ln \rho_n$, where ρ_n is the reduced density matrix. According to conformal field theory, the entanglement entropy in periodic systems depends on the size of the block according to [17]:

$$S_N(n) = \frac{c}{3} \ln \left[\frac{N}{\pi} \sin\left(\frac{\pi n}{N}\right) \right] + s_1 \tag{4.21}$$

In the vicinity of this phase transition the convergence of the entanglement entropy in DMRG algorithm is very slow. This results in big oscillations that appear on top of the curve given by Eq. 4.21. In principle these oscillations can be removed by increasing the number of sweeps and the number of states kept in DMRG. We went up to 16 sweeps keeping up to 900 states in two-site DMRG. With these parameters, oscillations disappear only for chains smaller than 30 sites. For larger systems, we have extracted the central charge for lower and upper curves of the entanglement entropy separately, as shown in Fig. 4.26a). Note that the finite-size corrections to Eq.4.21 are minimal when the block size n is as far as possible from the extreme values 1 and N [59]. Therefore we discard a few points close to the edges while fitting. Alternatively, one

Energy level	CFT Ising	DMRG $J_2 = 0.7$, $J_3 = 0.058$
OBC, Even, ground state	-1/48	-1/48
OBC, Even, 1st excited state	2	1.99
OBC, Even, 2nd excited state	3	2.90
OBC, Even, 3rd excited state	4	3.82
OBC, Even, 4th excited state	4	3.87
OBC, Odd, ground state	$23/48 \simeq 0.479$	0.477
OBC, Odd, 1st excited state	1	1.00
OBC, Odd, 2nd excited state	2	1.98
OBC, Odd, 3rd excited state	3	2.98
OBC, Odd, 4th excited state	4	3.97
PBC, Even, ground state	$-1/12 \simeq -0.0833$	-0.094
PBC, Odd, ground state	$1/6 \simeq 0.167$	0.196

Table 4.1 – Energy levels on Ising line. Ground state refers to the $1/N$ term in the ground state energy. For excited states, the gap above the ground state is given. Results are in units of $\pi v/N$. Note the degeneracy of the 3rd and 4th excited state, for OBC, N even, which occurs in the Ising conformal tower [87] and is well-reproduced by our DMRG results.

can estimate the finite-size central charge by calculating it in the middle of the curve with only two points (see sketches with diamonds in Fig. 4.26(a)). Using Eq. 4.21 leads to the estimates:

$$c_k = \frac{3\left[S_N(\frac{N}{2}-(k+2)) - S_N(\frac{N}{2}-k)\right]}{\ln\left[\cos(\frac{(k+2)\pi}{N})/\cos(\frac{k\pi}{N})\right]}, \tag{4.22}$$

where $k = 0, 1$ for upper and lower curves.

For each system size, we then extrapolate the extracted values of the central charges with the number of states kept in DMRG algorithm. The extrapolated values of the central charge as a function of system size N are shown in Fig. 4.27(c). They are consistent with $c = 1/2$ in the thermodynamic limit however not conclusive due to strong finite-size effects.

It is well established that DMRG algorithm has better performances for open systems, and much bigger system sizes can be reached then. In systems with open boundary conditions, the entanglement entropy scales with the block size according to:

$$S_N(n) = \frac{c}{6}\ln\left[\frac{2N}{\pi}\sin\left(\frac{\pi n}{N}\right)\right] + s_1 + \ln g \tag{4.23}$$

Since we are dealing here with much larger system sizes it is useful to present results in a logarithmic scale by introducing the conformal distance d:

$$d = \frac{2N}{\pi}\sin\left(\frac{\pi n}{N}\right) \tag{4.24}$$

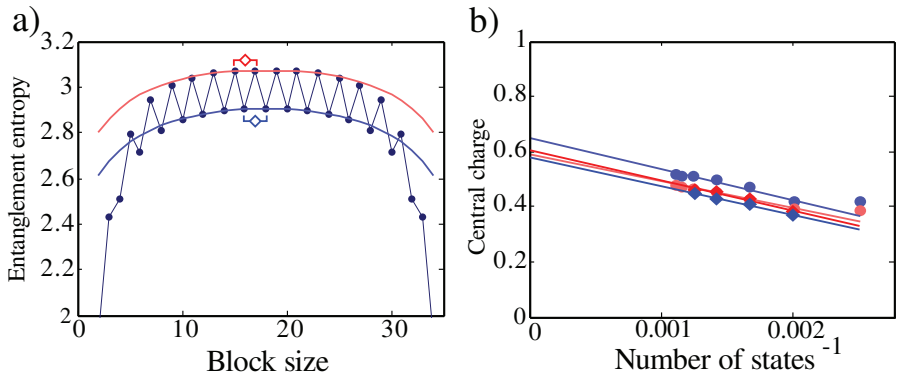

Figure 4.26 – Extraction of the central charge for periodic boundary conditions and $J_2 = 0.7$, $J_3 = 0.058$. a) Example of entanglement entropy as a function of block size n for $N = 36$ sites and 800 states kept in DMRG. Light red and light blue lines are fits to the Calabrese-Cardy formula of Eq. 4.21. Red and blue diamonds schematically show how the formula (4.22) can be applied. b) Scaling of the central charge extracted in different ways with the number of states kept in the DMRG calculation. The lines are linear fits to the data-points (circles for the Calabrese-Cardy fit and diamonds for central charge calculated in the middle of the chain).

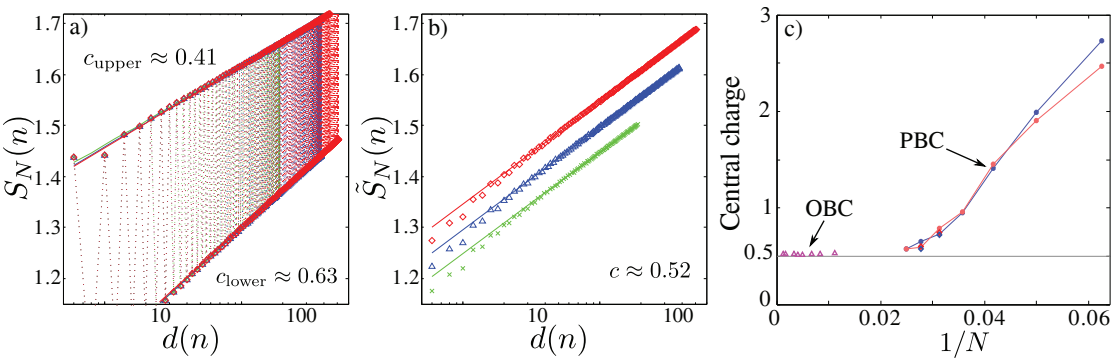

Figure 4.27 – Extraction of the central charge for open boundary conditions. Entanglement entropy as a function of the conformal distance for $N = 300$ (green), 600 (blue) and 800 (red) sites at $J_2 = 0.7$ and $J_3 = 0.058$. a) The solid lines are fits of the upper and lower curves to Eq. 4.23. The slopes of the fits give upper and lower limits for the central charge. b) Entanglement entropy after removing the Friedel oscillations with weight $\zeta \approx 2/9$. The data for $N = 300$ and 600 are shifted downward by 0.1 and 0.05 for clarity. (c) Central charge for the Ising transition as a function of $1/N$. The light blue and red circles have been obtained with the fits of the upper and lower curves of the entanglement entropy with Calabrese-Cardy formula. The red and blue diamonds stand for the central charge extracted in the middle of each curve. All results are extrapolated with the inverse number of sweeps. Magenta triangles stand for the central charge extracted from the entanglement entropy in open chains.

As in the case of periodic boundary conditions, big oscillations appear on top of the prediction of Eq. 4.23. However, in open systems, the oscillations are caused by Friedel oscillations and cannot be removed by increasing the number of sweeps or the number of states. Separate fits of the upper and lower curves of the entanglement entropy leads to rough estimates of the

central charge: $c_{\text{lower}} \approx 0.41$ and $c_{\text{upper}} \approx 0.63$ (see Fig. 4.27a)).

In order to remove the oscillations, following Ref.[18], we have subtracted the spin-spin correlation on the corresponding link from the entanglement entropy with some weight ζ. Then the reduced entanglement entropy as a function of the conformal distance takes the form:

$$\tilde{S}_N(n) = \frac{c}{6} \ln d(n) + \zeta \langle \mathbf{S}_n \mathbf{S}_{n+1} \rangle + s_1 + \ln g \tag{4.25}$$

The results of the numerical calculation of the central charge from the entanglement entropy for both OBC and PBC are summarized in Fig 4.27. These results are consistent with $c = 1/2$.

4.5.4 Triple point

According to conformal field theory, there are two possible scenarios for the triple point of Ising critical line: it can be in either in the Ising or in the tricritical Ising universality class. According to conformal field theory, the first scenario is characterized by a scaling dimension $d = 1/8$ and a central charge $c = 1/2$, while the second one is characterized by $d = 1/24$ and $c = 7/10$.

We have looked at the critical point along a line that is very close to the first order transition and perpendicular to the Ising critical line. According to conformal field theory, the local dimerization depends on the chain length N and bond index j as $D(j,N) = \left[N \sin(\pi j/N)\right]^{-d}$. The values of J_2 and J_3, for which the scaling of the mid-chain dimerization $D(N/2,N)$ is a separatrix is taken as the critical point (Fig.4.28a). At the critical point the fit of $D(j,N)$ is also good (Fig.4.28b). The resulting values of $d \approx 0.158$ and 0.155 point rather towards Ising than towards tricritical Ising criticality.

The central charge was extracted at the critical point from the scaling of reduced entanglement entropy given by Eq.4.25. Although our numerical result point out to a central charge $c \approx 0.6$, that is in between the two expected values, the monotonous decrease and the fact that for $N = 150, 200$ the central charge is below 0.7 suggests that the critical point is in the Ising universality class.

4.5.5 $J_2 - J_3$ model

We have studied the limit of large J_2 and J_3 couplings by setting the nearest neighbor interaction to zero: $J_1 = 0$. As above, we locate the critical point by looking for the separatrix in the scaling of the mid-chain dimerization $D(N/2,N)$ with the chain length N. The slope gives a critical exponent $d \approx 0.126$, in excellent agreement with the Ising one (see Fig.4.29a). We also looked at the local dimerization $D(j,N)$ as a function of the bond position j. Although the dimerization remains large close to the boundary, one can clearly see that some edge effects appear in the absence of a J_1 coupling. A similar picture arises in the Ising chain in a

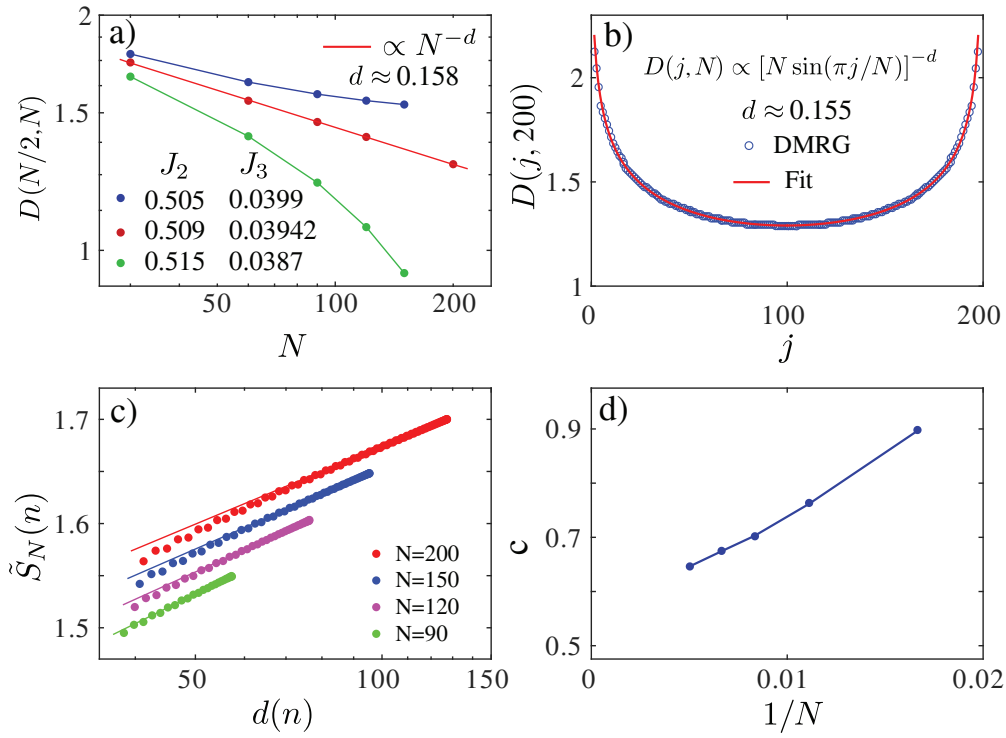

Figure 4.28 – (a) Log-log plot of the mid-chain dimerization as a function of the number of sites N for different parameters J_2 and J_3 along the line close to the first order phase transition and perpendicular to the Ising critical line. The linear curve corresponds to the critical point and the slope gives the critical exponent $d \approx 0.158$. (b) Site dependence of $D(j,N)$ at the critical point fitted to $1/\left[N\sin(\pi j/N)\right]^d$. This determines the exponent $d \approx 0.155$. (c) Scaling of the entanglement entropy of open chains after removing the Friedel oscillations with conformal distance $d(n)$. (d) Central charge extracted from the entanglement entropy of open chains as a function of $1/N$

transverse field if the up-up boundary field is weak with respect to the transverse field. We have thus excluded a few edge points from the fit. The rest of the curve is again in excellent agreement with the Ising prediction $d = 1/8$ (see Fig.4.29b).

As discussed in the context of Ising transition for non-zero J_1 term, the ground-state energy of an open system with an even number of sites scales as $E = \varepsilon_0 N + \varepsilon_1 - \pi v/(48N)$, where ε_0 is a ground-state energy per site, ε_1 - is a non-universal constant, and v is the velocity. For odd N the scaling is of the form $E = \varepsilon_0 N + \varepsilon_1 + 23\pi v/(48N)$ [14]. We present the fit of the numerical data in the Fig.4.30(a) and (b). The extracted values of the velocities $v_{\text{even}} \approx 8.03$ and $v_{\text{odd}} \approx 7.62$ are in reasonable agreement with each other.

The conformal tower for even N corresponds to the Ising conformal tower of I, while for odd N it corresponds to the Ising conformal tower of ϵ. We have used the velocity v_{even} deduced from the finite-size scaling of the ground state energy for even N in order to plot the Ising towers of I and of ϵ in Fig.4.30(c)-(d) as references.

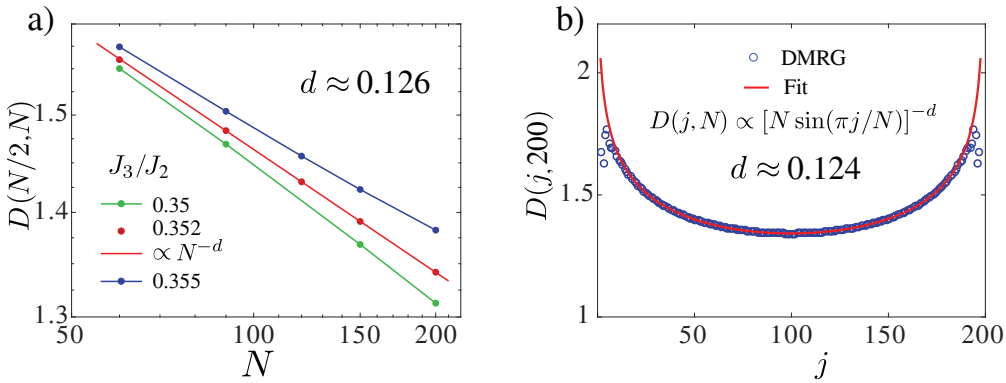

Figure 4.29 – (a) Log-log plot of the mid-chain dimerization as a function of the number of sites N for $J_1 = 0$, $J_2 = 1$ and different values of J_3. The linear curve corresponds to the Ising critical point and the slope gives a critical exponent $d = 0.126$, in good agreement with 1/8 for the Ising transition. (b) Site dependence of $D(j,N)$ at the critical point fitted to $1/\left[N\sin(\pi j/N)\right]^d$. This leads to an exponent $d = 0.124$, again close to the Ising prediction 1/8

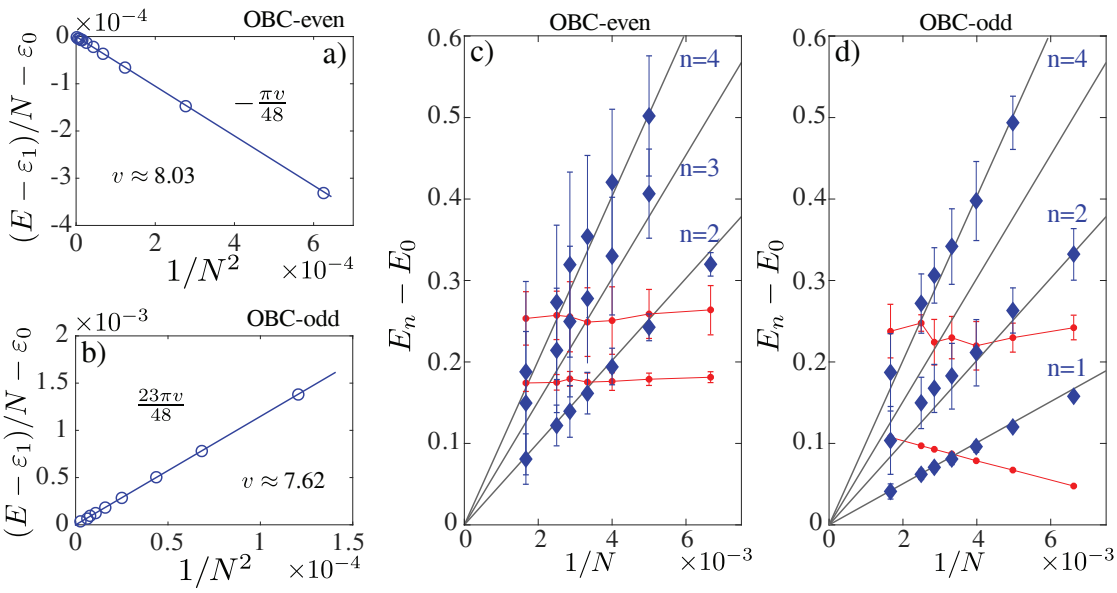

Figure 4.30 – Ground state and excitation energy as $J_1 = 0$, $J_2 = 1$ and $J_3 = 0.352$, on the Ising line. a) and b) Linear scaling of the ground-state energy per site in an open chain with $1/N^2$ after subtracting the ε_0 and ε_1 terms for even (a) and odd (b) number of sites. c) and d) Energy gap in singlet (blue) and triplet (red) sectors for OBC as a function of $1/N$ for even and odd number of sites. Each magnetic excitation is twofold degenerate. Grey lines mark the Ising conformal towers of I c) and of ϵ d) with the velocity $v = 8.03$ deduced from the finite-size scaling of the ground state energy for even N.

We have calculated the excitation energy for even and odd numbers of sites in the singlet $S^z_{\text{tot}} = 0$ and triplet $S^z_{\text{tot}} = 1$ sectors. As discussed in the sections 2.2 The absence of the J_1 term releases low-lying magnetic excitations that are shown with red lines in Fig.4.30(c) and (d). Each red line is twofold degenerate, corresponding to the excitation close to the left and to

the right edges. The first singlet excitation appears below the triplet one only for $N > 300$. By looking at the excitation energy as a function of the number of DMRG iterations, or, more specifically, as a function of the position of the state tensor updated at each iteration, we were able to distinguish bulk excitations from the excitations at the edges, even when they were above the first triplet excitation (for further details see sections 2.2). Note that by edge excitation we understand a localized magnetic excitation of a bond that is located close to the chain boundary.

Since the calculations had to be done for very large systems (in Fig.4.30(c)-(d), we present the results for N in the range 150 to 601.), the convergence of the algorithm is quite slow, implying significant error bars (explicit meaning of the error bar here is explained in sec 2.3). In systems with non-zero J_1 coupling, we saw that for an odd number of sites the fourth excitation was more stable in the DMRG sense than the third one (see e.g. Fig.2.14(c)). This explains the 'missing' third excitation on panel (d): we were not able to converge enough excited states for systems that are so large.

To summarize, we have have provided numerical evidence that the phase transition between the NNN-Haldane and dimerized phases is always in the Ising universality class all along the critical line, including the triple point where the Haldane, NNN-Haldane and dimerized phases touch, and the limiting case of the $J_2 - J_3$ model.

4.6 The end point of WZW SU(2)$_2$ critical line

The critical line that corresponds to the continuous WZW SU(2)$_2$ transition can be extracted in the same way as it has been done in for Ising transition - by identifying a separatrix in log-log plot of finite-size scaling of the dimerization. The method is less precise in the context of WZW SU(2)$_2$ transition due to non-zero logarithmic corrections that changes both, slope and curvature of the scaling curve. However, as we shall see later the accuracy of identified position of the critical line is sufficiently good.

As stated above in the section 4.4, the end point of the WZW SU(2)$_2$ is characterized by the absence of logarithmic corrections. So this is the only point along the line where the critical exponents can be accurately extracted from finite sizes. For the WZW SU(2)$_2$ model, CFT predicts

$$D(j,N) \propto 1/[(N/\pi)\sin(\pi x/N)]^{3/8} \tag{4.26}$$

By fitting a separatrix for each fixed J_2 we can extract an 'apparent' critical exponent (see Fig. 4.31(a)). Interestingly, this apparent exponent can be extracted also along first order phase transition, if sufficiently close to the end point. This is the result of strong finite-size effect that comes from exponentially slow opening of a gap along first order transition above the end point. The apparent exponent decreases from $\simeq 0.43$ for $J_2 = 0$ until it reaches 3/8 at $J_2 \simeq 0.12$ (see Fig. 4.31(b)).

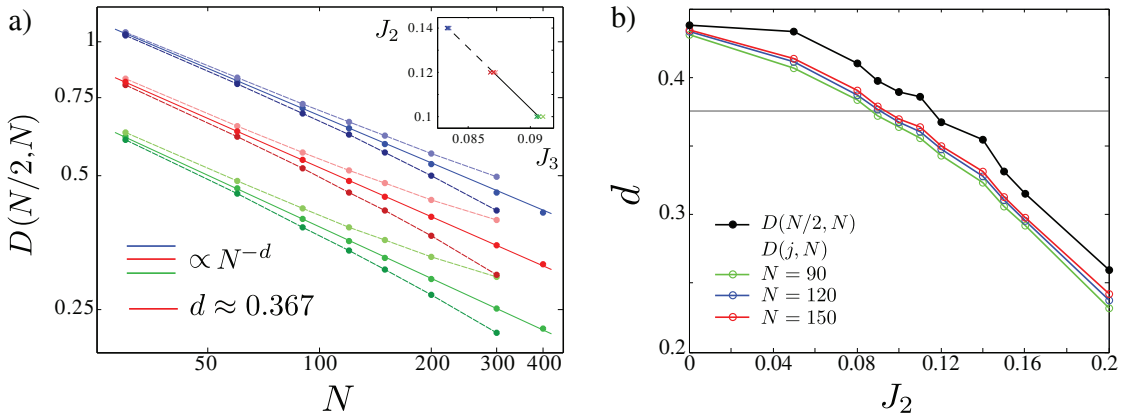

Figure 4.31 – (a) Examples of finite-size scaling of the dimerization $D(N/2,N)$ in the vicinity of the end point in log-log scale. Points for which the finite-size scalings are shown are marked on $J_2 - J_3$ parameter space in the inset. Solid lines are fit to Eq.4.26 the slope gives an apparent critical exponent, dashed lines are guide to the eyes. (b) Apparent critical exponent along the $SU(2)_2$ critical line as a function of J_2. Black solid circles: from the slope of the log-log plot $D(N/2,N)$ as a function of N for the value of J_3 for which it is linear. Open color circles: from fitting $D(j,N)$ for different sizes at the same points. The dashed line is the theoretical value of the exponent, 3/8. Thus the end point is located at $J_2 = 0.12$ and $J_3 = 0.087$

The scaling of the dimerization induced by open boundaries is also characterized by Eq.4.26. The example of this scaling is provided in Fig.4.32.

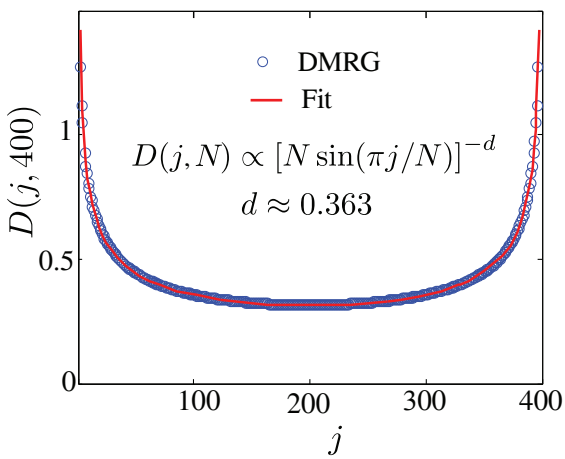

Figure 4.32 – Scaling of the dimerization parameter $D(j,N)$ along the chain with $N = 400$ sites at the $SU(2)_2$ critical end point fitted to Eq.4.26. The extracted exponent is in good agreement with $d = 3/8$.

The central charge extracted from entanglement entropy in periodic chain with Calabrese-Cardy formula [17] given by Eq.4.21 is equal to $c = 3/2$ that corresponds to WZW SU(2)$_2$ and decreases when transition becomes first order. From Fig.4.33 one can immediately deduce the upper bound to the end point - it has to occur below $J_2 \approx 0.22$. Importantly, the central charge never significantly exceeds the value $c = 3/2$. We disagree with this regard with the reference

[81], where the end point of WZW $SU(2)_2$ critical line in the related model is predicted to be in WZW $SU(2)_4$ universality class with central charge $c = 2$. We will come back to this discussion in the next chapter.

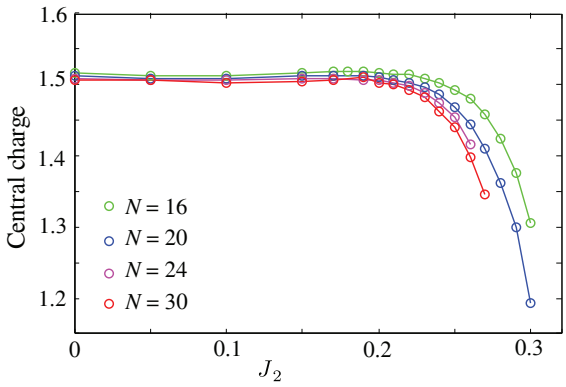

Figure 4.33 – Central charge along the critical line as determined from fitting the entanglement entropy of periodic chains with the Calabrese-Cardy formula, given by Eq.4.21

Until now, we only assume, that the end point can be associated with the critical exponent closed to the field theory predictions, due to vanishing logarithmic corrections. In order to confirm this hypothesis, we extract the low-energy spectra for open boundary conditions with N even and odd.

For the $SU(2)_2$ WZW model there are 3 conformal towers labeled by the spin of the lowest energy states, $j = 0$, $1/2$ and 1. Finite size spectra with conformally invariant boundary boundary conditions at both ends of the system can be determined from the corresponding boundary states, which are labeled by the primary operators. [21] OBC with N even in our model corresponds to the $|0\rangle$ boundary state at both ends of the system and the corresponding conformal tower in the finite-size spectrum is $j = 0$. Going to an odd number of sites is formally analogous to the infrared fixed point spectrum of a spin-1 Kondo model and the corresponding boundary state changes to $|1\rangle$ at one end of the system. [4] The resulting finite-size spectrum contains the $j = 1$ conformal tower. Thus the ground state energies of an open chain with an even or odd number of sites are:

$$E_{\text{even}} = \varepsilon_0 N + \varepsilon_1 - \frac{\pi v}{16N}, \tag{4.27}$$

$$E_{\text{odd}} = \varepsilon_0 N + \varepsilon_1 + \frac{7\pi v}{16N}. \tag{4.28}$$

In order to build the conformal tower at the end point $J_2 = 0.12$ and $J_3 = 0.087$, we calculate the gap between the ground state energy and the lowest energies in different sectors of S^z_{tot}. The gap scales linearly with $1/N$ and the slope gives access to the velocity. By calculating excited states in the sectors $S^z_{\text{tot}} = 0, 1$, we could determine the multiplicity of two lowest energy levels. In a chain with an even number of sites, the ground state is a singlet and the first excited state is a triplet, while for a chain with an odd number of sites, the ground state is a triplet and

the first excited state is degenerate and consists of one triplet and one singlet, in complete agreement with CFT predictions. The DMRG data on the scaling is presented in Fig.4.34 (a) and (b) and summarised in Table II.

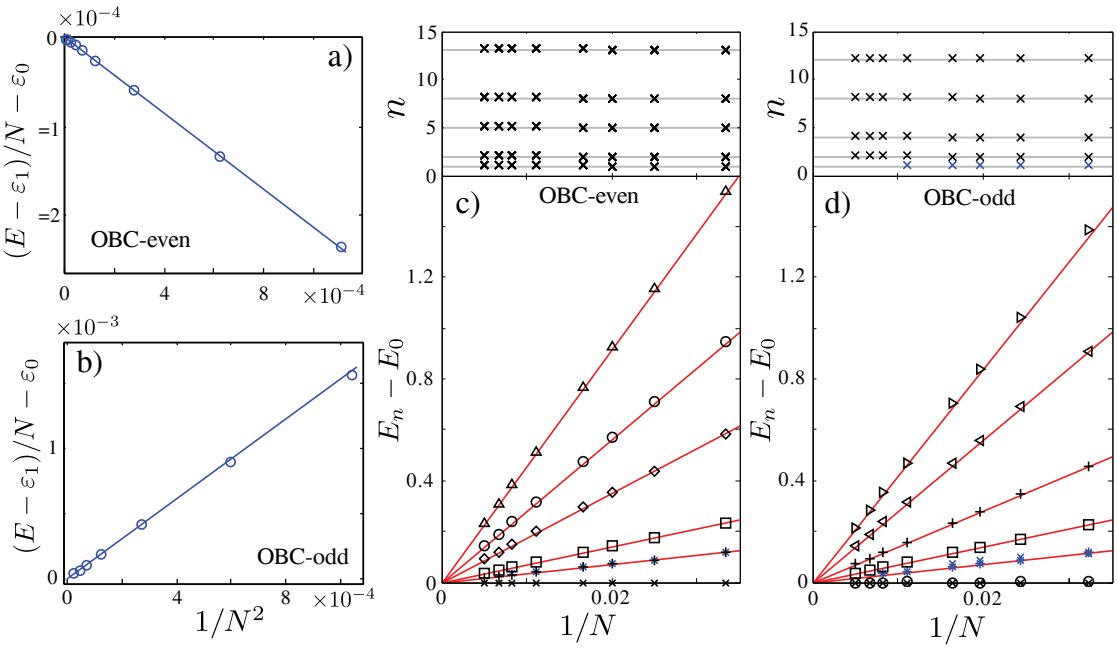

Figure 4.34 – Ground state and excitation energy at $J_2 = 0.12$ and $J_3 = 0.087$, on the critical line between the Haldane and the Dimerized phases. (a) and (b): Linear scaling of the ground state energy per site with $1/N^2$ after subtracting ε_0 and ε_1 in open chains with (a) even and (b) odd numbers of sites N. (c) and (d): Energy gap between the ground state and the lowest energies in different sectors of $S_z^{\text{tot}} = 0, 1, ..., 5$ (black symbols) as a function of $1/N$ for even and odd numbers of sites. The multiplicity of the ground state and of the first excited states has been obtained by calculating excited states in the sectors $S_z^{\text{tot}} = 0$ (blue crosses) and $S_z^{\text{tot}} = 1$ (blue pluses). Insets: Conformal towers for even and odd N. Black and blue symbols are DMRG data for the ground states in different sectors of S_z^{tot} and for the first excited state in the sector $S_z^{\text{tot}} = 1$

Moreover, we have checked that the conformal tower is destroyed by moving along the critical line away from the end point. To demonstrate this, we have plotted the velocities extracted from three different excitation levels n (fig.4.35). At the end point, all velocities are expected be the same, implying that the conformal tower is restored. This occurs around $J_2 = 0.12$, in agreement with the value determined from the critical exponent.

4.7 Magnetic and non-magnetic domain walls. Solitons

Regarding the alternative between Ising and WZW $SU(2)_2$, if the transition is continuous, we would like to suggest that it is intimately related to the nature of the domain walls between the phases (see Fig. 4.36). A domain wall between Haldane and Dimerized phases necessarily

Energy level	CFT SU(2)$_2$	DMRG $J_2 = 0.12, J_3 = 0.087$
OBC, Even, ground state $S_z^{\text{tot}} = 0$	-1/16	-1/16
OBC, Even, ground state $S_z^{\text{tot}} = 1$	1	1.027
OBC, Even, ground state $S_z^{\text{tot}} = 2$	2	2.052
OBC, Even, ground state $S_z^{\text{tot}} = 3$	5	5.14
OBC, Even, ground state $S_z^{\text{tot}} = 4$	8	8.29
OBC, Even, ground state $S_z^{\text{tot}} = 5$	13	13.50
OBC, Odd, ground state $S_z^{\text{tot}} = 1$	7/16 $\simeq 0.4375$	0.443
OBC, Odd, 1st exited state $S_z^{\text{tot}} = 1$	1	1.052
OBC, Odd, ground state $S_z^{\text{tot}} = 2$	2	2.052
OBC, Odd, ground state $S_z^{\text{tot}} = 3$	4	4.12
OBC, Odd, ground state $S_z^{\text{tot}} = 4$	8	8.26
OBC, Odd, ground state $S_z^{\text{tot}} = 5$	12	12.52

Table 4.2 – Energy levels at $SU(2)_2$ critical point. Ground state for N even $S_z^{\text{tot}} = 0$ and odd $S_z^{\text{tot}} = 1$ refers to the $1/N$ term in the ground state energy. For the rest, the gap above the ground state is given. Results are in units of $\pi v/N$.

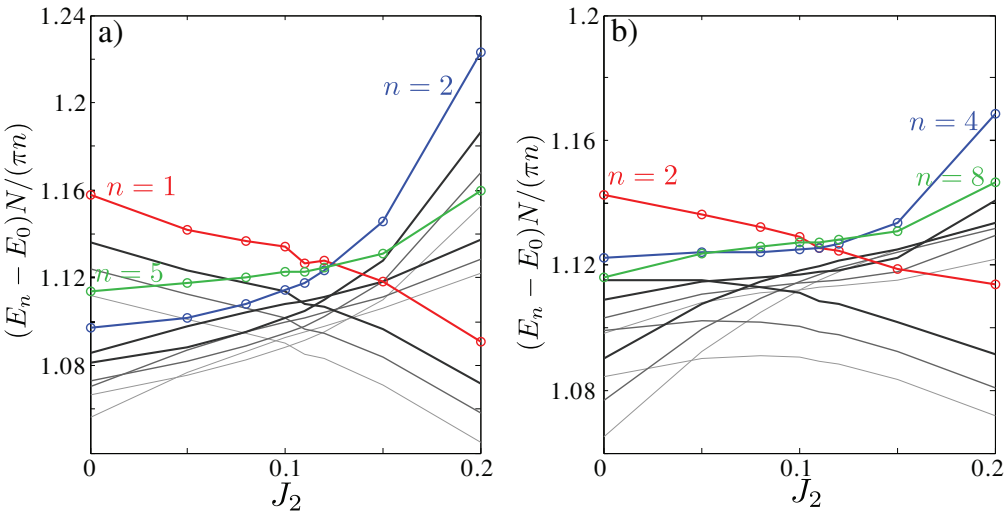

Figure 4.35 – Velocity along the critical line between the Haldane and the dimerized phases extracted from the gap between n's energy level and a ground state. Red, blue and green lines show results for a) $N = 50$ and b) $N = 51$. Similar results for a) $N = 30, 24, 20$ and b) $N = 31, 25, 21$ are shown in gray (from dark thick to light thin).

carries spin-1/2 because the Haldane phase is topological and has edge states, leading to a transition with magnetic excitations (WZW SU(2)$_2$ if it is continuous), whereas a domain wall between NNN-Haldane and dimerized phases does not because the NNN-Haldane phase is topologically trivial with no edge states, leading to an Ising transition in the singlet sector with gapped magnetic excitations. These observations are consistent with the field theory

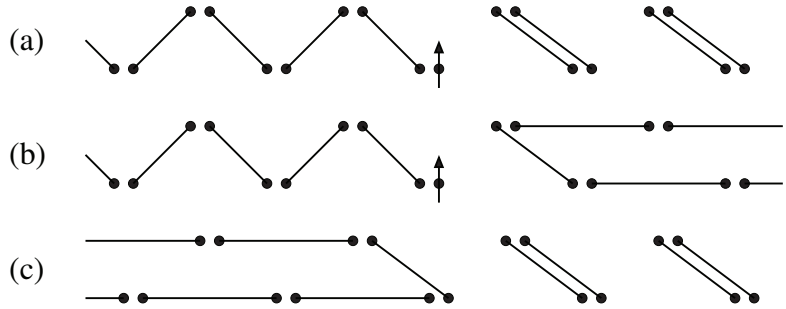

Figure 4.36 – Sketch of domain walls between (a) the Haldane and Dimerized phases, (b) the Haldane and NNN Haldane phases, and (c) the NNN Haldane and Dimerized phases. A spin-1/2 appears at the domain wall in the first two cases, but not in the third one.

argument discussed in the end of Section 4.4.

The alternative between Ising and $SU(2)_2$ universality classes has been first pointed out by Nersesyan and Tsvelik in the related context of spin-1/2 ladders with four-spin interactions using a Majorana fermion representation of the field theory. [75, 92] Calculations on specific models with ring-exchange or frustrated leg coupling have supported this prediction. [15, 76, 72, 45, 46, 89, 61, 38, 65, 33, 101, 64, 47] In that respect, the main difference with our model is that, in the model of Nersesyan and Tsvelik, one goes from Ising to $SU(2)_2$ through a trivial point of decoupled chains [101, 47] and central charge $c = 2$, with no indication of an end-point of the $SU(2)_2$ line followed by a first-order transition, a generic feature of our approach due to the presence of a marginal operator.

Coming back to the role of edge states at the transition, the result summarized in Fig. 4.36 can easily be extended to ladders to explain the fundamental difference between Ising and $SU(2)_2$ universality classes: spontaneous dimerization transitions between phases which are both topologically trivial (rung singlet and columnar dimer) or non trivial (Haldane and staggered dimer) can be expected to be generically Ising because edge states are absent or compensate each other, while spontaneous dimerization transitions between a topological and a non-topological phase (staggered dimer and rung singlet or Haldane and columnar dimer) must include magnetic excitations because of the edge states and can be expected to be generically $SU(2)_2$, or possibly first-order with spin-1/2 solitons. Similar ideas might be extended to transitions between valence-bond solids and dimerized phases in other contexts, possibly in higher dimension.

We have studied numerically the soliton formation around the first order phase transition between the Haldane and dimerized phases. In Fig.4.37 we show results for the lowest-lying $S^z_{\rm tot} = 1$ states of a $N = 121$ site chain for $J_2 = 0.3$ and different values of J_3. The most relevant quantities are: i) the local magnetization $\langle S^z_j \rangle$ that reveals edge states or solitons; ii) the spin-spin correlation between nearest neighbors $\langle S^z_j S^z_{j+1} \rangle$ that reflects the presence of dimerization; and iii) the expectation value of the three-site interaction $\langle (\mathbf{S}_{i-1}\mathbf{S}_i)(\mathbf{S}_i\mathbf{S}_{i+1}) - \text{h.c.} \rangle$, an indicator of the Haldane phase - it is large and positive in the Haldane phase since spin-spin correlations

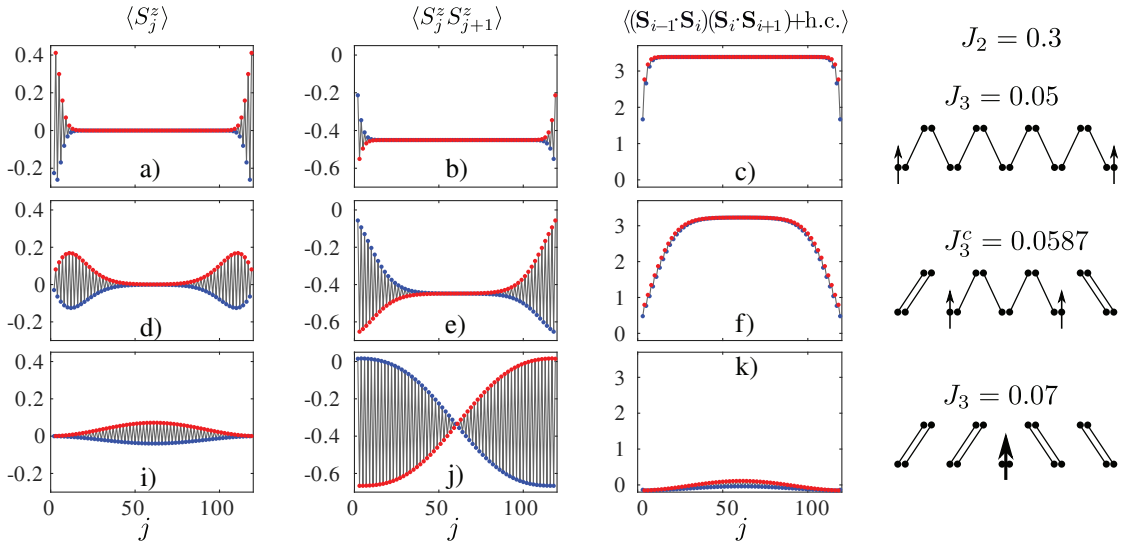

Figure 4.37 – Spin solitons in chains with $N = 121$ at $J_2 = 0.3$ and $S^z_{\text{tot}} = 1$ below (a-c), above (i-k) and on the critical line (d-f). Left panels: On-site magnetization. It reveals a) spin-1/2 edge states, d) spin-1/2 solitons inside the chain, and i) spin-1 soliton. Middle panels: Spin-spin correlations. They provide evidence of a small dimerization all along the chain in the Haldane phase (b), of a large dimerization at the edges and of its fast decrease in the middle, when the two phases coexist (e), and of a large dimerization all along the chain except in the narrow window in the middle, where the spin-1 soliton is located (j). Right panel: Expectation value of the three-body term. It is large and positive all along the chain in he Haldane phase (c), it is small at the dimerized edges but remains large in a domain of Haldane phase in the middle of a chain (f), and it almost vanishes in the dimerized phase (k). The sketches on the right show the VBS picture of solitons in different phases. Thin and thick arrows indicates spin-1/2 and spin-1 solitons. For clarity, each even (odd) data point corresponds to a blue (red) symbol.

on adjacent bonds are (almost) equal and negative, it is very small and positive in the dimerized phase close to the transition, it vanishes when the state is exactly dimerized, and it is negative everywhere else in dimerized phase.

Our main results can be summarized as follows: Deep inside the Haldane phase there are spin-1/2 edge states as seen from the local magnetization of Fig.4.37a. The small dimerization and the large expectation value of the three-body interaction all along the chain confirm that the entire chain is in the Haldane phase. Around the phase transition, two phases coexist: the dimerized state is favored close to the edges, while the central part of a chain remains in the Haldane phase. (Fig.4.37e-f). The two humps of the local magnetization curve (Fig.4.37d) show that free spins have moved away from the boundaries and form a pair of spin-1/2 solitons that separates the Haldane and dimerized domains. Deep inside the dimerized phase, the two spins-1/2 recombine into a delocalized spin $S = 1$, and two dimerized domains with different orientations occupy half of the chain each (Fig.4.37i-k). The transition between two dimerization domains with different dimer orientations can also be deduced from the crossing of the lines formed by red and blue points in the spin-spin correlation (see Fig.4.37j)

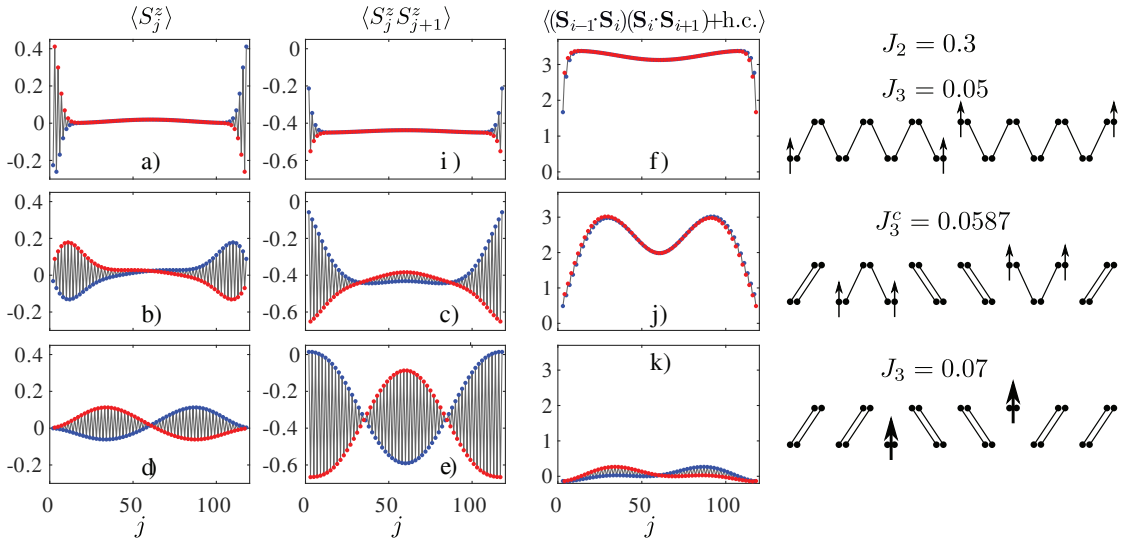

Figure 4.38 – Same as Fig.4.37 for $N = 120$ at $J_2 = 0.3$ and $S^z_{\text{tot}} = 2$ (see main text for the details).

The soliton picture remains true for higher values of the total spin. Fig.4.38 provides an example of solitons in a chain with $N = 120$ and $S^z_{\text{tot}} = 2$. As in the previous case, one can clearly distinguish spin-1/2 edge states in Fig.4.38a). On top of it, a slight increase of the on-site magnetization occurs in the middle of the chain, indicating the appearance of a spin-1 bond in the bulk. The Haldane phase is then perturbed. This is reflected in the suppressed three-body term measured in the middle of the chain (Fig.4.38c). The formation of the dimerized phase starts at the edges, but also in the bulk when approaching the phase transition. Different dimerization domains are separated by domains of Haldane phase, each carrying a total spin-1. Numerically, three dimerization domains are clearly seen with the spin-spin correlations in Fig.4.38e), while the two maxima in the three-body term correspond to two Haldane domains. Inside the dimerized phase, the Haldane domains are suppressed, the dimerization is essentially different from zero everywhere along the chain except at two points symmetric with respect to the middle of the chain. The domain walls are located at the points with vanishing dimerization. The four spins-1/2 recombine into a pair of spins-1, each of them delocalized along half the chain. The lines formed by red and blue points in the spin-spin correlation intersect twice in Fig.4.38e,c), implying that the orientation of the dimers is different in neighboring domains.

4.8 Short-range order

4.8.1 Disorder and Lifshitz lines

As mentioned in Section 4.2, several types of short-range order are present in the Haldane, NNN-Haldane and dimerized phases (see Fig.4.39). A detailed description of each phase has already be given in Section 4.2. In this section, we describe the numerical results that led to

this phase diagram in more detail.

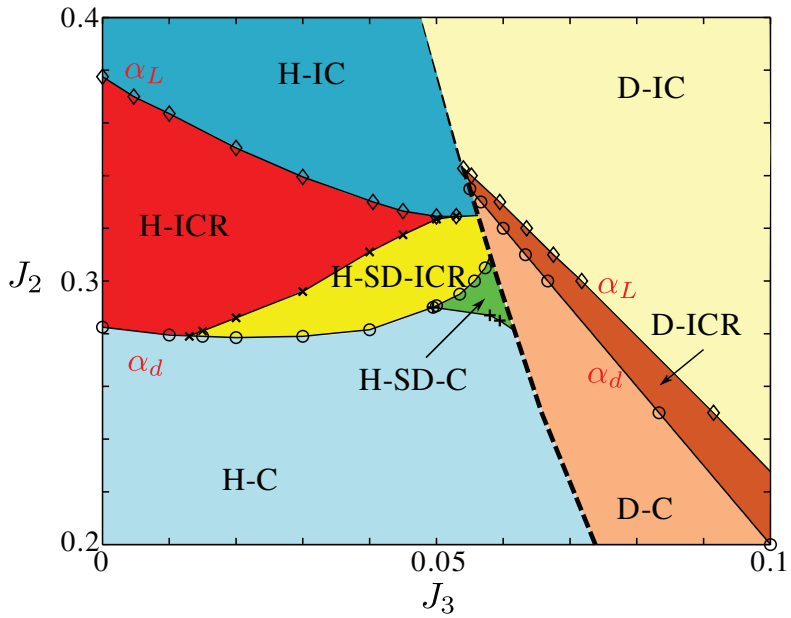

Figure 4.39 – Enlarged part of phase diagram on Fig.4.5 indicating short-range order within the thermodynamic phases. Lifshitz line α_L is marked with diamonds and disorder line α_d is marked with open circles. Dashed line is a line of the first order phase transition

The most important result is that, by tuning either the next-nearest-neighbor or the three-body interaction, short-range incommensurate order can be induced beyond the so-called disorder and Lifshitz lines. Disorder points were first discussed by Stephenson in models of classical statistical mechanics [94, 95, 93]. On one side of a disorder point, the correlation function decays in a commensurate way, while on the other side it decays in an incommensurate way. The disorder point is said to be of the first kind if the wave number in the incommensurate phase depends on the temperature, and of the second kind if it does not [95]. In the present case, we have only found disorder points of the first kind.

By contrast, at a Lifshitz transition, the spin-spin correlation function becomes incommensurate in momentum space, each peak being replaced by two symmetric peaks in the structure factor $SF(q)$ defined in Eq.4.8.

By keeping track of real space and momentum space correlations, we found that disorder and Lifshitz lines cross the transition line at $J_2 \simeq 0.335$ and $J_2 \simeq 0.342$.

4.8.2 Dimerized phase

By fitting the numerical results of the spin-spin correlations with the dimerized OZ form given by Eq.4.7, we have extracted the wave number q and the short-range dimerization parameter δ. Examples of fits for $J_2 = 0.25$ are shown in Fig.4.40.

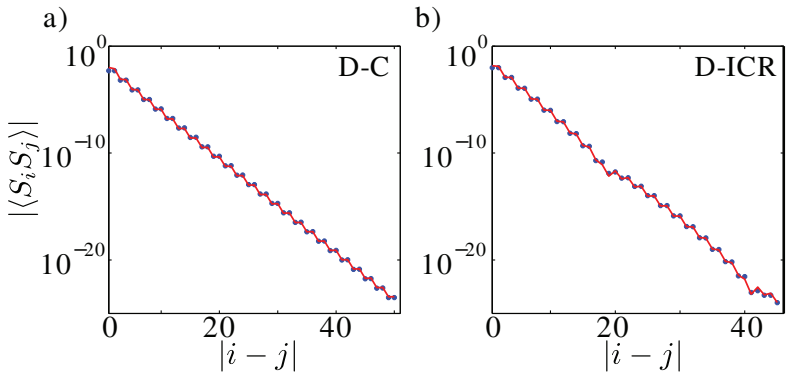

Figure 4.40 – Spin-spin correlation function $\langle S_i S_j \rangle$ for $J_2 = 0.25$ with a) $J_3 = 0.083$ and b) $J_3 = 0.084$; The red lines are fit to the data with the dimerized OZ form given by Eq.4.7 with a) $q = \pi$ and b) $q > \pi$

We have found that, with very high accuracy, the disorder line coincides with the line where the fully dimerized wave-function is the exact ground state of the model (see Fig.4.41).

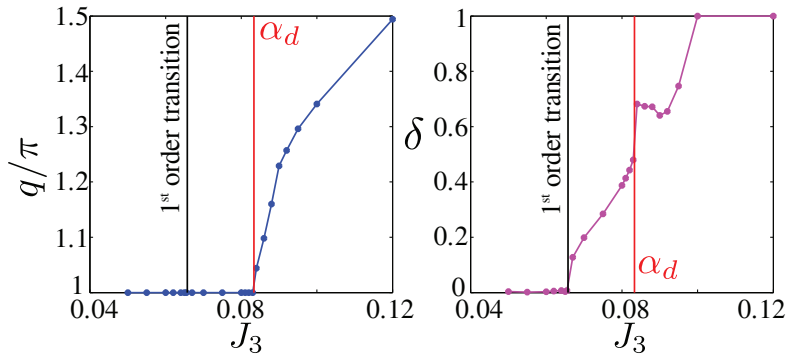

Figure 4.41 – Wave number q and dimerization δ deduced from a fit of the spin-spin correlation function with Eq.4.7 for $J_2 = 0.25$. The position of the first order phase transition and the line α_d where the ground state is fully dimerized are marked with black and red lines respectively.

In order to determine the Lifshitz line, we have looked for the appearance of a two-peak structure in $SF(q)$ given by Eq.4.8, where we have restricted the sum to the interval $20 < i, j \leq N - 20$ in order to eliminate edge effects. Some examples of structure factor calculated for fixed $J_2 = 0.25$ are presented in Fig.4.42.

The conclusion that emerges from these results is that, to go from the commensurate to the incommensurate part of the dimerized phase, one has to cross first a disorder line, and then a Lifshitz line. These results are very similar to those obtained for the spin-1/2 chain with next-nearest-neighbor interaction, the fully-dimerized line of our model being the equivalent of the Majumdar-Ghosh point [69]. At that point, the correlation length vanishes, and it coincides with the disorder point $J_2^d = 1/2$, while the Lifshitz point of the spin-1/2 chain is located at $J_2^L = 0.52036(6)$ [16], well above the disorder point.

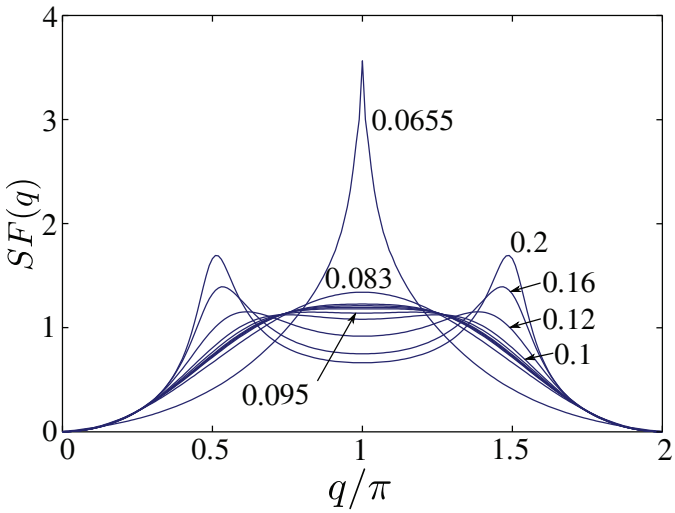

Figure 4.42 – Structure factor $SF(q)$ for $J_2 = 0.25$ and various values of J_3. The Lifshitz point is at $J_3 = 0.0915 \pm 0.0005$.

4.8.3 Haldane phase

Depending on the type of correlation in the Haldane phase we have fitted the numerical data with either non-dimerized OZ or dimerized OZ forms given by Eq.4.6 and Eq.4.7. Below we provide several examples of spin-spin correlations and some fits.

The wave number q and the short-range dimerization parameter δ extracted from the fit for fixed $J_3 = 0.03$ are summarized in Fig.4.44. Note that there is a finite region where the dimerization is essentially different from zero.

Crossing the transition line at $J_2 \simeq 0.335$, the disorder line is separated from the transition line in Haldane phase by a thin tail of commensurate phase with short-order dimerization (H-SD-C).

The Lifshitz line in the Haldane phase is obtained in the same way as in the dimerized phase. Close to the crossing point $J_2 \simeq 0.342$, the Lifshitz line is very close to the boundary of the H-SD-ICR phase, making the H-ICR phase vanishingly small in this region.

4.9 Conclusion

Combining field theory arguments with DMRG (and occasionally exact diagonalizations), we have shown that the dimerization transitions of the spin-1 Heisenberg model with next-nearest neighbor and three-site interaction can be precisely located and fully characterized. In particular, the transition between the Haldane phase and the dimerized phase is in the $SU(2)_2$ WZW universality class for small J_2, and it becomes first order at an end point also in the $SU(2)_2$ WZW universality class. This happens because the WZW $\mathrm{SU}(2)_2$ model has a

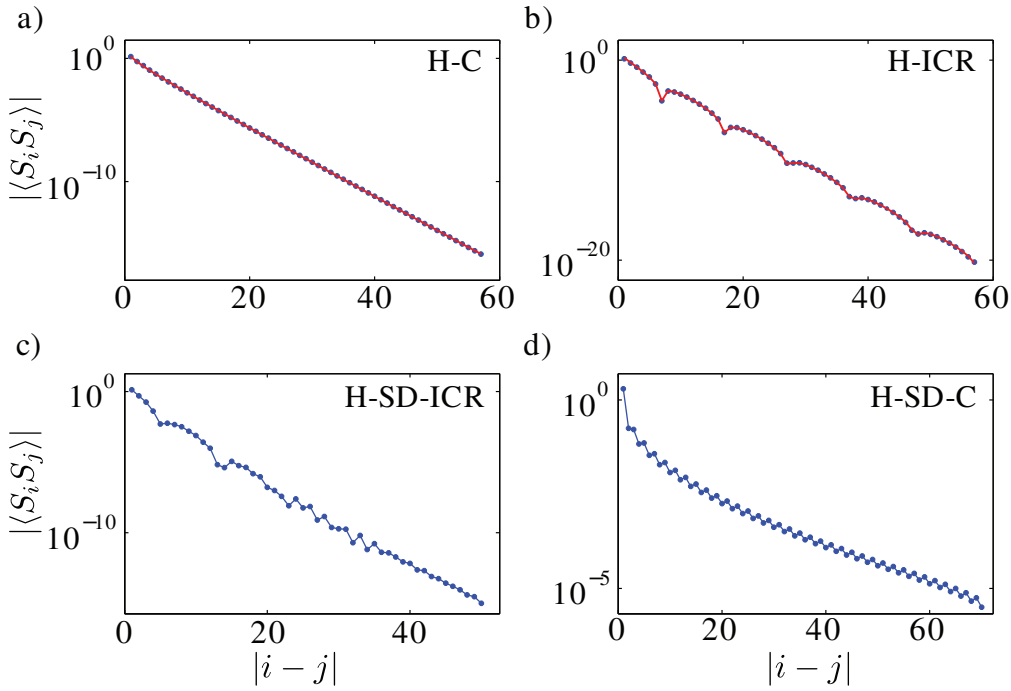

Figure 4.43 – Spin-spin correlation function $\langle S_i S_j \rangle$ for a) $J_2 = 0.27$, $J_3 = 0$; b) $J_2 = 0.3$, $J_3 = 0$; c) $J_2 = 0.3$, $J_3 = 0.04$ and d) $J_2 = 0.3$, $J_3 = 0.059$. The red line on a) and b) is a fit to the data with the OZ form.

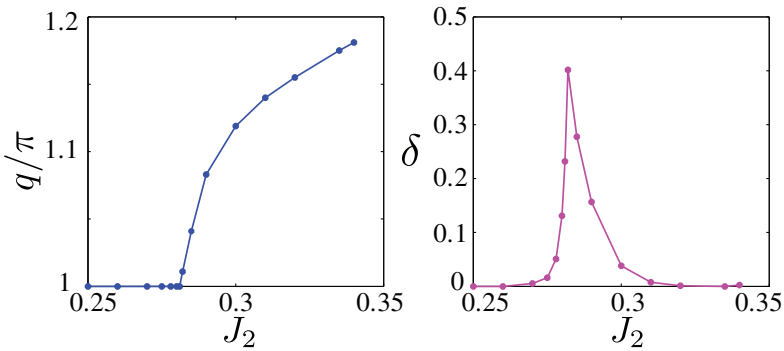

Figure 4.44 – Wave number q and dimerization δ deduced from a fit of the spin-spin correlation function with Eq.4.7 for $J_3 = 0.03$.

marginal operator, and the coupling constant of this operator changes its sign at the end point. Reformulating the low-energy Hamiltonian with conformal embedding in terms of Ising and boson fields, one can deduce that in the vicinity of the end point, the transition (whether continuous or first order) occurs simultaneously in the Ising and boson sectors. However, far from the end point they can split. The Ising transition between NNN-Haldane and dimerized phases has been confirmed numerically with the finite-size scaling of the energy spectrum, the central charge, and the critical exponents.

The alternative between Ising and WZW $SU(2)_2$ universality classes is related to the nature of

the domain walls between corresponding phases(see Fig. 4.36). A domain wall between the Haldane and Dimerized phases necessarily carries a spin-1/2 because the Haldane phase is topological and has edge states, leading to a transition with magnetic excitations (WZW $SU(2)_2$ if it is continuous), whereas a domain wall between NNN-Haldane and dimerized phases does not because the NNN-Haldane phase is topologically trivial with no edge states, leading to an Ising transition in the singlet sector with gapped magnetic excitations. These observations are consistent with the field theory approach and with the numerical observation of magnetic solitons at the first order phase transition between the Haldane and dimerized phases. The observed solitons are in qualitative agreement with the fact that along the $SU(2)_2$ line, there are low-lying magnetic excitations. By contrast, the transition between the next-nearest neighbor Haldane phase and the dimerized phase is in the Ising universality class. Along this transition line, the spin-gap remains open, and the low-lying excitations are all in the singlet sector.

To fully characterize the transitions, DMRG with open boundary conditions turned out to be extremely useful. This is due to the fact that the conformal tower of a critical model with open boundary conditions is often just the tower of a single primary field. By contrast, the conformal tower of a critical model with periodic boundary conditions is in general the superposition of different towers. We think that a systematic use of these ideas might turn out to be useful in other one-dimensional quantum systems.

In addition, we have shown that short-range correlations can be commensurate or incommensurate, with several disorder and Lifshitz lines, leading to a remarkably rich phase diagram. Interestingly, several of these phases occur for relatively small, hence physically realistic values of the couplings J_2 and J_3. So it is our hope that the present investigation will encourage experimentalists to try and check some aspects of this phase diagram.

5 The spin-1 chain with next-nearest neighbor and biquadratic interactions

5.1 Introduction

In the present chapter we continue to study the appearance of spontaneously dimerized phase induced by frustration and the nature of the corresponding critical lines. This chapter is dedicated to the spin-1 model with bilinear-biquadratic and next-nearest neighbor interactions.

The phase diagram of this model has been investigated by Pixley, Shashi and Nevidomskyy [Phys. Rev. B **90**, 214426 (2014)]. It consists of three phases, and the nature of the phase transitions has been determined using Density Matrix Renormalization Group (DMRG) and field-theory arguments. In the previous chapter, we have investigated a similar model in which the biquadratic interaction is replaced by a three-site interaction that provides the appropriate generalization of the spin-1/2 Majumdar-Ghosh chain. Much to our surprise, while the competing phases are the same as for the model with biquadratic interaction - Haldane, NNN-Haldane (called NNN-AKLT in Ref. [81]) and dimerized - we came to significantly different conclusions regarding the transitions between them:

i) We provide numerical evidence of a continuous Ising transition between the NNN-Haldane phase and the dimerized phase;

ii) We show that the tri-critical end point, where the continuous transition between the Haldane phase and the dimerized phase turns into a first order transition, is distinct from the triple point where the three phases meet;

iii) Finally, we demonstrate that the tri-critical end point is in the same Wess-Zumino-Witten (WZW) $SU(2)_2$ universality class as the continuous transition line that ends at this point.

The goal of this chapter is to re-investigate the nature of the phase transitions in the model with biquadratic interactions. As we will see, this leads to a new phase diagram that turns out to be qualitatively similar to that of the model with three-site interactions.

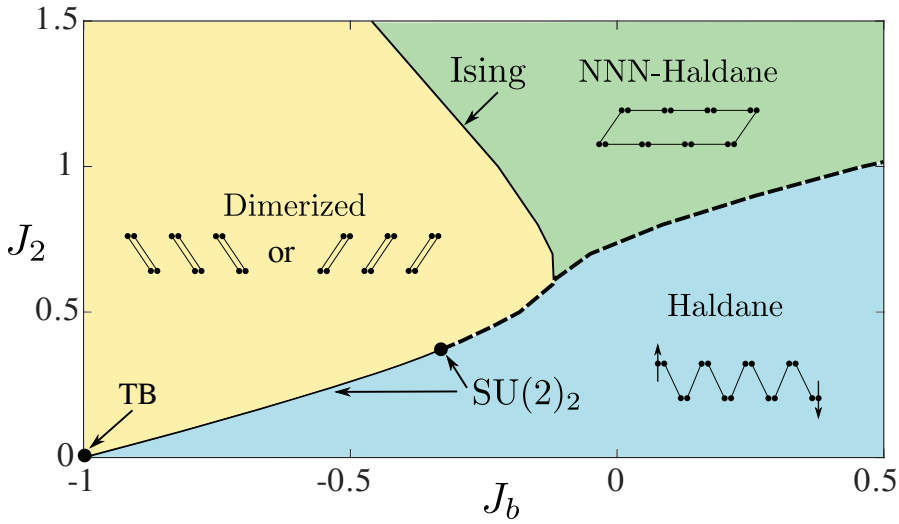

Figure 5.1 – Phase diagram of the spin-1 chain with next-nearest neighbor coupling J_2 and biquadratic interaction J_b. The transition from the dimerized phase to the Haldane phase starts at the Takhtajan-Babudjian (TB) point[96, 9], is continuous along the solid line, with central charge $c = 3/2$, and first order along the dashed line. The transition from the NNN-Haldane phase to the dimerized phase is a continuous transition in the Ising universality class with central charge $c = 1/2$. The transition between the Haldane phase and the NNN-Haldane phase is always first order.

5.2 Phase Diagram

The $J_1 - J_2 - J_b$ model is described by the Hamiltonian:

$$H = \sum_i J_1 \mathbf{S}_i \cdot \mathbf{S}_{i+1} + J_2 \mathbf{S}_{i-1} \cdot \mathbf{S}_{i+1} + J_b (\mathbf{S}_{i-1} \cdot \mathbf{S}_i)^2, \tag{5.1}$$

$J_1 = 1$ throughout the paper. In the convention of Ref.[81], $J_2 = \alpha$ and $J_b = \beta$. Our main results are summarized in the phase diagram of Fig.4.4. Each phase may be schematically illustrated by valence bond pictures, as it has been done in the context of $J_1 - J_2 - J_3$ model

Below, with the help of extensive density matrix renormalization group (DMRG)[103, 90, 78, 91] calculations, we will demonstrate that: *i)* The phase transition between the NNN-Haldane phase and the dimerized phase is continuous and in the Ising universality class, and *not* first order; *ii)* The continuous WZW SU(2)$_2$ transition starts at the Takhtajan-Babujian (TB) point and terminates at a tri-critical point that is *distinct* from the triple point; *iii)* Beyond the tri-critical point, the phase transition between the Haldane phase and the dimerized phase is first order; *iv)* The tri-critical point is in the same WZW SU(2)$_2$ universality class as the critical line that ends at that point, and *not* in the WZW SU(2)$_4$ universality class, as suggested in Ref.[81].

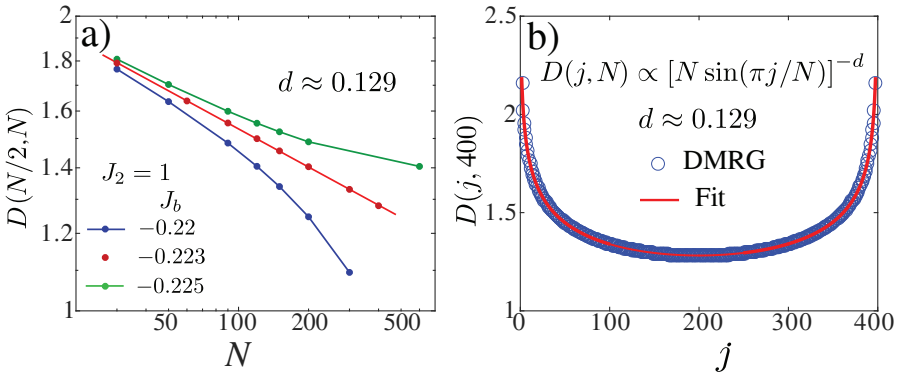

Figure 5.2 – (a) Log-log plot of the mid-chain dimerization in open chain as a function of the number of sites N for $J_2 = 1$ and different values of J_b. The linear curve corresponds to the Ising critical point, and its slope to the critical exponent d. This leads to $J_b = -0.223$ and $d = 0.129$, in good agreement with the prediction 1/8 for Ising. (b) Site dependence of $D(j,N)$ at the critical point fitted to $1/\left[N\sin(\pi j/N)\right]^d$. This leads to an exponent $d = 0.128$, again close to Ising prediction 1/8.

5.3 Ising transition

Let us first consider the transition between the NNN-Haldane phase and the dimerized phase. We define the local dimerization as $D(j,N) = |\langle\vec{S}_j \cdot \vec{S}_{j+1}\rangle - \langle\vec{S}_{j-1} \cdot \vec{S}_j\rangle|$, where j is the site index and N is the total number of spins. In order to locate the phase boundaries, we look at the mid-chain dimerization $D(N/2,N)$ around the transition as a function of system size N. In the NNN-Haldane phase, the dimerization vanishes with the system size, while in the dimerized phase it stays finite. In finite-size chains, we found that the dimerization increases continuously from NNN-Haldane phase to the dimerized phase, in agreement with the numerical results of Ref.[81]. The separatrix in a log-log plot corresponds to the phase transition, and its slope is equal to the critical exponent (see Fig.5.2). Since open boundaries favor dimerization, they correspond to non-zero boundary magnetic field in the Ising model. From boundary conformal field theory (CFT), the magnetization at the critical point is expected to decay away from the boundary as [19] $\langle\sigma(x)\rangle \propto 1/x^{1/8}$. Moreover, for a finite system $\langle\sigma(x)\rangle \propto 1/[(N/\pi)\sin(\pi x/N)]^{1/8}$. Identifying the local dimerization with $\sigma(x)$, one gets $D(j,N) \propto 1/[N\sin(\pi j/N)]^{1/8}$ and in particular $D(N/2,N) \propto 1/N^{1/8}$. The critical exponent obtained numerically $d \approx 0.129$ is in good agreement with the Ising prediction.

In a complete analogy with $J_1 - J_2 - J_3$ model we identify open boundary conditions in our model with $\uparrow,\uparrow$ boundary conditions in the Ising model for N even and with $\uparrow,\downarrow$ boundary conditions for N odd, where the arrows refer to the directions of boundary magnetic fields in the Ising model. Then according to conformal field theory (CFT), the ground state energy in an open Ising chain scales with the system size N as $E = \varepsilon_0 N + \varepsilon_1 - \pi v/(48N)$ for N even and $E = \varepsilon_0 N + \varepsilon_1 + \pi v/(23N)$ for N odd [14]. The scaling of the DMRG data for the ground-state energy are presented in Fig.5.3 (a) and (b).

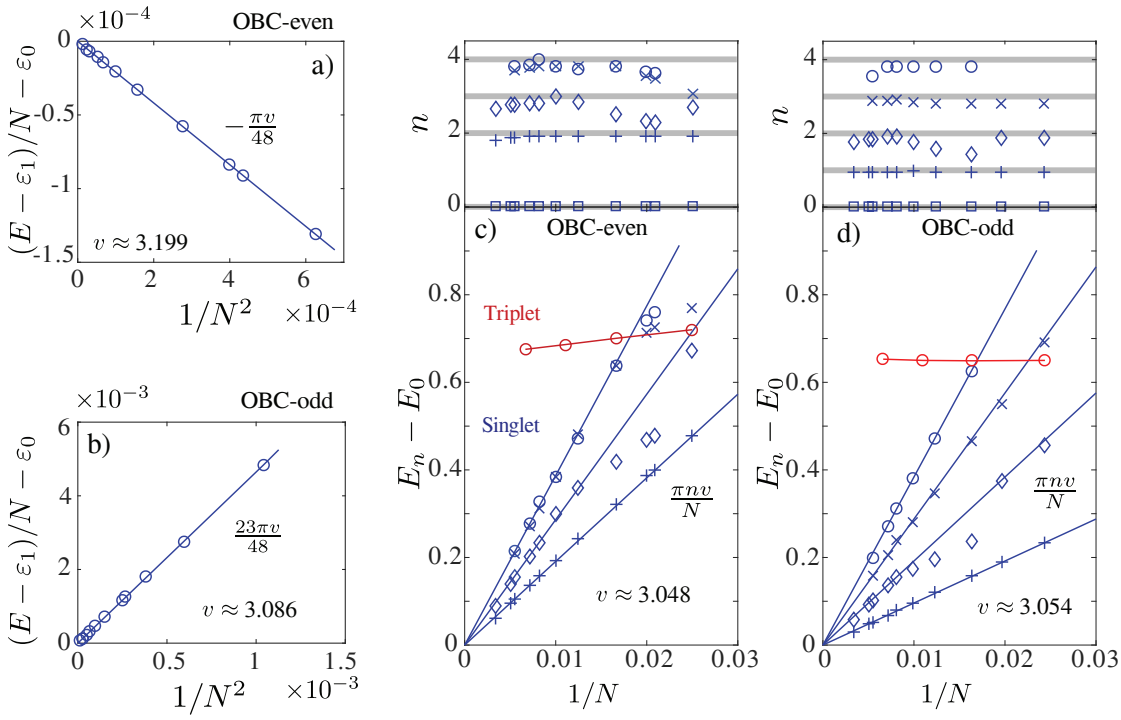

Figure 5.3 – Ground-state and excitation energy at $J_2 = 1$ and $J_b = -0.223$, a point that belongs to the Ising critical line. (a) and (b) Linear scaling of the ground-state energy per site in an open chain with $1/N^2$ after subtracting the ε_0 and ε_1 terms for even and odd number of sites. (c) and (d) Energy gaps in the singlet and triplet sectors for OBC as a function of $1/N$ for even and odd number of sites. The slope of the singlet gap gives access to the value of the velocity. Insets: Conformal towers. Grey lines show Ising conformal towers for I (N even) and for ϵ (N odd). Blue symbols correspond to DMRG data.

We have calculated the lowest four excited state energies for both parities of N in the singlet sector as well as the triplet gap; see Fig.5.3(c) and (d). The excitation energies in the singlet sector reveal the expected Ising conformal tower of the identity primary field I for N even and of the energy primary field ϵ for N odd with scaling dimensions 0 and 1/2 respectively [21]. This definitely establishes that the transition is continuous and in the Ising universality class.

By contrast, the singlet-triplet gap remains finite. In Ref. [81], the authors came to the same conclusion regarding the singlet-triplet gap. However, they did not investigate the singlet sector. So they came to the conclusion that there is no gap closing at the transition, and accordingly that the transition must be first order.

5.4 Transition between Haldane and dimerized phases

As mentioned above, the transition between the Haldane phase and the dimerized phase starts at the TB point, where it is continuous in the WZW $SU(2)_2$ universality class, and terminates at the tri-critical point, where the transition becomes first order. The $SU(2)_2$ phase transition is

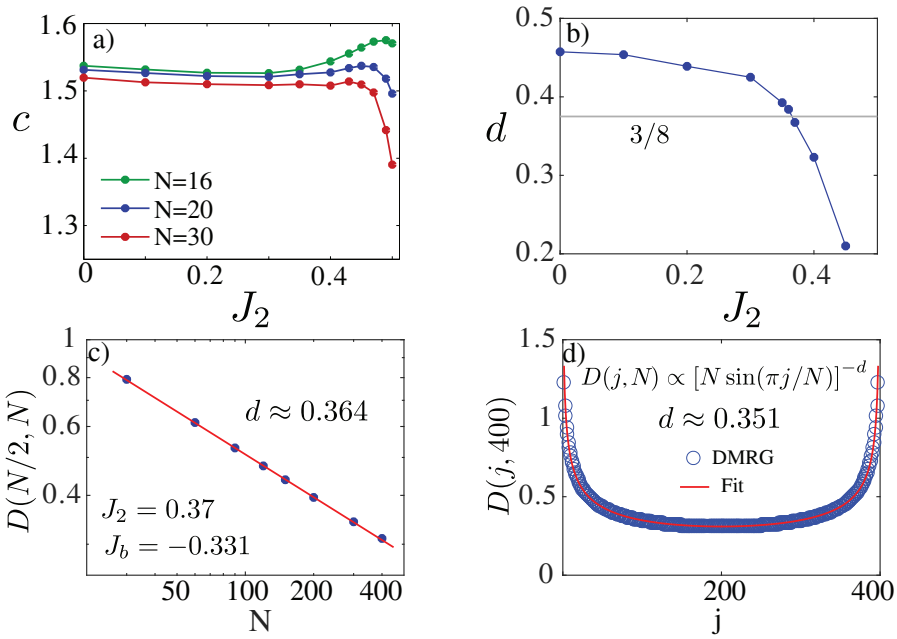

Figure 5.4 – (a) Central charge along the critical line as determined from fitting the entanglement entropy of periodic chains with the Calabrese-Cardy formula[17]. (b) Apparent critical exponent along the SU(2)$_2$ critical line as a function of J_2 from the slope of the log-log plot $D(N/2,N)$ as a function of N for the values J_b for which it is linear. The grey line is the theoretical value of the exponent, 3/8. (c) Log-log plot of the mid-chain dimerization as a function of the number of sites N at the critical point $J_2 = 0.37$ and $J_b = -0.331$. The slope corresponds to the critical exponent $d = 0.364$, in good agreement with 3/8 for WZW SU(2)$_2$. (d) Site dependence of $D(j,N)$ at the critical point fitted to $1/\left[N\sin(\pi j/N)\right]^d$. This leads to an exponent $d = 0.351$, again close to WZW SU(2)$_2$ prediction 3/8.

characterized by a central charge $c = 3/2$ and by the critical exponent $d = 3/8$ of the operator tr g, the $j = 1/2$ primary operator in the SU(2)$_2$ WZW model that describes dimerization:

$$\vec{S}_i \cdot \vec{S}_{i+1} \propto (-1)^i \mathrm{tr}\, g + \text{uniform part.}$$

In Ref.[81], the main argument in favor of the WZW SU(2)$_4$ universality class at the end point was based on the central charge. It was extracted from the scaling of the entanglement entropy $S_N(n)$ with block size n in open chains of size N according to the Calabrese-Cardy formula[17]:

$$S(n) = \frac{c}{6} \ln\left[\frac{2N}{\pi}\sin\left(\frac{\pi n}{n}\right)\right] + s_1 + \ln g. \tag{5.2}$$

Using an open chain with $N = 90$ sites, the authors of Ref.[81] came to the conclusion that the central charge is around $c = 2$.

Since the finite-size effects for open systems are usually quite strong for the extraction of the

central charge, we have revisited this conclusion using periodic systems. In Fig.5.4 (a), we present results for the central charge extracted from fits of the entanglement entropy to the Calabrese-Cardy formula for *periodic* systems:

$$S(n) = \frac{c}{3} \ln \left[\frac{N}{\pi} \sin\left(\frac{\pi n}{n}\right) \right] + s_1 \tag{5.3}$$

The results for $N = 16$, 20 and 30 sites are shown. The central charge extracted from periodic chains has very small finite-size dependence, and it is clear that it never exceeds significantly the value $c = 3/2$. This implies that the end point is in the WZW $SU(2)_2$ universality class. To recover this result with open boundary conditions, one should presumably use systems much larger than 90 sites.

We now confirm these results by calculating the critical exponent and the conformal towers. The marginal operator changes its sign at the tri-critical point, therefore logarithmic corrections present all along continuous part of the transition vanish at this point. It is thus the only point on the critical where the critical exponents can be accurately extracted from finite sizes. We again look for the separatrix in the scaling of the mid-chain dimerization in order to locate the critical line, as described in the previous section. The slope gives an apparent critical exponent, presented in Fig.5.4(c). The point at which the slope is the closest to the predicted value 3/8 (Fig.5.4a) is identified with the end point. The critical exponent obtained at the end point from a scaling analysis of the dimerization $D(j, N)$ with the spin position j for a fixed chain length N is also in good agreement with the prediction $d = 3/8$; see Fig.5.4b). The position of the end point deduced from this analysis is $J_2 = 0.37 \pm 0.01$, $J_b = -0.331 \pm 0.001$, well separated from the triple point.

In Ref.[81] it was suggested that these two points coincide. While the estimate of the triple point $0.47 < J_2 < 0.55$ and $-0.2 < J_b < -0.15$ reported in Ref. [81] is consistent with our results, we think that the two points do not coincide, and that the tri-critical point lies clearly outside this interval.

As it was shown already in the contex of $J_1 - J_2 - J_3$ model the ground-state energies for even and odd number of sites are expected to scale according to:

$$E_{\text{even}} = \varepsilon_0 N + \varepsilon_1 - \frac{\pi v}{16N}, \tag{5.4}$$

$$E_{\text{odd}} = \varepsilon_0 N + \varepsilon_1 + \frac{7\pi v}{16N}. \tag{5.5}$$

In order to build the conformal tower at the end point $J_2 = 0.37$ and $J_b = -0.331$, we calculate the gap between the ground-state energy and the lowest energies in different sectors of S^z_{tot}. The gap scales linearly with $1/N$, and the slope gives access to the velocity. In a chain with an even number of sites, the ground state is a singlet and the first excited states is a triplet, while in a chain with an odd number of sites, the ground state is in the triplet sector. The DMRG

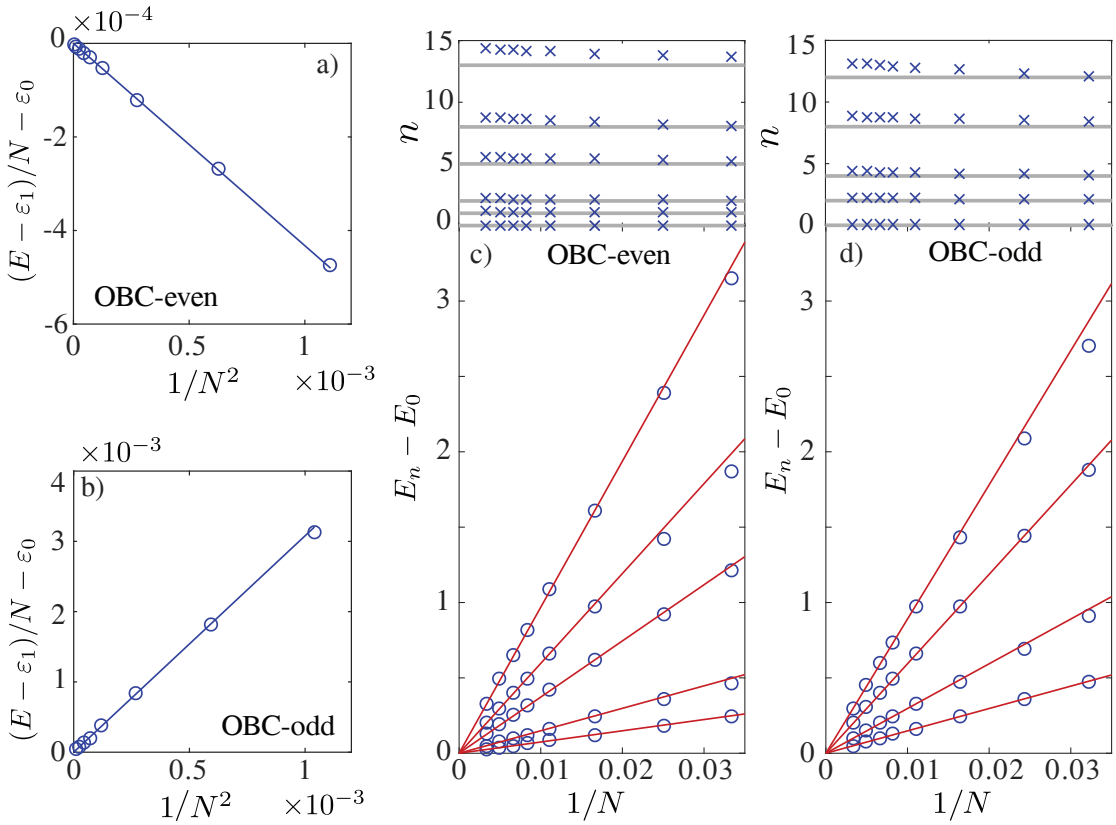

Figure 5.5 – Ground-state and excitation energy at $J_2 = 0.37$ and $J_b = -0.331$, a point that belongs to the critical line between the Haldane and the Dimerized phases. a) and b) Linear scaling of the ground-state energy per site in an open chain with $1/N^2$ after subtracting the ε_0 and ε_1 terms for even and odd number of sites. c) and d) Energy gap between the ground state and the lowest energy states in different sectors of $S_z^{\text{tot}} = 0, 1, ..., 5$ as a function of $1/N$ for even and odd number of sites. Insets: Conformal towers. Blue symbols correspond to DMRG data. Red lines are the expected conformal towers [24], with a velocity defined by the finite-size scaling of the ground state energy for N even.

data on the scaling are presented in Fig.5.5.

In order to prove that the point $J_2 = 0.37$ and $J_b = -0.331$ is indeed the end point, we checked that the logarithmic corrections destroy the conformal towers away from this point [24]. In order to do so, we have calculated the velocities by performing a linear fit of the gap for the first three levels in each tower. The conformal towers are reconstructed only when all velocities take the same values. Otherwise the structure is perturbed. Fig.5.6 provides examples of velocities extracted along the critical line for different sizes. The crossing points around $J_2 = 0.37$ are compatible with our determination of the tri-critical point. Note, that discrepancy of the velocities develops slowly for smaller J_2, that corresponds to logarithmic corrections to WZW $SU(2)_2$ critical theory along continuous transition. In contrast, the towers are destroyed much faster on the side of first order pase transition.

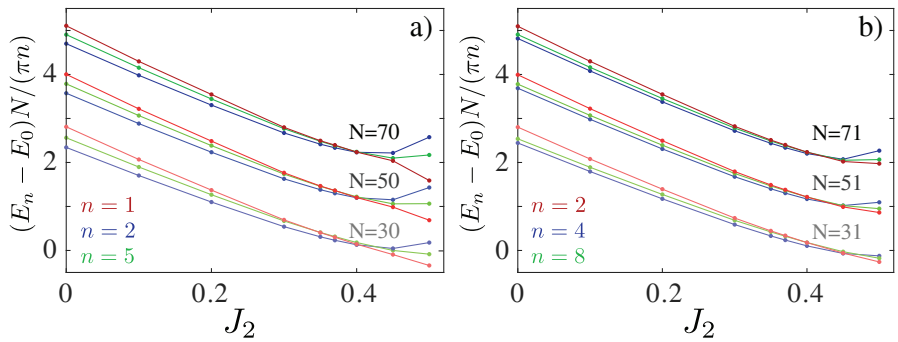

Figure 5.6 – Velocity along the critical line between the Haldane phase and the dimerized phase extracted from the gap between various energy levels and the ground state. For clarity, results for $N = 50$, 51 and $N = 30$, 31 are shifted vertically by 1 and 2 respectively.

5.5 Conclusion

Extensive DMRG calculations coupled to CFT arguments have revealed significant differences with the original phase diagram of Ref.[81] regarding the nature of the phase transitions: *i)* In accordance to the original paper [81] we have found that the singlet-triplet gap does not close at the phase transition between the NNN-Haldane and dimerized phases. However, the excitation spectrum obtained with DMRG calculations within the singlet sector shows critical finite-size scaling. The structure of the excitation spectra, the finite-size scaling of the ground-state energy and the extracted critical exponents imply that the transition between the NNN-Haldane and dimerized phases is continuous and in the Ising universality class, something that had been overlooked in the original study, where this transition was identified as first order. *ii)* The tri-critical point at which the continuous WZW $SU(2)_2$ transition turns into a first order one occurs below the triple point and thus, there exists an interval of first order transition between the Haldane and dimerized phases. *iii)* A detailed analysis of the central charge, critical exponent and excitation spectra allows us to conclude that the tri-critical point is in the same WZW $SU(2)_2$ universality class as the critical line that ends at this point and not in the $SU(2)_4$ universality class proposed in the original study [81].

The similarities of the phase diagrams for biquadratic and three-site interactions suggest that their main features are generic properties of spontaneous dimerization transitions of spin-1 chains. Finally, since the end point of the WZW $SU(2)_2$ critical line and the triple point do not coincide but are separated by a first-order transition line between the Haldane and the dimerized phases, as in the model of Ref.[24], we anticipate that the conclusions of Ref.[81] regarding the end points of the disorder lines will also be modified, and that they might end at the first-order transition line and not at the triple point or at the WZW $SU(2)_2$ critical line. This goes beyond the scope of this Chapter however and is left for future investigation.

6 The spin-3/2 chain with next-nearest-neighbor and three-site interactions

6.1 Introduction

In this chapter we continue the discussion of properties of the $J_1 - J_2$ model with an additional three-site interaction, now for a spin chain with $S = 3/2$. We recall the form of the Hamiltonian for $J_1 - J_2 - J_3$ model:

$$H_{J_1-J_2-J_3} = J_1 \sum_i \mathbf{S}_i \cdot \mathbf{S}_{i+1} + J_2 \sum_i \mathbf{S}_{i-1} \cdot \mathbf{S}_{i+1} + J_3 \sum_i [(\mathbf{S}_{i-1} \cdot \mathbf{S}_i)(\mathbf{S}_i \cdot \mathbf{S}_{i+1}) + \mathrm{H}.c.] , \tag{6.1}$$

and, as before, we set $J_1 = 1$ throughout this chapter and restrict ourselves to the case $J_2, J_3 \geq 0$.

Let us first review the main results previously obtained for two limiting cases of the $J_1 - J_2 - J_3$ spin-3/2 chain. For $J_3 = 0$, it has been shown by Roth and Schollwöck [88] that the model has a transition into a dimerized phase at a critical value $0.29 < J_2/J_1 < 0.33$. The transition is in the Kosterlitz-Thouless universality class [60]. Moreover, spin-1/2 edge states disappear when the ratio of the coupling exceeds $J_2/J_1 \approx 0.48$[88].

In the $J_1 - J_3$ model, the transition to a spontaneously dimerized phase occurs at $J_3/J_1 = 0.063$[70]. The phase transition is continuous and belongs to the $\mathrm{SU}(2)_{k=3}$ WZW universality class [6]. As we will show later, the dimerized phase induced by three-site interaction corresponds to the *fully* dimerized phase, while in the $J_1 - J_2$ model the Kosterlitz-Thouless transition separates critical phase occurs from *partially* dimerized one.

The fully dimerized state is an exact eigenstate[71, 70, 102] along the line $J_3 = 1/13(1 - 2J_2)$ as can be immediately obtained from Eq.4.5 by setting the value of the spin to $S = 3/2$. For $J_2 = 0$, this fully dimerized eigenstate is also a ground-state at $J_3 = 1/13$. The aim of the present chapter is to study the full phase diagram of $J_1 - J_2 - J_3$ model.

6.2 Phase diagram

Let us first summarize our main numerical results. They are presented in the phase diagram of Fig.6.1. For a moment, we concentrate on small values of next-nearest neighbor coupling $J_2 \leq 0.5$ (higher values of next-nearest neighbor couplings will be briefly discussed in the end of the chapter). The phase diagram contains three phases: a non-dimerized critical phase, and two different dimerized phases: a partially dimerized phase and a fully dimerized one. Each phase can be schematically illustrated using a valence bond singlet (VBS) representation as shown in sketches of Fig. 6.1. Fully dimerized phase corresponds to three valence-bonds on every other J_1 bond; while the partially dimerized one corresponds to alternating one and two valence bonds. The critical phase might be schematically illustrated as one valence bond per J_1 bonds and on top of that one valence bond that resonates between two neighboring bonds that is shown schematically with dashed line.

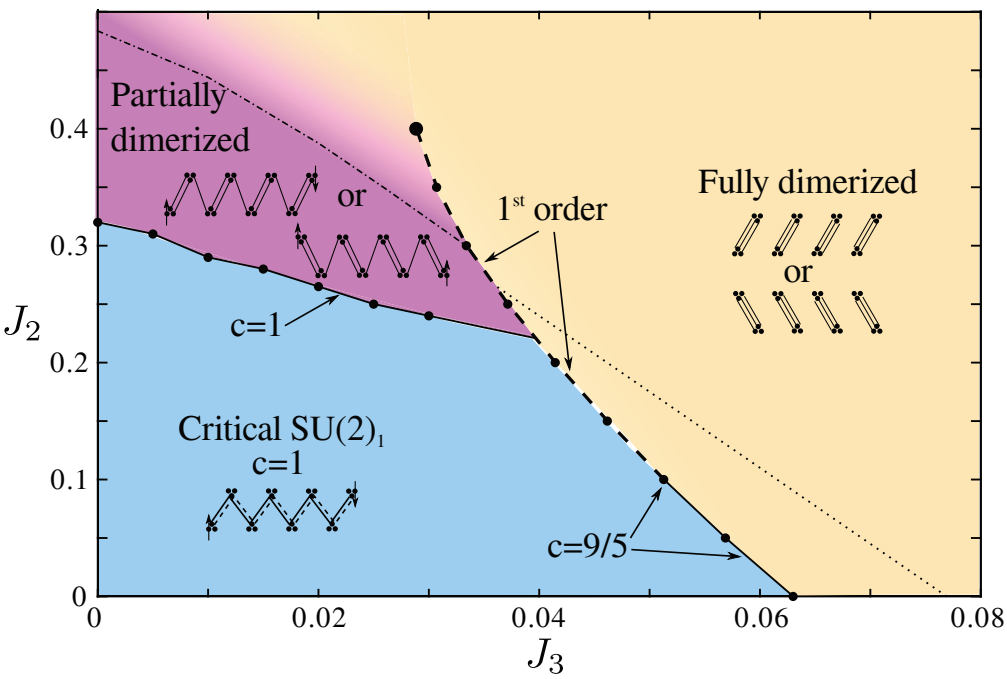

Figure 6.1 – Phase diagram of the $J_1 - J_2 - J_3$ spin $S = 3/2$ chain. It contains three phases: critical, fully dimerized and partially dimerized. The critical phase is in the WZW $SU(2)_1$ universality class. The transition between the critical phase and the partially dimerized phase is in the Kosterlitz-Thouless universality class and corresponds to WZW $SU(2)_1$. The transition between the critical and dimerized phases is continuous in the WZW $SU(2)_3$ universality class along the solid line and first order along the dashed line. The transition between the partially dimerized and dimerized phases is first order for $J_2 < 0.4$. Beyond this point, the two dimerized phases are connected via a crossover through an intermediate 'ladder' state. The fully dimerized state is an exact ground-state along the dotted line. The spin-1/2 edge states disappear at dot-dashed line

The transition between the critical and partially dimerized phases is in the Kosterlitz-Thouless[60]

universality class, in agreement with previous study of $J_1 - J_2$ model[88]. Both the critical phase and the Kosterlitz-Thouless transition line are described by WZW SU(2)$_{k=1}$ critical theory. However, in complete analogy with the critical $J_1 - J_2$ spin-1/2 chain, logarithmic corrections are present and significant inside the critical phase but vanish at the Kosterlitz-Thouless critical line. The numerical confirmation will be provided in Section 6.4. This happens because the marginal coupling constant becomes zero at the transition.

The transition between the critical and fully dimerized phases is continuous in the WZW SU(2)$_{k=3}$ universality below and at the end point and first order beyond it. The end point is located around $J_2 \approx 0.1$ and $J_3 \approx 0.05128$. As discussed in the context of spin-1 chain (see section 4.4), the switch from continuous to first order transition is induced by the change of sign of a marginal operator. The logarithmic corrections that are non-zero all along the continuous transition vanish at the end point, where the marginal coupling vanishes. Interestingly, the value of the next-nearest neighbor coupling J_2 at which the end point occur changes only slightly between between spin-1 ($J_2 = 0.12$) and spin-3/2 $J_2 \approx 0.1$ cases.

The first order transition line continues towards small J_3 and separates the fully dimerized from the partially dimerized phases below the end point located at $J_3 \approx 0.4$. Beyond this point, the two dimerized phases are connected by a crossover.

In order to distinguish non-dimerized and dimerized phases we use dimerization $D(j,N) = |\langle \vec{S}_j \cdot \vec{S}_{j+1}\rangle - \langle \vec{S}_{j-1} \cdot \vec{S}_j\rangle|$ as an order parameter to probe numerically the phase diagram. Fig.6.2 shows examples of the middle chain dimerization $D(N/2,N)$ as a function of J_3 for three different values of J_2. The dimerization changes continuously for $J_2 = 0$ (Fig.6.2 (a)), in agreement with a continuous WZW SU(2)$_3$ transition. A finite jump in dimerization as in Fig.6.2(b) for $J_2 = 0.2$ implies a first order phase transition. Both transitions occur from non-dimerized to fully dimerized phases.

For $J_2 = 0.3$, the dimerization grows continuously from zero to approximately one that corresponds the transition from critical to partially dimerized phase. The Kosterlitz-Thouless transition between the two occurs around $J_3 \approx 0.008$. Under further increase of the J_3 coupling, the dimerization jumps abruptly to approximately $D(N/2,N) \approx 4$ indicating a first order phase transition to a fully dimerized phase. Note also that if one keeps track of the sign of the dimerization $D_s(j,N) = \langle \vec{S}_j \cdot \vec{S}_{j+1}\rangle - \langle \vec{S}_{j-1} \cdot \vec{S}_j\rangle$, there is a small region before the first order transition where the sign of the dimerization changes. It corresponds to the disappearance of edge states and to the reorientation of dimers in the partially dimerized phase as sketched in Fig.6.3. The line along which the edge states disappear is marked with a dot-dashed line in the phase diagram of Fig,6.1.

6.3 The end point of the WZW SU(2)$_3$ critical line

In order to determine the precise location of the critical line between the non-dimerized critical phase and the fully dimerized phase, we follow the same logic as for the spin-1 chain.

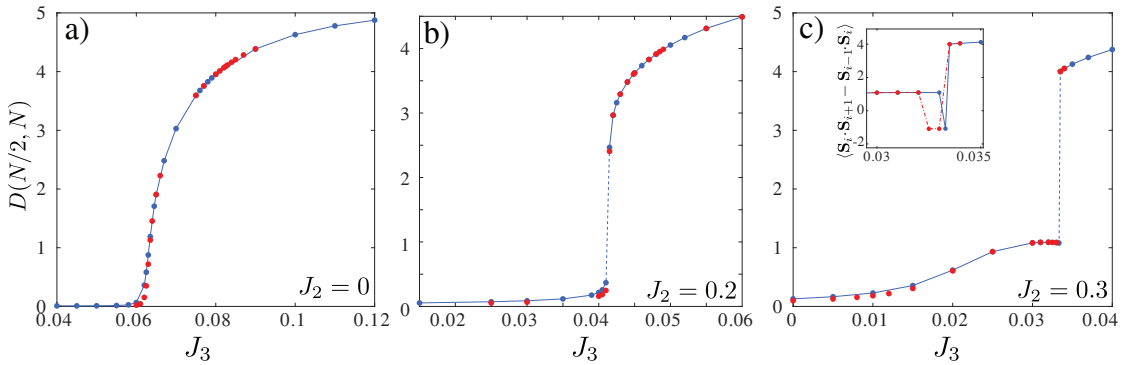

Figure 6.2 – Middle chain dimerization for $N = 90$ (blue) and $N = 150$ (red) across different transitions. (a) Continuous growth of dimerization across the WZW SU(2)$_3$ critical line. (b) Finite jump in dimerization across the first order phase transition from the critical phase to the fully dimerized phase. (c) Continuous change of the dimerization from the non-dimerized critical phase to the partially dimerized phase across Kosterlitz-Thouless transition (the critical line goes through $J_2 = 0.3$, $J_3 \approx 0.008$) and finite-jump of dimerization across the first order transition from the partially to the fully dimerized phase around $J_3 \approx 0.033$. Inset: Sign preserved dimerization across first order transition. The negative value of dimerization indicates a change of the dimer orientation induced by open boundary (see Fig.6.3)

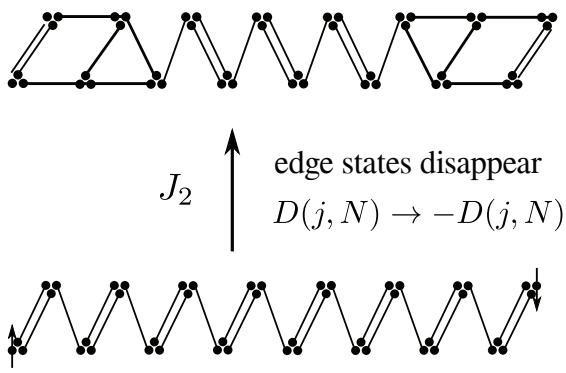

Figure 6.3 – Disappearance of the edge states inside the partially dimerized phase and resulting reorientation of the dimers (sketches).

The critical line is associated with the straight line in the log-log plot of the dimerization $D(N/2,N)$ as a function of chain length N (see Fig.6.4(a)). CFT for WZW SU(2)$_{k=3}$ predicts the scaling dimension of the dimerization operator to be $d = 3/[2(2+k)] = 3/10$. The slope of the separatrix gives an 'apparent' critical exponent, different from $d = 3/10$ due to logarithmic corrections. At the end point, the logarithmic corrections vanish, since coupling constant of the marginal operator vanishes, so this is the only point along the line where the critical exponents can be accurately extracted from finite sizes. By by keeping track of the apparent critical exponent along the critical line, we find that it crosses the line $d = 3/10$ at $J_2 \approx 0.10$ and $J_3 \approx 0.05128$.

As discussed in Chapter 4, open boundaries in the spin-1 $J_1 - J_2 - J_3$ chain favor dimerization.

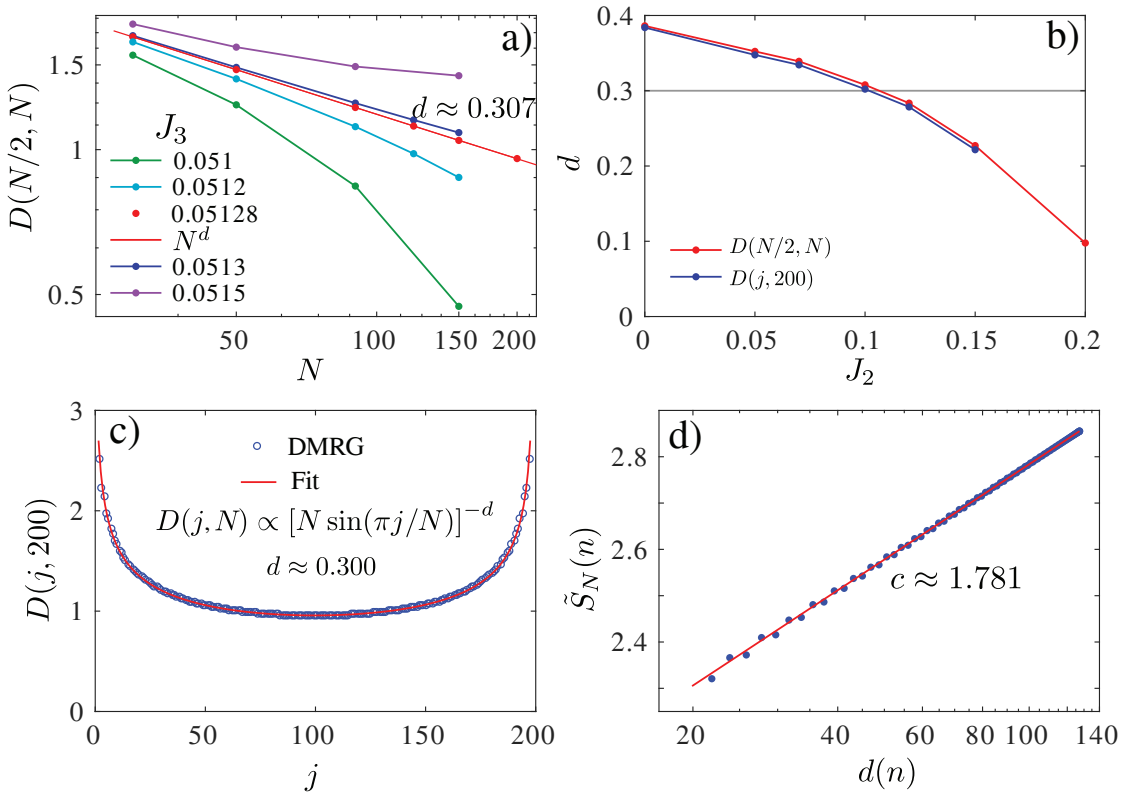

Figure 6.4 – (a) Log-log plot of the middle-chain dimerization $D(N/2,N)$ as a function of the number of sites N for $J_2 = 0.1$ and different parameters J_3 around critical value. The linear curve corresponds to the critical point and the slope gives the critical exponent $d \approx 0.307$ in good agreement with CFT prediction 3/10 for WZW SU(2)$_{k=3}$ critical theory. (b) Apparent critical exponent along the $SU(2)_3$ critical line as a function of J_2. Red circles: from the slope of the log-log plot $D(N/2,N)$ as a function of N for the value of J_3 for which it is linear. Blue circles: from fitting $D(j,200)$. Black line is the theoretical value of the exponent, 3/10. Thus the end point is located at $J_2 = 0.1$ and $J_3 = 0.05128$. (c) Scaling of the dimerization parameter $D(j,N)$ along the chain with $N = 200$ sites at the $SU(2)_3$ critical end point fitted to Eq.6.2. The extracted exponent is in excellent agreement with $d = 3/10$. (d) Entanglement entropy at the end point for $N = 200$ after removing the Friedel oscillations with weight $\zeta \approx -1.3$. The central charge obtained from the fit to Calabrese-Cardy formula[17] $c \approx 1.781$ agrees within 2% with 9/5 predicted by CFT

This remains true for larger values of the spin and the dimerization scales along the chain according to:

$$D(j,N) \propto 1/[(N/\pi)\sin(\pi x/N)]^d \tag{6.2}$$

with $d = 3/10$ for WZW SU(2)$_{k=3}$. An example of the scaling of the dimerization along a finite chain is shown in Fig.6.4(c). The critical exponents extracted along the transition line are summarized in Fig.6.4(b) and are in a perfect agreement with those extracted from the finite-size scaling of the middle-chain dimerization $D(N/2,N)$.

Numerically, we compute the central charge from the entanglement entropy in an open chain:

$$\tilde{S}_N(n) = \frac{c}{6}\ln d(n) + \zeta\langle \mathbf{S}_n\mathbf{S}_{n+1}\rangle + s_1 + \ln g, \tag{6.3}$$

where $d = \frac{2N}{\pi}\sin\left(\frac{\pi n}{N}\right)$ is the conformal distance and ζ is a non-universal constant introduced in order to suppress Friedel oscillations (see Sec. 4.5.3 for more details). An example of fit of the reduced entanglement entropy $\tilde{S}_N(n)$ with Eq.6.3 is provided in Fig.6.4(d). The obtained values of the central charge along the continuous part of the transition always agree within 3% with the CFT prediction $c = 9/5$ for the critical WZW $\mathrm{SU}(2)_3$ theory.

For any conformally invariant boundary condition, the ground state scales with the system size as

$$E = \varepsilon_0 N + \varepsilon_1 + \frac{\pi v}{N}\left(-\frac{c}{24} + x\right), \tag{6.4}$$

where ε_0 and ε_1 are non-universal constants, c is the central charge and x is the scaling dimension of the corresponding primary field. For the $SU(2)_{k=3}$ WZW model there are 4 conformal towers labeled by the spin of the lowest energy states, $j = 0$, $1/2$, 1 and $3/2$. The scaling dimension of the corresponding operator is given by $x = j(j+1)/(2+k)$. As we have seen in the context of the spin-1 case, chains with an even number of sites have a singlet ground-state and are thus described by the conformal tower $j = 0$ with scaling dimension $x = 0$. By contrast, the ground state of a chain with an odd number of sites belongs to the conformal tower with the largest $j = 3/2$ with scaling dimension $x = 3/4$. Thus the ground state energies of an open chain with even or odd numbers of sites scale as:

$$E_{\text{even}} = \varepsilon_0 N + \varepsilon_1 - \frac{3\pi v}{40N}, \tag{6.5}$$

$$E_{\text{odd}} = \varepsilon_0 N + \varepsilon_1 + \frac{27\pi v}{40N}. \tag{6.6}$$

Examples of finite-size scaling of the ground-state energy for even and odd numbers of sites are shown in Fig.6.5(a) and (b).

We have extracted several excited states by calculating the lowest states within different symmetry sectors of total magnetization $0 \le S^z_{\text{tot}} < 6$. In order to construct WZW $\mathrm{SU}(2)_{k=3}$ conformal towers we have followed Ref.[3]. Since we are interested only in the lowest state for different values of the total spin s, the energy level that corresponds to this state can be found with a rather simple formula:

$$n = \left\lceil \frac{j^2 - S^2}{k} \right\rceil, \tag{6.7}$$

where $\lceil x \rceil$ is a ceiling function that returns an integer n in the range $x \le n < x+1$. The results

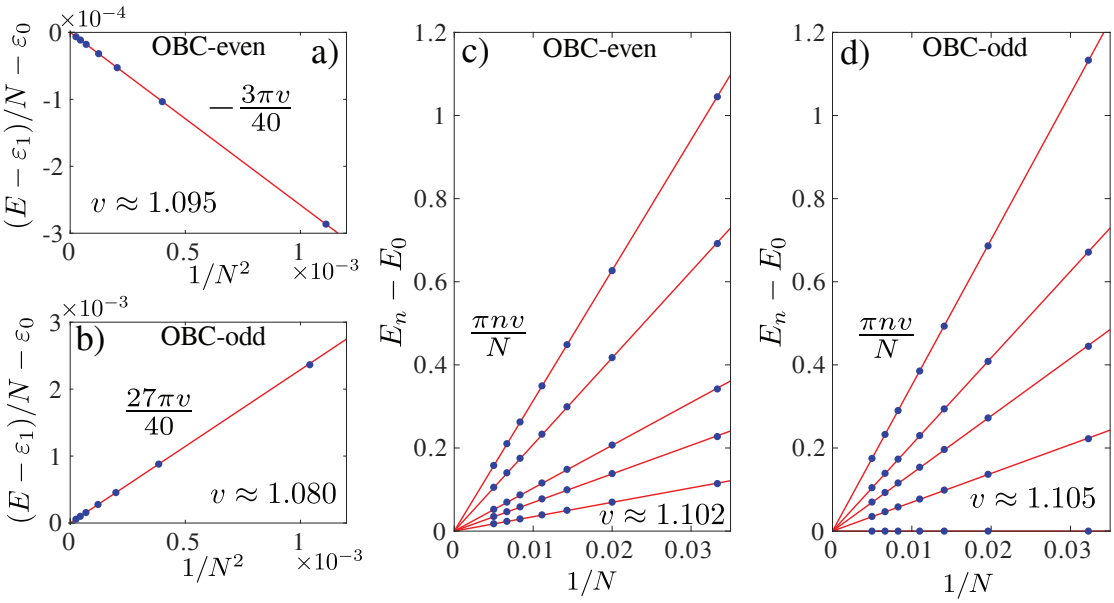

Figure 6.5 – Ground state and excitation energy at $J_2 = 0.1$ and $J_3 = 0.05128$, on the critical line between the critical and the fully dimerized phases. (a) and (b): Linear scaling of the ground state energy per site with $1/N^2$ after subtracting ε_0 and ε_1 in open chains with (a) even and (b) odd numbers of sites N. (c) and (d): Energy gap between the ground state and the lowest energies in different sectors of $S_z^{\text{tot}} = 1, ..., 5$ for even and $S_z^{\text{tot}} = 5/2, ..., 11/2$ for odd (blue circles) as a function of $1/N$ for even and odd numbers of sites. Red lines are CFT predictions for $j = 0$ and $j = 3/2$ towers with the velocities extracted from first lowest excitation level and indicated in each panel.

for $j = 0$ and $j = 3/2$ WZW SU(2)$_3$ conformal towers are summarized in Table 6.1. For the $j = 3/2$ tower, the ground-state is in the sector with $S_{\text{tot}} = 3/2$, and it appears as the lowest state in the two sectors of total magnetization $S_{\text{tot}}^z = 1/2$ and $3/2$.

j=0

s	0	1	2	3	4	5
$(E-E_0)N/\pi v$	0	1	2	3	6	9

j=3/2

s	1/2	3/2	5/2	7/2	9/2	11/2
$(E-E_0)N/\pi v$,	2	0	2	4	6	10

Table 6.1 – Lowest excitation energy with spin s for both $j = 0$ and $j = 3/2$ WZW SU(2)$_3$ conformal towers.

The conformal towers obtained numerically for both even and odd numbers of sites are shown in Fig.6.5(c) and (d) and summarized in Table 6.2.

Finally, in order to prove that the pair of parameters $J_2 = 0.1$ and $J_3 = 0.05128$ indeed corresponds to the end point, we will show that the conformal tower is destroyed by moving along the critical line away from the end point. Following the procedure established in the context of

Energy level	CFT SU(2)$_3$	DMRG $J_2 = 0.1, J_3 = 0.05128$
OBC, Even, ground state $S_z^{\text{tot}} = 0$	-3/40	-3/40
OBC, Even, ground state $S_z^{\text{tot}} = 1$	1	1.0065
OBC, Even, ground state $S_z^{\text{tot}} = 2$	2	2.0003
OBC, Even, ground state $S_z^{\text{tot}} = 3$	3	2.9999
OBC, Even, ground state $S_z^{\text{tot}} = 4$	6	6.057
OBC, Even, ground state $S_z^{\text{tot}} = 5$	9	9.12
OBC, Odd, ground state $S_z^{\text{tot}} = 3/2$	27/40 =0.675	0.666
OBC, Odd, ground state $S_z^{\text{tot}} = 5/2$	2	2.018
OBC, Odd, ground state $S_z^{\text{tot}} = 7/2$	4	4.028
OBC, Odd, ground state $S_z^{\text{tot}} = 9/2$	6	6.058
OBC, Odd, ground state $S_z^{\text{tot}} = 11/2$	10	10.19

Table 6.2 – Energy levels at the $SU(2)_3$ critical point. Ground state for N even $S_z^{\text{tot}} = 0$ and odd $S_z^{\text{tot}} = 3/2$ refers to the $1/N$ term in the ground state energy. For the rest, the gap above the ground state is given. Results are in units of $\pi v/N$ with $v = 1.095$.

the spin-1 chain, we have plotted the velocities extracted from three different excitation levels n according to $v_n = (E_n - E_0)N/(\pi n)$ (Fig.6.6). At the end point, all velocities are the same, implying that the conformal tower is restored. This occurs around $J_2 = 0.1$, in agreement with the value determined from the critical exponent. Velocities splits but remain relatively close to each along continuous transition due to the logarithmic corrections to the WZW SU(2)$_3$ critical theory. Above the end point, along the first order transition the spitting of $(E_n - E_0)N/(\pi n)$ is much faster.

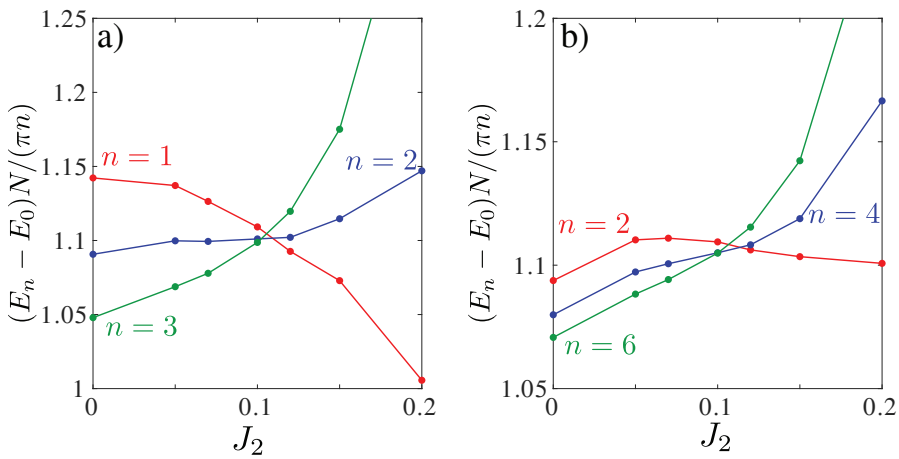

Figure 6.6 – Velocity along the critical line between the critical and the fully dimerized phases extracted from the gap between n'th energy level and the ground state for (a) $N = 50$ and (b) $N = 51$

6.4 Critical phase and Kosterlitz-Thouless transition

The critical phase and the Kosterlitz-Thouless transition are both characterized by the WZW $SU(2)_1$ critical theory. This critical theory has central charge $c = 1$. We have calculated the central charge numerically by fitting the reduced entanglement entropy to Eq.6.3. Examples of fit of finite-size results are provided in Fig.6.7. Due to the logarithmic corrections deep inside critical phase, the central charge extracted from the entanglement entropy in finite-size clusters differs significantly from the expected value $c = 1$, as can be deduced from Fig.6.7(a). By contrast, close to the Kosterlitz-Thouless critical line, the logarithmic corrections are suppressed, and the central charge can be extracted with sufficient accuracy even from relatively small chains Fig.6.7(b).

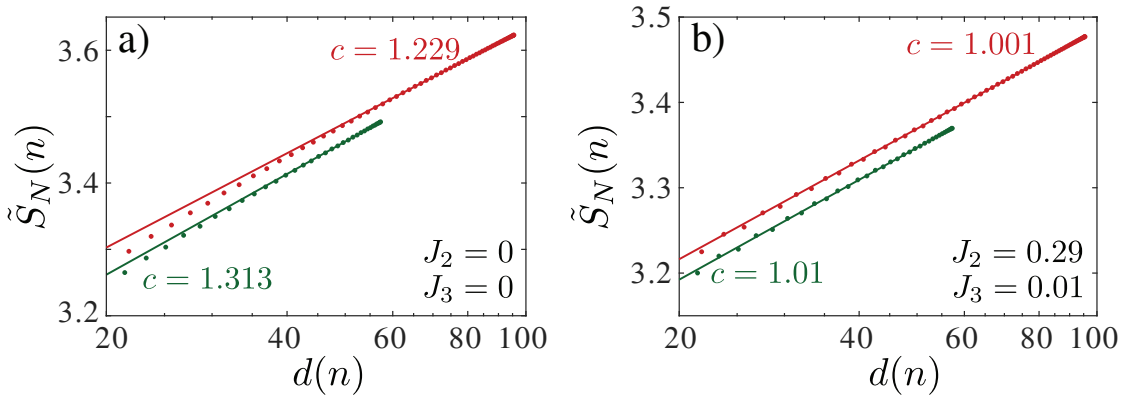

Figure 6.7 – Extraction of the central charge for open chains with $N = 90$ (green) and $N = 150$ (red) by fitting the reduced entanglement entropy $\tilde{S}_N(n)$ with the Calabrese-Cardy formula of Eq.6.3 (a) inside critical phase and (b) at Kosterlitz-Thouless transition

Close to the Kosterlitz-Thouless transition the dimerization decreases almost linearly in log-log scale at both sides of the transition, and the precise location of the critical line by looking for a separatrix becomes challenging (see Fig.6.8(a)). In order to locate the phase boundary, we have extracted the apparent critical exponent in the vicinity of the critical line. Since logarithmic corrections are absent at the Kosterlitz-Thouless transition, the phase boundary can be associated with the J_2 for which the apparent critical exponent is closest to the CFT prediction for WZW $SU(2)_{k=1}$ for the scaling dimension of dimerization operator $d = 3/[2(2+k)] = 1/2$. Moreover, one can extract the central charge, that differs slightly from $c = 1$ inside critical phase close to the transition, but rapidly decreases in the gapped partially dimerized phase, as shown in Fig.6.8. The phase boundaries extracted in these two ways agree with each other within errorbars.

In order to check that along the Kosterlitz-Thouless critical line the logarithmic corrections are absent and the underlying critical theory can be extracted from finite-size systems, we have calculated the velocities for some levels of the excitation spectrum for even and odd numbers of sites. For the $SU(2)_{k=1}$ WZW model, there are only two conformal towers labeled by total spin: $j = 0$ and $1/2$. The levels corresponding to the lowest states with different magnetization

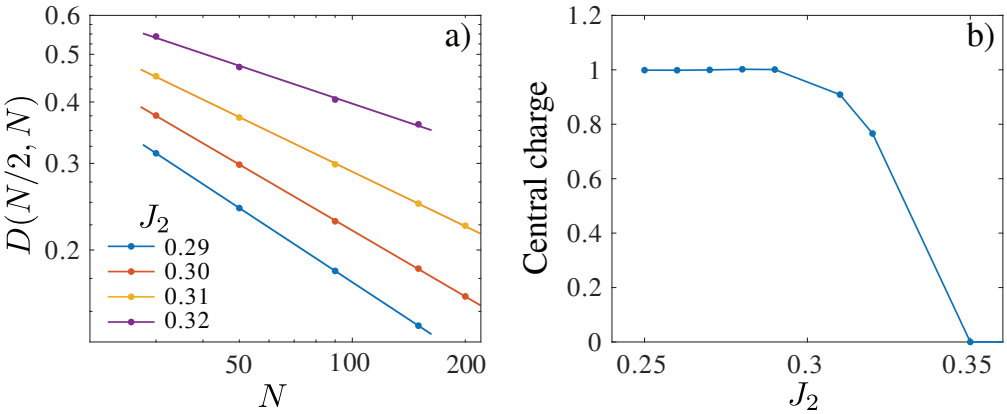

Figure 6.8 – (a) Middle-chain dimerization $D(N/2, N)$ as a function of the system size N for $J_3 = 0.01$. The dimerization scales linearly even above the transition that occur at $0.29 \geq J_2 \geq 0.30$. (b) Central charge is equal to $c = 1$ inside critical phase close to the transition and decreases towards zero in the gapped partially dimerized phase. Results for open chain with $N = 150$ sites and $J_2 = 0.1$ are shown. The transition is around $J_2 \approx 0.30$.

sectors can be extracted from Eq.6.7. They are summarized in Table 6.3. Due to presence of the low-lying edge states close to the Kosterlitz-Thouless transition, the listed states can be found as ground states in symmetry sector $S^z_{\text{tot}} = s + 1$. The obtained numerical results for $J_3 = 0.01$ are summarized in Fig.6.9. The crossing point where all velocities are the same and therefore the conformal towers are restored is around $J_2 \approx 0.31$ and slowly moves towards smaller values with increasing the size of the chain. Therefore these results are consistent with our previous estimate of the critical point $J_2 \approx 0.3$ for $J_3 = 0.01$.

j=0

s	0	1	2	3	4	5
$(E - E_0)N/\pi v$	0	1	4	9	16	25

j=1/2

s	1/2	3/2	5/2	7/2	9/2	11/2
$(E - E_0)N/\pi v,$	0	2	6	12	20	30

Table 6.3 – Lowest excitation energy with spin s for both $j = 0$ and $j = 1/2$ WZW $SU(2)_1$ conformal towers.

6.5 Transition between dimerized phases

A phase transition between the partially and fully dimerized phases occurs for $0.22 \leq J_2 \leq 0.4$ and is of first order. This transition can be seen as a pronounced kink in the energy per site ϵ_{mid} calculated in the middle of the chain (see Eq.4.10 for definition). A small hysteretic behavior appears due to open boundary conditions that favor dimerization (see Fig.6.10) and decreases with increasing the system size. Apart from that, the finite-size effects are very small, and the location of the critical point can be extracted accurately from relatively small clusters.

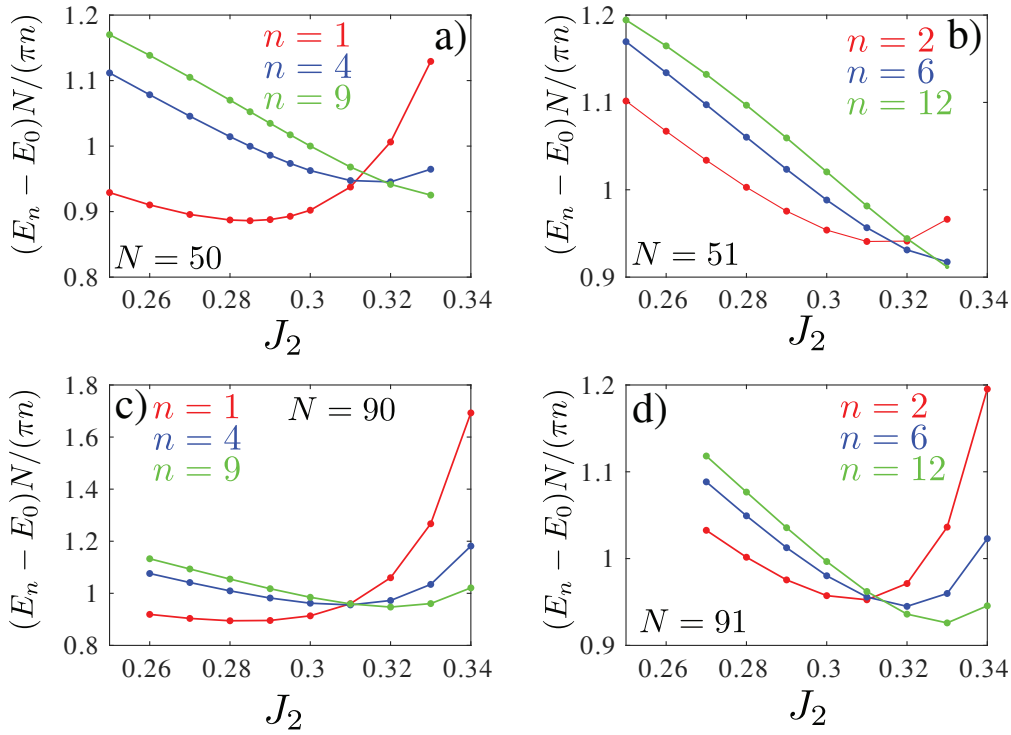

Figure 6.9 – Velocities across the Kosterlitz-Thouless transition between critical and partially dimerized phases extracted from the gap between various energy levels and the ground state as a function of J_2 for fixed value of $J_3 = 0.01$ and different system sizes

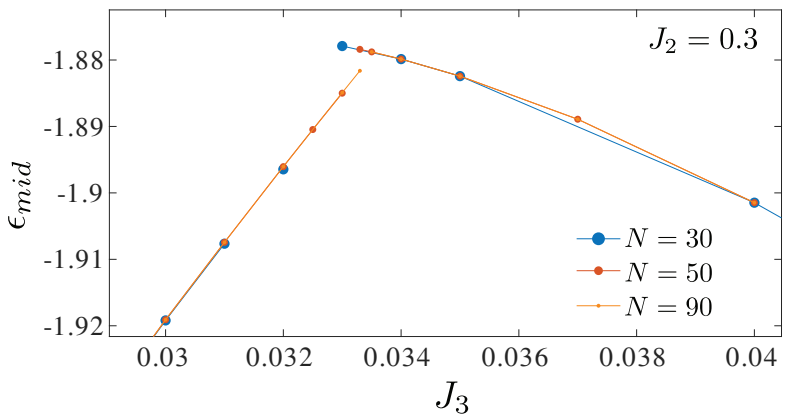

Figure 6.10 – Kink in the energy across the first order phase transition between partially and fully dimerized phases. Small hysteretic behavior is induced by open boundaries. Finite-size effects are negligibly small.

In order to understand what happens at large J_2, we start by looking at the entanglement spectrum. An example of the entanglement spectrum as a function of J_2 is shown in Fig.6.11. In the dimerized phase, the lowest level in the entanglement spectrum is four-fold degenerate when the system is cut across the J_1 bond that contains a dimer and non-degenerate otherwise. In the critical phase, the degeneracy of the entanglement spectrum is the same as in the

fully dimerized one. Perhaps, this is due to finite-size effects. In the partially dimerized phase the lowest level in the entanglement spectrum is three-fold (respectively two-fold) degenerate, when the chain is cut across the J_1 bond that contains two (respectively one) VBS singlets. Apart from these three phases, there are two regions with different degeneracy of the entanglement spectrum. The degeneracy $(3,2)$ of the partially dimerized phase changes to the degeneracy $(2,3)$. This change occurs approximately at the line at which the edge states disappears. Interestingly, the degeneracy remains the same until large values of $J_2 \approx 1.15$, where it changes to $(2,1)$. The latter is consistent with the VBS representation where every J_2 bond and every other J_1 bond contain one VBS singlet. In the following, we will refer to this state as the 'ladder state'. The results on the entanglement spectrum are summarized in Fig.6.12.

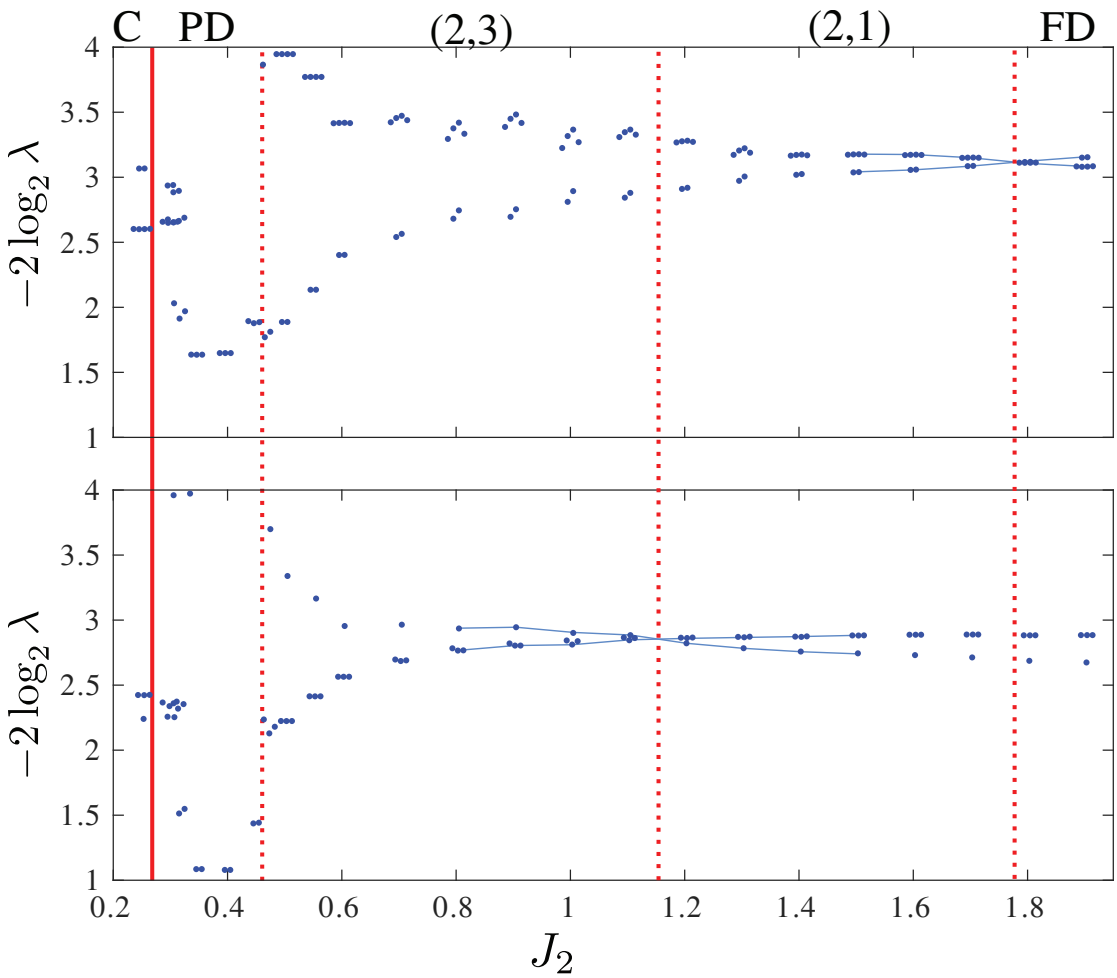

Figure 6.11 – Entanglement spectrum as a function of J_2 for $N = 150$, $J_3 = 0.005$ when the system is cut across odd (a) and even (b) bonds. Short-hand notation are used for the three phases: C for critical, PD for partially dimerized, FD for fully dimerized. In addition to these phases, there are two regions with different degeneracy of the entanglement spectrum: 2(3) and 2(1) when the system is cut across an odd (even) bond.

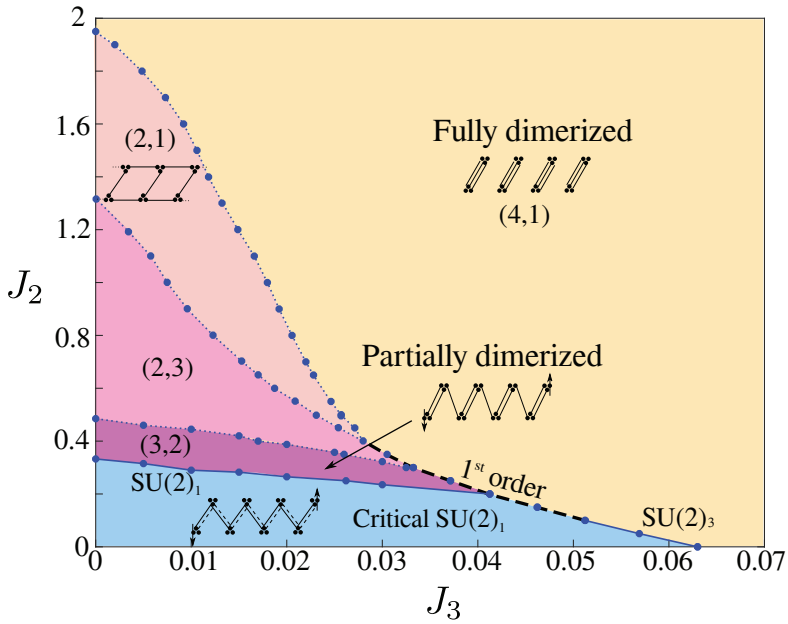

Figure 6.12 – Phase diagram of the $J_1 - J_2 - J_3$ model with $S = 3/2$ chain obtained from entanglement spectrum. In addition to critical, partially and fully dimerized phases, there are two regions with different degeneracy of the entanglement spectrum. The degeneracy of the lowest level of the entanglement spectra is indicated with the pair of integers (m, n), where m (n) is the degeneracy obtained when system is cut across an odd (even) bond.

In order to understand these two topologically different phases observed with the entanglement spectrum, we have looked at the spin-spin correlation $\langle \mathbf{S}_j \cdot \mathbf{S}_{j+1} \rangle$ as a function of J_2 for j even and odd. The results for $J_3 = 0.015$ and $N = 150$ are shown in Fig.6.13. The two curves are

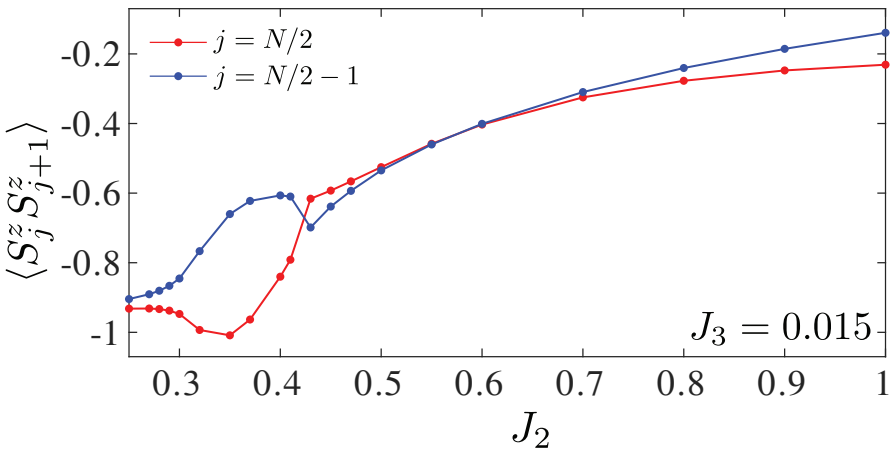

Figure 6.13 – Spin-spin correlation $\langle S_j^z S_{j+1}^z \rangle$ in the critical and dimerized phases. $\langle S_j^z S_{j+1}^z \rangle$ is significantly different for even and odd bonds for $0.28 < J_2 < 0.42$, (partially dimerized phase). For $J_2 < 0.28$, the dimerization vanishes, indicating a critical non-dimerized phase. For $J_2 \approx 0.57$ the two curves cross due to open boundary conditions. In the thermodynamic limit, the system belongs to the dimerized phase for all $J_2 > 0.28$.

close to each other for $J_2 < 0.28$, and then becomes significantly different. This corresponds to the partially dimerized phase. Around $J_2 \approx 0.42$, the two curves cross. Then, the two curves approach each other, cross and go away. This leads to a dimerized phase. Although the two curves are very close to each other for $0.45 < J_2 < 0.7$ and therefore the dimerization in this region is very small, we think that the crossing between the spin-spin correlation on even and odd bonds is induced by open boundaries. Thus it should be considered as a finite-size effect. Moreover, smooth evolution of spin-spin correlation suggests a crossover between the partially and fully dimerized phases rather than a quantum phase transition.

As sketched in Fig.6.14, with periodic boundary conditions, each dimerized phase has a two-fold degenerate ground-state, while with open boundary conditions the ground state is non-degenerate. In the oversimplified picture, the ground state of the open system can be understood as one of the two degenerate states. In reality, however, the picture is mode complicated due to the extremely strong edge effects. In particular, the topological transition (see Fig.6.14), at which the spin-1/2 edge states disappear and the dimers change their orientation, is induced by open boundary conditions.

The two intermediate phases observed with entanglement spectrum can be understood as regions of the dimerized phase within one topological sector that can be distinguished from each other with a local topological order parameter. A change of the local topological order parameter (here the degeneracy of the entanglement spectrum) does not necessary indicate a quantum phase transition, but rather a crossover between different regions of the dimerized phase. A similar observation has been made in the context of spin-S ladders [26], where a change of the topological order parameter - the Berry phase on the rungs - indicates only a crossover, and not a quantum phase transition.

6.6 Summary

In the present chapter, we have investigated the properties of a spin-3/2 chain with nearest J_1, next-nearest J_2 and three-site J_3 interactions. We have found a rich phase diagram, that contains three phases - critical in WZW $\mathrm{SU}(2)_{k=1}$, partially and fully dimerized. The transition between the critical phase and the fully dimerized one is continuous in the WZW $\mathrm{SU}(2)_{k=3}$ universality class below and including at the end point, and the first order beyond it. The change from continuous to first order transition along the critical line is due to change of sign of the coupling constant of the marginal operator, that vanishes at the end point $J_2 \approx 0.1$ and $J_3 \approx 0.05128$. In this respect, the result for spin-3/2 is very similar to those obtained in the context of the spin-1 chain for $J_1 - J_2 - J_3$ and $J_1 - J_2 - J_b$ models and therefore can be expected to be a generic result for the transition between uniform and fully dimerized phase in spin-S chains with $S = 1, 3/2$.

The critical and partially dimerized phases are separated by a Kosterlitz-Thouless transition, that is in WZW $\mathrm{SU}(2)_{k=1}$ universality class. At the phase transition, the coupling constant of the marginal operator changes sign, and the logarithmic corrections disappear along the

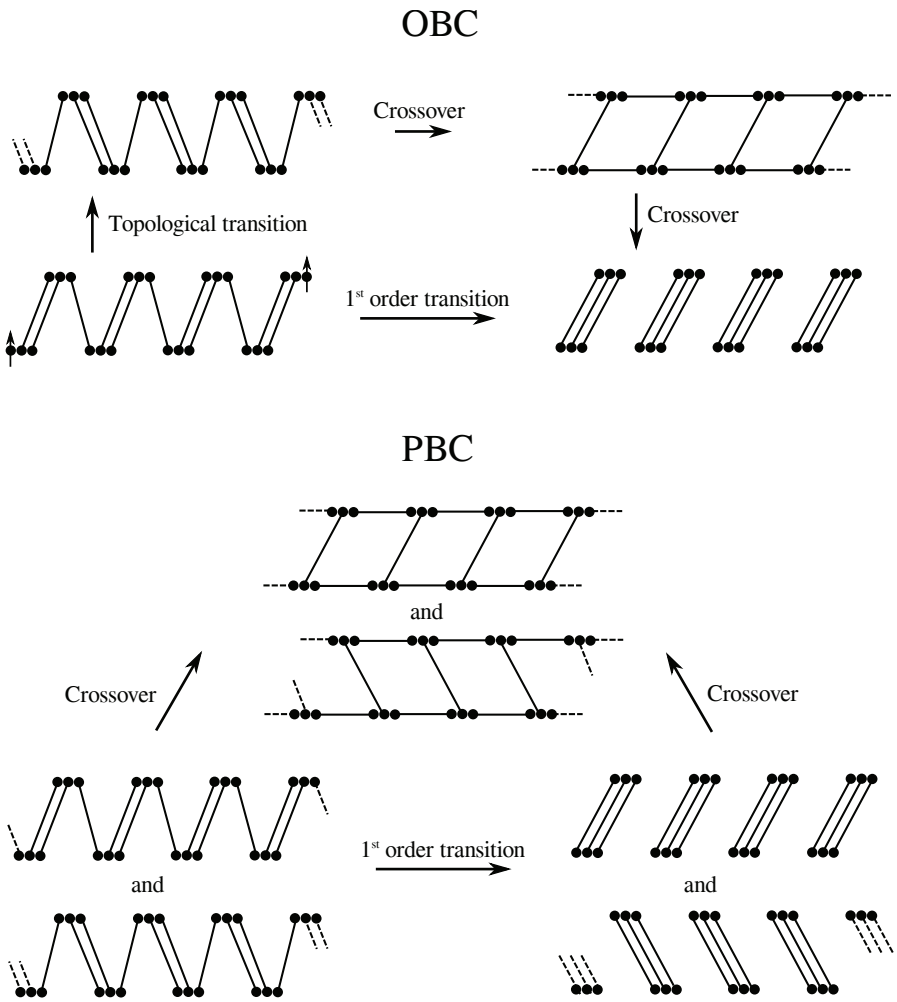

Figure 6.14 – The transition between partially and fully dimerized states is first order for $J_2 < 0.4$. For larger values of J_2 these two phases are connected through a cross overs via intermediate topologically different state that has ladder geometry. The ground-state of the system with periodic boundary conditions (PBS) is two-fold degenerate in each sector of the dimerized phase. System with open boundary conditions (OBC) has non-degenerate ground state. As a consequence, there is an intermediate topological phase transition induced by edge effects, between two partially dimerized states in different topological sectors.

Kosterlitz-Thouless transition. By extracting the velocities for different excitation levels, one can not only confirm the disappearance of the logarithmic corrections and the restoration of the excitation spectra, but also locate rather accurately the position of the critical lines using the properties (absence of logarithmic corrections) of the Kosterlitz-Thouless transition.

The transition between the partially dimerized and the fully dimerized phases is always first order and ends around $J_2 \approx 0.4$. Beyond this point, the two dimerized phases are smoothly connected by a crossover via a state that can be represented with valence-bond-singlets as a ladder.

In the thermodynamic limit, we expect that the gap and the dimerization decrease (but always remain finite) with J_2 in analogy with the $J_1 - J_2$ spin-1/2 chain[104], and possibly increases again due to the three-site interaction. This is consistent with our preliminary numerical results but requires further numerical investigation.

7 Spin-1 chain with three-site interaction

7.1 Introduction

In this chapter we continue our study of the spin-1 chain with three-site interaction. The $J_1 - J_3$ model is defined by the Hamiltonian:

$$H_{J_1-J_3} = J_1 \sum_i \mathbf{S}_i \cdot \mathbf{S}_{i+1} + J_3 \sum_i [(\mathbf{S}_{i-1} \cdot \mathbf{S}_i)(\mathbf{S}_i \cdot \mathbf{S}_{i+1}) + \text{H.c.}] , \tag{7.1}$$

where the coupling constants J_1 and J_3 can be positive or negative. The following parametrization is introduced for convenience: $J_1 = J\cos\theta$ and $J_3 = J\sin\theta$ with $\theta \in [0, 2\pi]$ and without loss of generality we set $J = 1$.

The segment of the phase diagram with positive couplings J_1 and J_3 has been first studied in Ref.[71] and discussed at length in Chapter 4. Here we repeat the most important points previously established for this part of the phase diagram:

- For small values of the parameter θ the system is in the Haldane phase. Upon increasing θ, the three-site interaction induces spontaneous dimerization [71].
- The transition between the two phases is located at $J_3/J_1 \simeq 0.111$ ($\theta \approx 0.0352\pi$) [71]. The critical point is in the WZW $SU(2)_2$ universality class.
- There is an exactly dimerized point at $J_3/J_1 = 1/6$ ($\theta \approx 0.0526\pi$) [71]. This point coincides with the first disorder point, where spin-spin correlations become incommensurate [24].
- The Lifshitz point, beyond which the structure factor has two symmetric peaks at wave number $q \neq \pi/2, \pi$, is located at $J_3/J_1 \simeq 0.1855$ ($\theta \approx 0.0584\pi$). It coincides with the second disorder point, at which spin-spin correlations become commensurate with $q = \pi/2$.

While the physics for $\theta \in [0, \pi/2]$ is well understood, the rest of the phase diagram remains unexplored. In the rest of the chapter we will study the complete phase diagram of the spin-1 chain described by $J_1 - J_3$ model. In particular, we will show that positive three-site interactions added to ferromagnetic nearest-neighbor Hamiltonian leads to a rich phase diagram with an unusual critical quadrupolar phase.

7.2 Phase diagram

Let us first summarize the main results obtained numerically with DMRG simulations. The phase diagram as a function of θ is shown in Fig.7.1 and consists of five phases: Haldane, dimerized, next-nearest-neighbor (NNN) Haldane, critical quadrupolar and ferromagnetic (FM).

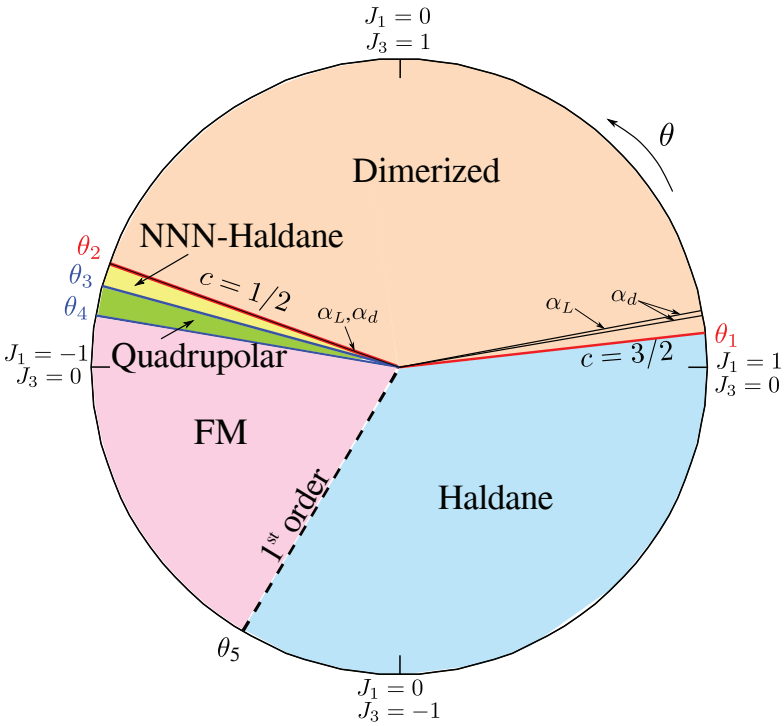

Figure 7.1 – Phase diagram of spin-1 chain with nearest-neighbor and three-site interactions. The transition between the Haldane and the dimerized phases at $\theta_1 \approx 0.03519\pi$ is in the WZW $SU(2)_2$ universality class. The transition between the dimerized and NNN-Haldane phases is continuous in the Ising universality class and located at $\theta_2 \approx 0.8913\pi$. Between $\theta_3 \approx 0.915\pi$ and $\theta_4 \approx 0.947\pi$, the system is in a critical quadrupolar phase. The transition between the ferromagnetic (FM) and Haldane phases is at $\theta_5 \approx 1.33\pi$ and is first order.

The transition between the Haldane and dimerized phases is continuous, and in WZW $SU(2)_2$ universality class[71]. It is characterized by central charge $c = 3/2$. Inside the dimerized phase, there is a transition between the two possible ground states with open boundary conditions: for $\theta < 0.55\pi$ a strong dimer is formed on the first bond, while for $\theta \geq 0.55\pi$ a strong dimer is

formed on the second bond. So, in finite chain with open boundary conditions the orientation of the dimers changes at this point. As a consequence, the spin-1 edge states appear for $\theta \geq 0.55\pi$. The transition between the dimerized and NNN-Haldane phase is in the Ising universality class with central charge $c = 1/2$, in agreement with our previous results on the spin-1 $J_1 - J_2 - J_3$ model. The NNN-Haldane phase is separated from the FM phase by an intermediate critical phase with dominant quadrupolar correlations. The underlying critical theory is under construction. The transition between the ferromagnetic and Haldane phases is first order.

7.3 Energy

The ground-state energy per bond calculated in the middle of the chain is shown in Fig.7.2. The ferromagnetic phase can be well described by the classical state with all spins aligned. The classical energy per site of this state is given by $\epsilon_{FM} = J_1 + 2J_3 = \cos\theta + 2\sin\theta$. A pronounced kink around $\theta = 1.33\pi$ signals a first order phase transition between the ferromagnetic phase and the Haldane phase as indicated in the phase diagram of Fig.7.1.

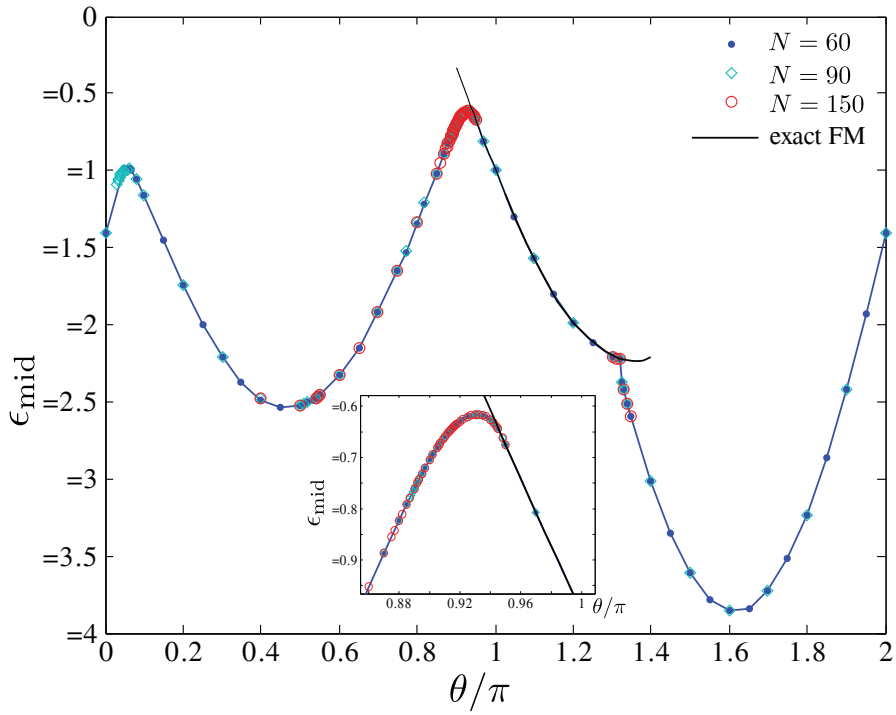

Figure 7.2 – Ground-state energy per bond calculated in the middle of the finite-size chain as a function of θ. In the ferromagnetic phase, the DMRG data coincide exactly with the analytic prediction $\epsilon_{FM} = \cos\theta + 2\sin\theta$.

We have also calculated the first derivative of the energy per site with respect to θ. The results are shown in Fig.7.3. In such a plot, a first order phase transition is clearly seen as a finite jump in the derivative. The kink in the derivative of the energy around $\theta = 0.95\pi$ suggests a second

order phase transition to the ferromagnetic phase. For the other values of θ, both the energy and its derivatives remain continuous, implying that, apart from the transition at $\theta = 1.33\pi$, all phase transitions that appear in the phase diagram are continuous.

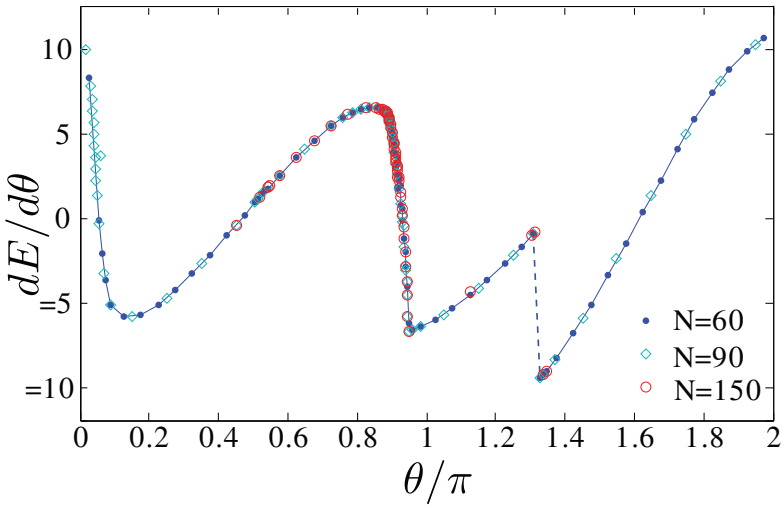

Figure 7.3 – Derivative of the ground-state energy per bond with respect to θ. The finite jump of the derivative around $\theta = 1.33\pi$ corresponds to the first order phase transition between the Haldane and the ferromagnetic phases. A pronounced kink around $\theta = 0.95\pi$ implies a second order phase transition from the other side of the ferromagnetic phase.

7.4 Variational phase diagram

The first step in the understanding the phase diagram in Fig.7.1 is to construct a variational phase diagram using the mean-field approach. In this approach, the entanglement between the selected unit cell and the rest of the system is set to zero. Then the wave-functions of the whole system $|\Psi\rangle$ can be written as a product of the local wave-functions $|\Psi\rangle = \otimes|\psi\rangle_j$. The local wave-functions $|\psi\rangle_j$ depend on the set of the parameters determined by minimizing the energy $\langle\Psi|h|\Psi\rangle$.

Let us first try to describe with the variational approach the four gapped phases of the phase diagram 7.1 - Haldane, dimerized, NNN-Haldane and ferromagnetic.

i) For $\theta = 0$ ($J_1 = 1$, $J_3 = 0$), the system is known to be in the ordered antiferromagnetic phase with anti-align neighboring spins. The local wave-function is given by $|1\bar{1}\rangle$, the energy is equal to:

$$E_{|1\bar{1}\rangle} = -J_1 + 2J_3 \tag{7.2}$$

ii) For $\theta = \pi$ ($J_1 = -1$, $J_3 = 0$) the system has ferromagnetic order with all spins align. The local

wave-function is then given by $|11\rangle$ and the corresponding variational energy is:

$$E_{|11\rangle} = J_1 + 2J_3 \tag{7.3}$$

iii) As pointed above, a large three-site interaction favors dimerization. In the variational approach, the dimerized phase is described by the wave-function $|11\bar{1}\bar{1}\rangle$ with four spins in the unit cell. The energy of this variational state is given by:

$$E_{|11\rangle} = -2J_3 \tag{7.4}$$

iv) The same variational wave-function $|11\bar{1}\bar{1}\rangle$ describes the NNN-Haldane phase with anti-alignes spins on next-nearest-neighbor bonds. The variational energy of these two phases are the same and they cannot be distinguished within the variational approach.

The most general spin-1 state is described by six complex amplitudes:

$$|\hat{\Omega}\rangle = a_1 e^{i\varphi_1}|1\rangle + a_2 e^{i\varphi_2}|0\rangle + a_3 e^{i\varphi_3}|\bar{1}\rangle \tag{7.5}$$

Two out of these six parameters can be fixed with the normalization constraint and by fixing the overall phase:

$$a_1^2 + a_2^2 + a_3^2 = 1 \tag{7.6}$$

$$\varphi_1 + \varphi_2 + \varphi_3 = 0; \tag{7.7}$$

The remaining four parameters give a big flexibility. However, the complexity grows very fast with the number of spins in the unit cell n, since the energy has to be minimized with respect to 4^n parameter. The usual way to proceed it to restrict further the number of parameters. Purely quadrupolar states are usually described in the following basis, invariant under the time-reversal symmetry:

$$|x\rangle = i\frac{|1\rangle - |\bar{1}\rangle}{\sqrt{2}} \tag{7.8}$$

$$|y\rangle = \frac{|1\rangle + |\bar{1}\rangle}{\sqrt{2}} \tag{7.9}$$

$$|z\rangle = -i|0\rangle \tag{7.10}$$

The action of the spin operators on these states are given by $S^\alpha|\beta\rangle = i\varepsilon_{\alpha\beta\gamma}|\gamma\rangle$, where α, β, γ is one of the coordinates x, y, z and $\varepsilon_{\alpha\beta\gamma}$ is the Levi-Civita symbol. Therefore, any pure quadrupolar states (e.g. ferroquadrupolar $|zz\rangle$, or antiferroquadrupolar $|xyz\rangle$) gives zero

energy.

As briefly mentioned in Chapter 2 the J_3 term can be rewritten in terms of quadrupole operator $Q^{\alpha\beta} = S^\alpha S^\beta + S^\beta S^\alpha - \frac{2}{3}S(S+1)\delta_{\alpha\beta}$ (see Eq.C.2 for the derivation):

$$\sum_i J_3\left[(\mathbf{S}_{i-1}\cdot\mathbf{S}_i)(\mathbf{S}_i\cdot\mathbf{S}_{i+1}) + \mathrm{H.}c.\right] = \sum_i \sum_{\alpha,\beta=x,y,z} J_3 S^\alpha_{i-1} Q^{\alpha\beta}_i S^\beta_{i+1} + \frac{4}{3}\sum_i J_3 \mathbf{S}_{i-1}\cdot\mathbf{S}_{i+1} \tag{7.11}$$

This first term in the right hand side suggests that, instead of a purely quadrupolar state, one has to look at a state with both spin and quadrupole degrees of freedom. Moreover, as we will show later, we are interested in a helical state with wave-vector $q \neq 0, \pi/2, \pi$. All these conditions are fulfilled with the following basis, that contains only two free parameters:

$$|W\rangle = \frac{1}{2}e^{-i\varphi}\left(\cos\frac{\vartheta}{2} - \sin\frac{\vartheta}{2}\right)|1\rangle + \frac{-i}{\sqrt{2}}\left(\cos\frac{\vartheta}{2} + \sin\frac{\vartheta}{2}\right)|0\rangle + \frac{-1}{2}e^{i\varphi}\left(\cos\frac{\vartheta}{2} - \sin\frac{\vartheta}{2}\right)|\bar{1}\rangle \tag{7.12}$$

In this basis, the spin degrees of freedom is confined in the $x-y$ plane and the quadrupole director is perpendicular to it. The parameter φ_i describes the angle of the spin at site i with respect to y axis, while $\cos\vartheta_i$ gives the length of the spin at site i. The energy per site (i) of this state is derived in the Appendix C.1 and is given by:

$$\begin{aligned} E = &\frac{J_1}{2}(\cos\vartheta_{i-1}\cos\vartheta_i\cos(\varphi_{i-1}-\varphi_i) + \cos\vartheta_i\cos\vartheta_{i+1}\cos(\varphi_i-\varphi_{i+1})) \\ &+\frac{1}{2}J_3\cos\vartheta_{i-1}\cos\vartheta_{i+1}\left[\cos(\varphi_{i+1}-\varphi_{i-1})(3+\sin\vartheta_i) + \cos(\varphi_{i-1}+\varphi_{i+1}-2\varphi_i)(1-\sin\vartheta_i)\right] \end{aligned} \tag{7.13}$$

If we restrict the spin length at each site to be the same $\vartheta_i = \vartheta = \text{const}$ and allow the rotation of the spin between any pair of neighboring sites by the same angle $\varphi_{i+1} - \varphi_i = \varphi$, the energy per site simplifies to:

$$E = J_1\cos^2\vartheta\cos\varphi + \frac{1}{2}J_3\cos^2\vartheta\left[\cos 2\varphi(3+\sin\vartheta) + (1-\sin\vartheta)\right] \tag{7.14}$$

This energy can then be minimized numerically. The results obtained for the variational energies of different states are summarized in Fig.7.4(a). The corresponding values of ϑ and φ that minimize the energy of the state $|W\rangle$ are shown in Fig.7.4(b) and (c). Since ϑ takes relatively small values, spin component dominates over the quadrupolar one. The phase with $\pi \leq \varphi < \pi/2$ is identified with anti-ferroquadrupolar phase, while the phase with $\pi/2 < \varphi \leq 0$

corresponds to the ferroquadrupolar one.

We have checked that the energies remain unchanged if ϑ is allowed to alternate between even and odd sites $\vartheta_{2i} = \vartheta_1$ and $\vartheta_{2i+1} = \vartheta_2$ while the angle difference φ remains uniform. The energy is also the same if φ alternates on even and odd bonds while θ remains uniform.

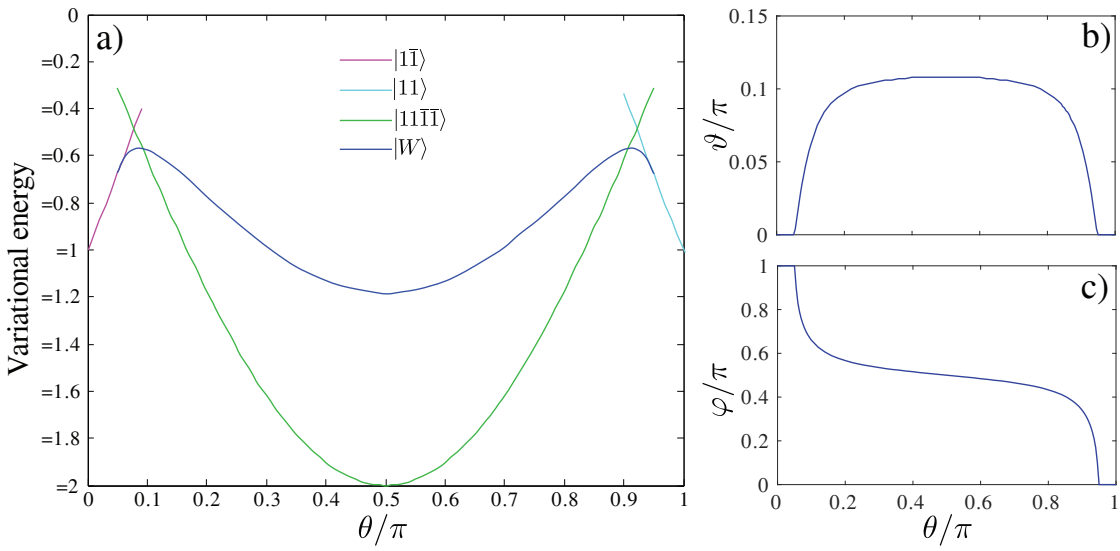

Figure 7.4 – (a) Variational energy as a function of θ for different variational states: antiferromagnetic $|1\bar{1}\rangle$, ferromagnetic $|11\rangle$, dimerized $|11\bar{1}\bar{1}\rangle$ and helical quadrupolar $|W\rangle$, defined by Eq.7.12. Parameters (b) ϑ and (c) φ for which the energy of the $|W\rangle$ state is minimized as a function of θ. The phase with $\pi \leq \varphi < \pi/2$ is identified as an anti-ferroquadrupolar phase, while the phase with $\pi/2 < \varphi \leq 0$ corresponds to a ferroquadrupolar one.

The variational phase diagram obtained with the energies of Fig.7.4 is compared to the phase diagram obtained with the DMRG one in Fig.7.5. In the mean-field phase diagram, a helical quadrupolar state appears between the Haldane and the dimerized phases, however the quantum phase transition to the dimerized phase at smaller θ and quadrupolar phase does not appear for $J_1 > 0$. On the other side of the phase diagram, as expected the variational phase diagram does not distinguish the dimerized and NNN-Haldane phase. The phase boundaries of the helical quadrupolar phase is in good agreement with our DMRG data.

7.5 Ising transition

7.5.1 Dimerization

In order to distinguish the dimerized phase from non-dimerized one, we introduce the dimerization parameter $D(j,N) = |\langle \vec{S}_j \cdot \vec{S}_{j+1} \rangle - \langle \vec{S}_{j-1} \cdot \vec{S}_j \rangle|$. It remains finite in the thermodynamic limit in the dimerized phase and vanishes in the non-dimerized one. Following the logic of the previous chapters we plot the values of the middle chain dimerization as a function of the system size in a log-log scale. The phase transition is then associated with the separatrix.

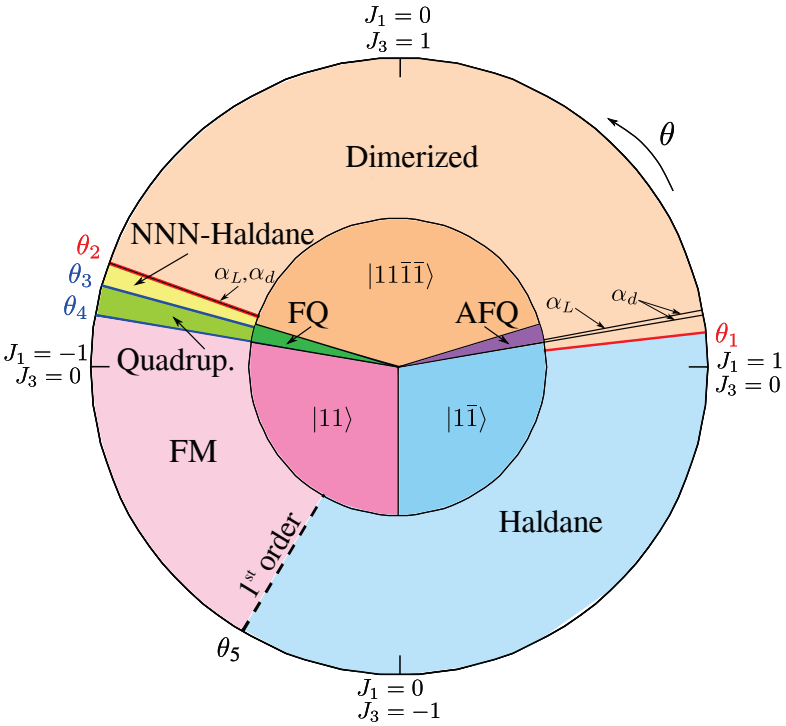

Figure 7.5 – Comparison between the variational phase diagram (inner circle) and the phase diagram obtained with DMRG.

The slope gives the critical exponent. In Fig.7.6(a) we present our numerical results for the dimerization around the transition located at $\theta \approx 0.8913\pi$. The critical exponent extracted from the scaling of the middle chain dimerization is $d \approx 0.141$. It agrees within 15% with the corresponding Ising critical exponent 1/8.

This critical exponent can also be extracted from the scaling of the dimerization along a finite-size chain. According to conformal field theory (see Eq.4.20), at the critical point it scales as $D(j,N) \propto 1/[N\sin(\pi j/N)]^d$. The fit of our numerical data for $N = 300$ and $N = 400$ is shown in Fig.7.6(b). Since edge effects are very strong, we exclude from the fit at least 25 points at each edge. The obtained critical exponent $d \approx 0.140$ agrees with the one computed above.

7.5.2 NNN-Haldane phase

In order to understand the nature of the non-dimerized phase, we computed the entanglement spectrum as a function of θ. The obtained entanglement spectra for a system cut across odd and even bonds are shown in Fig.7.7 (a) and (b) respectively. For $\theta < 0.55\pi$ open boundaries favor dimerization and therefore every odd bonds in the dimerized phase is occupied with the spin-1 dimer. Thus the lowest level in the entanglement spectra is three fold degenerate when the system is cut across an odd bond and non-degenerate otherwise (see for example Fig.4.12(a)). For $\theta > 0.55\pi$, edges favor a bond without dimer and the two branches (even and

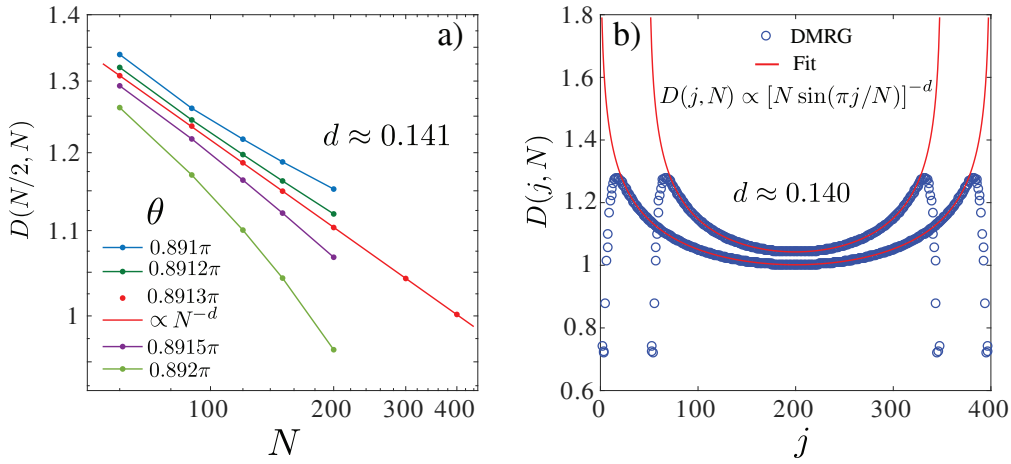

Figure 7.6 – Scaling of the dimerization at the critical Ising point. (a) Log-log plot of the dimerization. The linear curve corresponds to the Ising critical point, and the slope to the critical exponent. This leads to $\theta^c = 0.8913\pi$, and to a slope 0.141, that agrees within 15% with the prediction 1/8 for Ising critical point. (b) Site dependence of $D(j,N)$ at the critical point fitted to $1/[N\sin(\pi j/N)]^d$. This leads to an exponent $d = 0.140$, that also agrees with the Ising prediction 1/8 within 15%.

odd) are exchanged, as shown in Fig.7.7.

In the non-dimerized phase the lowest level in the entanglement spectrum is always three-fold degenerate. Therefore the ground state is translational invariant by one site. We interpret this non-dimerized phase as two next-nearest-neighbor Haldane chains ferromagnetically coupled with J_1 interaction. In the case of antiferromagnetic nearest-neighbor coupling, the entanglement spectrum in the NNN-Haldane phase is non-degenerate, since the two spin-1/2 created at each edge when the system is cut couple with each other and form a singlet. By contrast, the ferromagnetic coupling between two spin-1/2 at the edge induces a triplet, and the degeneracy of the entanglement spectrum is three.

In order to confirm our interpretation of the non-dimerized phase, we interpolate between the considered $J_1 - J_3$ model and a model with ferromagnetic nearest-neighbor $J_1 < 0$ and antiferromagnetic next-nearest-neighbor $J_2 > 0$ interactions, for which the appearance of the NNN-Haldane phase is natural. We consider the following Hamiltonian:

$$H_{J_1J_3\to J_1J_2} = \cos\theta \sum_i [\mathbf{S}_i\cdot\mathbf{S}_{i+1} - \alpha\mathbf{S}_i\cdot\mathbf{S}_{i+2}] + (1-\alpha)\sin\theta \sum_i [(\mathbf{S}_{i-1}\cdot\mathbf{S}_i)(\mathbf{S}_i\cdot\mathbf{S}_{i+1}) + \text{H.c.}], \quad (7.15)$$

where α interpolates between $J_1 - J_3$ and $J_1 - J_2$ model. When $\alpha = 0$, the Hamiltonian 7.15 is reduced to the $J_1 - J_3$ model with our usual parametrization $J_1 = \cos\theta$ and $J_3 = \sin\theta$. Here we take $\theta = 0.9\pi$, inside the NNN-Haldane phase. When $\alpha = 1$, the last term vanishes and the Hamiltonian is reduced to the $J_1 - J_2$ model with $J_1 = -J_2 = \cos\theta$. As it will be shown later

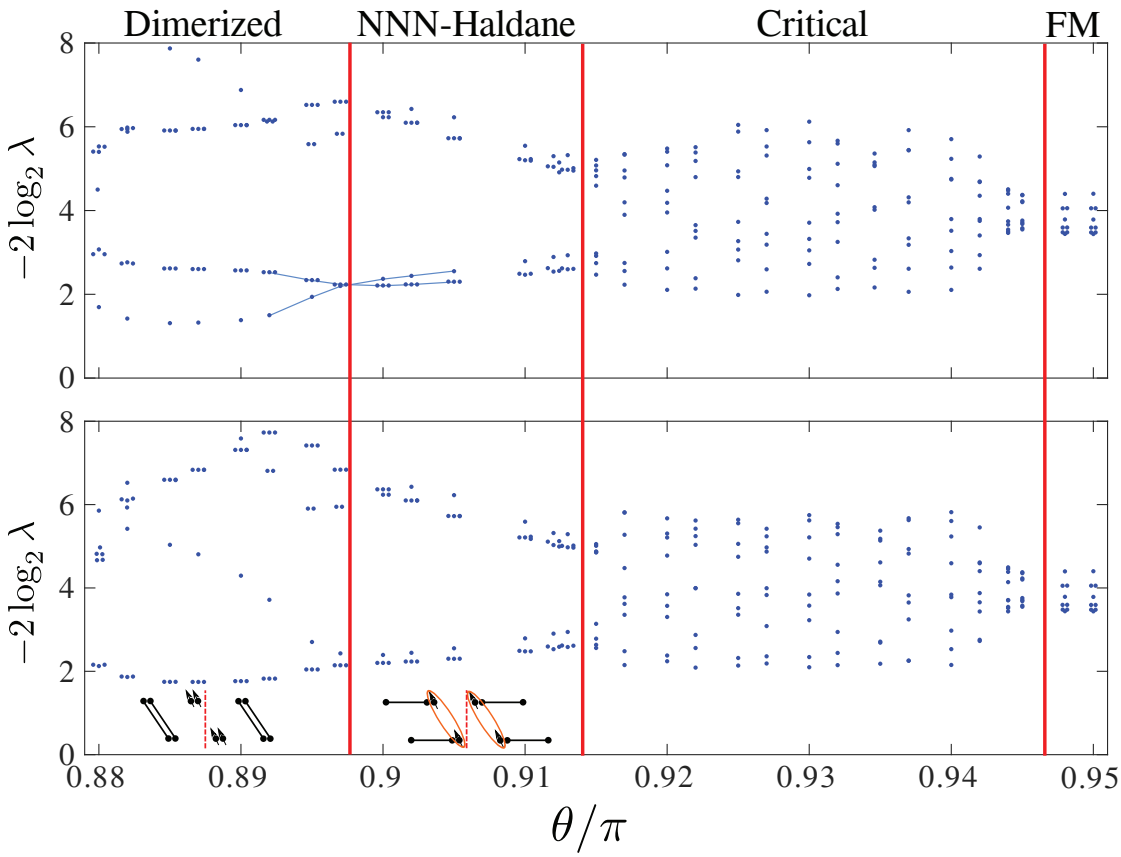

Figure 7.7 – Entanglement spectrum for an open chain with $N = 150$ sites as a function of θ when cut across (a) odd and (b) even bond. Only the lower part of the spectrum is shown. The dots show the multiplicity of the Schmidt values. Insets: VBS sketches of various boundaries created by the cut of the chain inside the dimerized and NNN-Haldane phases. The two spin-1/2 created at each edge in NNN-Haldane phase couple with each other and form a triplet, which is represented as an orange ellipse. This leads to the three-fold degeneracy of the lowest state of the entanglement spectrum. The entanglement spectrum is non-degenerate and rather chaotic when the system is in the critical phase.

this point also belongs to the NNN-Haldane phase (see Fig.7.15). As shown in Fig.7.8, the gap, calculated within the symmetry sector of the ground state, never closes while interpolating between the $J_1 - J_3$ and $J_1 - J_2$ models with the parameters specified above. Therefore, the non-dimerized phase that appears at $\theta = 0.8913\pi$ of $J_1 - J_3$ model can indeed be identified as a NNN-Haldane phase.

Then, with respect to our previous investigation on the phase transition between dimerized and NNN-Haldane phase discussed in Chapter 4, it is natural to expect the critical point to be in Ising universality class. The critical exponents $d \approx 0.14$ extracted from the scaling of the dimerization parameters in Fig.7.6 agrees within 13% with the Ising prediction $d = 1/8$. The relatively big discrepancy between numerically computed critical exponent and field theory predictions presumably comes from strong edge effects.

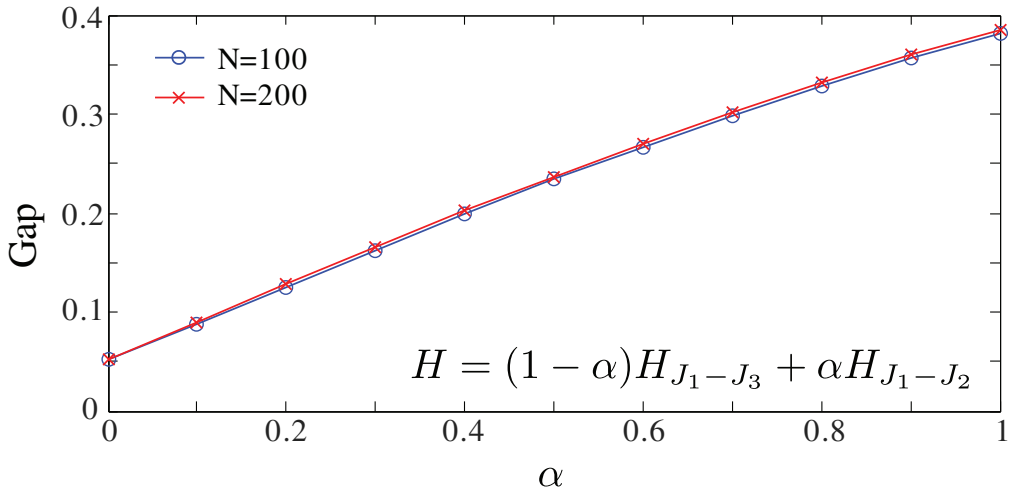

Figure 7.8 – Energy gap while interpolating between the $J_1 - J_3$ model ($\alpha = 0$) with $J_3/J_1 = \tan(0.9\pi)$ to $J_1 - J_2$ ($\alpha = 1$) model with $J_1 = -J_2$. The latter corresponds to the NNN-Haldane phase. Since the gap remains open for all the values of the interpolation parameter α, the non-dimerized phase in the $J_1 - J_3$ model is identified as a NNN-Haldane phase.

7.5.3 Central charge

The confirmation of the Ising universality class of the critical point between the dimerized and the NNN-Haldane phases can be obtained by computing the central charge. The fit of the reduced entanglement entropy (the entanglement entropy after removing the Friedel oscillations) to the Calabrese-Cardy formula 4.25 is provided in Fig.7.9. Obtained values of the central charge agrees within 7.5% with the field theory prediction $c = 1/2$ for Ising.

7.5.4 Energy spectrum

As a further confirmation of the Ising universality class of the critical point between the dimerized and the NNN-Haldane phase, we computed the finite-size scaling of the ground-state energy and excitation energies for open chains with even and odd numbers of sites. Since both open edges favor bonds without dimers, we associate the spin-1 chain with even (odd) number of sites with Ising $\uparrow,\uparrow$ ($\uparrow,\downarrow$) boundary condition, in complete analogy with the case of antiferromagnetic nearest-neighbor coupling (see Sections 4.4 and 4.5).

The ground-state energy of the system with conformally invariant boundary conditions at the Ising critical point scales according to Eq.3.13, that we recall here:

$$E = \varepsilon_0 N + \varepsilon_1 + \frac{\pi v}{N}\left[-\frac{1}{48} + x\right], \tag{7.16}$$

where ε_0 and ε_1 are non-universal coupling constants and x is the corresponding conformal dimension. As predicted by Cardy[21] for $\uparrow,\uparrow$ the energy spectrum is given by the identity conformal tower I and for $\uparrow,\downarrow$ boundary conditions - by ϵ conformal tower. The corresponding

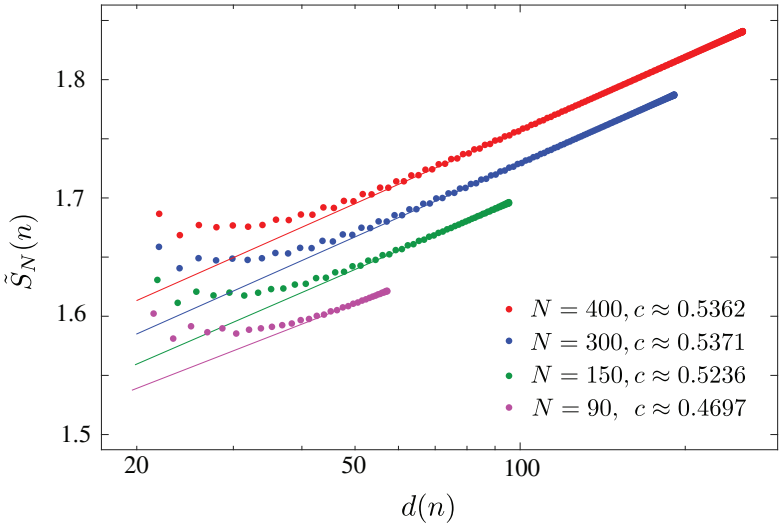

Figure 7.9 – Scaling of the entanglement entropy of open chains after removing the Friedel oscillations with conformal distance $d(n)$ for $\theta = 0.8913\pi$ and different system sizes. The extracted values of the central charge agree within 8% with the field-theory prediction $c = 1/2$ for the Ising critical theory.

scaling dimensions are $x_I = 0$ and $x_\epsilon = 1/2$. The finite-size scaling of the numerically obtained values of the ground-state energy for even and odd number of sites are shown in Fig.7.10(a) and (b). The extracted values of the velocities agree with each other within 15%.

We have also calculated the excitation energy of the lowest excited state in the sector $S^z_{\text{tot}} = 0$ (see Fig,7.10(c)). The bulk gap scales linearly with $1/N$, in agreement with conformally invariant critical theory. Moreover, according to conformal field theory (see sec3.2), the lowest excitation energy that belongs to the ϵ conformal tower scales with the system size as $\pi v/N$, while for the I conformal tower, the lowest excitation energy scales as $2\pi v/N$.

The low-lying excitations shown in green in Fig.7.10(c) have been computed in the sector of $S^z_{\text{tot}} = 0$ and are localized edge excitations. Due to spin-1 edge states induced by the ferromagnetic J_1 coupling, there are three low-lying states are expected - singlet, triplet and quintuplet. Depending on the sizes of the system, one of them becomes the ground state, and the other two are separated by an exponentially small gap. The singlet-triplet gap can be thus obtained as the difference between the ground-state energy and the third state in the sector of $S^z_{\text{tot}} = 0$. However, one can neglect the exponentially small gap for long enough chains. Then effectively the singlet-triplet gap can be obtained as the lowest state in the sector of $S^z_{\text{tot}} = 3$, since this state is, loosely speaking, a bulk triplet plus spin-2 in-gap state of negligible energy. This is much simpler to detect from the numerical point of view. The gap between the lowest states in the sectors $S^z_{\text{tot}} = 3$ and $S^z_{\text{tot}} = 0$ is in good agreement with the localized edge excitations, obtained by calculating several energy levels in the sector of $S^z_{\text{tot}} = 0$. Therefore we interpret these excitations as triplet excitations. Since these localized edge excitations occur at both edges, the corresponding energy levels are two-fold degenerate. Note also that this

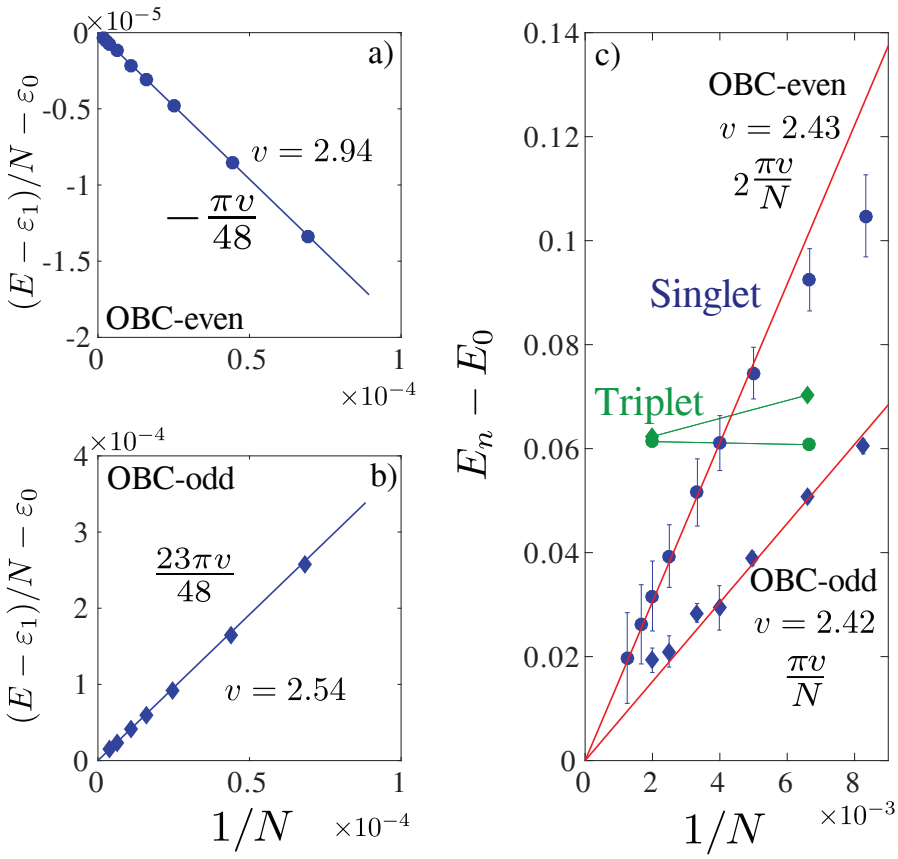

Figure 7.10 – Left panels: Linear scaling of the ground state energy per site in open chains with $1/N^2$ after subtracting ε_0 and ε_1 terms for (a) even and (b) odd number of sites. The extracted values of the velocities agree with each other within 15%. Right panel: Energy gaps in singlet (blue) and triplet (green) sectors for open boundary conditions as a function of $1/N$ for even (circles) and odd (diamonds) number of sites

singlet-triplet gap is small, and the first singlet excitation appears below the triplet one at relatively large system size ($N > 120$ for odd chains and $N > 250$ for even chains).

7.5.5 Domain wall between the NNN-Haldane phase and the dimerized phase

In the context of a spin chain with antiferromagnetic nearest and next-nearest-neighbor couplings and positive three-site interaction (see Chapter 4), we argue that the Ising transition at which the gap closes in the singlet sector while the singlet-triplet gap remains open occurs because the domain walls between the corresponding phases are non-magnetic.

In the present case, due to the ferromagnetic nearest-neighbor coupling, a pair of spins-1/2 at the edge of a domain in the NNN-Haldane phase does not form a singlet, but a triplet, as can be deduced from the entanglement spectra of Fig.7.7. However, a positive J_1 also favors a state without a dimer at the edge of the dimerized phase.

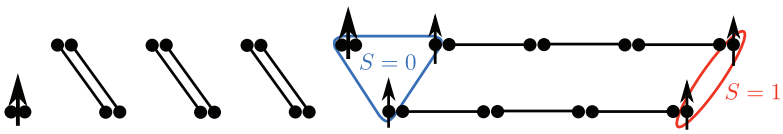

Figure 7.11 – Sketches of the non-magnetic domain wall between the NNN-Haldane and the dimerized phases.

The fact that the transition is in the Ising universality class leads us to speculate that the spins-1 that appear at the boundaries of the Haldane and the dimerized domains couple to each other and form a singlet, leading to a non-magnetic domain wall between these two phases, as sketched in Fig.7.11.

7.6 Critical quadrupolar phase

7.6.1 Spin and quadrupolar correlations

The most intriguing part of the phase diagram of this model is a critical phase that appears between the NNN-Haldane and ferromagnetic phases (see phase diagram of Fig. 7.1). The first indication of the presence of a critical phase comes from the entanglement spectrum. The chaotic and non-degenerate structure of the entanglement spectrum can be due to either the presence of a critical phase, or to non-convergent DMRG results. The latter, however, usually signals that the system approaches a critical regime.

To check the nature of this critical phase, we have looked at the spin-spin and quadrupole-quadrupole correlations defined as follows:

$$C_S(i,j) = \langle S_i^z S_j^z \rangle - \langle S_i^z \rangle \langle S_j^z \rangle; \tag{7.17}$$

$$\begin{aligned} C_{Q,0}(i,j) = \frac{4}{3} \left\langle \left[(S_i^z)^2 - \frac{1}{4}(S_i^+ S_i^i + S_i^- S_i^+) \right] \cdot \left[(S_j^z)^2 - \frac{1}{4}(S_j^+ S_j^- + S_j^- S_j^+) \right] \right\rangle \\ - \frac{4}{3} \left\langle (S_i^z)^2 - \frac{1}{4}(S_i^+ S_i^i + S_i^- S_i^+) \right\rangle \left\langle (S_j^z)^2 - \frac{1}{4}(S_j^+ S_j^- + S_j^- S_j^+) \right\rangle \end{aligned} \tag{7.18}$$

$$C_{Q,1}(i,j) = \frac{1}{2} \left\langle (S_i^z S_i^+ + S_i^+ S_i^z)(S_j^z S_j^- + S_j^- S_j^z) + \text{h.c.} \right\rangle \tag{7.19}$$

$$C_{Q,2}(i,j) = \frac{1}{2} \left\langle (S_i^+)^2 (S_j^-)^2 + \text{h.c.} \right\rangle \tag{7.20}$$

Longitudinal correlations C_S and $C_{Q,0}$ only contain terms that conserve S^z_{tot}, while transverse $C_{Q,1}$ and pairing $C_{Q,2}$ components contain the entries of the quadrupolar operator with

$\Delta S^z = \pm 1$ and $\Delta S^z = \pm 2$ respectively.

An example of the scaling of these correlation functions with the distance $|j-i|$ in different phases is shown in Fig.7.12. In the dimerized phase (Fig.7.12(a)) both spin and quadrupolar correlations are commensurate and decay exponentially fast with the distance between the spins. In the NNN-Haldane phase (Fig.7.12(b) and (c)) the correlations become incommensurate, but they still decay exponentially fast with the distance. In the dimerized and NNN-Haldane phases all three components of the quadrupolar correlations coincide showing that the system is SU(2) invariant. The small discrepancy between $C_{Q,0}$, $C_{Q,1}$ and $C_{Q,2}$ that occurs for $\theta = 0.9\pi$ is due to edge effects.

In Fig.7.12(f) and (g), the quadrupolar correlations dominate over the spin-spin correlations and both of them are incommensurate. This phase is reminiscent of the helical quadrupolar phase found in the classical phase diagram between the dimerized phase and the ferromagnetic phase (see Fig.7.5). The very slow decay of the quadrupolar correlations implies that the phase between the NNN-Haldane phase and the ferromagnetic one is critical. Moreover, the three components of the quadrupolar correlations split, signaling a broken SU(2) symmetry.

7.6.2 Spin gap in the critical quadrupolar phase

As pointed out above, the open boundaries and ferromagnetic nearest-neighbor coupling imply that starting from $\theta = 0.55\pi$ spin-1 edge states are present in the dimerized and the NNN-Haldane phases. For system with even number of sites, the ground-state is in the singlet sector, and the triplet and quintuplet in-gap states are separated from the ground-state by exponentially small gap. As expected, the gap closes in all sectors of total magnetization at the quantum phase transition between the critical quadrupolar and ferromagnetic phases. However, it turns out that in the critical phase the total magnetization of the ground-state gradually increases, as shown in Fig.7.13. The fact that only few states come down and the total magnetization remains relatively small in comparison to the fully polarized ferromagnetic state, suggests that the increase of the ground-state magnetization is an edge effect and not a bulk property.

7.6.3 One magnon instability

In order to understand what happens in the vicinity of the ferromagnetic phase, we look at the one-magnon instability from the ferromagnetic state. We start with the ferromagnetic wave-function polarized in the z-direction $|0\rangle = |S, S, ..., S, S\rangle$, such that for any site l $S_l^+|0\rangle = 0$, and $S = 1$. The energy of this state can be obtained by applying the Hamiltonian 7.1 to this state:

$$E_{FM} = (J_1 + 2J_3)N = (\cos\theta + 2\sin\theta)N \tag{7.21}$$

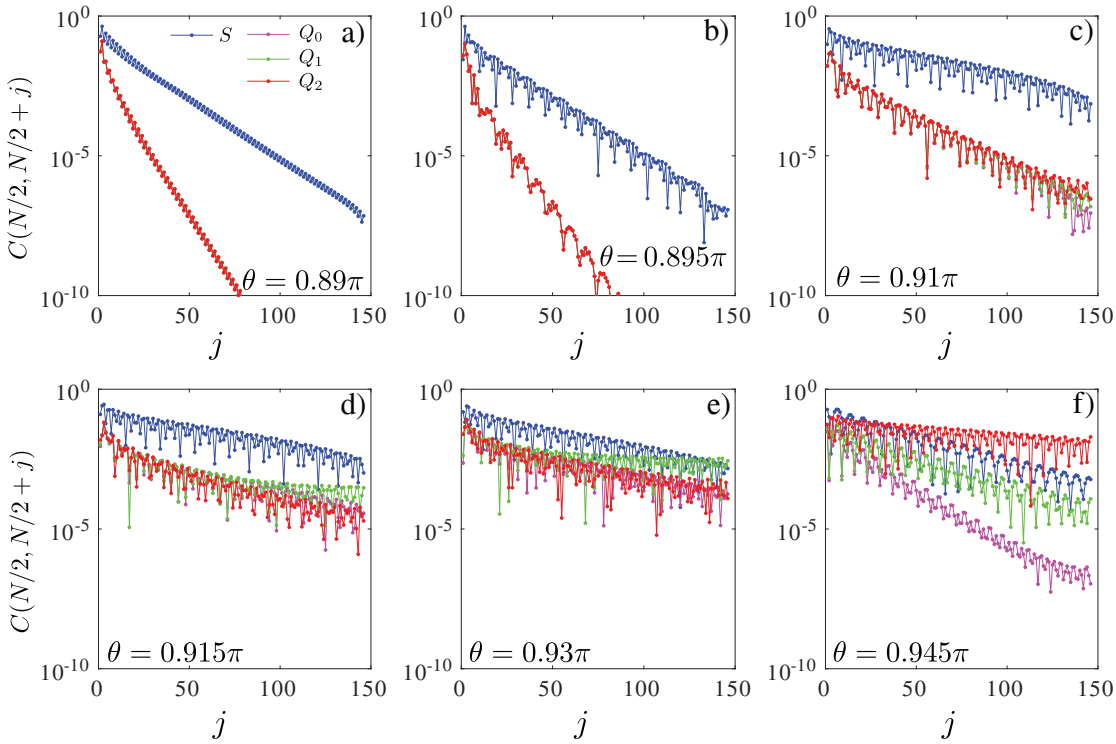

Figure 7.12 – Spin-spin and quadrupole-quadrupole correlations defined by Eq. 7.17, 7.18, 7.19 and 7.20 calculated in (a) the dimerized, (b) and (c) the NNN-Haldane, and (d), (e) and (f) the critical quadrupolar phases. The correlations are commensurate in the dimerized phase and incommensurate in the NNN-Haldane and critical phases. In the critical phase, quadrupolar correlations decay slowly and dominate over spin correlations. The splitting of the three branches of quadrupolar correlations in (d), (e) and (f) implies that the SU(2) symmetry is broken.

We consider a single magnon state from the ferromagnetic state $|0\rangle$ defined by:

$$|\varphi(q)\rangle = \frac{1}{\sqrt{2NS}} \sum_{l=1}^{N} e^{iql} S_l^- |0\rangle \tag{7.22}$$

where q is the momentum, and $1/\sqrt{2NS}$ is a normalization factor. The energy of this state (see derivation in the AppendixC.2) as a function of θ and q is given by:

$$E(q) = f_1 + 2f_2 \cos q + 2f_3 \cos 2q, \tag{7.23}$$

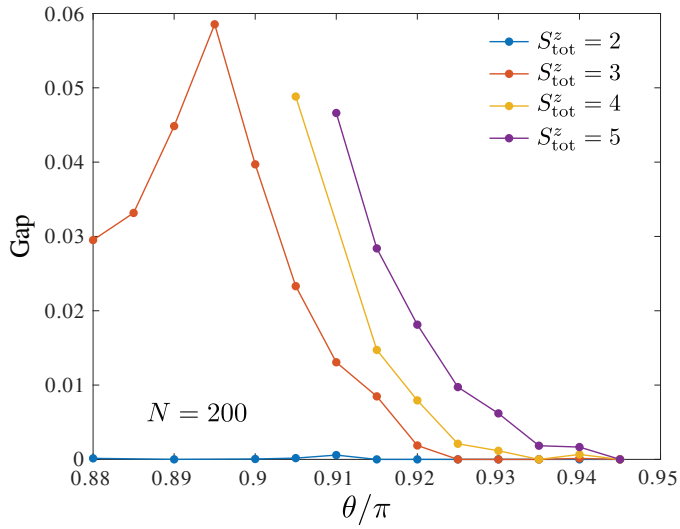

Figure 7.13 – The gap between the ground-state energy calculated in the sector of $S^z_{\rm tot} = 0$ and the energy of the lowest states in different sectors of $S^z_{\rm tot}$.

with

$$\begin{aligned} f_1 &= (N-2)\cos\theta + 2(N+1)\sin\theta \\ f_2 &= \cos\theta + 2\sin\theta \\ f_3 &= \sin\theta \end{aligned} \tag{7.24}$$

At $\theta = \pi$ ($J_1 = -1$ and $J_3 = 0$) the system is in the ferromagnetic state, the energy given by Eq.7.23 has a minimum at $q = 0$ and is equal to the ferromagnetic energy. Upon decreasing the θ, the curvature of the energy as a function of q decreases at $q = 0$. The phase transition occurs, when the curvature changes sign:

$$C = \left.\frac{dE(q)}{dq}\right|_{q=0} = -2f_2\cos q - 8f_3\cos q\big|_{q=0} = 0 \tag{7.25}$$

The solution is

$$\frac{f_2}{f_3} = \frac{J_1 + 2J_3}{J_3} = -4. \tag{7.26}$$

This leads to $J_3/J_1 = -1/6$, i.e. $\theta \approx 0.9474\pi$. This value is in the perfect agreement with our DMRG data. The wave-vector for which the energy is minimized is given by:

$$-2f_2\sin q - 4f_3\sin 2q = 0. \tag{7.27}$$

The non-trivial solution of this equation is $\cos q = -f_2/4f_3$, leading to:

$$q = \arccos\left(-\frac{1}{2} - \frac{1}{4}\cot\theta\right). \tag{7.28}$$

The wave-vector q as a function of θ is shown in the Fig.7.14(d). It is in good agreement with the wave-vector extracted numerically from our DMRG data.

7.7 Short-range order

In addition to five quantum phase transitions, the phase diagram contains several disorder and Lifshitz lines. The disorder and Lifshitz points are the points where the correlation function in real space becomes incommensurate with a wave-vector $q \neq 0, \pi/2, \pi$, or where the structure factor has two peaks at $q \neq 0, \pi/2, \pi$, respectively. In order to find the location of the disorder points, we have extracted the wave-number q by calculating the spin-spin correlations defined by Eq. 7.17 and we have fitted it with the dimerized Ornstein-Zernicke form:

$$C_{\mathrm{DOZ}} \propto (1 + \delta(-1)^x)\cos(q \cdot x)\frac{e^{-x/\xi}}{\sqrt{x}}, \tag{7.29}$$

where the wave number q, the correlation length ξ, and the dimerization parameter δ are fitting parameters. The location of the Lifshitz point is determined by the position of the peak in the structure factor $SF(q)$, defined by the Fourier transform of real space correlations:

$$SF(q) = \frac{1}{N}\sum_{i,j} e^{iq(i-j)}\langle 0|\mathbf{S}_i \cdot \mathbf{S}_j|0\rangle. \tag{7.30}$$

As discussed in Chapter 4, the first disorder point is located at $\theta_{\alpha_d,1} = \arctan(1/6) \approx 0.0526\pi$, where the ground state is given by the exactly dimerized state. At this point the wave-number extracted from the fit of the spin-spin correlations with Eq.7.29 changes from $q = \pi$ to $\pi/2 < q < \pi$. The second disorder point coincides with the first Lifshitz point at $\theta_{\alpha_d,2} = \theta_{\alpha_L,1} \approx 0.0584\pi$. At this point the wave-number of the real space spin-spin correlation becomes $q = \pi/2$, while the structure factor $SF(q)$ starts to have two symmetric peaks at $q \neq \pi$. For larger values of θ, the peaks in the structure factor asymptotically approach the value $q = \pi/2$.

On the other side of the phase diagram, both the disorder and Lifshitz points coincides with the quantum critical point between the dimerized and NNN-Haldane phases at $\theta_2 = 0.8913\pi$. In the NNN-Haldane and critical quadrupolar phases spin-spin correlations are incommensurate in both real and momentum space. Fig.7.14(a) provides an example of fit of the spin-spin correlation to the dimerized Ornstein-Zernicke form defined by Eq.7.29. The extracted values of the correlation length ξ and short-range dimerization parameter δ as a function of θ for $N = 150$ are shown in Fig.7.14(b) and (c). The wave-numbers extracted from real-space correlation and from the position of the peak of the structure factor are in a good agreement with each other and with the wave-numbers obtained from the analysis base onm the one-

magnon instability.

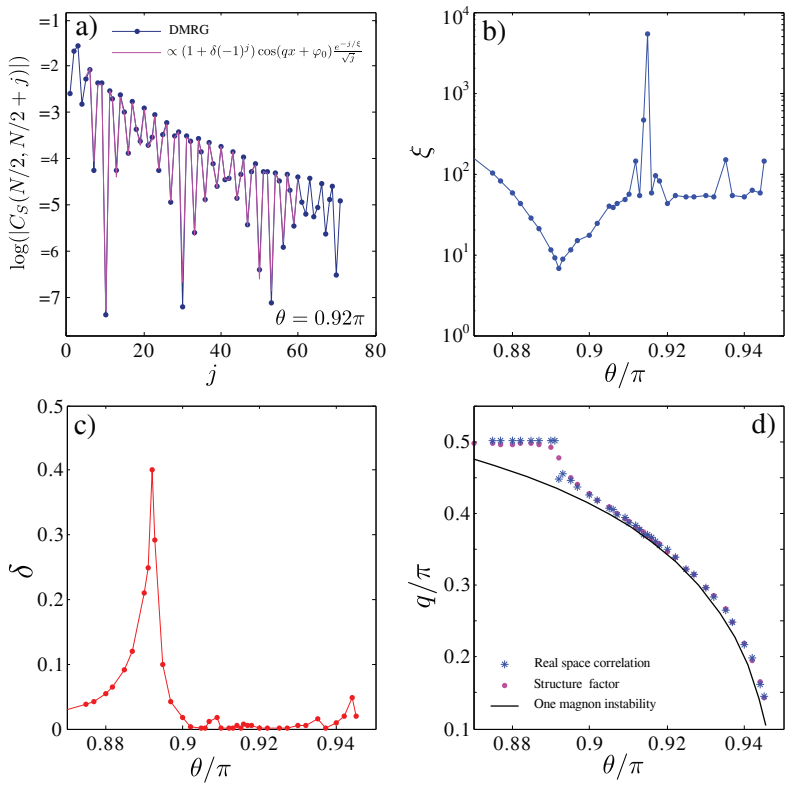

Figure 7.14 – Incommensurate correlations in the NNN-Haldane and critical quadrupolar phase extracted from an open chain with $N+150$. (a) Examples of fit of the spin-spin correlations to the dimerized Ornstein-Zernicke form defined by Eq.7.29. (b) Correlation length and (c) dimerization extracted as shown in (a) as a function of θ. (d) Wave-number, extracted from a fit of the real-space correlation with the Ornstein-Zernicke form (blue stars), and from the location of the peak of the structure factor (magenta circles). The DMRG data agree well with the wave-number obtained analytically for the one-magnon instability (black line).

7.8 Spin-1 chain with ferromagnetic nearest-neighbor and antiferromagnetic next-nearest-neighbor interactions

Interestingly, the critical phase with dominant quadrupolar correlations also appears as an intermediate phase between the NNN-Haldane and ferromagnetic phases in the spin-1 chain with ferromagnetic nearest-neighbor and antiferromagnetic next-nearest-neighbor interactions. The model is defined by the following Hamiltonian:

$$H_{J_1-J_2} = J_1 \sum_i \mathbf{S}_i \cdot \mathbf{S}_{i+1} + J_2 \sum_i \mathbf{S}_i \cdot \mathbf{S}_{i+2} \tag{7.31}$$

where the coupling constants J_1 and J_2 are parametrized by $J_1 = \cos\theta$ and $J_2 = \sin\theta$ with $\theta \in [0,\pi]$, that restricts the next-nearest neighbor coupling to be antiferromagnetic. The phase diagram is shown in Fig.7.15. The transition between the Haldane and NNN-Haldane phase is topological and is of the first order [56, 58]. The critical phase occurs in the range $0.87\pi < \theta < 0.922\pi$ and separates the NNN-Haldane phase form the ferromagnetic phase. The quadrupolar correlations dominate over spin-spin correlation in a similar was as in the model with three-site interaction discussed above.

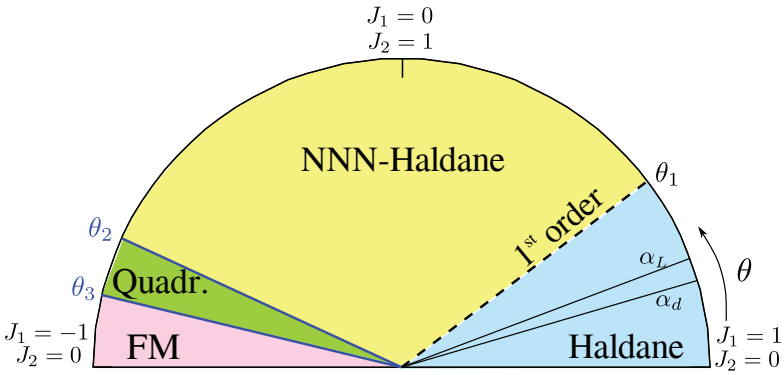

Figure 7.15 – Phase diagram of the spin-1 chain with nearest and next-nearest-neighbor interactions. The transition between the Haldane and the NNN-Haldane phases is first order and located at $\theta_1 \approx 0.205\pi$. Between $\theta_3 \approx 0.87\pi$ and $\theta_4 \approx 0.922\pi$, the system is in a critical quadrupolar phase.

The real-space correlations becomes incommensurate at the disorder point located at $\theta_d \approx 0.0881\pi$ structure factor has two peaks at $q \neq 0, pi/2, pi$ starting from the Lifshitz point $\theta_L \approx 0.1135\pi$[56]. This remains true until the phase transition to the ferromagnetic phase.

The energy of a single magnon state from the ferromagnetic state $|0\rangle$ defined by:

$$|\varphi(q)\rangle = \frac{1}{\sqrt{2NS}} \sum_{l=1}^{N} e^{iql} S_l^- |0\rangle, \tag{7.32}$$

takes the following form:

$$E(q) = (J_1 + J_2)(N-2) + 2J_1 \cos q + 2J_2 \cos 2q. \tag{7.33}$$

The curvature of the energy as a function of the wave-number q is the given by:

$$c = -2J_1 \cos q - 8J_2 \cos 2q. \tag{7.34}$$

As before, the transition is associated with the point where the sign of the curvature computed at $q = 0$ changes. This leads to $\frac{J_2}{J_1} = -\frac{1}{4}$, i.e. $\theta = 0.9220\pi$, in good agreement with our DMRG data.

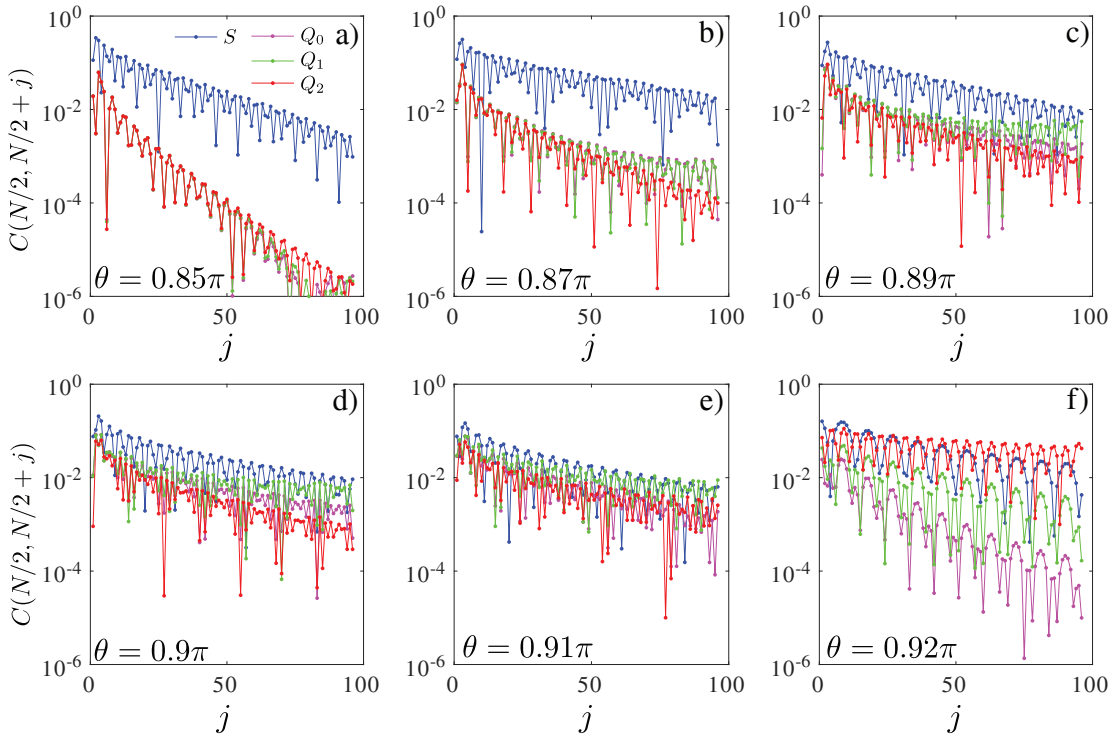

Figure 7.16 – Spin-spin and quadrupole-quadrupole correlations defined by Eq. 7.17, 7.18, 7.19 and 7.20 calculate (a) NNN-Haldane, and (c)-(f) the critical quadrupolar phase. In the critical phase, quadrupolar correlations decay slowly and dominate over spin correlations. The splitting of the three branches of quadrupolar correlations in (c)-(f) implies that the SU(2) symmetry is broken.

7.9 Conclusion

To summarize, we have shown that nearest-neighbor Heisenberg interactions combined with three-site interactions lead to a rich phase diagram that consists of Haldane, dimerized, NNN-Haldane, critical quadrupolar and ferromagnetic phases. While the main phases - Haldane, dimerized and ferromagnetic ones - are the same as in the phase diagram of the spin-1 bilinear-biquadratic chain, we want to stress the main differences between these two models: *i)* The critical trimerized phase that appears between the Haldane and the ferromagnetic phases [34] in the bilinear-biquadratic chain is absent in the chain with three-site interaction, for which these two phases are separated by a first order phase transition. *ii)* According to the most recent numerical investigation of the bilinear-biquadratic chain, the transition occurs directly from the dimerized to the ferromagnetic state [63], although the field theory predicts some intermediate gapped quadrupolar phase[27]. By contrast, in the spin-1 chain with three-site interactions we have observed two intermediate phases - a NNN-Haldane phase and a critical quadrupolar phase - between the dimerized phase and the ferromagnetic one. The transition between the Haldane and dimerized phases is continuous and is in the WZW $SU(2)_2$ universality class [71].

The transition between the dimerized and NNN-Haldane phase is in the Ising universality class, in agreement with our previous results on the spin-1 chain described by the $J_1 - J_2 - J_3$ model, where the critical line between the NNN-Haldane phase and the dimerized phase has been shown to be Ising transition. We argue that two spin-1/2 that appear at the edges of the domain in the NNN-Haldane phase couple to a spin-1 at the edge of the dimerized domain and form a singlet. So the domain wall between these phases is non-magnetic, consistent with an Ising transition that occurs completely in the singlet sector, with a singlet-triplet gap that remains open. This also agrees with our previous arguments on the nature of the domain walls at Ising and WZW critical lines.

Perhaps the most interesting part of the phase diagram is the critical phase between NNN-Haldane and ferromagnetic phases. Surprisingly, while the spin-spin correlations remains short-ranged, the quadrupolar correlations becomes critical. This phase is incommensurate. This is consistent with the variational calculation, that suggests a helical state with mixed spin and quadrupolar components. The same phase has been observed in a spin-1 chain with ferromagnetic nearest-neighbor and antiferromagnetic next-nearest-neighbor coupling. So the presence of a critical quadrupolar phase between the NNN-Haldane phase and the ferromagnetic phase seems to be generic. It would be interesting to investigate this region of the phase diagram with field theory methods.

8 Summary and outlook

In this thesis we have investigated the emergence of spontaneous dimerization in spin-S chains under frustration induced by the competition between nearest-neighbor Heisenberg interaction an the interactions that show up in the higher order states for Hubbard model: next-nearest-neighbor, biquadratic, and three-site interactions. We specially focus on the nature of dimerization transitions in various spin models.

For pedagogical reasons we have provided a brief review of Density Matrix Renormalization Group (DMRG), formulated in terms of Matrix Product State. We realized that the effective Hamiltonian written in the truncated basis of the reduced density matrix of the ground-state also encodes information about excited states when the system is critical. The fact that the ground state encodes essentially all the information of the underlying conformal field theory, in particular the conformal towers of states, has been pointed already in the context of entanglement spectrum by Läuchli [62]. This allowed us to extend the standard DMRG algorithm and to compute the energy spectrum at low computational cost. Moreover, it turns out that by looking at the excitation energy calculated in such a way as a function of iterations one can distinguish bulk and edge excitations and reach conclusions about the convergence of different states.

The described method has been benchmarked on the critical systems described by two minimal models - the transverse field Ising model and the three-state Potts model. For both models the conformal towers extracted for various boundary conditions are in a good agreement with the predictions of boundary conformal filed theory. Interestingly, we have found that in the three-state Potts model finite-size effects are significant for some conformal towers.

Combining extensive numerical simulations with conformal field theory analysis, we have the investigated the phase diagram of the Heisenberg spin-1 chain with additional next-nearest-neighbor and three-site interactions. It consist of three phases Haldane, NNN-Haldane and dimerized. The transition between the two non-dimerized phases - Haldane and NNN-Haldane - is topological and is first order in agreement with previous study of the model with nearest and next-nearest neighbor interactions [56, 57]. We have shown that the transitions

to spontaneously dimerized phase can be continuous in WZW $SU(2)_2$ or Ising universality classes, or first order. For small values of next-nearest-neighbor interactions, the transition between the Haldane and the dimerized phases is in the WZW $SU(2)_2$ universality class, in agreement with previously obtained results for spin-1 chain with nearest-neighbor and three-site interactions[71]. However, the WZW $SU(2)_2$ critical line turns into a first order line at the tri-critical point that also belongs to the WZW $SU(2)_2$ universality class. This is possible due to the presence of a marginal operator in the WZW $SU(2)_2$ model. At the tri-critical point the coupling constant of this operator changes sign. According to a conformal embedding, close to the WZW $SU(2)_2$ tri-critical point, the phase transition (whether continuous or first order) occurs simultaneously in the Ising and boson sectors, while far from this point, the two transitions can split. This leads to an Ising critical line between the NNN-Haldane and dimerized phases. The alternative between WZW $SU(2)_2$ and Ising transitions relies on the topological properties of the phases and on the nature of the domain walls between them. Domains of topologically non-trivial Haldane phase have spin-1/2 edge states, while domains of the topologically trivial NNN-Haldane and dimerized phases do not. Therefore, the domain wall between the Haldane and the dimerized phases carries a spin-1/2 and leads to a magnetic WZW $SU(2)_2$ critical line, while the domain wall between the dimerized and NNN-Haldane phases does not carry any spin and leads to a non-magnetic Ising transition. We have confirmed the presence of free spin-1/2 at the domain wall between the Haldane and the dimerized phases by looking at the emergent magnetic solitons at the first order phase transition between the corresponding phases. In the future, this idea might be extended to transitions between valence-bond solids and dimerized phases, possibly in higher dimensions. Finally, we show that short-range correlations change character in the Haldane and dimerized phases through disorder and Lifshitz lines, as well as through the development of short-range dimer correlations in the Haldane phase, leading to a remarkably rich phase diagram.

The phase diagram of the related spin-1 model with nearest, next-nearest-neighbor and biquadratic coupling had already been studied in Ref.[81]. Careful DMRG calculations coupled to conformal field theory arguments have revealed significant differences with the original phase diagram of Ref.[81] regarding the nature of the phase transitions: *i)* The phase transition between the NNN-Haldane phase and the dimerized phase turns out to be continuous, and in the Ising universality class; *ii)* The tri-critical point at which the continuous WZW $SU(2)_2$ transition turns to first order occurs below the triple point; *iii)* This tri-critical point is in the same WZW $SU(2)_2$ universality class as the critical line that ends at this point. To summarize, on a qualitative level the phase diagram for this model is similar to the one obtained for the spin-1 chain with three-site interaction. Since the end point of the WZW $SU(2)_2$ critical line and the triple point do not coincide but are separated by the first-order transition line between the Haldane and the dimerized phases, as in the model with three-site interaction, we anticipate that the conclusions of Ref.[81] regarding the end points of the disorder lines will also be modified, and that they might end at a first-order transition line and not at the triple point or at the WZW $SU(2)_2$ critical line. It would be interesting to continue the investigation of the model with biquadratic interaction in this direction and to compare the results with

those obtained for the model with three-site interaction.

By studying the full phase diagram of the Heisenberg spin-1 chain with an additional three-site interaction, we have obtained a numerical evidence of two intermediate phases that separates the dimerized and the ferromagnetic phases, in contrast to the previous results on a bilinear-biquadratic spin-1 chain, where the transition occurs directly from the dimerized phase into the ferromagnetic one [63]. We have justified that one of these phases is NNN-Haldane phase with ferromagnetic coupling between two Haldane chains. The transition between the dimerized and NNN-Haldane phase is in the Ising universality class. We provide numerical evidence of a gap closing in the singlet sector, while the singlet-triplet gap remains open. The most interesting and numerically challenging part of the phase diagram is the presence of a critical phase, that separates NNN-Haldane phase from the ferromagnetic one. This phase is characterized by critical quadrupolar correlations, while the spin-spin correlations remain gapped. These correlations all are incommensurate, in agreement with the helical quadrupolar phase predicted by the variational approach. The location of the phase transition between the critical quadrupolar phase and the ferromagnetic phase, obtained by calculating an energy of the one magnon instability is in good agreement with the DMRG data. A similar critical phase with dominant quadrupolar correlations has been found between the NNN-Haldane phase and the ferromagnetic phase in the model with ferromagnetic nearest-neighbor interaction and antiferromagnetic next-nearest-neighbor exchange. So the presence of a critical quadrupolar phase between the NNN-Haldane phase and the ferromagnetic phase seems to be generic. It would be interesting to investigate this region of the phase diagram with field theory methods.

By studying the properties of the spin-3/2 chain with nearest, next-nearest neighbor and three-site interactions, we had generalized the results obtained for spin-1. In particular, we have shown that the transition between the uniform critical phase and the fully dimerized phase is continuous in the WZW $\mathrm{SU}(2)_{2S=3}$ universality class, in agreement with the previous results for zero next nearest-neighbor coupling [70]. As in the case of spin-1 chain, the transition remains continuous up to and including at the tri-critical end point, where it turns into a first order transition. The transition between the critical and partially dimerized phase is in the Kosterlitz-Thouless universality class. Interestingly, the partially dimerized phase is separated from the fully dimerized one by a first order transition only for relatively small value of next-nearest-neighbor coupling. For larger values of this coupling, there is a continuous crossover between partially and fully dimerized phases via the topological sector with two-leg ladder geometry. This picture has to be clarified with further investigation.

As a further perspective, it would be interesting to generalized the results obtained for spin-3/2 with nearest and next-nearest neighbor coupling and three-site interaction to the model, where the dimerization is induced by the bilinear interaction. Since for the spin-1 chain the two phase diagrams are essentially the same, it would be important to figure out whether it remains true for larger values of spin. As we have shown, the three-site interaction lead to a rich physics. So, it would be interesting to study this kind of frustration in the combination

with other other terms, such as biquadratic coupling, or on a lattice with different geometry.

Of course, it would be important to check what happens when all next-order terms (next-nearest-neighbor, biquadratic, and three-site) are present. This model would be more realistic since all these terms show up in the expansion of the two-band Hubbard model. As we have shown, many interesting phenomena appear at relatively small (and hence physically realistic) values of the coupling constant of the three-site term in the Hamiltonian. We hope that this will inspire an active search for experimental realizations. One could for instance try to look for materials where the on-site repulsion U in the Hubbard model is small enough to generate significant corrections to the Heisenberg Hamiltonian.

We have also shown that the conformal towers extracted with the DMRG algorithm is a powerful tool in the identification of the universality classes of critical systems. It can be considered as a complement to the usual method that only relies on the central charge or on the critical exponents. It would be very interesting to extract the conformal towers of other quantum critical one-dimensional models along the lines of the present work.

A Minimal model

Symmetry property of the conformal dimension $h_{r,s}$ can be deduced directly from the Eq.3.3:

$$h_{p'-r,p-s} = \frac{(pp' - pr - p'p + p's)^2 - (p-p')^2}{4pp'} = h_{r,s} \tag{A.1}$$

A.1 Ising model

The small-q expansion of $1/\varphi(q)$ up to eight's order term:

$$\begin{aligned}
&\frac{1}{\varphi(q)} = \prod_{n=1}^{\infty} \frac{1}{1-q^n} = \\
&(1+q+q^2+q^3+q^4+q^5+q^6+q^7+q^8)(1+q^2+q^4+q^6+q^8) \\
&\times (1+q^3+q^6)(1+q^4+q^8)(1+q^5)(1+q^6)(1+q^7)(1+q^8) \\
&\qquad = 1+q+2q^2+3q^3+5q^4+7q^5+11q^6+15q^7+22q^8.
\end{aligned} \tag{A.2}$$

We compute the characters of the three conformal towers of transverse field Ising model using the definition of Eq.3.6. For identity conformal tower:

$$\begin{aligned}
&\chi_{(1,1)}(q) = K_{1,1}^{(4,3)}(q) - K_{1,-1}^{(4,3)}(q) = \frac{q^{-1/24}}{\varphi(q)} \sum_{n\in\mathbb{Z}} q^{(24n+1)^2/48} - q^{(24n+7)^2/48} \\
&= q^{-1/24}\left(1+q+2q^2+3q^3+5q^4+7q^5+11q^6+15q^7+22q^8\right) q^{1/48}\left(1-q-q^6+O(q^{11})\right) \\
&\qquad = q^{-1/48}\left(1+q^2+q^3+2q^4+2q^5+3q^6+3q^7+5q^8\right)
\end{aligned} \tag{A.3}$$

	free		$\uparrow,\uparrow$		$\uparrow,\downarrow$		free,$\uparrow$	
ground-state	I_0	0.4914	I_0	0.5092	ϵ_0	0.5088	σ_0	0.5000
1st excited	ϵ_0	0.4950	I_2	0.5049	ϵ_1	0.5048	σ_1	0.4999
2nd excited	ϵ_1	0.4949	I_3	0.5046	ϵ_2	0.5043	σ_2	0.4996
3rd excited	I_2	0.4949	I_4	0.5041	ϵ_3	0.5038	σ_3	0.4992
4th excited	ϵ_2	0.4945	I_4	0.5046	ϵ_4	0.5030	σ_3	0.4997
5th excited	I_3	0.4946	I_5	0.5034	ϵ_4	0.5047	σ_4	0.4986
6th excited	ϵ_3	0.4940	I_5	0.5042	ϵ_5	0.5021	σ_4	0.4995
7th excited	I_4	0.4941	I_6	0.5025	ϵ_5	0.5047	σ_5	0.4978
8th excited	I_4	0.4947	I_6	0.5037	ϵ_6	0.5010	σ_5	0.4988
9th excited	ϵ_4	0.4933	I_6	0.5044	ϵ_6	0.5037	σ_5	0.4993
10th excited	ϵ_4	0.4949	I_7	0.5016	ϵ_6	0.5055	σ_6	0.4967
11th excited	I_5	0.4936	I_7	0.5032	ϵ_7	0.4999	σ_6	0.4980
12th excited	I_5	0.4945	I_7	0.5043	ϵ_7	0.5030	σ_6	0.4989
13th excited	ϵ_5	0.4926	I_8	0.5007	ϵ_7	0.5038	σ_6	0.4994
14th excited	ϵ_5	0.4949	I_8	0.5022	ϵ_7	0.5046	σ_7	0.4956
15th excited	I_6	0.4927	I_8	0.5032	ϵ_8	0.4990	σ_7	0.4972
16th excited	I_6	0.4935	I_8	0.5039	ϵ_8	0.5021	σ_7	0.4983
17th excited	I_6	0.4940	I_8	0.5048	ϵ_8	0.5032	σ_7	0.4988
18th excited	ϵ_6	0.4911	I_9	0.5089	ϵ_8	0.5038	σ_7	0.4991
19th excited	ϵ_6	0.4935	I_9	0.5015	ϵ_8	0.5050	σ_8	0.4947
20th excited	ϵ_6	0.4941	I_9	0.5028	ϵ_9	0.4988	σ_8	0.4963

Table A.1 – Velocities extracted for transverse field Ising model from finite-size scaling of the ground state and first 20 excited states for open chain with different boundary conditions.

For ϵ conformal tower:

$$\begin{aligned}\chi_{(2,1)}(q) &= K^{(4,3)}_{2,1}(q) - K^{(4,3)}_{2,-1}(q) = \frac{q^{-1/24}}{\varphi(q)} \sum_{n\in\mathbb{Z}} q^{(24n+5)^2/48} - q^{(24n+11)^2/48} \\ &= q^{-1/24}\left(1+q+2q^2+3q^3+5q^4+7q^5+11q^6+15q^7+22q^8\right) q^{25/48}\left(1-q^2-q^3+q^7+O(q^{17})\right) \\ &= q^{1/2-1/48}\left(1+q+q^2+q^3+2q^4+2q^5+3q^6+4q^7+5q^8\right) \quad \text{(A.4)}\end{aligned}$$

Finally, σ conformal tower is given by:

$$\begin{aligned}\chi_{(1,2)}(q) &= K^{(4,3)}_{1,2}(q) - K^{(4,3)}_{1,-2}(q) = \frac{q^{-1/24}}{\varphi(q)} \sum_{n\in\mathbb{Z}} q^{(24n-2)^2/48} - q^{(24n+10)^2/48} \\ &= q^{-1/24}\left(1+q+2q^2+3q^3+5q^4+7q^5+11q^6+15q^7+22q^8\right) q^{4/48}\left(1-q^2-q^4+O(q^{10})\right) \\ &= q^{1/16-1/48}\left(1+q+q^2+2q^3+2q^4+3q^5+4q^6+5q^7+6q^8\right) \quad \text{(A.5)}\end{aligned}$$

A.2 Three-state Potts model

The small-q expansions of the characters for ten fields of the theory are derived below:

$$\chi_{(1,1)}(q) = K_{1,1}^{(6,5)}(q) - K_{1,-1}^{(6,5)}(q) = \frac{q^{-1/24}}{\varphi(q)} \sum_{n\in\mathbb{Z}} q^{(60n+1)^2/120} - q^{(60n+11)^2/120}$$
$$= q^{-1/24}\left(1+q+2q^2+3q^3+5q^4+7q^5+11q^6+15q^7+22q^8\right) q^{1/120}\left(1-q-O(q^{20})\right)$$
$$= q^{-1/30}\left(1+q^2+q^3+2q^4+2q^5+4q^6\right) \quad \text{(A.6)}$$

$$\chi_{(2,1)}(q) = K_{2,1}^{(6,5)}(q) - K_{2,-1}^{(6,5)}(q) = \frac{q^{-1/24}}{\varphi(q)} \sum_{n\in\mathbb{Z}} q^{(60n+7)^2/120} - q^{(60n+17)^2/120}$$
$$= q^{-1/24}\left(1+q+2q^2+3q^3+5q^4+7q^5+11q^6+15q^7+22q^8\right) q^{49/120}\left(1-q^2-O(q^{15})\right)$$
$$= q^{-1/30+2/5}\left(1+q+q^2+2q^3+3q^4+4q^5+6q^6\right) \quad \text{(A.7)}$$

$$\chi_{(3,1)}(q) = K_{3,1}^{(6,5)}(q) - K_{3,-1}^{(6,5)}(q) = \frac{q^{-1/24}}{\varphi(q)} \sum_{n\in\mathbb{Z}} q^{(60n+13)^2/120} - q^{(60n+23)^2/120}$$
$$= q^{-1/24}\left(1+q+2q^2+3q^3+5q^4+7q^5+11q^6+15q^7+22q^8\right) q^{169/120}\left(1-q^3-O(q^{10})\right)$$
$$= q^{-1/30+7/5}\left(1+q+2q^2+2q^3+4q^4+5q^5+8q^6\right) \quad \text{(A.8)}$$

$$\chi_{(4,1)}(q) = K_{4,1}^{(6,5)}(q) - K_{4,-1}^{(6,5)}(q) = \frac{q^{-1/24}}{\varphi(q)} \sum_{n\in\mathbb{Z}} q^{(60n+19)^2/120} - q^{(60n+29)^2/120}$$
$$= q^{-1/24}\left(1+q+2q^2+3q^3+5q^4+7q^5+11q^6+15q^7+22q^8\right) q^{361/120}\left(1-q^4-q^5-O(q^{11})\right)$$
$$= q^{-1/30+3}\left(1+q+2q^2+3q^3+4q^4+5q^5+8q^6\right) \quad \text{(A.9)}$$

$$\chi_{(1,2)}(q) = K_{1,2}^{(6,5)}(q) - K_{1,-2}^{(6,5)}(q) = \frac{q^{-1/24}}{\varphi(q)} \sum_{n\in\mathbb{Z}} q^{(60n-4)^2/120} - q^{(60n+16)^2/120}$$
$$= q^{-1/24}\left(1+q+2q^2+3q^3+5q^4+7q^5+11q^6+15q^7+22q^8\right) q^{16/120}\left(1-q^2-O(q^{16})\right)$$
$$= q^{-1/30+1/8}\left(1+q+q^2+2q^3+3q^4+4q^5+6q^6\right) \quad \text{(A.10)}$$

$$\chi_{(2,2)}(q) = K^{(6,5)}_{2,2}(q) - K^{(6,5)}_{2,-2}(q) = \frac{q^{-1/24}}{\varphi(q)} \sum_{n\in\mathbb{Z}} q^{(60n+2)^2/120} - q^{(60n+22)^2/120}$$
$$= q^{-1/24}\left(1+q+2q^2+3q^3+5q^4+7q^5+11q^6+15q^7+22q^8\right) q^{1/30}\left(1-q^4-O(q^{12})\right)$$
$$= q^{-1/30+1/40}\left(1+q+2q^2+3q^3+4q^4+6q^5+9q^6\right) \quad \text{(A.11)}$$

$$\chi_{(3,2)}(q) = K^{(6,5)}_{3,2}(q) - K^{(6,5)}_{3,-2}(q) = \frac{q^{-1/24}}{\varphi(q)} \sum_{n\in\mathbb{Z}} q^{(60n+2)^2/120} - q^{(60n+22)^2/120}$$
$$= q^{-1/24}\left(1+q+2q^2+3q^3+5q^4+7q^5+11q^6+15q^7+22q^8\right) q^{8/15}\left(1-q^6-O(q^8)\right)$$
$$= q^{-1/30+21/40}\left(1+q+2q^2+3q^3+5q^4+7q^5+10q^6\right) \quad \text{(A.12)}$$

$$\chi_{(4,2)}(q) = K^{(6,5)}_{4,2}(q) - K^{(6,5)}_{4,-2}(q) = \frac{q^{-1/24}}{\varphi(q)} \sum_{n\in\mathbb{Z}} q^{(60n+14)^2/120} - q^{(60n+34)^2/120}$$
$$= q^{-1/24}\left(1+q+2q^2+3q^3+5q^4+7q^5+11q^6+15q^7+22q^8\right) q^{49/30}\left(1-q^4-O(q^8)\right)$$
$$= q^{-1/30+13/8}\left(1+q+2q^2+3q^3+4q^4+6q^5+9q^6\right) \quad \text{(A.13)}$$

$$\chi_{(1,3)}(q) = K^{(6,5)}_{1,3}(q) - K^{(6,5)}_{1,-3}(q) = \frac{q^{-1/24}}{\varphi(q)} \sum_{n\in\mathbb{Z}} q^{(60n-9)^2/120} - q^{(60n+21)^2/120}$$
$$= q^{-1/24}\left(1+q+2q^2+3q^3+5q^4+7q^5+11q^6+15q^7+22q^8\right) q^{27/40}\left(1-q^3-O(q^{12})\right)$$
$$= q^{-1/30+2/3}\left(1+q+2q^2+2q^3+4q^4+5q^5+8q^6\right) \quad \text{(A.14)}$$

$$\chi_{(2,3)}(q) = K^{(6,5)}_{2,3}(q) - K^{(6,5)}_{2,-3}(q) = \frac{q^{-1/24}}{\varphi(q)} \sum_{n\in\mathbb{Z}} q^{(60n-3)^2/120} - q^{(60n+27)^2/120}$$
$$= q^{-1/24}\left(1+q+2q^2+3q^3+5q^4+7q^5+11q^6+15q^7+22q^8\right) q^{3/40}\left(1-q^6-O(q^9)\right)$$
$$= q^{-1/30+1/15}\left(1+q+2q^2+3q^3+5q^4+7q^5+10q^6\right) \quad \text{(A.15)}$$

Therefore, the character of the identity operator is given by:

$$\begin{aligned}\chi_I &= \chi_{(1,1)}(q) + \chi_{(4,1)}(q) \\ &= q^{-1/30}\left(1+q^2+q^3+2q^4+2q^5+4q^6\right) + q^{-1/30+3}\left(1+q+2q^2+3q^3+4q^4+5q^5+8q^6\right) \\ &= q^{-1/30}\left(1+q^2+2q^3+3q^4+4q^5+7q^6\right) \end{aligned} \tag{A.16}$$

The character of the ϵ operator is given by:

$$\begin{aligned}\chi_\epsilon &= \chi_{(2,1)}(q) + \chi_{(3,1)}(q) \\ &= q^{-1/30+2/5}\left(1+q+q^2+2q^3+3q^4+4q^5+6q^6\right) + q^{-1/30+7/5}\left(1+q+2q^2+2q^3+4q^4+5q^5+8q^6\right) \\ &= q^{-1/30+2/5}\left(1+2q+2q^2+4q^3+5q^4+8q^5+11q^6\right) \end{aligned} \tag{A.17}$$

	free		A-A		A-B		A-free	
ground-state	I_0	0.8274	I_0	0.8573	ψ_0	0.8622	$(1,2)_0$	0.8391
1st excited	ψ_0	0.8438	I_2	0.8691	ψ_1	0.8669	$(1,2)_1$	0.8576
2nd excited	ψ_0	0.8438	I_3	0.8583	ψ_2	0.8619	$(4,2)_0$	0.8518
3rd excited	ψ_1	0.8468	I_3	0.8689	ψ_2	0.8672	$(1,2)_2$	0.8588
4th excited	ψ_1	0.8468	I_4	0.8590	ψ_3	0.8626	$(4,2)_1$	0.8547
5th excited	I_2	0.8517	I_4	0.8680	ψ_3	0.8666	$(1,2)_3$	0.8590
6th excited	ψ_2	0.8434	I_4	0.8703	ψ_4	0.8619	$(1,2)_3$	0.8630
7th excited	ψ_2	0.8434	I_5	0.8587	ψ_4	0.8636	$(4,2)_2$	0.8541
8th excited	ψ_2	0.8477	I_5	0.8597	ψ_4	0.8660	$(4,2)_2$	0.8569
9th excited	ψ_2	0.8477	I_5	0.8679	ψ_4	0.8726	$(1,2)_4$	0.8521
10th excited	I_3	0.8409	I_5	0.8703	ψ_5	0.8626	$(1,2)_4$	0.8561
11th excited	I_3	0.8513	I_6	0.8590	ψ_5	0.8635	$(1,2)_4$	0.8614
12th excited	ψ_3	0.8451	I_6	0.8605	ψ_5	0.8645	$(4,2)_3$	0.8462
13th excited	ψ_3	0.8451	I_6	0.8610	ψ_5	0.8656	$(4,2)_3$	0.8518
14th excited	ψ_3	0.8481	I_6	0.8639	ψ_5	0.8732	$(4,2)_3$	0.8537
15th excited	ψ_3	0.8481	I_6	0.8673	ψ_6	0.8557	$(1,2)_5$	0.8528
16th excited	I_4	0.8421	I_6	0.8700	ψ_6	0.8594	$(1,2)_5$	0.8554
17th excited	I_4	0.8508	I_6	0.8714	ψ_6	0.8606	$(1,2)_5$	0.8608
18th excited	I_4	0.8533	I_7	0.8598	ψ_6	0.8626	$(1,2)_5$	0.8648
19th excited	ψ_4	0.8454	I_7	0.8604	ψ_6	0.8637	$(4,2)_4$	0.8475
20th excited	ψ_4	0.8466	I_7	0.8616	ψ_6	0.8644	$(4,2)_4$	0.8508
stand. dev.	0.0033		0.0049		0.0040		0.0049	

Table A.2 – Velocities extracted for three-state Potts model from finite-size scaling of the ground state and first 20 excited states for open chain with free and fixed boundary conditions

	AB-AB		AB-AC		A-AB		A-BC		AB-free	
ground-state	I_0	0.8576	σ_0	1.0791	σ_0	0.6187	ϵ_0	0.9844	$(2,2)_0$	0.2003
1st excited	ϵ_0	0.7670	ψ_0	0.8503	σ_1	0.8370	ϵ_1	0.7733	$(3,2)_0$	0.7913
2nd excited	ϵ_1	0.8131	σ_1	0.8760	σ_2	0.8450	ϵ_1	0.8867	$(2,2)_1$	0.8971
3rd excited	ϵ_1	0.8853	ψ_1	0.8613	σ_2	0.8972	ϵ_2	0.8125	$(3,2)_1$	0.8242
4th excited	I_2	0.8688	σ_2	0.8069	σ_3	0.8487	ϵ_2	0.8825	$(2,2)_2$	0.8358
5th excited	ϵ_2	0.8220	σ_2	0.8705	σ_3	0.8514	ϵ_3	0.8219	$(2,2)_2$	0.8850
6th excited	ϵ_2	0.8769	ψ_2	0.8592	σ_3	0.8904	ϵ_3	0.8272	$(3,2)_2$	0.8200
7th excited	I_3	0.8576	ψ_2	0.8637	σ_4	0.8355	ϵ_3	0.8412	$(3,2)_2$	0.8343
8th excited	I_3	0.8708	σ_3	0.8194	σ_4	0.8509	ϵ_3	0.8797	$(2,2)_3$	0.8411
9th excited	ϵ_3	0.8298	σ_3	0.8666	σ_4	0.8535	ϵ_4	0.8312	$(2,2)_3$	0.8797
10th excited	ϵ_3	0.8612	σ_3	0.8684	σ_4	0.8853	ϵ_4	0.8361	$(2,2)_3$	0.8814
11th excited	ϵ_3	0.8727	ψ_3	0.8610	σ_4	0.8868	ϵ_4	0.8472	$(3,2)_3$	0.8295
12th excited	ϵ_3	0.8735	ψ_3	0.8643	σ_5	0.8390	ϵ_4	0.8784	$(3,2)_3$	0.8410
13th excited	I_4	0.8591	σ_4	0.8238	σ_5	0.8524	ϵ_4	0.8827	$(3,2)_3$	0.8777
14th excited	I_4	0.8702	σ_4	0.8269	σ_5	0.8549	ϵ_5	0.8344	$(2,2)_4$	0.8424
15th excited	I_4	0.8730	σ_4	0.8660	σ_5	0.8573	ϵ_5	0.8387	$(2,2)_4$	0.8460
16th excited	ϵ_4	0.8291	σ_4	0.8674	σ_5	0.8815	ϵ_5	0.8431	$(2,2)_4$	0.8768
17th excited	ϵ_4	0.8324	σ_4	0.8710	σ_5	0.8833	ϵ_5	0.8507	$(2,2)_4$	0.8795
18th excited	ϵ_4	0.8618	ψ_4	0.8615	σ_5	0.8859	ϵ_5	0.8507	$(3,2)_4$	0.8303
19th excited	ϵ_4	0.8698	ψ_4	0.8624	σ_6	0.8410	ϵ_5	0.8749	$(3,2)_4$	0.8349
20th excited	ϵ_4	0.8711	ψ_4	0.8638	σ_6	0.8456	ϵ_5	0.8784	$(3,2)_4$	0.8436
stand. dev.	0.0290		0.0196		0.0206		0.0292		0.0276	

Table A.3 – Velocities extracted for three-state Potts model from finite-size scaling of the ground state and first 20 excited states for open chain with partially fixed boundary conditions. The standard deviation for towers where the finite-size corrections are observed is more then five times larger than standard Deviations computed in Table A.2

B Non-abelian bosonization

Wess-Zumino-Witten (WZW) models describe conformal field theories that obey the symmetries defined by Lie-algebra. WZW model are based on the non-linear sigma model[35] defined by the action:

$$S_{\mathrm{NLSM}} = \frac{1}{4a^2}\int d^2x \mathrm{Tr}'(\partial^\mu g^{-1}\partial_\mu g), \tag{B.1}$$

where a^2 is a positive coupling constant and $g(x)$ is a matrix bosonic field that obey Lie algebra, the trace is chosen to have representation-independent normalization $\mathrm{Tr}'(M^a, M^b) = 2\delta_{a,b}$ with $[M^a, M^b] = \sum_c i f_{abc} M^c$, where the f_{abc}'s are the structure constants of the Lie algebra and the M^a are the generators of the algebra in the matrix representation. This field theory is not scale invariant, since the dimensionless coupling constant a^2 at the quantum level acquires a scale dependence. Moreover, the currents defined as

$$J_z = \partial_z g g^{-1}, \qquad J_{\bar{z}} g^{-1}\partial_{\bar{z}} g \tag{B.2}$$

are not conserved in the nonlinear sigma model.

In order to preserve the symmetry and current conservation, a Wess-Zumino term

$$\Gamma = \frac{-i}{24\pi}\int d^3y \epsilon_{\alpha\beta\gamma}\mathrm{Tr}'(\tilde{g}^{-1}\partial^\alpha \tilde{g}\tilde{g}^{-1}\partial^\beta \tilde{g}\tilde{g}^{-1}\partial^\gamma \tilde{g}) \tag{B.3}$$

should be added to the action in Eq.B.1. The integral is defined on a three-dimensional manifold, the boundary of which corresponds to the original two-dimensional space. The field g is extended correspondingly to its three-dimensional version $\tilde{g}$. Then the Wess-Zumino-Witten action is given by:

$$S_{\mathrm{WZW}} = S_{\mathrm{NLSM}} + k\Gamma, \tag{B.4}$$

where integer k is the topological coupling constant that labels the levels of the WZW model. The currents B.2 are conserved for $a^2 = 4\pi/k$ [35].

It was suggested by Affleck [2] that in some cases critical antiferromagnetic spin-S chains are described by the WZW $\mathrm{SU}(2)_k$ model with $k = 2S$. The central charge is given by $c = 3k/(2+k)$. As shown in Ref.[6] relevant operators emerge for all $k > 1$ and the number of such relevant operators is the largest integer j such that $j \leq k/2$ and $j(j+1) < 2+k$. Thus, for WZW $\mathrm{SU}(2)_2$, the largest integer that satisfies both conditions is equal to $j = 1$. This is consistent with the effective Hamiltonian 4.16 that contains only one relevant operator $\lambda_1(\mathrm{tr}g)^2$ that controls the quantum phase transition from the Haldane phase to the dimerized one.

In non-abelian bosonization, a spin-S is treated as a collection of $n_c = 2S$ spins-1/2 of different colors such that

$$\mathbf{S}_n = \sum_i \mathbf{S}_{in} = \frac{1}{2}\sum_{i\alpha,\beta} \psi_n^{\dagger i\alpha}\vec{\sigma}^{\alpha\beta}\psi_{i\beta n}, \tag{B.5}$$

where i is a color index, n is a position index and σ is a vector of Pauli's matrices. Fermionic operator $\psi_{i\beta n}$ annihilates an electron of color i and spin β at site n.

Thus, the spin-S antiferromagnetic Heisenberg Hamiltonian

$$H = J\sum_n \mathbf{S}_n \cdot \mathbf{S}_{n+1} \tag{B.6}$$

can be expressed in terms of the fermionic creation and annihilation aperators introduced above:

$$\begin{aligned}
H &= J\sum_n \sum_{i\alpha\beta} \frac{1}{2}\psi_n^{\dagger i\alpha}\vec{\sigma}^{\alpha\beta}\psi_{i\beta n} \cdot \sum_{j\alpha'\beta'} \frac{1}{2}\psi_{n+1}^{\dagger j\alpha'}\vec{\sigma}^{\alpha'\beta'}\psi_{j\beta'(n+1)} \\
&= J\frac{1}{4}\sum_n \sum_{ij} \sum_{\alpha\beta\alpha'\beta'} \psi_n^{\dagger i\alpha}\psi_{i\beta n}\psi_{n+1}^{\dagger j\alpha'}\psi_{j\beta'(n+1)}\vec{\sigma}^{\alpha\beta}\cdot\vec{\sigma}^{\alpha'\beta'} \\
&= J\frac{1}{4}\sum_n \sum_{ij} \sum_{\alpha\beta\alpha'\beta'} \psi_n^{\dagger i\alpha}\psi_{i\beta n}\psi_{n+1}^{\dagger j\alpha'}\psi_{j\beta'(n+1)}2\delta^{\alpha\beta'}\delta^{\alpha'\beta} \\
&= J\frac{1}{2}\sum_n \sum_{ij} \sum_{\alpha\beta} \psi_n^{\dagger i\alpha}\psi_{i\beta n}\psi_{n+1}^{\dagger j\beta}\psi_{J\alpha(n+1)} \\
&= \frac{-J}{2}\sum_n \sum_{ij} \sum_{\alpha\beta} \psi_n^{\dagger i\alpha}\psi_{j\alpha(n+1)}\psi_{n+1}^{\dagger j\beta}\psi_{i\beta n}
\end{aligned} \tag{B.7}$$

One can decompose an annihilation operator into a pair of slowly varying ones on a lattice space operators $\psi_{L(R)}$ that annihilates left- (right-) moving electrons and create left- (right-)

moving holes:

$$\frac{1}{\sqrt{a}}\psi_{i\alpha n} \approx e^{i\pi an/2}\psi_{Li\alpha}(an) + e^{-i\pi an/2}\psi_{Ri\alpha}(an) \tag{B.8}$$

This leads to a continuum Hamiltonian (after setting the Fermi-velocity to one)[6]:

$$H = i\int dx\left[\psi_L^{\dagger i\alpha} d_x \psi_{Li\alpha} - \psi_R^{\dagger i\alpha} d_x \psi_{Ri\alpha}\right]. \tag{B.9}$$

The corresponding Lagrangian density is given by:

$$\mathscr{L} = i\left(\psi_L^{\dagger i\alpha}\partial_- \psi_{Li\alpha} + \psi^{\dagger i\alpha\partial_+\psi_{Ri\alpha}}\right), \tag{B.10}$$

where $\partial_\pm = \partial_t \pm \partial_x$. The energy momentum tensor can be also defined in terms of the left- and right-moving fermionic operators:

$$T_{L,R} = i\psi_{L,R}^{\dagger i\alpha}\partial_\pm \psi_{L,Ri\alpha} \tag{B.11}$$

Following Ref.[6], left and right moving U(1) currents are defined as:

$$J_{L,R} =: \psi_{L,R}^{\dagger i\alpha}\psi_{L,Ri\beta} :, \tag{B.12}$$

where the double dots denote normal ordering. Left and right moving spin currents are:

$$\vec{J}_{L,R} = \psi_{L,R}^{\dagger i\alpha}\frac{\vec{\sigma}_\alpha^\beta}{2}\psi_{L,Ri\beta} \tag{B.13}$$

For a critical spin-1/2 chain in the WZW $SU(2)_2$ universality class, the continuum representation of the spin operators in terms of the spin currents is given by:

$$\vec{S}_j \approx \vec{J}_L(j) + \vec{J}_R(j) + \frac{1}{2}(-1)^j(\psi_L^{\dagger\alpha}\vec{\sigma}_\alpha^\beta\psi_{R\beta}). \tag{B.14}$$

Applying bosonization to the second term one can find the expression for the spin operators[6] as it appears in Eq.4.15:

$$\vec{S}_j \approx \vec{J}_L(j) + \vec{J}_R(j) + C(-1)^j \mathrm{tr}(g\vec{\sigma}) \tag{B.15}$$

Now, let us consider two copies of spin chains with nearest-neighbor interactions (that is equivalent to J_2 next-nearest-neighbor coupling in the original Hamiltonian 4.4). The two chains are coupled with J_1 and J_3 interactions. The spin operators for each of the two chains

can be written as:

$$\vec{S}_{2j} \approx \vec{J}_L(2j) + \vec{J}_R(2j) + C(-1)^j \mathrm{tr}(g_1(2j)\vec{\sigma}), \tag{B.16}$$

$$\vec{S}_{2j+1} \approx \vec{J}_L(2j+1) + \vec{J}_R(2j+1) + C(-1)^j \mathrm{tr}(g_2(2j+1)\vec{\sigma}) \tag{B.17}$$

The dimerization order parameter is then:

$$D(j) = \vec{S}_{2j} \cdot [\vec{S}_{2j+1} - \vec{S}_{2j-1}] \propto [\vec{J}_L(2j) + \vec{J}_R(2j) + C(-1)^j \mathrm{tr}(g_1(2j)\vec{\sigma})] \times$$
$$[\vec{J}_L(2j+1) + \vec{J}_R(2j+1) + C(-1)^j \mathrm{tr}(g_2(2j+1)\vec{\sigma} - \vec{J}_L(2j-1) - \vec{J}_R(2j-1) - C(-1)^{j-1} \mathrm{tr}(g_2(2j-1)\vec{\sigma}], \tag{B.18}$$

Assuming that fields $\vec{J}_{L,R}$ and $g_{1,2}$ vary slowly on the lattice and thus $J_{L,R}(2j+1) \approx J_{L,R}(2j-1)$ and $g_2(2j+1) \approx g_2(2j-1)$, we get:

$$D(j) \propto [\vec{J}_L(2j) + \vec{J}_R(2j) + C(-1)^j \mathrm{tr}(g_1(2j)\vec{\sigma})] \times [C(-1)^j \mathrm{tr}(g_2(2j+1)\vec{\sigma}) - C(-1)^{j-1} \mathrm{tr}(g_2(2j-1)\vec{\sigma})]$$
$$\approx [\vec{J}_L + \vec{J}_R + C(-1)^j \mathrm{tr}(g_1\vec{\sigma})] \cdot 2C(-1)^j \mathrm{tr}(g_2\vec{\sigma}) \tag{B.19}$$

For the same reason, the alternating terms $(-1)^j \vec{J}_{L,R} \mathrm{tr}(g_2\vec{\sigma})$ can be dropped. The remaining term is:

$$D(j) \propto \mathrm{tr}(g_1\vec{\sigma}) \cdot \mathrm{tr}(g_2\vec{\sigma}) \tag{B.20}$$

On top of the WZW Hamiltonian there are, in principle, six operators that are allowed by the symmetry of the Hubbard model[6], but only two of them appear in the effective Hamiltonian for the spin-1 $J_1 - J_2 - J_3$ chain. As pointed out in the beginning of this Appendix, only one relevant operator is allowed for the WZW $SU(2)_2$ model. This operator can be written as $\lambda_1(\mathrm{tr}g)^2$. When $\lambda_1 < 0$ the energy of this term is minimized for $\langle \mathrm{tr}g \rangle \neq 0$ that, according to Ref.[6], corresponds to the dimerized phase with spontaneously broken translation symmetry. The second term that appears in the Hamiltonian is marginal and takes the form $\lambda_2 \vec{J}_L \cdot \vec{J}_R$. The effect of this term is explained in details in the main text.

C Variational calculations for spin-1 $J_1 - J_3$ chain

We recall the form of the Hamiltonian:

$$H_{J_1-J_3} = J_1 \sum_i \mathbf{S}_i \cdot \mathbf{S}_{i+1} + J_3 \sum_i [(\mathbf{S}_{i-1} \cdot \mathbf{S}_i)(\mathbf{S}_i \cdot \mathbf{S}_{i+1}) + \text{H.c.}] \,, \tag{C.1}$$

C.1 Variational phase diagram

First we derive the three-site interaction $\sum_i J_3 [(\mathbf{S}_{i-1} \cdot \mathbf{S}_i)(\mathbf{S}_i \cdot \mathbf{S}_{i+1}) + \text{H.}c.]$ in terms of quadrupolar operators $Q^{\alpha\beta} = S^\alpha S^\beta + S^\beta S^\alpha - \frac{2}{3} S(S+1)\delta_{\alpha\beta}$:

$$\begin{aligned}
&\sum_i (\mathbf{S}_{i-1} \cdot \mathbf{S}_i)(\mathbf{S}_i \cdot \mathbf{S}_{i+1}) + \text{H.}c. \\
&= \sum_i \sum_{\alpha,\beta} (S^\alpha_{i-1} S^\alpha_i)(S^\beta_i S^\beta_{i+1}) + \text{H.}c. \\
&= \sum_i \sum_{\alpha,\beta} S^\alpha_{i-1} (S^\alpha_i S^\beta_i + S^\beta_i S^\alpha_i) S^\beta_{i+1} \\
&= \sum_i \sum_{\alpha,\beta} S^\alpha_{i-1} (S^\alpha_i S^\beta_i + S^\beta_i S^\alpha_i - \frac{4}{3}\delta_{\alpha,\beta} + \frac{4}{3}\delta_{\alpha,\beta}) S^\beta_{i+1} \\
&= \sum_i \sum_{\alpha,\beta} S^\alpha_{i-1} Q^{\alpha\beta}_i S^\beta_{i+1} + \frac{4}{3} \sum_i \sum_{\alpha,\beta} S^\alpha_{i-1} S^\beta_{i+1} \delta_{\alpha,\beta} \\
&\qquad = \sum_i \sum_{\alpha,\beta} S^\alpha_{i-1} Q^{\alpha\beta}_i S^\beta_{i+1} + \frac{4}{3} \sum_i (\mathbf{S}_{i-1} \cdot \mathbf{S}_{i+1})
\end{aligned} \tag{C.2}$$

We compute variational energy for the state given by Eq. 7.12, here we recall the form of the

state:

$$|W\rangle = \frac{1}{2}e^{-i\varphi}\left(\cos\frac{\vartheta}{2} - \sin\frac{\vartheta}{2}\right)|1\rangle + \frac{-i}{\sqrt{2}}\left(\cos\frac{\vartheta}{2} + \sin\frac{\vartheta}{2}\right)|0\rangle + \frac{-1}{2}e^{i\varphi}\left(\cos\frac{\vartheta}{2} - \sin\frac{\vartheta}{2}\right)|\bar{1}\rangle \quad \text{(C.3)}$$

We introduce short-hand notations $a_i = \cos\frac{\vartheta_i}{2} - \sin\frac{\vartheta_i}{2}$ and $b_i = \cos\frac{\vartheta_i}{2} + \sin\frac{\vartheta_i}{2}$. We apply the Hamiltonian C.1 to this state:

J_1 contribution:

$\langle 11\|11\rangle$	$\frac{1}{16}a_1^2a_2^2$	$\langle 10\|01\rangle$ and $\langle 01\|10\rangle$	$\frac{2}{8}a_1b_1a_2b_2\cos(\varphi_1-\varphi_2)$
$\langle 1\bar{1}\|1\bar{1}\rangle$	$\frac{-1}{16}a_1^2a_2^2$	$\langle 1\bar{1}\|00\rangle$ and $\langle 00\|1\bar{1}\rangle$	$\frac{2}{8}a_1b_1a_2b_2\cos(\varphi_1-\varphi_2)$
$\langle \bar{1}1\|\bar{1}1\rangle$	$\frac{-1}{16}a_1^2a_2^2$	$\langle \bar{1}1\|00\rangle$ and $\langle 00\|\bar{1}1\rangle$	$\frac{2}{8}a_1b_1a_2b_2\cos(\varphi_1-\varphi_2)$
$\langle \bar{1}\bar{1}\|\bar{1}\bar{1}\rangle$	$\frac{1}{16}a_1^2a_2^2$	$\langle 0\bar{1}\|\bar{1}0\rangle$ and $\langle \bar{1}0\|0\bar{1}\rangle$	$\frac{2}{8}a_1b_1a_2b_2\cos(\varphi_1-\varphi_2)$

The terms from the left column vanish, the terms from the right column gives:

$$\langle W|H_1|W\rangle = J_1a_1b_1a_2b_2\cos(\varphi_1-\varphi_2) = J_1\left(\cos^2\frac{\vartheta_1}{2} - \sin^2\frac{\vartheta_1}{2}\right)\left(\cos^2\frac{\vartheta_2}{2} - \sin^2\frac{\vartheta_2}{2}\right)\cos(\varphi_1-\varphi_2) \quad \text{(C.4)}$$

Therefore:

$$\langle W|H_1|W\rangle = \boxed{J_1\cos\vartheta_1\cos\vartheta_2\cos(\varphi_1-\varphi_2)} \quad \text{(C.5)}$$

J_3 contribution:

1. Canceling terms:

$\langle 111\|111\rangle$	$\frac{2}{64}a_1^2a_2^2a_3^2$	$\langle 11\bar{1}\|11\bar{1}\rangle$	$\frac{-2}{64}a_1^2a_2^2a_3^2$	$\langle 1\bar{1}1\|1\bar{1}1\rangle$	$\frac{2}{64}a_1^2a_2^2a_3^2$	$\langle 1\bar{1}\bar{1}\|1\bar{1}\bar{1}\rangle$	$\frac{-2}{64}a_1^2a_2^2a_3^2$
$\langle \bar{1}11\|\bar{1}11\rangle$	$\frac{-2}{64}a_1^2a_2^2a_3^2$	$\langle \bar{1}1\bar{1}\|\bar{1}1\bar{1}\rangle$	$\frac{2}{64}a_1^2a_2^2a_3^2$	$\langle \bar{1}\bar{1}1\|\bar{1}\bar{1}1\rangle$	$\frac{-2}{64}a_1^2a_2^2a_3^2$	$\langle \bar{1}\bar{1}\bar{1}\|\bar{1}\bar{1}\bar{1}\rangle$	$\frac{2}{64}a_1^2a_2^2a_3^2$

$\langle 011\|101\rangle$ and $\langle 101\|011\rangle$	$\frac{2}{32}a_1b_1a_2b_2a_3^2\cos(\varphi_2-\varphi_1)$
$\langle 01\bar{1}\|10\bar{1}\rangle$ and $\langle 10\bar{1}\|01\bar{1}\rangle$	$\frac{-2}{32}a_1b_1a_2b_2a_3^2\cos(\varphi_2-\varphi_1)$
$\langle 001\|1\bar{1}1\rangle$ and $\langle 1\bar{1}1\|001\rangle$	$\frac{-2}{32}a_1b_1a_2b_2a_3^2\cos(\varphi_2-\varphi_1)$
$\langle 00\bar{1}\|1\bar{1}\bar{1}\rangle$ and $\langle 1\bar{1}\bar{1}\|00\bar{1}\rangle$	$\frac{2}{32}a_1b_1a_2b_2a_3^2\cos(\varphi_2-\varphi_1)$
$\langle 001\|\bar{1}11\rangle$ and $\langle \bar{1}11\|001\rangle$	$\frac{2}{32}a_1b_1a_2b_2a_3^2\cos(\varphi_2-\varphi_1)$
$\langle 00\bar{1}\|\bar{1}1\bar{1}\rangle$ and $\langle \bar{1}1\bar{1}\|00\bar{1}\rangle$	$\frac{-2}{32}a_1b_1a_2b_2a_3^2\cos(\varphi_2-\varphi_1)$
$\langle 0\bar{1}1\|\bar{1}01\rangle$ and $\langle \bar{1}01\|0\bar{1}1\rangle$	$\frac{-2}{32}a_1b_1a_2b_2a_3^2\cos(\varphi_2-\varphi_1)$
$\langle 0\bar{1}\bar{1}\|\bar{1}0\bar{1}\rangle$ and $\langle \bar{1}0\bar{1}\|0\bar{1}\bar{1}\rangle$	$\frac{2}{32}a_1b_1a_2b_2a_3^2\cos(\varphi_2-\varphi_1)$

$$
\begin{array}{ll}
\langle 101|110\rangle \text{ and } \langle 110|101\rangle & \frac{2}{32}a_1^2 a_2 b_2 a_3 b_3 \cos(\varphi_3-\varphi_2) \\
\langle 100|11\bar{1}\rangle \text{ and } \langle 11\bar{1}|100\rangle & \frac{2}{32}a_1^2 a_2 b_2 a_3 b_3 \cos(\varphi_3-\varphi_2) \\
\langle 100|1\bar{1}1\rangle \text{ and } \langle 1\bar{1}1|100\rangle & \frac{-2}{32}a_1^2 a_2 b_2 a_3 b_3 \cos(\varphi_3-\varphi_2) \\
\langle 1\bar{1}0|10\bar{1}\rangle \text{ and } \langle 10\bar{1}|1\bar{1}0\rangle & \frac{-2}{32}a_1^2 a_2 b_2 a_3 b_3 \cos(\varphi_3-\varphi_2) \\
\langle \bar{1}10|\bar{1}01\rangle \text{ and } \langle \bar{1}01|\bar{1}10\rangle & \frac{-2}{32}a_1^2 a_2 b_2 a_3 b_3 \cos(\varphi_3-\varphi_2) \\
\langle \bar{1}1\bar{1}|\bar{1}00\rangle \text{ and } \langle \bar{1}00|\bar{1}1\bar{1}\rangle & \frac{-2}{32}a_1^2 a_2 b_2 a_3 b_3 \cos(\varphi_3-\varphi_2) \\
\langle \bar{1}00|\bar{1}\bar{1}1\rangle \text{ and } \langle \bar{1}\bar{1}1|\bar{1}00\rangle & \frac{2}{32}a_1^2 a_2 b_2 a_3 b_3 \cos(\varphi_3-\varphi_2) \\
\langle \bar{1}0\bar{1}|\bar{1}\bar{1}0\rangle \text{ and } \langle \bar{1}\bar{1}0|\bar{1}0\bar{1}\rangle & \frac{2}{32}a_1^2 a_2 b_2 a_3 b_3 \cos(\varphi_3-\varphi_2)
\end{array}
$$

2. The non-vanishing terms:

$$
\begin{array}{ll}
\langle 011|110\rangle \text{ and } \langle 110|011\rangle & \frac{2}{32}a_1 b_1 a_2^2 a_3 b_3 \cos(\varphi_3-\varphi_1) \\
\langle 010|11\bar{1}\rangle \text{ and } \langle 11\bar{1}|010\rangle & \frac{2}{32}a_1 b_1 a_2^2 a_3 b_3 \cos(\varphi_3-\varphi_1) \\
\langle 0\bar{1}1|1\bar{1}0\rangle \text{ and } \langle 1\bar{1}0|0\bar{1}1\rangle & \frac{2}{32}a_1 b_1 a_2^2 a_3 b_3 \cos(\varphi_3-\varphi_1) \\
\langle 0\bar{1}0|1\bar{1}\bar{1}\rangle \text{ and } \langle 1\bar{1}\bar{1}|0\bar{1}0\rangle & \frac{2}{32}a_1 b_1 a_2^2 a_3 b_3 \cos(\varphi_3-\varphi_1) \\
\langle 010|\bar{1}11\rangle \text{ and } \langle \bar{1}11|010\rangle & \frac{2}{32}a_1 b_1 a_2^2 a_3 b_3 \cos(\varphi_3-\varphi_1) \\
\langle 0\bar{1}\bar{1}|\bar{1}\bar{1}0\rangle \text{ and } \langle \bar{1}\bar{1}0|0\bar{1}\bar{1}\rangle & \frac{2}{32}a_1 b_1 a_2^2 a_3 b_3 \cos(\varphi_3-\varphi_1) \\
\langle 0\bar{1}0|\bar{1}\bar{1}1\rangle \text{ and } \langle \bar{1}\bar{1}1|0\bar{1}0\rangle & \frac{2}{32}a_1 b_1 a_2^2 a_3 b_3 \cos(\varphi_3-\varphi_1) \\
\langle 01\bar{1}|\bar{1}10\rangle \text{ and } \langle \bar{1}10|01\bar{1}\rangle & \frac{2}{32}a_1 b_1 a_2^2 a_3 b_3 \cos(\varphi_3-\varphi_1)
\end{array}
$$

$$
\begin{aligned}
\frac{1}{2}J_3\cos(\varphi_3-\varphi_1)\left(\cos^2\frac{\vartheta_1}{2}-\sin^2\frac{\vartheta_1}{2}\right)\left(\cos\frac{\vartheta_2}{2}-\sin\frac{\vartheta_2}{2}\right)^2\left(\cos^2\frac{\vartheta_3}{2}-\sin^2\frac{\vartheta_3}{2}\right) \\
=\frac{1}{2}J_3\cos(\varphi_3-\varphi_1)\cos\vartheta_1(1-\sin\vartheta_2)\cos\vartheta_3
\end{aligned}
$$

$$
\begin{array}{ll}
\langle 010|1\bar{1}1\rangle \text{ and } \langle 1\bar{1}1|010\rangle & \frac{4}{32}a_1 b_1 a_2^2 a_3 b_3 \cos(\varphi_1+\varphi_3-2\varphi_2) \\
\langle 01\bar{1}|1\bar{1}0\rangle \text{ and } \langle 1\bar{1}0|01\bar{1}\rangle & \frac{4}{32}a_1 b_1 a_2^2 a_3 b_3 \cos(\varphi_1+\varphi_3-2\varphi_2) \\
\langle 0\bar{1}1|\bar{1}10\rangle \text{ and } \langle \bar{1}10|0\bar{1}1\rangle & \frac{4}{32}a_1 b_1 a_2^2 a_3 b_3 \cos(\varphi_1+\varphi_3-2\varphi_2) \\
\langle 0\bar{1}0|\bar{1}1\bar{1}\rangle \text{ and } \langle \bar{1}1\bar{1}|0\bar{1}0\rangle & \frac{4}{32}a_1 b_1 a_2^2 a_3 b_3 \cos(\varphi_1+\varphi_3-2\varphi_2)
\end{array}
$$

$$
\begin{aligned}
\frac{1}{2}J_3\cos(\varphi_1+\varphi_3-2\varphi_2)\left(\cos^2\frac{\vartheta_1}{2}-\sin^2\frac{\vartheta_1}{2}\right)\left(\cos\frac{\vartheta_2}{2}-\sin\frac{\vartheta_2}{2}\right)^2\left(\cos^2\frac{\vartheta_3}{2}-\sin^2\frac{\vartheta_3}{2}\right) \\
=\frac{1}{2}J_3\cos(\varphi_1+\varphi_3-2\varphi_2)\cos\vartheta_1(1-\sin\vartheta_2)\cos\vartheta_3
\end{aligned}
$$

$$
\begin{array}{ll}
\langle 000|10\bar{1}\rangle \text{ and } \langle 10\bar{1}|000\rangle & \frac{4}{16}a_1 b_1 b_2^2 a_3 b_3 \cos(\varphi_3-\varphi_1) \\
\langle 001|100\rangle \text{ and } \langle 100|001\rangle & \frac{4}{16}a_1 b_1 b_2^2 a_3 b_3 \cos(\varphi_3-\varphi_1) \\
\langle 000|\bar{1}01\rangle \text{ and } \langle \bar{1}01|000\rangle & \frac{4}{16}a_1 b_1 b_2^2 a_3 b_3 \cos(\varphi_3-\varphi_1) \\
\langle 00\bar{1}|\bar{1}00\rangle \text{ and } \langle \bar{1}00|00\bar{1}\rangle & \frac{4}{16}a_1 b_1 b_2^2 a_3 b_3 \cos(\varphi_3-\varphi_1)
\end{array}
$$

$$J_3 \cos(\varphi_3 - \varphi_1)\left(\cos^2\frac{\vartheta_1}{2} - \sin^2\frac{\vartheta_1}{2}\right)\left(\cos\frac{\vartheta_2}{2} + \sin\frac{\vartheta_2}{2}\right)^2\left(\cos^2\frac{\vartheta_3}{2} - \sin^2\frac{\vartheta_3}{2}\right)$$
$$= J_3 \cos(\varphi_3 - \varphi_1)\cos\vartheta_1(1+\sin\vartheta_2)\cos\vartheta_3$$

$$\langle W|H_3|W\rangle = \frac{1}{2}J_3\cos(\varphi_3-\varphi_1)\cos\vartheta_1\cos\vartheta_3(1-\sin\vartheta_2) + \frac{1}{2}J_3\cos(\varphi_1+\varphi_3-2\varphi_2)\cos\vartheta_1\cos\vartheta_3(1-\sin\vartheta_2)$$
$$+J_3\cos(\varphi_3-\varphi_1)\cos\vartheta_1\cos\vartheta_3(1+\sin\vartheta_2)$$

$$\langle W|H_3|W\rangle = \boxed{\frac{1}{2}J_3\cos\vartheta_1\cos\vartheta_3\left[\cos(\varphi_3-\varphi_1)(3+\sin\vartheta_2) + \cos(\varphi_1+\varphi_3-2\varphi_2)(1-\sin\vartheta_2)\right]}$$

Finally, the energy per site is given by:

$$E = \frac{J_1}{2}(\cos\vartheta_{i-1}\cos\vartheta_i\cos(\varphi_{i-1}-\varphi_i) + \cos\vartheta_i\cos\vartheta_{i+1}\cos(\varphi_i-\varphi_{i+1}))$$
$$+\frac{1}{2}J_3\cos\vartheta_{i-1}\cos\vartheta_{i+1}\left[\cos(\varphi_{i+1}-\varphi_{i-1})(3+\sin\vartheta_i) + \cos(\varphi_{i-1}+\varphi_{i+1}-2\varphi_i)(1-\sin\vartheta_i)\right] \tag{C.6}$$

C.2 One-magnon instability

In the vicinity of the ferromagnetic phase. We start with the ferromagnetic wave-function $|0\rangle = |S, S, ..., S, S\rangle$, such that $S_l^+|0\rangle = 0$.

Consider first the action of the Hamiltonian C.1 on the state $S_l^-|0\rangle$:

J_1-terms:

$$a_1 = J_1\frac{1}{2}\sum_{j=1}^{N} S_j^+ S_{j+1}^- S_l^-|0\rangle = \left\|\begin{cases} S_{l+1}^- S_l^+ S_l^-|0\rangle & \text{if } j = l \\ 0 & \text{otherwise}\end{cases}\right\| = \frac{1}{2}J_1 S_{l+1}^-(2S_l^z + S_l^- S_l^+)|0\rangle = \boxed{J_1 S\cdot S_{l+1}^-|0\rangle}$$

$$a_2 = J_1\frac{1}{2}\sum_{j=1}^{N} S_j^- S_{j+1}^+ S_l^-|0\rangle = \left\|\begin{cases} J_1 S_{l-1}^- S_l^+ S_l^-|0\rangle & \text{if } j = l-1 \\ 0 & \text{otherwise}\end{cases}\right\| = \frac{1}{2}J_1 S_{l-1}^-(2S_l^z + S_l^- S_l^+)|0\rangle = \boxed{J_1 S\cdot S_{l-1}^-|0\rangle}$$

$$a_3 = J_1 \sum_{j=1}^{N} S_j^z S_{j+1}^z S_l^- |0\rangle = \left\| \begin{cases} S^2 S_l^- |0\rangle & \text{if } j, j+1 \neq l \\ S(S-1) S_l^- |0\rangle & \text{otherwise} \end{cases} \right\| = J_1((N-2)S^2 + 2S(S-1)) \cdot S_l^- |0\rangle$$

$$= \boxed{J_1 S(NS-2) \cdot S_l^- |0\rangle}$$

J_3-terms:

$$b_{1,1} = J_3 \frac{1}{4} \sum_{j=1}^{N} S_{j-1}^+ S_j^- S_j^+ S_{j+1}^- S_l^- |0\rangle = 0$$

$$c_{1,1} = J_3 \frac{1}{4} \sum_{j=1}^{N} S_{j+1}^+ S_j^- S_j^+ S_{j-1}^- S_l^- |0\rangle = 0$$

$$b_{1,2} = J_3 \frac{1}{4} \sum_{j=1}^{N} S_{j-1}^+ S_j^- S_j^- S_{j+1}^+ S_l^- |0\rangle = 0$$

$$c_{1,2} = J_3 \frac{1}{4} \sum_{j=1}^{N} S_{j+1}^+ S_j^- S_j^- S_{j-1}^+ S_l^- |0\rangle = 0$$

$$b_{1,3} = J_3 \frac{1}{2} \sum_{j=1}^{N} S_{j-1}^+ S_j^- S_j^z S_{j+1}^z S_l^- |0\rangle = \left\| \begin{cases} S^2 \cdot S_{l+1}^- S_l^+ S_l^- |0\rangle & \text{if } j = l+1 \\ 0 & \text{otherwise} \end{cases} \right\|$$

$$= J_3 \frac{1}{2} S^2 \cdot S_{l+1}^- (2S_l^z + S_l^- S_l^+)|0\rangle = \boxed{J_3 S^3 \cdot S_{l+1}^- |0\rangle}$$

$$c_{1,3} = J_3 \frac{1}{2} \sum_{j=1}^{N} S_{j+1}^+ S_j^- S_j^z S_{j-1}^z S_l^- |0\rangle = \left\| \begin{cases} S^2 \cdot S_{l-1}^- S_l^+ S_l^- |0\rangle & \text{if } j = l-1 \\ 0 & \text{otherwise} \end{cases} \right\|$$

$$= J_3 S^2 \cdot S_{l-1}^- (2S_l^z + S_l^- S_l^+)|0\rangle = \boxed{J_3 S^3 \cdot S_{l-1}^- |0\rangle}$$

$$b_{2,1} = J_3 \frac{1}{2} \frac{1}{4} \sum_{j=1}^{N} S_{j-1}^- S_j^+ S_j^+ S_{j+1}^- S_l^- |0\rangle = 0$$

$$c_{2,1} = J_3 \frac{1}{4} \sum_{j=1}^{N} S_{j+1}^- S_j^+ S_j^+ S_{j-1}^- S_l^- |0\rangle = 0$$

$$b_{2,2} = J_3 \frac{1}{4} \sum_{j=1}^{N} S^-_{j-1} S^+_j S^-_j S^+_{j+1} S^-_l |0\rangle = \left\| \begin{cases} S^-_{l-2} S^+_{l-1} S^-_{l-1} S^+_l S^-_l |0\rangle & \text{if } j = l-1 \\ 0 & \text{otherwise} \end{cases} \right\|$$
$$= J_3 \frac{1}{4} S^-_{l-2} (2S^z_{l-1} + S^-_{l-1} S^+_{l-1})(2S^z_l + S^-_l S^+_l)|0\rangle$$
$$= \boxed{J_3 S^2 \cdot S^-_{l-2} |0\rangle}$$

$$c_{2,2} = J_3 \frac{1}{4} \sum_{j=1}^{N} S^-_{j+1} S^+_j S^-_j S^+_{j-1} S^-_l |0\rangle = \left\| \begin{cases} S^-_{l+2} S^+_{l+1} S^-_{l+1} S^+_l S^-_l |0\rangle & \text{if } j = l+1 \\ 0 & \text{otherwise} \end{cases} \right\|$$
$$= J_3 \frac{1}{4} S^-_{l+2} (2S^z_{l+1} + S^-_{l+1} S^+_{l=1})(2S^z_l + S^-_l S^+_l)|0\rangle$$
$$= \boxed{J_3 S^2 \cdot S^-_{l+2} |0\rangle}$$

$$b_{2,3} = J_3 \frac{1}{2} \sum_{j=1}^{N} S^-_{j-1} S^+_j S^z_j S^z_{j+1} S^-_l |0\rangle = \left\| \begin{cases} S^-_{l-1} S^+_l S^z_l S^z_{l+1} S^-_l |0\rangle & \text{if } j = l \\ 0 & \text{otherwise} \end{cases} \right\|$$
$$= J_3 \frac{1}{2} S(S-1) \cdot S^-_{l-1} (2S^z_l + S^-_l S^+_l)|0\rangle$$
$$= \boxed{J_3 S^2 (S-1) \cdot S^-_{l-1} |0\rangle}$$

$$c_{2,3} = J_3 \frac{1}{2} \sum_{j=1}^{N} S^-_{j+1} S^+_j S^z_j S^z_{j-1} S^-_l |0\rangle = \left\| \begin{cases} S^-_{l+1} S^+_l S^z_l S^z_{l-1} S^-_l |0\rangle & \text{if } j = l \\ 0 & \text{otherwise} \end{cases} \right\|$$
$$= J_3 \frac{1}{2} S(S-1) \cdot S^-_{l+1} (2S^z_l + S^-_l S^+_l)|0\rangle$$
$$= \boxed{J_3 S^2 (S-1) \cdot S^-_{l+1} |0\rangle}$$

$$b_{3,1} = J_3 \frac{1}{2} \sum_{j=1}^{N} S^z_{j-1} S^z_j S^+_j S^-_{j+1} S^-_l |0\rangle = \left\| \begin{cases} S^z_{l-1} S^z_l S^+_l S^-_{l+1} S^-_l |0\rangle & \text{if } j = l \\ 0 & \text{otherwise} \end{cases} \right\|$$
$$= J_3 \frac{1}{2} S^z_{l-1} S^z_l S^-_{l+1} (2S^z_l + S^-_l S^+_l)|0\rangle$$
$$= \boxed{J_3 S^3 \cdot S^-_{l+1} |0\rangle}$$

$$c_{3,1} = J_3 \frac{1}{2} \sum_{j=1}^{N} S^z_{j+1} S^z_j S^+_j S^-_{j-1} S^-_l |0\rangle = \left\| \begin{cases} S^z_{l+1} S^z_l S^+_l S^-_{l-1} S^-_l |0\rangle & \text{if } j = l \\ 0 & \text{otherwise} \end{cases} \right\|$$
$$= J_3 \frac{1}{2} S^z_{l+1} S^z_l S^-_{l-1} (2S^z_l + S^-_l S^+_l)|0\rangle$$
$$= \boxed{J_3 S^3 \cdot S^-_{l-1}|0\rangle}$$

$$b_{3,2} = J_3 \frac{1}{2} \sum_{j=1}^{N} S^z_{j-1} S^z_j S^-_j S^+_{j+1} S^-_l |0\rangle = \left\| \begin{cases} S^z_{l-2} S^z_{l-1} S^-_{l-1} S^+_l S^-_l |0\rangle & \text{if } j = l-1 \\ 0 & \text{otherwise} \end{cases} \right\|$$
$$J_3 \frac{1}{2} S^z_{l-2} S^z_{l-1} S^-_{l-1} (2S^z_l + S^-_l S^+_l)|0\rangle$$
$$= \boxed{J_3 S^2 (S-1) \cdot S^-_{l-1}|0\rangle}$$

$$c_{3,2} = J_3 \frac{1}{2} \sum_{j=1}^{N} S^z_{j+1} S^z_j S^-_j S^+_{j-1} S^-_l |0\rangle = \left\| \begin{cases} S^z_{l+2} S^z_{l+1} S^-_{l+1} S^+_l S^-_l |0\rangle & \text{if } j = l+1 \\ 0 & \text{otherwise} \end{cases} \right\|$$
$$= J_3 \frac{1}{2} S^z_{l+2} S^z_{l+1} S^-_{l+1} (2S^z_l + S^-_l S^+_l)|0\rangle$$
$$= \boxed{J_3 S^2 (S-1) \cdot S^-_{l+1}|0\rangle}$$

$$b_{3,3} + c_{3,3} = 2J_3 \sum_{j=1}^{N} S^z_{j-1} S^z_j S^z_j S^z_{j+1} S^-_l |0\rangle = \left\| \begin{cases} S^3 (S-1) \cdot S^-_l |0\rangle & \text{if } j-1, j+1 = l \\ S^2 (S-1)^2 \cdot S^-_l |0\rangle & \text{if } j = l \\ S^4 \cdot S^-_l |0\rangle & \text{otherwise} \end{cases} \right\|$$
$$= 2J_3 S^2 (2S(S-1) + (S-1)^2 + (N-3)S^2) \cdot S^-_l |0\rangle$$
$$= \boxed{2J_3 S^2 (NS^2 + 1) \cdot S^-_l |0\rangle}$$

Then after adding all the terms:

$$\begin{aligned} HS^-_l|0\rangle = &\left(J_1 S(NS-2) + 2J_3 S^2 (NS^2+1)\right) S^-_l |0\rangle \\ &+ S\left(J_1 + 4J_3 S^2 - 2J_3 S\right)(S^-_{l-1} + S^-_{l+1})|0\rangle \\ &+ \left(J_3 S^2\right)(S^-_{l-2} + S^-_{l+2})|0\rangle \end{aligned}$$

We introduce a short-hand notation: $HS_l^-|0\rangle = f_1 S_l^-|0\rangle + f_2(S_{l-1}^- + S_{l+1}^-)|0\rangle + f_3(S_{l-2}^- + S_{l+2}^-)|0\rangle$, where

$$f_1 = J_1 S(NS-2) + 2J_3 S^2(NS^2+1) = E_{FM} + 2S(J_3 S - J_1) \tag{C.7}$$

$$f_2 = S(J_1 + 4J_3 S^2 - 2J_3 S) \tag{C.8}$$

$$f_3 = J_3 S^2 \tag{C.9}$$

For the case of $S = 1$ the coefficients become:

$$f_1 = E_{FM} + 2(J_3 - J_1) \tag{C.10}$$

$$f_2 = J_1 + 2J_3 \tag{C.11}$$

$$f_3 = J_3 \tag{C.12}$$

The state $S_l^-|0\rangle$ itself is not a ground state of the Hamiltonian C.1. However, the following combination of these states is indeed a ground-state of the Hamiltonian C.1:

$$|\tilde{\varphi}(q)\rangle = \sum_{l=1}^{N} e^{iql} S_l^-|0\rangle \tag{C.13}$$

This state is not normalized yet:

$$\langle\tilde{\varphi}|\tilde{\varphi}\rangle = \sum_{l,k=1}^{N} \langle 0|e^{iq(l-k)} S_k^+ S_l^-|0\rangle = \left\| \begin{cases} \langle 0|2S_l^z + S_l^- S_l^+|0\rangle & \text{if } l = k \\ 0 & \text{otherwise} \end{cases} \right\| = \sum_{l=1}^{N} \langle 0|2S_l^z|0\rangle = 2SN \tag{C.14}$$

Then the normalized one-magnon state is given by:

$$|\varphi(q)\rangle = \frac{1}{\sqrt{2NS}} \sum_{l=1}^{N} e^{iql} S_l^-|0\rangle \tag{C.15}$$

Then, the energy of this state is

$$E(q) = f_1 + 2f_2 \cos q + 2f_3 \cos 2q \tag{C.16}$$

Bibliography

[1] I. Affleck. *Nucl. Phys. B*, 265:409, 1986.

[2] I. Affleck. Exact critical exponents for quantum spin chains, non-linear sigma-models at thetas=pi and the quantum hall effect. *Nuclear Physics B*, 265:409–447, March 1986.

[3] I Affleck, D Gepner, H J Schulz, and T Ziman. Critical behaviour of spin-s heisenberg antiferromagnetic chains: analytic and numerical results. *Journal of Physics A: Mathematical and General*, 23(20):4725, 1990.

[4] I. Affleck and A. W. W. Ludwig. The Kondo effect, conformal field theory and fusion rules. *Nuclear Physics B*, 352:849–862, April 1991.

[5] Ian Affleck. Universal term in the free energy at a critical point and the conformal anomaly. *Phys. Rev. Lett.*, 56:746–748, Feb 1986.

[6] Ian Affleck and F. D. M. Haldane. Critical theory of quantum spin chains. *Phys. Rev. B*, 36:5291–5300, Oct 1987.

[7] Ian Affleck, Tom Kennedy, Elliott H. Lieb, and Hal Tasaki. Rigorous results on valence-bond ground states in antiferromagnets. *Phys. Rev. Lett.*, 59:799–802, Aug 1987.

[8] T. Asano, Y. Ajiro, M. Mekata, H. Yamazaki, N. Hosoito, T. Shinjo, and H. Kikuchi. Single crystal susceptibility of the S = 1 one-dimensional Heisenberg antiferromagnet AgVP $_2$S $_6$. *Solid State Communications*, 90:125–128, April 1994.

[9] H. M. Babujian. Exact solution of the isotropic heisenberg chain with arbitrary spins: Thermodynamics of the model. *Nuclear Physics B*, 215(3):317 – 336, 1983.

[10] A. A. Belavin, Alexander M. Polyakov, and A. B. Zamolodchikov. Infinite Conformal Symmetry in Two-Dimensional Quantum Field Theory. *Nucl. Phys.*, B241:333–380, 1984.

[11] A. K. Bera, B. Lake, A. T. M. N. Islam, B. Klemke, E. Faulhaber, and J. M. Law. Field-induced magnetic ordering and single-ion anisotropy in the quasi-one-dimensional haldane chain compound $srni_2v_2o_8$: A single-crystal investigation. *Phys. Rev. B*, 87:224423, Jun 2013.

[12] M. V. Berry. Quantal phase factors accompanying adiabatic changes. *Proceedings of the Royal Society of London. A. Mathematical and Physical Sciences*, 392(1802):45–57, 1984.

[13] H. Bethe. Zur theorie der metalle. *Zeitschrift für Physik*, 71(3):205–226, 1931.

[14] H. W. J. Blöte, John L. Cardy, and M. P. Nightingale. Conformal invariance, the central charge, and universal finite-size amplitudes at criticality. *Phys. Rev. Lett.*, 56:742–745, Feb 1986.

[15] S. Brehmer, H.-J. Mikeska, M. Müller, N. Nagaosa, and S. Uchida. Effects of biquadratic exchange on the spectrum of elementary excitations in spin ladders. *Phys. Rev. B*, 60:329–334, Jul 1999.

[16] R. Bursill, G. A. Gehring, D. J. J. Farnell, J.B. Parkinson, Tao Xiang, and Chen Zeng. Numerical and approximate analytical results for the frustrated spin- 1/2 quantum spin chain. *Journal of Physics: Condensed Matter*, 7(45):8605, 1995.

[17] P. Calabrese and J. Cardy. Entanglement entropy and conformal field theory. *J. Phys. A: Math. Theor.*, 42:504005, 2009.

[18] S. Capponi, P. Lecheminant, and M. Moliner. Quantum phase transitions in multileg spin ladders with ring exchange. *Phys. Rev. B*, 88:075132, Aug 2013.

[19] J.L. Cardy and D. Llewelyn. *Phys. Lett. B*, 259:274, 1991.

[20] John L. Cardy. Effect of boundary conditions on the operator content of two-dimensional conformally invariant theories. *Nuclear Physics B*, 275(2):200 – 218, 1986.

[21] John L. Cardy. Boundary conditions, fusion rules and the verlinde formula. *Nuclear Physics B*, 324(3):581 – 596, 1989.

[22] Y. Chen, Z. Honda, A. Zheludev, C. Broholm, K. Katsumata, and S. M. Shapiro. Field-induced three- and two-dimensional freezing in a quantum spin liquid. *Phys. Rev. Lett.*, 86:1618–1621, Feb 2001.

[23] Natalia Chepiga, Ian Affleck, and Frédéric Mila. Comment on “frustration and multicriticality in the antiferromagnetic spin-1 chain”. *Phys. Rev. B*, 94:136401, Oct 2016.

[24] Natalia Chepiga, Ian Affleck, and Frédéric Mila. Dimerization transitions in spin-1 chains. *Phys. Rev. B*, 93:241108(R), Jun 2016.

[25] Natalia Chepiga, Ian Affleck, and Frédéric Mila. Spontaneous dimerization, critical lines, and short-range correlations in a frustrated spin-1 chain. *Phys. Rev. B*, 94:205112, Nov 2016.

[26] Natalia Chepiga, Frédéric Michaud, and Frédéric Mila. Berry phase investigation of spin-s ladders. *Phys. Rev. B*, 88:184418, Nov 2013.

[27] A. V. Chubukov. Spontaneous dimerization in quantum-spin chains. *Phys. Rev. B*, 43:3337–3344, Feb 1991.

[28] J. Darriet and L.P. Regnault. The compound y2banio5: A new example of a haldane gap in a s = 1 magnetic chain. *Solid State Communications*, 86(7):409 – 412, 1993.

[29] V. S. Dotsenko. Critical Behavior and Associated Conformal Algebra of the Z(3) Potts Model. *Nucl. Phys.*, B235:54–74, 1984.

[30] Y. Endoh, G. Shirane, R. J. Birgeneau, Peter M. Richards, and S. L. Holt. Dynamics of an $s = \frac{1}{2}$, one-dimensional heisenberg antiferromagnet. *Phys. Rev. Lett.*, 32:170–173, Jan 1974.

[31] Glen Evenbly and Guifre Vidal. *Quantum Criticality with the Multi-scale Entanglement Renormalization Ansatz*, pages 99–130. Springer Berlin Heidelberg, Berlin, Heidelberg, 2013.

[32] V.A. Fateev and A.B. Zamolodchikov. *Sov. Phys. JETP*, 62:215, 1985.

[33] G. Fáth, Ö. Legeza, and J. Sólyom. String order in spin liquid phases of spin ladders. *Phys. Rev. B*, 63:134403, Feb 2001.

[34] G. Fáth and J. Sólyom. Period tripling in the bilinear-biquadratic antiferromagnetic S =1 chain. *Phys. Rev. B*, 44:11836–11844, Dec 1991.

[35] P. Francesco P., Mathieu and Sénéchal. Conformal field theory. 1997.

[36] Daniel Friedan, Zong-an Qiu, and Stephen H. Shenker. Superconformal Invariance in Two-Dimensions and the Tricritical Ising Model. *Phys. Lett.*, B151:37–43, 1985.

[37] Daniel Friedan, Zongan Qiu, and Stephen Shenker. Conformal invariance, unitarity, and critical exponents in two dimensions. *Phys. Rev. Lett.*, 52:1575–1578, Apr 1984.

[38] V. Gritsev, B. Normand, and D. Baeriswyl. Phase diagram of the heisenberg spin ladder with ring exchange. *Phys. Rev. B*, 69:094431, Mar 2004.

[39] Zheng-Cheng Gu and Xiao-Gang Wen. Tensor-entanglement-filtering renormalization approach and symmetry-protected topological order. *Phys. Rev. B*, 80:155131, Oct 2009.

[40] I. Hagiwara, K. Katsumata, I. Affleck, B.I. Halperin, and J.P. Renard. *Phys. Rev. Lett.*, 65:3181, 1990.

[41] F. D. M. Haldane. Continuum dynamics of the 1-D heisenberg antiferromagnet: Identification with the o(3) nonlinear sigma model. *Physics Letters A*, 93(9):464–468, February 1983.

[42] M. Hälg, D. Hüvonen, T. Guidi, D. L. Quintero-Castro, M. Boehm, L. P. Regnault, M. Hagiwara, and A. Zheludev. Finite-temperature scaling of spin correlations in an experimental realization of the one-dimensional ising quantum critical point. *Phys. Rev. B*, 92:014412, Jul 2015.

[43] Masashi Hase, Minoru Soda, Takatsugu Masuda, Daichi Kawana, Tetsuya Yokoo, Shinichi Itoh, Akira Matsuo, Koichi Kindo, and Masanori Kohno. Experimental confirmation of spin gap in antiferromagnetic alternating spin-$\frac{3}{2}$ chain substances $r\mathrm{CrGeO_5}$ ($r = y$ or ^{154}Sm) by inelastic neutron scattering experiments. *Phys. Rev. B*, 90:024416, Jul 2014.

[44] I. U. Heilmann, G. Shirane, Y. Endoh, R. J. Birgeneau, and S. L. Holt. Neutron study of the line-shape and field dependence of magnetic excitations in $\mathrm{cucl_2{\cdot}2n(c_5d_5)}$. *Phys. Rev. B*, 18:3530–3536, Oct 1978.

[45] Keigo Hijii and Kiyohide Nomura. Universality class of an $s = \frac{1}{2}$ quantum spin ladder system with four-spin exchange. *Phys. Rev. B*, 65:104413, Feb 2002.

[46] Keigo Hijii, Shaojin Qin, and Kiyohide Nomura. Staggered dimer order and criticality in an $s = \frac{1}{2}$ quantum spin ladder system with four-spin exchange. *Phys. Rev. B*, 68:134403, Oct 2003.

[47] Keigo Hijii and Tôru Sakai. Ground state phase diagram of an $s = \frac{1}{2}$ two-leg heisenberg spin ladder system with negative four-spin interaction. *Phys. Rev. B*, 88:104403, Sep 2013.

[48] T. Hirano, H. Katsura, and Y. Hatsugai. Topological classification of gapped spin chains: Quantized berry phase as a local order parameter. *Phys. Rev. B*, 77:094431, Mar 2008.

[49] Z. Honda, H. Asakawa, and K. Katsumata. Magnetic field versus temperature phase diagram of a quasi-one-dimensional $S = 1$ heisenberg antiferromagnet. *Phys. Rev. Lett.*, 81:2566–2569, Sep 1998.

[50] Z Honda, K Katsumata, H Aruga Katori, K Yamada, T Ohishi, T Manabe, and M Yamashita. Inducing a magnetic ordering in the haldane material $\mathrm{ni(c_5h_14n_2)_2n_3(clo_4)}$ by magnetic field. *Journal of Physics: Condensed Matter*, 9(7):L83, 1997.

[51] Z. Honda, K. Katsumata, Y. Nishiyama, and I. Harada. Field-induced long-range ordering in an $s = 1$ quasi-one-dimensional heisenberg antiferromagnet. *Phys. Rev. B*, 63:064420, Jan 2001.

[52] O. Janson, S. Chen, A. A. Tsirlin, S. Hoffmann, J. Sichelschmidt, Q. Huang, Z.-J. Zhang, M.-B. Tang, J.-T. Zhao, R. Kniep, and H. Rosner. Structure and magnetism of $\mathrm{cr_2[bp_3o_{12}]}$: Towards the quantum-classical crossover in a spin-$\frac{3}{2}$ alternating chain. *Phys. Rev. B*, 87:064417, Feb 2013.

[53] V. G. Kac. *Contravariant form for infinite-dimensional Lie algebras and superalgebras*, pages 441–445. Springer Berlin Heidelberg, Berlin, Heidelberg, 1979.

[54] T. Kennedy. Exact diagonalisations of open spin-1 chains. *Journal of Physics: Condensed Matter*, 2(26):5737, 1990.

[55] Alexei Kitaev and John Preskill. Topological entanglement entropy. *Phys. Rev. Lett.*, 96:110404, Mar 2006.

[56] A. Kolezhuk, R. Roth, and U. Schollwöck. First order transition in the frustrated antiferromagnetic heisenberg $S = 1$ quantum spin chain. *Phys. Rev. Lett.*, 77:5142–5145, Dec 1996.

[57] A. Kolezhuk, R. Roth, and U. Schollwöck. Variational and density-matrix renormalization-group studies of the frustrated antiferromagnetic heisenberg s=1 quantum spin chain. *Phys. Rev. B*, 55:8928–8939, Apr 1997.

[58] A. K. Kolezhuk and U. Schollwöck. Connectivity transition in the frustrated $s = 1$ chain revisited. *Phys. Rev. B*, 65:100401, Feb 2002.

[59] Andrey R. Kolovsky. Atomic current in optical lattices: Reexamination of the esaki-tsu equation. *Phys. Rev. A*, 77:063604, Jun 2008.

[60] J. M. Kosterlitz and D. J. Thouless. Ordering, metastability and phase transitions in two-dimensional systems. *Journal of Physics C: Solid State Physics*, 6(7):1181, 1973.

[61] A. Läuchli, G. Schmid, and M. Troyer. Phase diagram of a spin ladder with cyclic four-spin exchange. *Phys. Rev. B*, 67:100409, Mar 2003.

[62] A. M. Läuchli. Operator content of real-space entanglement spectra at conformal critical points. *ArXiv e-prints*, March 2013.

[63] Andreas Läuchli, Guido Schmid, and Simon Trebst. Spin nematics correlations in bilinear-biquadratic $s = 1$ spin chains. *Phys. Rev. B*, 74:144426, Oct 2006.

[64] Arthur Lavarélo, Guillaume Roux, and Nicolas Laflorencie. Melting of a frustration-induced dimer crystal and incommensurability in the J_1-J_2 two-leg ladder. *Phys. Rev. B*, 84:144407, Oct 2011.

[65] P. Lecheminant and K. Totsuka. Phases of the generalized two-leg spin ladder: A view from the su(4) symmetry. *Phys. Rev. B*, 71:020407, Jan 2005.

[66] Michael Levin and Xiao-Gang Wen. Detecting topological order in a ground state wave function. *Phys. Rev. Lett.*, 96:110405, Mar 2006.

[67] Hui Li and F. D. M. Haldane. Entanglement spectrum as a generalization of entanglement entropy: Identification of topological order in non-abelian fractional quantum hall effect states. *Phys. Rev. Lett.*, 101:010504, Jul 2008.

[68] Elliott Lieb, Theodore Schultz, and Daniel Mattis. Two soluble models of an antiferromagnetic chain. *Annals of Physics*, 16(3):407 – 466, 1961.

[69] Chanchal K. Majumdar and Dipan K. Ghosh. On next nearest neighbor interaction in linear chain 1. *Journal of Mathematical Physics*, 10:1388–1398, 1969.

[70] Frédéric Michaud, Salvatore R. Manmana, and Frédéric Mila. Realization of higher wess-zumino-witten models in spin chains. *Phys. Rev. B*, 87:140404, Apr 2013.

[71] Frédéric Michaud, François Vernay, Salvatore R. Manmana, and Frédéric Mila. Antiferromagnetic spin-s chains with exactly dimerized ground states. *Phys. Rev. Lett.*, 108:127202, Mar 2012.

[72] M. Müller, T. Vekua, and H.-J. Mikeska. Perturbation theories for the $s = \frac{1}{2}$ spin ladder with a four-spin ring exchange. *Phys. Rev. B*, 66:134423, Oct 2002.

[73] H. Mutka, C. Payen, P. Molinié, J. L. Soubeyroux, P. Colombet, and A. D. Taylor. Dynamic structure factor [s(q,ω)] of the s=1 quasi-one-dimensional heisenberg antiferromagnet: Neutron-scattering study on $agvp_2s_6$. *Phys. Rev. Lett.*, 67:497–500, Jul 1991.

[74] Yasuo Narumi, Masayuki Hagiwara, Masanori Kohno, and Koichi Kindo. Evidence for the singlet-dimer ground state in an $S = 1$ antiferromagnetic bond alternating chain. *Phys. Rev. Lett.*, 86:324–327, Jan 2001.

[75] A. A. Nersesyan and A. M. Tsvelik. One-dimensional spin-liquid without magnon excitations. *Phys. Rev. Lett.*, 78:3939–3942, May 1997.

[76] Tamara S. Nunner, Philipp Brune, Thilo Kopp, Marco Windt, and Markus Grüninger. Cyclic spin exchange in cuprate spin ladders. *Phys. Rev. B*, 66:180404, Nov 2002.

[77] Kiyomi Okamoto and Kiyohide Nomura. Fluid-dimer critical point in s = 12 antiferromagnetic heisenberg chain with next nearest neighbor interactions. *Physics Letters A*, 169(6):433 – 437, 1992.

[78] Stellan Östlund and Stefan Rommer. Thermodynamic limit of density matrix renormalization. *Phys. Rev. Lett.*, 75:3537–3540, Nov 1995.

[79] B. Pahari, K. Ghoshray, R. Sarkar, B. Bandyopadhyay, and A. Ghoshray. Nmr study of ^{51}V in quasi-one-dimensional integer spin chain compound $Srni_2v_2o_8$. *Phys. Rev. B*, 73:012407, Jan 2006.

[80] Pierre Pfeuty. The one-dimensional ising model with a transverse field. *Annals of Physics*, 57(1):79 – 90, 1970.

[81] J. H. Pixley, Aditya Shashi, and Andriy H. Nevidomskyy. Frustration and multicriticality in the antiferromagnetic spin-1 chain. *Phys. Rev. B*, 90:214426, Dec 2014.

[82] Frank Pollmann, Ari M. Turner, Erez Berg, and Masaki Oshikawa. Entanglement spectrum of a topological phase in one dimension. *Phys. Rev. B*, 81:064439, Feb 2010.

[83] L. P. Regnault, I. Zaliznyak, J. P. Renard, and C. Vettier. Inelastic-neutron-scattering study of the spin dynamics in the haldane-gap system $ni(c_2h_8n_2)_2no_2clo_4$. *Phys. Rev. B*, 50:9174–9187, Oct 1994.

[84] L. P. Regnault, A. Zheludev, M. Hagiwara, and A. Stunault. Low-energy excitations in the magnetized state of the bond-alternating quantum $s = 1$ chain system $Ni(C_9D_{24}N_4)(NO_2)ClO_4$. *Phys. Rev. B*, 73:174431, May 2006.

[85] J. P. Renard, M. Verdaguer, L. P. Regnault, W. A. C. Erkelens, J. Rossat-Mignod, J. Ribas, W. G. Stirling, and C. Vettier. Quantum energy gap in two quasi-one-dimensional S=1 Heisenberg antiferromagnets (invited). *Journal of Applied Physics*, 63:3538–3542, April 1988.

[86] J. P. Renard, M. Verdaguer, L. P. Regnault, W. A. C. Erkelens, J. Rossat-Mignod, and W. G. Stirling. Presumption for a quantum energy gap in the quasi-one-dimensional S = 1 Heisenberg antiferromagnet $Ni(C_2H_8N_2)_2NO_2(ClO_4)$. *EPL (Europhysics Letters)*, 3:945, April 1987.

[87] A. Rocha-Caridi. *Vertex Operators in Mathematics and Physics: Proceedings of a Conference November 10–17, 1983*, chapter Vacuum Vector Representations of the Virasoro Algebra, pages 451–473. Springer US, New York, NY, 1985.

[88] R. Roth and U. Schollwöck. Frustrated antiferromagnetic quantum spin chains for spin length $s \geq 1$. *Phys. Rev. B*, 58:9264–9268, Oct 1998.

[89] K. P. Schmidt, H. Monien, and G. S. Uhrig. Rung-singlet phase of the $s = \frac{1}{2}$ two-leg spin-ladder with four-spin cyclic exchange. *Phys. Rev. B*, 67:184413, May 2003.

[90] U. Schollwöck. The density-matrix renormalization group. *Rev. Mod. Phys.*, 77:259–315, Apr 2005.

[91] Ulrich Schollwöck. The density-matrix renormalization group in the age of matrix product states. *Annals of Physics*, 326(1):96 – 192, 2011. January 2011 Special Issue.

[92] D. G. Shelton, A. A. Nersesyan, and A. M. Tsvelik. Antiferromagnetic spin ladders: Crossover between spin S =1/2 and S =1 chains. *Phys. Rev. B*, 53:8521–8532, Apr 1996.

[93] J. Stephenson and D. D. Betts. Ising model with antiferromagnetic next-nearest-neighbor coupling. ii. ground states and phase diagrams. *Phys. Rev. B*, 2:2702–2706, Oct 1970.

[94] John Stephenson. Close-packed anisotropic antiferromagnetic ising lattices. i. *Canadian Journal of Physics*, 47(23):2621–2631, 1969.

[95] John Stephenson. Ising model with antiferromagnetic next-nearest-neighbor coupling: Spin correlations and disorder points. *Phys. Rev. B*, 1:4405–4409, Jun 1970.

[96] L. A. Takhtajan. The picture of low-lying excitations in the isotropic heisenberg chain of arbitrary spins. *Physics Letters A*, 87(9):479 – 482, 1982.

[97] M. Takigawa, T. Asano, Y. Ajiro, and M. Mekata. Static properties of the s=1 one-dimensional antiferromagnet $agvp_2s_6$. *Phys. Rev. B*, 52:R13087–R13090, Nov 1995.

[98] M. Takigawa, T. Asano, Y. Ajiro, M. Mekata, and Y. J. Uemura. Dynamics in the $S = 1$ one-dimensional antiferromagnet $agvp_2s_6$ via ^{31}p and ^{51}v nmr. *Phys. Rev. Lett.*, 76:2173–2176, Mar 1996.

[99] H. N. V. Temperley and E. H. Lieb. Relations between the 'percolation' and 'colouring' problem and other graph-theoretical problems associated with regular planar lattices: some exact results for the 'percolation' problem. *Proc. Roy. Soc. Lond.*, A322:251–280, 1971.

[100] Y. Uchiyama, Y. Sasago, I. Tsukada, K. Uchinokura, A. Zheludev, T. Hayashi, N. Miura, and P. Böni. Spin-vacancy-induced long-range order in a new haldane-gap antiferromagnet. *Phys. Rev. Lett.*, 83:632–635, Jul 1999.

[101] Y.-J. Wang. Phase diagrams of the generalized spin-$\frac{1}{2}$ ladder under staggered field and dimerization: A renormalization-group study. *Phys. Rev. B*, 68:214428, Dec 2003.

[102] Zheng-Yuan Wang, Shunsuke C. Furuya, Masaaki Nakamura, and Ryo Komakura. Dimerizations in spin-s antiferromagnetic chains with three-spin interaction. *Phys. Rev. B*, 88:224419, Dec 2013.

[103] Steven R. White. Density matrix formulation for quantum renormalization groups. *Phys. Rev. Lett.*, 69:2863–2866, Nov 1992.

[104] Steven R. White and Ian Affleck. Dimerization and incommensurate spiral spin correlations in the zigzag spin chain: Analogies to the kondo lattice. *Phys. Rev. B*, 54:9862–9869, Oct 1996.

[105] Guangyong Xu, J. F. DiTusa, T. Ito, K. Oka, H. Takagi, C. Broholm, and G. Aeppli. y_2. *Phys. Rev. B*, 54:R6827–R6830, Sep 1996.

[106] A. Zheludev, T. Masuda, B. Sales, D. Mandrus, T. Papenbrock, T. Barnes, and S. Park. Distribution of exchange energy in a bond-alternating $s = 1$ quantum spin chain. *Phys. Rev. B*, 69:144417, Apr 2004.

[107] A. Zheludev, T. Masuda, I. Tsukada, Y. Uchiyama, K. Uchinokura, P. Böni, and S.-H. Lee. Magnetic excitations in coupled haldane spin chains near the quantum critical point. *Phys. Rev. B*, 62:8921–8930, Oct 2000.

Curriculum Vitae

Name: Natalia Chepiga
Nationality: Ukrainian
Place of birth: Kharkiv, Ukraine
Date of birth: December 27, 1988
Marital status: married
Address: Institute of Physics
École Polytechnique Fédérale de Lausanne
BSP 713.3 Rte de la Sorge
CH-1015 Lausanne, Switzerland
Phone: +41 78 9601133
Email: natalia.chepiga@epfl.ch
Languages: Russian, English, Ukrainian (fluent),
French(B1), German(A1)

Main research fields:

Condensed matter physics, Quantum many-body physics and strongly correlated systems, Quantum magnetism, Systems with topological order, Detection of Topological order (Berry phase, Entanglement spectrum and Entanglement Entropy, Sting Order Parameters, etc.), Quantum phase transitions, Conformal field theory, Computational physics, Algorithms for the simulation of strongly correlated many-body systems (Exact Diagonalization, Tensor Network Algorithms)

Current project:

Currently we are studying spin $S > 1$ chains with nearest (J_1) and next-nearest (J_2) neighbors interaction with an additional three-body term (J_3). Our previous study of this model on spin-1 chain revealed a very unusual Ising transition between Next-Nearest-Neighbor-Haldane phase and dimerized phase. The one of the aims of this projects is to check weather the non-magnetic transitions are present also in the phase diagrams for larger spins. Moreover, the transition from uniform to dimerized phases were found to be continuous in WZW $SU(2)_{2S}$ universality class for spins up to $S = 2$, while according to the field theory this is impossible for $S \geq 5/2$, because there are at least two relevant operators. We are trying to determine numerically the nature of the phase transition.

Education:

04/13 – now Ph.D. student at Institute of Physics, École Polytechnique Fédérale de Lausanne,
Supervisor: prof. Frédéric Mila
Thesis Title: *Dimerization and exotic criticality in spin-S chains*
Private defense: 21/02/2017
Public defense: 23/03/2017 (expected)

08/11 – 02/13 Master in Physics, École Polytechnique Fédérale de Lausanne,
Supervisor: prof. Frédéric Mila
Thesis Title: *Topological phase transitions in spin ladders*

09/07 – 07/11 BSc in Applied Physics with First Class Honors, V.N.Karazin Kharkiv National

University, Department of Theoretical Nuclear Physics
Supervisor: Sergey I. Shevchenko
Thesis Title: *Electrons-holes superfluidity description in terms of the order parameter*

09/00 – 06/07 High School Certificate with First Class Honors

Publications:

Natalia Chepiga, Frédéric Michaud, and Frédéric Mila,
Berry phase investigation of spin-S ladders
Phys. Rev. B **88**, 184418 (2013)

Natalia Chepiga, Ian Affleck, and Frédéric Mila,
Dimerization transitions in spin-1 chains
Phys. Rev. B **93**, 241108(R) (2016)

Natalia Chepiga, Ian Affleck, and Frédéric Mila,
Comment on "Frustration and Multicriticality in the Antiferromagnetic Spin-1 Chain"
Phys. Rev. B **94**, 136401 (2016)

Natalia Chepiga, Ian Affleck, and Frédéric Mila,
Spontaneous dimerization, critical lines, and short-range correlations in a frustrated spin-1 chain
Phys. Rev. B **94**, 205112 (2016)

Conference contributions:

Contributed talks:

02/17 Entanglement if strongly correlated systems, Benasque, Spain, *Dimerization and exotic criticality in spin-S chains*
09/16 Recent Progress in Low-Dimensional Quantum Magnetism, Lausanne, Switzerland, C*ritical lines and short-range correlations in a frustrated spin-1 chain*
07/16 Swiss Physical Society Meeting, Lugano, Switzerland, *Dimerization transitions in spin-1 chains*
07/16 Swiss Workshop on Materials with Novel Electronic Properties 2016, Les Diablerets, Switzerland, *Dimerization transitions in spin-1 chains*
05/16 Japan-Swiss Workshop 'Trends in Theory of Correlated Materials', PSI, Villigen, Switzerland, *Dimerization transitions in spin-1 chains*
10/14 Japan-Swiss Workshop 'Trends in Theory of Correlated Materials', Tokyo, Japan, *Berry phase investigation of spin-S ladders*
07/14 Swiss Physical Society Annual Meeting, Fribourg, Switzerland, *Berry phase investigation of spin-S ladders*

Poster presentations:

09/16 8th International Conference on Highly Frustrated Magnetism, Taipei, Taiwan, *Dimerization transitions in spin-1 chains*

01/15 Theory Winter School on New Trends in Frustrated Magnetism, Tallahassee, Florida, USA, *Frustration and spontaneous dimerization in spin-1 chain*

10/13 School on Advanced Algorithms for Correlated Quantum Matter, Würzburg, Germany, *Berry phase investigation of spin-S ladders*

07/13 Swiss Workshop on Materials with Novel Electronic Properties, Les Diablerets, Switzerland, *Berry phase investigation of frustrated quantum magnets*

Grant:

04/17-09/18 (expected) University of California, Irvine, US. **Project title:** Efficient Density Matrix Renormalization Group algorithm for two-dimensional systems and its applications. Grant is provided by Swiss National Science Foundation

Selected Awards:

10/11 – 02/13 Excellence scholarship provided by École Polytechnique Fédérale de Lausanne

09/06 – 08/08 Scholarship of the President of Ukraine

09/07 – 06/11 Governmental scholarships for students with excellent study results

09/03 – 08/06 Scholarship of the Kharkiv City Mayor

10/09 3rd prize in Open Olympiad in Applied Physics and Theoretical Mechanics, MIPT, Moscow, Russian Federation

09/07 – 06/11 Several diploma including 2nd prize in Olympiads in Physics for University Students (Supported by Ukrainian government)

04/06 – 04/07 1st and 2nd prizes in Ukrainian Competition of Research projects for High School Students in Physics

09/03 – 06/07 Several diploma including 1st and 2nd prizes in Olympiads in Physics for High School Students (Supported by Ukrainian government)

Teaching experience:

09/14 – 01/17 Teaching Assistant in 'Physique Statistique I' at EPFL

02/16 – 06/16 Teaching Assistant in 'Mathematical Methods for Physicists' at EPFL

02/15 – 06/15 Teaching Assistant in 'Physique Statistique II' at EPFL

09/13 – 12/13 Teaching Assistant in 'Statistiques et probabilités' at EPFL

11/07 – 06/11 High School Teacher in Advanced Physics and Mathematics at Private Boiko School, Kharkiv, Ukraine

08/08 – 08/09 Summer School Teacher for Granted Youth (supported by Kharkov City Council), Lyubotin, Kharkiv district, Ukraine

Volunteer projects:

07/10 Camp leader in the international volunteer project in Lyubotin, Kharkiv district, Ukraine

08/10 Environmental volunteer program in Vichy, France

08/09 Volunteer in Summer Camp in Schpangenberg, Germany

11/07 Team leader in Ukraine-China High School exchange program in Shitzyatjuan, China

References:

1. Prof. Frédéric Mila, École Polytechnique Fédérale de Lausanne, frederic.mila@epfl.ch

2. Prof. Ian Affleck, University of British Columbia, iaffleck@phas.ubc.ca